3 June 2002 VOL. 412 Nos. 1–2 ISSN 0040-6090

thin solid films

International Journal on the Science and Technology of Condensed Matter Films

Proceedings of the 4th Workshop on MBE and VPE Growth, Physics, Technology, Warsaw, Poland, 24–28 September 2001.

Guest Editor: J. Kossut

DISTRIBUTION STATEMENT A
Approved for Public Release
Distribution Unlimited

20030121 117

ELSEVIER

http://www.elsevier.com/locate/tsf

Editor-in-chief:
J. E. Greene

THIN SOLID FILMS

Types of Contributions
- original papers not previously published
- invited review articles
- letters, 1800–2500 words
- announcements, reports on conferences, news

More detailed instructions on the preparation of manuscripts for THIN SOLID FILMS are available at the journal's website at http://www.elsevier.com/locate/tsf

Sections
The journal is divided into the following sections.

A. **Synthesis and Characterization:** nucleation and growth from the gas, liquid and solid phases; microstructural and microchemical film characterization; new concepts and techniques for film synthesis, modification, processing and characterization.

B. **Surfaces, Interfaces and Colloidal Behaviour:** surface and interface phenomena: physics, chemistry and applications.

C. **Metallurgical, Protective and Hard Layers:** fundamental aspects of layers and coatings used in diffusion barrier, corrosion, high-temperature, wear, erosion, and other extreme environments.

D. **Mechanics and Nanomechanics of Thin Layers:** mechanical properties of thin layers and nanoscale structures; surface forces; micro- and nanoengineering.

E. **Electronics, Optics and Opto-electronics:** synthesis, properties and processing of layers used in electronic, optical and optoelectronic applications; device engineering.

F. **Magnetics and Magneto-optics:** fundamental aspects of layers used in magnetic and magneto-optic applications; magnetic, optical and magneto-optical recording devices.

G. **Superconductivity:** synthesis and properties of layers used in superconducting applications.

H. **Langmuir–Blodgett, Biological and Related Films:** synthesis and properties of Langmuir–Blodgett, biological and related layers; device applications.

I. **Thin Film Devices, Sensors and Actuators:** fabrication, processing and properties of devices including sensors and actuators based upon thin layers.

J. **Condensed Matter Film Behaviour:** interdisciplinary and multidisciplinary topics.

Submission of Papers
Manuscripts (original, two clear copies and accompanying diskette (MS-DOS or MAC format)) should be sent to:

Editorial Office of *THIN SOLID FILMS*
Département de génie physique,
École Polytechnique de Montréal,
C.P. 6079, Succursale Centre-ville,
Montréal, QC, CANADA H3C 3A7
Tel: (+1) 514-340-3730; Fax: (+1) 514-340-3218;
e-mail: tsf@polymtl.ca

To ensure an optimal refereeing process, we ask authors to provide, together with the manuscript, a list of 3 to 5 potential reviewers and their addresses/e-mail. All the authors of a paper should sign the covering letter. Contributions are accepted on the understanding that the authors have obtained the necessary authority for publication. Submission of a manuscript implies that it is not under consideration for publication elsewhere.

Publication Information

Thin Solid Films (ISSN 0040-6090). For 2002, volumes 400–422 are scheduled for publication. Subscription prices are available upon request from the Publisher or from the Regional Sales Office nearest you or from this Journal's website (http://www.elsevier.com/locate/tsf). Further information is available on this journal and other Elsevier Science products through Elsevier's website (http://www.elsevier.com). Subscriptions are accepted on a prepaid basis only and are entered on a calendar year basis. Issues are sent by standard mail (surface within Europe, air delivery outside Europe). Priority rates are available upon request. Claims for missing issues

Orders, claims, and product enquiries: please contact the Customer Support Department at the Regional Sales Office nearest you:

New York
Elsevier Science
P.O. Box 945
New York, NY 10159-0945, USA
Tel.: (+1)212-633-3730
[Toll free number for North American customers: 1-888-4ES-INFO (437-4636)]
Fax: (+1)212-633-3680
E-mail: usinfo-

Amsterdam
Elsevier Science
P.O. Box 211
1000 AE Amsterdam
The Netherlands
Tel.: (+31)20-4853757
Fax: (+31)20-4853432
E-mail: nlinfo-f@elsevier.com

Tokyo
Elsevier Science K.K.
9-15, Higashi-Azabu 1-chome
Minato-ku, Tokyo 106-0044
Japan
Tel.: (+81)3-5561-5033
Fax: (+81)3-5561-5047
E-mail: info@elsevier.com

Singapore
Elsevier Science
No. 1 Temasek Avenue
#17-01 MilleniaTower
Singapore 039192
Tel.: (+65)434-3727
Fax: (+65)337-2230
E-mail: asiainfo@elsevier.com

Rio de Janeiro
Elsevier Science
Rua Sete de Setembro 111/16 Andar
20050-002 Centro
Rio de Janeiro-RJ
Brazil
Tel. (+55)21-509-5340
Fax (+55)21-507-1991
E-mail: elsevier@campus.com.br
[Note (Latin America): for orders, claims and help desk information, please contact the Regional

REPORT DOCUMENTATION PAGE

Form Approved OMB No. 0704-0188

1. AGENCY USE ONLY (Leave blank)

2. REPORT DATE

2002

3. REPORT TYPE AND DATES COVERED

Conference Proceedings

4. TITLE AND SUBTITLE

Proceedings of the 4th Workshop on MBE and VPE Growth, Physics, Technology
Held in Warsaw, Poland, on 24-28 September 2001.

5. FUNDING NUMBERS

N68171-01-M-6331

6. AUTHOR(S)

7. PERFORMING ORGANIZATION NAME(S) AND ADDRESS(ES)

Institute of Physics, Poland

9. SPONSORING/MONITORING AGENCY NAME(S) AND ADDRESS(ES

United States Army, European Research Office, PSC 802 Box 15, FPO AE 09499-1500.

10. SPONSORING/MONITORING AGENCY REPORT NUMBER

R&D 9227-PH-03

11. SUPPLEMENTARY NOTES

Proceedings of the 4th Workshop on MBE and VPE Growth, Physics, Technology, held in Warsaw, Poland on 24-28 September 2001. Journal – Thin Solid Films, 3 June 2002, Vol. 412, No. 1-2, ISSN 0040-6090, 141 pages.

12a. DISTRIBUTION/AVAILABILITY STATEMENT

Approved for Public Release.

12b. DISTRIBUTION CODE

A

ABSTRACT (Maximum 200 words)

Contents: Preface (J. Kossut); Hybrid epitaxial structures for spintronics (J. De Boeck, W. Van Roy, V. Motsnyi, Z. Liu, K. Dessein, G. Borghs); Size effects in epitaxial films of magnetite (J. Korecki, B. Handke, N. Spiridis, T. I zak, I. Flis-Kabulska, J. Haber); Shadow mask technology (T. Schallenberg, C. Schumacher, S. Gundel, W. Faschinger); Trions as a probe of spin injection through II-VI magnetic/non-magnetic heterointerface (M. Ghali, J. Kossut, E. Janik, M. Kutrowski, L. Klopotowski, M. Potemski, R Teran); The growth modes of epitaxial Au/Co/Au sandwiches (A. Wawro, L.T. Baczewski, P. Pankowski, M. Kisielewski, I. Sveklo, A. Maziewski); Polarity selection process and polarity manipulation of GaN in MOVPE and RF-MBE growth (A. Yoshikawa, K. Xu); SiGe(C) epitaxial technologies-issues and prospectives (T.J. Grasby, T.E. Whall, E.H.C. Parker); Influence of covering on critical thickness of strained In_xGa_{1-x}-As layer (A. Jasik, K. Kosiel, Wlodzimierz. Strupi ski, M. Wesolowski); MOVPE technology and characterization of silicon δ-doped GaAs and $Al_xGa_{1-x}As$ (B. Ciana, D. Radziewicz, B. Paszkjewicz, M. Tlaczala, M. Utko, R Sitarek, G. S k, J. Misiewicz, R. Kinder, J. Kova, R. Srnanek); Explanation of the initial phase change vs. incident angle of the RHEED intensity oscillation (A. Nemcsics); Laterally overgrown structures as substrates for lattice mismatched epitaxy (Z.R. Zytkiewicz); Monitoring epiready semiconductor wafers (D.A. Allwood, S. Cox, N.J. Mason, R. Palmer, R. Young, P.J. Walker); Post-growth thermal treatment of self-assembled InAs/GaAs quantum dots (A. Babinski, J. Jasinski); CdSe quantum islands in ZnSe: a new approach (E. Kurtz, B. Dal Don, M. Schmidt, H. Kalt, C. Klingshirn, D. Litvinov, A. Rosenauer, D. Gerthsen); CdTe/ZnTe quantum dots-growth and optical properties (S. Mackowski); Investigations of optical properties of active regions in vertical cavity surface emitting lasers grown by MBE (K. Regi ski, T. Ochalski, J. Muszalski, M. Bugajski, J.P. Bergman, P.O. Holtz, B. Monemar); Photoluminescence mapping and angle-resolved photoluminescence of MBE-grown InGaAs/GaAs RC LED and VCSEL structures (A. Wojcik, T.J. Ochalski, J. Muszalski, E. Kowalczyk, K. Goszczy ski, M. Bugajski); Ferromagnetic GaMnAs/GaAs superlattices-MBE growth and magnetic properties (J. Sadowski, R. Mathieu, R Svedlindh, M. Karlsteen, J. Kanski, Y. Fu, J.T. Domagala, W. Szuszkiewicz, B. Hennion, D.K. Maude, R. Airey, G. Hill); MBE growth and characterization of Hg based compounds and heterostructures (C.R. Becker, X.C. Zhang, K. Ortner, J. Schmidt, A. Pfeuffer-Jeschke, V. Latussek, Y.S. Gui, V. Daumer, J. Liu, H. Buhmann, G. Landwebr, L.W. Molenkamp)

14. SUBJECT TERMS

US Army Research, Poland, Epitaxial structures, Epitaxial films, Shadow mask technology, Trions, Spin injection, Polarity selection, Polarity manipulation, Quantum dots-growth, Optical properties, Lasers, Magnetic properties

15. NUMBER OF PAGES

16. PRICE CODE

17. SECURITY CLASSIFICATION OF REPORT	18. SECURITY CLASSIFICATION OF THIS PAGE	19, SECURITY CLASSIFICATION OF ABSTRACT	20. LIMITATION OF ABSTRACT
Unclassified	Unclassified	Unclassified	Unclassified

thin solid films

Volume 412/1–2 (2002)

DISTRIBUTION STATEMENT A
Approved for Public Release
Distribution Unlimited

ELSEVIER

Amsterdam — London — New York — Oxford — Paris — Shannon — Tokyo

thin solid films

An International Journal on the Science
and Technology of Condensed Matter Films

Volume 412/1–2 (2002)

Proceedings of the 4th Workshop on MBE and VPE Growth, Physics, Technology, Warsaw, Poland, 24–28 September 2001.

ELSEVIER
AMSTERDAM — LONDON — NEW YORK — OXFORD — PARIS — SHANNON — TOKYO

AQ F03-02-0379

USA mailing info: *Thin Solid Films* (ISSN 0040-6090) is published bimonthly by Elsevier Science B.H.V. (P.O. Box 1000 AE Amsterdam, The Netherlands). Annual subscription price in the USA is US$ 9529.00 (valid in North, Central and South America), including air speed delivery. Periodical postage rate is paid at Jamaica, NY 11431.31

USA POSTMASTER: Send address changes to *Thin Solid Films*, Publications Expediting Inc., 200 Meacham Avenue, Elmont, NY 11003.

AIRFREIGHT AND MAILING in the USA by Publications Expediting Inc., 200 Meacham Avenue, Elmont, NY 11003.

Advertising Information

Advertising orders and enquiries may be sent to: **Europe and ROW**: Rachel Leveson–Gower, Elsevier Science LTD., Advertising Department, The Boulevard, Langford Lane, Kidlington, Oxford OX5 1GB, UK; phone (+44) (1865) 843565; fax (+44) (1865) 843976; e-mail: r.leveson-gower@elsevier.co.uk. **USA and Canada:** Elsevier Science Inc., Mr Tino DeCarlo, 655 Avenue of the Americas, New York, NY 10010-5107, USA; phone: (+1) (212) 633 3815; fax (+1) (212) 633 3820; e-mail: t.decarlo@elsevier.com. **Japan:** Elsevier Science K.K., Advertising Department, 1-9-15 Higashi-Azabu, Minatoku, Tokyo 106-0044, **Japan;** phone (+81) (3) 5561-5033; fax: (+81)(3) 5561-5047.

Abstracting and Indexing Services

This journal is cited by the following Abstracting and/or Indexing Services. Metal Abstracts, Chemical Abstracts, INSPEC-Physics Abstracts, Current Contents — Physical and Chemical Sciences, Current Contents — Engineering, Technology and Applied Sciences, Engineering Index, Cambridge Scientific Abstracts, Physikalische Berichte, Science Citation Index, Research Alert™, PASCAL (Centre National de la Recherche Scientifique), Fiz Karlsruhe. Pre-publication abstracts of articles in Thin Solid Films and other related journals are now available weekly in electronic form via CoDas, a new direct alerting service in condensed matter and materials science run jointly by Elsevier Science Publishers and Institute of Physics Publishing. For details on a free one-month subscription contact Paul Bancroft on fax +44 117 9294318 or e-mail bancroft@ioppublishing.co.uk

International Standard Serial Number 0040-6090

© 2002 Elsevier Science B.V. All rights reserved.

This journal and the individual contributions contained in it are protected under copyright by Elsevier Science B.V., and the following terms and conditions apply to their use:

Photocopying

Single photocopies of single articles may be made for personal use as allowed by national copyright laws. Permission of the publisher and payment of a fee is required for all other photocopying, including multiple or systematic copying, copying for advertising or promotional purposes, resale, and all forms of document delivery. Special rates are available for educational institutions that wish to make photocopies for non-profit educational classroom use.

Permissions may be sought directly from Elsevier Science via their homepage (http://www.elsevier.com) by selecting “Customer support” and then “Permissions”. Alternatively you can send an email to: permissions@elsevier.co.uk, or fax to: (+44) 1865 853 333.

In the USA, users may clear permissions and make payment through the Copyright Clearance Center, Inc., 222 Rosewood Drive, Danvers, MA 01923, USA; phone: (978) 7508400; fax: (978) 7504744, and in the UK through the Copyright Licensing Agency Rapid Clearance Service (CLARCS), 90 Tottenham Court Road, London W1P 0LP, UK; phone: (+) 171 436 5931; fax: (+44) 171 436 3986. Other countries may have a local reprographic rights agency for payments.

Derivative Works

Subscribers may reproduce tables of contents or prepare lists of articles including abstracts for internal circulation within their institutions. Permission of the publisher is required for resale or distribution outside the institution.

Permission of the publisher is required for all other derivative works, including compilations and translations.

Electronic Storage or Usage

Permission of the publisher is required to store electronically any material contained in this journal, including any article or part of an article. Contact the publisher at the address indicated.

Except as outlined above, no part of this publication may be reproduced, stored in a retrieval system or transmitted in any form or by any means, electronic, mechanical, photocopying, recording or otherwise, without prior written permission of the publisher.

Address permissions requests to: Elsevier Science Global Rights Department, at the mail, fax and e-mail addresses noted above.

Notice

No responsibility is assumed by the publisher for any injury and/or damage to persons or property as a matter of products liability, negligence or otherwise, or from any use or operation of any methods, products, instructions or ideas contained in the material herein.

Although all advertising material is expected to conform to ethical (medical) standards, inclusion in this publication does not constitute a guarantee or endorsement of the quality or value of such product or of the claims made of it by its manufacturer.

∞ The paper used in this publication meets the requirements of ANSI/NISO Z39.48-1992 (Permanence of Paper).

Printed in The Netherlands

ELSEVIER

Volume 412 3 June 2002

thin solid films

www.elsevier.com/locate/tsf

Contents

ELSEVIER

Thin Solid Films 412 (2002) 1–2

thin solid films

www.elsevier.com/locate/tsf

Preface

The series of workshop-style on molecular beam epitaxy (MBE GPT standing for molecular beam epitaxy-growth physics and technology) was initiated in 1994 in Warsaw by Professor Marian Herman, at that time of the Institute of Vacuum Technology. The second and the third Workshops from this series were held in 1996 and 1999 also in Warsaw. The selected papers presented during these three meetings were published in *Thin Solid Films* (in volumes 267 [1–2], 306 [2] and 367 [1–2], respectively). It was during the last Workshop in 1999 that a decision was made to broaden a topical scope of the meetings by including the second of the fundamental methods of fabrication low dimensional semiconductors structures and thin films of other materials, namely the metalorganic vapour phase epitaxy. The motivation for such decision was obvious: it allowed critical comparison of results rendered by both MBE and VPE/CVD, which are to a certain degree competing, methods. Additionally, it was to let specialists in MBE learn secrets of the trade from MOCVD experts and vice versa. This latter rationale proved to be indeed a good idea, during the most recent, 'Fourth Workshop on MBE and VPE Growth, Physics, Technology' as it is named now.

As on previous occasions there were several Warsaw institutions that participated in the organisation of the event: the Institute of Physics of the Polish Academy of Sciences through the Centre of Excellence CELDIS established in it by the EU within the 5th Framework Programme; the Institute of Electron Technology; the Department of Experimental Physics of Warsaw University and the High Pressure Research Centre of the Polish Academy of Sciences. The Workshop was held on the Institute of Physics premises in the week of 24–28 September 2001. The programme was put together by representatives of all organising institutions, and more specifically by Professor Jacek Baranowski, Professor Maciej Bugajski, Professor Sylwester Porowski, Professor Marian Herman (who, unfortunately, was appointed to a post abroad and could not, therefore, be as active as usual in the organisation of the Workshop) and myself acting also as the Chairman of the Organising Committee.

As mentioned, the Centre of Excellence CELDIS in the Institute of Physics of the Polish Academy of Sciences was the principal financial contributor, however, contributions from the State Committee for Scientific Research, Poland, Committee of Physics of the Polish Academy of Sciences, Army Research Laboratory—European Research Office, London, and from the industry—Applied EPI and COMEF (representatives of CAMECA, RIBER S.A. and SPECTRAVISION for Poland) are greatly appreciated.

The attendance included representatives from 10 countries, including speakers from Japan, the US, many European countries and, of course, from Poland. Unfortunately, the tragic events of September 11th affected our meeting: several institutions have imposed strict travel rules which prevented some of the invited speakers either to fully participate in the Workshop or forced them to resign from coming altogether. My own impression, judging from the correspondence I have carried out immediately before the meeting, is that the same reason reduced the total number of participants. Conspicuous was also smaller attendance of participants from Russia.

The program consisted of invited talks and contributed presentations on both novel aspects of the techniques central to the topic but also devoted to characterisation of the samples of various materials, mostly semiconductors but including also metallic layers. Apart from purely scientific sessions a presentation of new equipment by the representative of (then) Applied EPI was organised. Representatives of COMEF were also present and had some information concerning products they distribute available. Of course, the proceedings contain only records of scientific presentations. Those appearing here were accepted after a usual peer review procedure. Of the total 30 presentations, these proceedings contain 19 papers. No extended abstracts were accepted for publi-

PII: S0040-6090(02)00325-5

cation (they were available to the participants in a workshop booklet). The papers accepted include all types of presentations, invited talks and contributed talks. I would like to thank at this point all of the anonymous referees who have carefully and critically read all submitted manuscripts and selected those suitable for publication. Of course, most of the responsibility in this respect is with the Guest Editor.

Warsaw, December 12th 2001.

Jacek Kossut

ELSEVIER

Thin Solid Films 412 (2002) 3–13

www.elsevier.com/locate/tsf

Hybrid epitaxial structures for spintronics

J. De Boeck*, W. Van Roy, V. Motsnyi, Z. Liu, K. Dessein, G. Borghs

IMEC, Kapeldreef 75, B-3001 Leuven, Belgium

Abstract

The use of electron spin in future spintronic applications requires hybrid ferromagnetic/semiconductor structures with well controlled materials properties. Besides the control of the magnetic properties there are strict requirements for the material aspects of these devices: single phase, single crystal, perfect interfaces, defect control. Molecular beam epitaxy (MBE) has been used very successfully over the past 10 years to produce the most interesting spintronic heterostructures. In this paper we review our effort in using MBE to fabricate spintronic materials and heterostructures. We also discuss some aspects of future spintronic devices with the focus on the material aspects of transferring the electron spin information from the magnetic side of the heterostructure into the semiconductor side. © 2002 Elsevier Science B.V. All rights reserved.

Keywords: Molecular beam epitaxy; Spintronic materials; Magnetic semiconductors; Spin-injection

1. Introduction

Molecular beam epitaxy (MBE) has proven its strengths in many fields of research and development on (opto-)electronics over the past decades. Spintronics, the field of electronics where the use of the electron spin in semiconductor components is envisaged, is no exception. In order to fabricate devices that intend to combine magnetic and semiconductor properties in very intimate way, the physical combination of the materials is required. One important requirement for spintronic components is the injection of electron spin polarized current into a semiconductor heterostructure, a process mostly referred to as spin-injection. This spin-injection process can be achieved by realizing a magnetic contact on a semiconductor or by the incorporation of some sort of spin-filter. This paper aims to illustrate the strength of MBE in realizing materials combinations that can lead to efficient spin-injection. It is not the ambition to give an exhaustive description of all possible materials combinations, but rather to review some important aspects of spin-source fabrication illustrated with some recent results from our own research activity. In line with today's emphasis to demonstrate the spin-injection process in III–V (electroluminescent) semiconductor devices, the paper will be focused on GaAs based epitaxial heterostructures.

In the first part of the paper we will describe the epitaxy of metallic ferromagnetic elements and alloys on GaAs. We review some results of initial experiments on Fe and Co epitaxy, since these materials are in the picture for Schottky barrier spin-injection devices today. Further, a brief description of Mn-based alloys will be presented, justified by the wealth of possible Mn-III or Mn-V alloys that can be epitaxially grown on GaAs with various properties. This section is followed by a summary of the results obtained recently on the epitaxial growth of NiMnSb on GaAs, a half-metallic magnetic alloy, that has potential to serve as a spin-source with 100% spin-polarization. We will further briefly discuss some results on the realization of heterostructures including two magnetic layers spaced by a semiconductor or vice versa.

A very appealing class of materials for spintronics is that of magnetic semiconductors, illustrated in this paper by (Al,Ga)MnAs. A concluding section deals with the contact strategies (ohmic, Schottky barrier or tunnel barrier) for spin-injection reports in which where the described materials combinations play an important role.

2. Epitaxy of metallic ferromagnets on semiconductor substrates

2.1. Requirements for good epitaxy

With the continuing downscaling of devices and with the advent of nanoscale devices, the dimensions of, e.g.

---

*Corresponding author. Tel.: +32-16-281518; fax: +32-16-281501.

E-mail address: deboeck@imec.be (J. De Boeck).

0040-6090/02/$ - see front matter © 2002 Elsevier Science B.V. All rights reserved.
PII: S0040-6090(02)00305-X

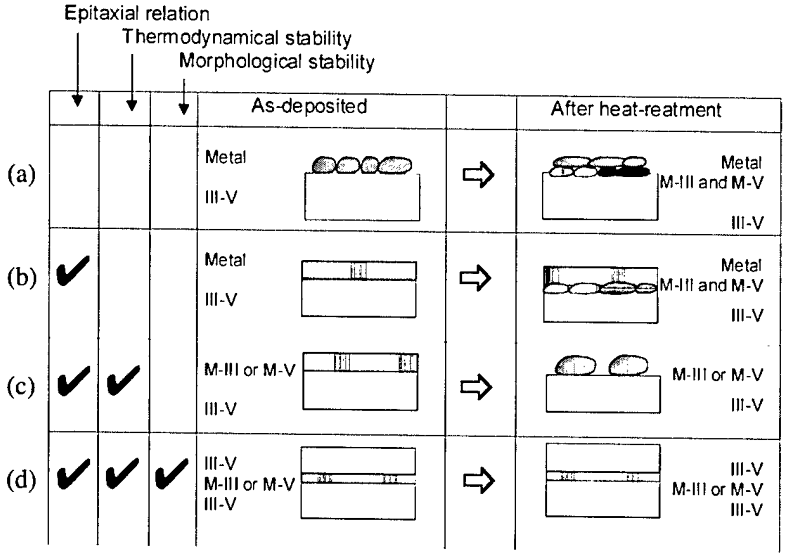

Fig. 1. Schematic representation of the conditions for realizing good epitaxial metal III-V heterostructures.

the metal contacts can be on the order of the grain size of the polycrystalline metals normally used. Although this might not be an important issue for standard electronic devices, it is a very important issue for devices working with the magnetic properties of the metallic contacts. Magnetic properties such as anisotropy and available spin-polarization, e.g. are very closely linked to crystal structure and orientation. MBE enables to realize epitaxial metallic structures with well-controlled crystal orientation and quality.

Epitaxy of metals on semiconductors has been an active area of research over the past two decades. Many successful attempts have been reported to deposit stable, single crystal metallic thin films on semiconductor surfaces. An excellent review of such studies for metal–III–V semiconductor combinations is published by Sands et al. [1]. The items of concern are schematically shown in Fig. 1. We finally want to arrive at a pinhole-free, monocrystalline metal. The interface should remain well defined after possible heat treatment during device fabrication or operation. Eventually, one may attempt to fabricate a metal/semiconductor/metal stack multilayer, in which case the epitaxy criterion is of importance to maintain good quality semiconductor overgrowth.

The result after annealing in conditions A of Fig. 1 is the typical case for a metal contact to a semiconductor structure, in, e.g. MESFET technology. After annealing many phases may form and the metal layer is polycrystalline in nature. In the as-grown condition there is no tendency to form a continuous layer due to the failure to meet the epitaxy criterion.

In case B (Fig. 1), there exists some epitaxial relation to the semiconductor, which helps to stabilize the metal layer. After heat treatment, phase separation occurs due to thermodynamical instability. When meeting both the epitaxy and the thermodynamical criteria, as in case C, the annealing will still cause problems due to insufficient morphological stability. The alloy phase that was deposited epitaxially as grown, will ball up into a highly textured polycrystalline film. Notice that, often metal-III or metal-V alloys have a higher chance to remain thermodynamically stable. In the final case (D), all three criteria are fulfilled and a stable metal/III–V heterostructure results. In this case, semiconductor overgrowth can be attempted with a reasonable chance of success. An example of the latter are GaAs/ErAs/GaAs resonant tunneling structures [2–4] and GaAs/AlAs/NiAl/AlAs/GaAs [5]. In the case of the GaAs/ErAs/GaAs heterostructures [6,7], a negative differential resistance was observed at room temperature for ErAs thicknesses in the range of 2.6–5 nm [8]. The success was attributed to the use of a Mn-template monolayer deposited prior to ErAs deposition.

2.2. *Co and Fe epitaxy on GaAs*

Fig. 2 shows a set of examples metallic and ferromagnetic structures that have been grown epitaxially on GaAs. The report on epitaxy of Co on GaAs by Prinz [9] is one of the pioneering papers on magnetic/semiconductor epitaxy [10]. Quite some research groups have been very active in the study of epitaxy of elemental magnetic thin films of Co and Fe on GaAs (for a review see also Bland and Heinrich [11]). Such studies have addressed in detail the evolution of the magnetic anisotropy of thin (a few monolayers) Fe [12] and Co films on GaAs. The substrate conditions prior to metal deposition are crucial in the control of this anisotropy since contributions to the net magnetic anisotropy arise from the formation of the interface and

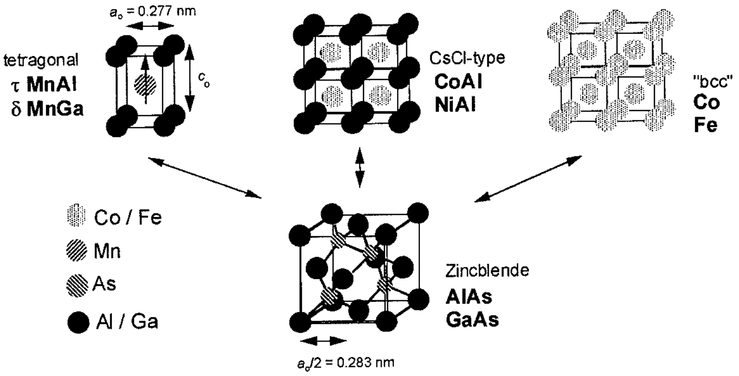

Fig. 2. A set of magnetic materials, well suited for epitaxy on the zinc-blende Ga(Al)As.

early stages of metal film growth. The determining factors are the initial metal adsorption sites and subsequent bond or site filling, and are strongly dependent on the semiconductor surface reconstruction [13,14]. Also, anisotropies can be influenced by surface topography, such as in the case of epitaxy on cross-hatched InGaAs epilayers [15], and by the early stages of the growth (e.g. step bunching and island formation). The domain structure and magnetization reversal processes, dictated by the induced magnetic anisotropy, have been studied in-situ and ex-situ.

In the case of Cobalt epitaxy on GaAs a forced phase [16] of Co, the bcc phase [9], can be realized due to the epitaxial relationship. A review of the bcc Co related work until 1991 was given by Prinz [17]. More recently the study of bcc Co as seed layers for epitaxial metal structures on GaAs has been reported, as well as further studies on the structural [18] and magnetic properties [19] of bcc Co and CoFe alloys [20]. The appearance of bcc Co in superlattices of Co/Fe [21–23], Co/Pd(111) [24] and Co/τ-MnAl [25] has been demonstrated. In the case of the Co/Fe superlattices, nuclear magnetic resonance (NMR) measurements on the short range chemical order in combination with hyperfine field experiments have illustrated the limits of stability. In superlattices with Co thicknesses above 2 nm, alloy formation with Fe at the interfaces is responsible for the observation of the bcc phase. From reflection high energy electron diffraction (RHEED) during the growth of the Co, it was concluded that the bcc phase is not sustained beyond approximately 1 nm.

2.3. Epitaxial Mn-based alloys on GaAs

When a metal alloy contains either a group III or a group V element, good interface characteristics can be expected. MnAs is such an alloy, that has been grown epitaxially on GaAs [26–28], for which it was shown that the preparation of the semiconductor surface before growth changes the orientation of the epilayer with respect to the crystal orientation of the substrate. Another example of this class is MnSb epitaxy which has been demonstrated recently [29,30]. As in the case of elemental metals, the magnetization of these epitaxially grown alloys is in the plane of the film. Another interesting class of epitaxial magnetic films is that of Mn-III alloys, in which the magnetization is out of the plane. Examples of this class are Mn-based magnetic thin films such as τ MnAl [31,32] and δ MnGa [33,34] (see Fig. 2). In these cases, the epitaxial growth on a III–V semiconductor substrate (such as GaAs) is the key to obtaining the desired perpendicular magnetization. The metastable phase τ MnAl can be stabilized by coherence to the semiconductor substrate and due to the epitaxial relationship, the *c*-axis of the tetragonal lattice is normal to the growth surface. As a consequence, the easy axis of the magnetization of the thin film points out of plane. The flexibility in engineering new epitaxial multilayers and new magnetic properties using this class of ferromagnetic films have been demonstrated: MnGa/NiGa [35] which multi-stepped hysteresis loops and ferrimagnetic τ MnAl/Co superlattices on GaAs [36–38], in which both magnetic sub-layers of the superlattice have a perpendicular magnetization, which are aligned anti-parallel at zero field. Very large antiferromagnetic interface coupling strength is observed, together with a strong perpendicular magnetic anisotropy for both the τ MnAl and the Co layers. Kerr hysteresis loops of τ MnAl/Co superlattices show abrupt transitions from anti-aligned to aligned states. The Co layers are found to be partially in the bcc phase.

In alloys like MnAl and MnGa, a large imbalance in density of states for majority and minority spins exists approximately 1 eV above the Fermi-level [39,40]. This property makes them interesting for ballistic magneto-transport studies in ferromagnet/semiconductor hybrid devices.

2.4. Epitaxial half-metallic ferromagnets

Even if one can realize perfect epitaxial metallic ferromagnets on a semiconductor, these structures will always suffer from the disadvantage that there is not a 100% polarization in the magnetic contact. Metallic ferromagnetic contacts have, at best, a polarization on the order of 40%. The spintronic device performance will be enhanced greatly, as described in more detail in the final section of this paper, when the spin-source for the device is polarized a full 100%. Such a situation occurs in half metallic ferromagnets, of which NiMnSb is one example which has been shown theoretically [41,42] and experimentally [43] to be half-metallic in the bulk. It has the interesting property that it meets the criteria to be grown epitaxially on GaAs [44]. The NiMnSb/GaAs combination is an excellent candidate for atomically controlled interfaces because its crystal structure is very closely related to the zinc-blende structure of III–V semiconductors [44]. With a bulk lattice constant [45] of 5.903 Å, NiMnSb shows a mismatch of 4.4% with GaAs ($c=5.6533$ Å). Our samples, typically consisting of a 200 nm GaAs buffer and 260–350-nm-thick NiMnSb films, were grown with a base pressure of less than 1×10^{-10} torr on either GaAs (001) or (111) [46]. The growth was initiated by simple co-evaporation of all three elements, i.e. no attempt was made to control the nucleation of NiMnSb on a particular plane in the initial experiments.

On GaAs (100), the best morphology was obtained at a substrate temperature of approximately 300 °C, where the RHEED patterns remained streaky throughout the entire growth. The stoichiometry of the films depended strongly on the Sb flux. Fig. 3 shows the Sb content x_{Sb} of NiMnSb 1:1:x_{Sb} films grown with an Sb BEP flux ϕSb=5~13×ϕNi, as measured by Rutherford back-scattering (RBS). In contrast to the growth of III–V semiconductors, there is no self-limiting mechanism for the incorporation of the group-V element. Rather, there is an optimum flux ratio ϕSb=10×ϕNi where stoichiometric films are obtained. Films grown with lower Sb flux are Sb deficient, while films grown at higher flux contain excess Sb. The total film thickness reflects these changes in Sb incorporation (Fig. 3b, determined by RBS).

All films grew in the (001) orientation as measured by XRD. Stoichiometric films showed a lattice constant c of 5.904–5.909 Å that is almost identical to the bulk lattice constant, while non-stoichiometric films, especially on the Sb-poor side, showed deviations, as indicated in Fig. 3c. NMR studies were performed on these films [47].

The room-temperature magnetization Ms shown in Fig. 3d correlates well with the structural properties of the films. Stoichiometric films have Ms of 450–570 kA/m slightly below the bulk value 720 kA/m and a coercive field, H_c of 2–4 mT. In addition, stoichiometric films show a varying degree of in-plane uniaxial anisotropy with the easy axis along ⟨110⟩ or ⟨1−10⟩ depending on the growth conditions and on the choice of interface layer. We are currently investigating the spin-polarization at the interface of the NiMnSb and GaAs/AlGaAs heterostructures by optical assessment of the spin-injection.

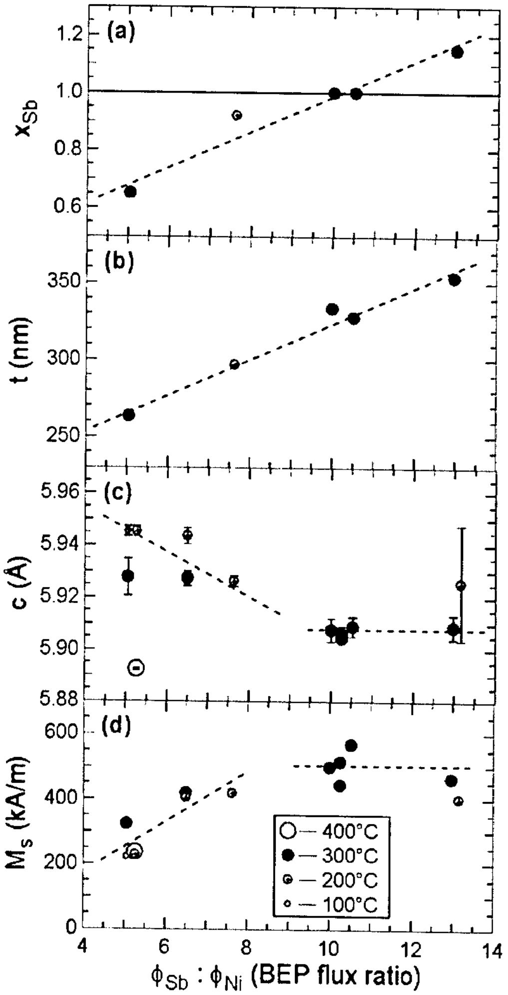

Fig. 3. Variations of the thin film properties of NiMnSb epitaxially grown on GaAs (001) with the variation of the Ni to Sb beam equivalent pressure.

Although there are many other candidates for half-metallic ferromagnetic contacts, such as Cr_2O with measured polarization of 96% and above [48], they all face the challenge to preserve the half-metallicity down to the injection interface, in addition to be stable and structurally compatible with the underlying semiconductor.

2.5. SC/FM/SC and FM/SC/FM heterostructures

As the technology of building artificial structures improves, even more challenging structures may become possible such as epitaxial multilayers of magnetic metal and semiconductors (case D in Fig. 1). Van Roy et al. reported magnetoresistance and coupling effects as a function of the (Ga,Mn,As) thickness in MnGa/

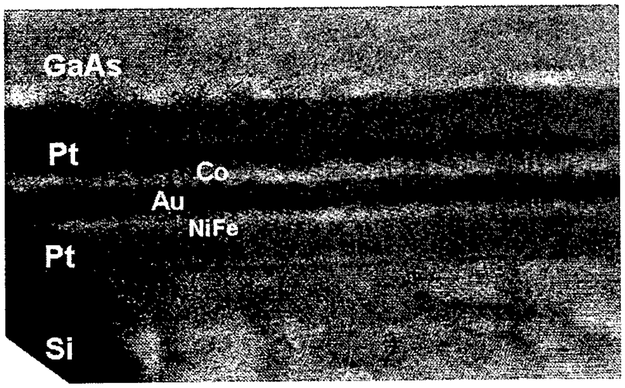

Fig. 4. A TEM cross-section of a GaAs/spin-valve/Si spin-valve transistor.

(Ga,Mn,As)/MnGa trilayers [49]. When such structures are further optimized, control of magnetic properties with external modulation sources such as optical power, may become reality. Butler et al. have performed calculations of the electronic structure of an Fe/GaAs/Fe structure. They conclude that the simple models relying on potential barriers or density of states from the bulk may not apply to such FM/SC/FM structure [50].

Magneto-optical properties of Co(100)/Ge/Co trilayers have been reported [51]. The coercivity and the anisotropy of these structures oscillate with the Ge thickness. CoPt/(Si, Ge)/Co trilayer and multilayer structures have been fabricated and analyzed using CPP magnetotransport [52]. In these structures a small steep CPP resistance change has been found that was ascribed to the change in the relative spin orientation of the Co (magnetic soft) and the CoP (magnetic hard) layers.

Although these structures show promising results, often stability at higher temperatures (even room temperature) is a critical issue.

One interesting example of a semiconductor/ferromagnetic/semiconductor is that of the spin-valve transistor (SVT) [53,54]. This device is a metal base transistor with a semiconductor emitter (either Si of GaAs) and a semiconductor collector (Si) in which the metal base is replaced by a spin-valve multilayer. Dessein et al. have succeeded in making a GaAs/SV/Si version of the SVT [55] in which MBE has played a crucial role for the fabrication of the Ga(Al)As emitter structure. The SVT device is fabricated by a room-temperature vacuum wafer bonding technique: two clean and smooth semiconductor substrates are brought into contact during the evaporation of the magnetic multilayer. The resulting bond is of very high structural and electrical quality. This is illustrated by Figs. 4 and 5. Fig. 4 shows a transmission electron microscopy (TEM) cross-section of the finished GaAs/Spin-valve/Si SVT. The magnetotransport characteristic in Fig. 5 illustrates the functionality of the device [56].

3. GaMnAs ferromagnetic semiconductor

3.1. Low-temperature MBE for GaMnAs

Although magnetic (half-)metallic materials offer great potential as contacts in hybrid spintronic devices, they do not offer any flexibility in terms of modulating their degree of spin-polarization. It would be nice to have a magnetic material that is fully compatible with a major class of semiconductors and that offers the possibility to change its ferromagnetic properties with light, voltage, current. Ferromagnetic semiconductors have that potential, in particular the ferromagnetic semiconductors that are based on GaAs and GaN III–V semiconductors. The most studied of this family is GaMnAs, in which a high concentration of Mn is incorporated in the zinc-blende lattice of the GaAs host. Again, MBE plays the leading role in the development of this material because of the need for growing the highly supersaturated GaMnAs far out of equilibrium conditions. The success in GaMnAs ferromagnetic material was initiated by the use of a low-temperature growth procedure [57,58]. Growth at such a low temperature is made necessary by the fact that at higher temperatures there is a tendency to form ferromagnetic MnAs precipitates within the GaMnAs alloy [59]. However, the low temperature necessary for such precipitate-free growth also results in the formation of As antisites that form deep levels, counteracting the effectiveness of the Mn^{2+} acceptors through compensation. Parameters such as temperature, relative cation fluxes and As overpressure play an important role in the quality of the final layer characterized often by the (critical-) paramagnetic-ferromagnetic transition temperature T_c. Efforts to optimize the incorporation of Mn into the III–V lattice have led to controversial statements [60,61] but good results

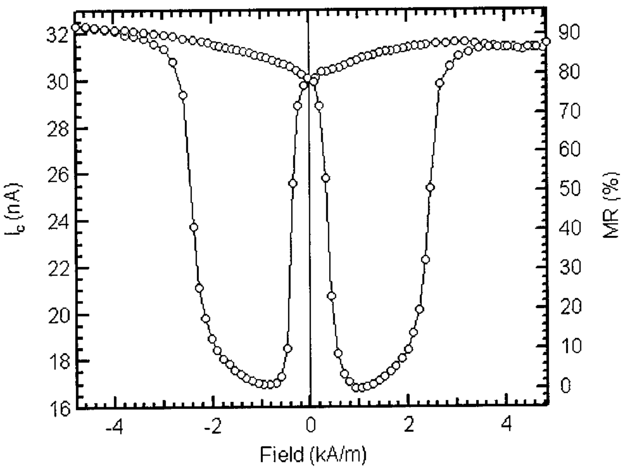

Fig. 5. The magnetocurrent characteristics of an optimized GaAs-spin-valve transistor.

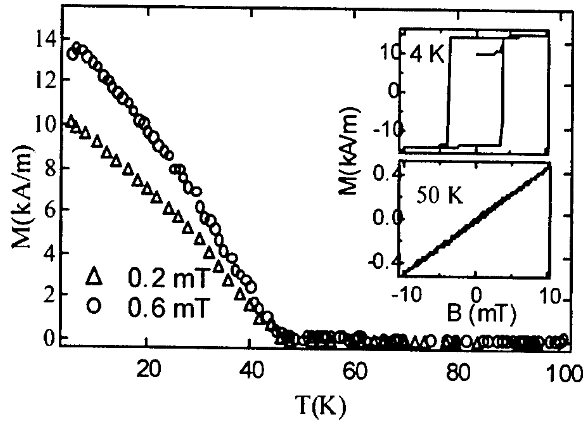

Fig. 6. SQUID magnetization measurements show the onset of magnetic ordering at $T_c = 45$ K. The insets show the hysteresis measured at $T = 4$ K with the field parallel to the surface and the paramagnetic signal at 50 K.

have been obtained by different groups and a T_c reaching 110 K has been reported [62].

3.2. The ferromagnetic properties of GaMnAs

The ferromagnetism of $III_{1-x}Mn_xAs$ alloys originates from two ingredients: the obvious presence of magnetic ions in the form of Mn^{2+} and the high concentration of holes in these systems, also supplied by the Mn^{2+} ion, which acts as an acceptor when substituted into the III–V lattice. The ferromagnetism of III–Mn-V as well as trends in the observed T_c have been explained by carrier-induced ferromagnetism in which uniform itinerant-carrier spin polarization mediates a long-range ferromagnetic interaction between the Mn^{2+} ions with spin 5/2 [63]. As was shown recently [64], the mean field theory based on the RKKY interaction has only limited validity, and although it can provide a realistic estimate of T_c it fails as a theory of the ferromagnetic state. It lacks dynamic correlations in the localized and itinerant spin system.

The most striking magnetic property of $III_{1-x}Mn_xV$ alloys is of course their ferromagnetic behavior below the Curie temperature. A characteristic hysteresis loop is demonstrated in the inset of Fig. 6.

3.3. Electronic properties of GaMnAs

Quantitative measurements of saturation magnetization Ms result in values close to the calculated value $N_{Mn}g\mu_bS$. However, annealing experiments have revealed that this value strongly depends on temperature during or after growth. Mn–As complexes can be formed during annealing, different from MnAs precipitates formed at higher temperatures. Also the number of holes for a given Mn concentration x can be maximized during growth by optimizing the growth parameters so as to reduce the As antisites.

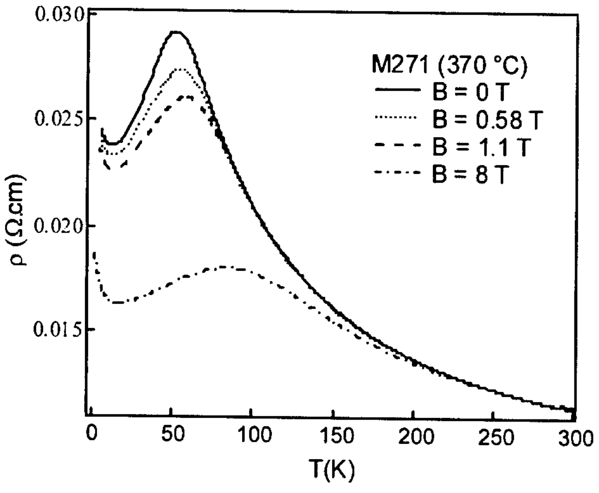

Fig. 7. Temperature dependence of the resistivity of Ga0.93Mn0.07As in a constant applied field of 0.58 T, 1.1 T and 8 T.

Hole concentrations in magnetic semiconductors are determined from Hall effect measurements but an accurate measurement is often troublesome, if possible at all, due to the contribution of the extra-ordinary Hall effect term. Moreover, the negative magnetoresistance effect and, at very low temperature, the contribution of a hopping component to the carrier transport further complicate the measurements.

According to Oiwa et al. [65] the magnetoelectronic states can be divided into three concentration regions: samples in the region $0.01 < x < 0.03$ are ferromagnetic but insulating (i.e. their resistivity increases dramatically with decreasing temperature; those in the range $0.03 < x < 0.06$ are metallic (i.e. their resistivity below T_c is approximately independent of temperature); and those samples with Mn concentration in the range above 0.06 again showing insulating behavior, most probably due to increased disorder of magnetic and coulombic nature. It is also striking that the metallic samples have the highest values of the Curie temperature.

For a given x there is an almost direct proportionality between the hole concentration p and the corresponding value of the Curie temperature, up to a value of almost $x = 0.06$ beyond which T_c drops again. The typical hole concentration is 20% below the Mn concentration due to compensation [62].

From the magnetic properties of GaMnAs it is clear that holes have a direct and decisive effect on the behavior of the system. It is not surprising that the inverse is also true: transport properties of the alloys are strongly linked to their magnetic character. One interesting feature common to these materials is that $\rho(T)$ displays a peak at the Curie temperature, that is assumed to arise from enhanced spin scattering as one passes through the critical temperature as shown in Fig. 7 where temperature sweeps of the resistivity of different $Ga_{1-x}Mn_xAs$ layers in a constant field of 0.58 T, 1.1 T and 8 T are given.

The temperature dependence of the resistivity can be interpreted as critical scattering by packets of magnetic spins with ferromagnetic short-range order characterized by the correlation length comparable with the wavelength of the carriers at the Fermi level [66]. In addition to critical scattering, alloys in the insulating regime also display an enormous negative magnetoresistance occurring at low temperatures, but even at temperatures above the critical temperature also shown in Fig. 7. Both rapid rise of the resistivity with decreasing temperature in the insulating samples, and its dramatic drop with magnetic field at cryogenic temperatures can be understood in terms of magnetic polarons. Magnetic polarons, which form continuously as the temperature decreases, are extremely efficient scatterers, thus accounting for the rise of resistivity. Application of a magnetic field destroys the polarons, restoring the resistivity to what it would have been in their absence.

The application of Mott's concept of a mobility edge, the formation of polarons and the localization in a magnetic system with coulomb disorder was used to describe the metal insulator transition in a magnetic semiconductor [67].

This transition, as well as the negative magnetoresistance is contrary to non-magnetic heavily doped semiconductors where a positive magnetoresistance results from a shrinkage of impurity states orbits in high applied fields. Localization occurs now because of the combined action of random potential fluctuations and the magnetic disorder.

The magnetic properties of diluted magnetic II–VI (and IV–VI) semiconductors have been studied theoretically in great detail and many results are applicable to the III–V materials as well, the important difference being the nature of the Mn impurity atom itself. The magnetic ion which occupies the cation (Ga) sublattice in zinc-blende GaMnAs provides a localized spin and at the same time act as an acceptor. Despite the strong doping compensation, all III–V Mn materials are heavily doped p^+.

Undoped II–VI magnetic semiconductors show a spin-glass transition at low temperature due to the direct antiferromagnetic coupling between Mn ions. Upon doping, the transition from a spin-glass antiferromagnetic to a ferromagnetic phase happens and is caused by a RKKY interaction between free carriers and localized Mn spins. A corresponding change in Curie temperature from negative to positive occurs and was first discovered in IV–VI materials by Story et al. [68].

It can be shown [69] that the critical temperature derived from the RKKY interaction, with the approximations made, compares well with that derived from a total low-field magnetic susceptibility of the coupled system of carriers and localized spins in the mean field approximation. This important conclusion justified the application of the mean field theory in GaMnAs and according to Dietl et al. [63] this model has its origin in one originally proposed by Zener [70] in an early attempt to explain ferromagnetism in transition metals. This semi-empirical approach allows to include e.g. spin-orbit splitting, the effect of strain and heavy doping effects based on carrier–carrier interactions and is able to explain quantitatively the Curie temperature Tc of GaMnAs (and ZnMnTe doped with nitrogen) and the influence of strain on the orientation of the magnetization.

The complex valence-band structure of zinc-blende ferromagnetic semiconductors was included in the theoretical model based on the mean field theory for hole mediated exchange. It was found that spin-orbit coupling had an important effect on the Curie temperature and the direction of the magnetization below T_c. Higher values for T_c are predicted for materials containing larger concentrations of holes and magnetic ions and for zinc-blende structures with lighter elements like GaN but also ZnO.

3.4. AlMnAs: a new magnetic semiconductor

With the intention to fabricate heterostructures in which modulation doping or spin-filtering will become possible, we studied the growth of $Al_{1-x}Mn_xAs$ with up to 4% Mn. Stoichiometric low-temperature MBE conditions are achieved by using an As_4 flux at the Ga-rich-to-As-rich growth boundary. The samples were grown on a GaAs(100) substrate at 230 °C. The two-dimensional growth as the dominating process is verified by clearly observed RHEED oscillations and streaky (1×2) patterns during growth. Structural characterization with XRD reveals crystal quality comparable to GaMnAs. The change of the lattice constant of AlMnAs is roughly proportional to the Mn flux, suggesting complete incorporation of Mn atoms.

Fig. 8 illustrates the magnetization measurements on (a) $Al_{0.97}Mn_{0.03}As$ and (b) $Al_{0.96}Mn_{0.04}As$. These indicate that the 3% Mn sample follows the Brillouin function quite nicely and shows no ferromagnetic behavior, while the 4% Mn sample shows a ferromagnetic signal at low temperatures. The ferromagnetic signal is ascribed to the presence of nanometer-scale magnetic particles formed in the AlMnAs layer, most likely MnAs. AlMnAs layers were then incorporated in heterostructures. One interesting heterostructure is AlMnAs/δ-Mn/GaAs where a 2DHG is formed at the AlMnAs/GaAs interface. Below the transition temperature of the AlMnAs, in this case 10 K, we found evidence of a strong interaction between the magnetic moments near the interface and the 2DHG. This interaction is visible in

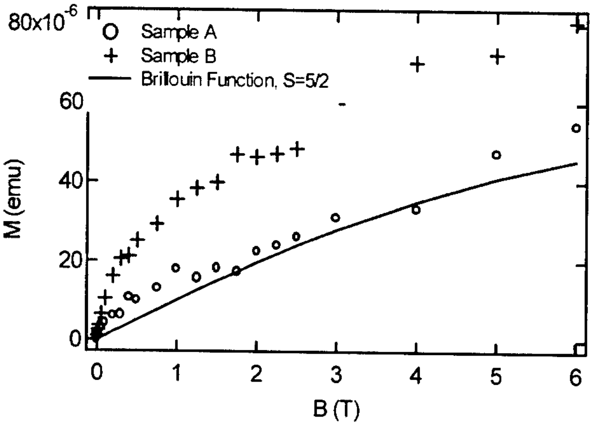

Fig. 8. SQUID magnetization measurements of AlMnAs layers with (a) 3% and (b) 4% Mn.

the Hall-effect measurements. These observations will be published elsewhere [71].

4. Spin-injection device trials

In order to demonstrate a spintronic effect, existing semiconductor devices are mimicked using a combination of magnetic and semiconductor materials. Examples are: the spin-FET [72], where magnetic source and drain are used in a field-effect transistor layout, the hot-electron metal-base transistor, the spin-valve transistor [53], where a magnetic multilayer is replacing the metal base, and light-emitting devices [73,74]. It is important to realize that for all such attempts, the spintronic device will not deliver the same functionality or the same performance as the original semiconductor device. It would be a mistake to believe that a well-known transistor structure could be turned into an improved version by making it function with electron spins rather than charge. In the best case they illustrate a novel, magnetic functionality and/or show the effect of spin transport. Their importance lies in the fact that with the fabrication of such novel 'transistors' the complexity of the magnetic/semiconductor materials combination is revealed and our understanding of spin-transport improves.

4.1. Ohmic or tunnel contact?

Let's concentrate on the efforts of injecting a spin-polarized current in a semiconductor from a metallic magnetic contact. Many attempts have been made to fabricate such a spin-injection structure using an ohmic contact. It was recently described [75] why such attempts are unsuccessful [76,77] when the ferromagnetic and the semiconductor are in the diffusive contact regime. The effectiveness of spin-injection from the ferromagnetic is reduced by a factor M expressing the mismatch in conductivity and spin-flip length between the two materials:

$$M = 1 + \frac{\sigma_F}{\sigma_N}\frac{\lambda_N}{\lambda_F}(1-\alpha_F^2)$$

$$\alpha_F = \frac{\sigma_\uparrow - \sigma_\downarrow}{\sigma_\uparrow + \sigma_\downarrow}$$

is the bulk polarization of the electrodes, $\sigma_{(\downarrow\uparrow)}$ are the spin up (down) conductivities, σ_N (σ_F) is the total conductivity in the semiconductor (ferromagnetic metal) and λ_N (λ_F) is the spin flip length in the semiconductor (ferromagnetic metal). For metallic ferromagnets the value of M is on the order of 100, effectively suppressing the spin-injection [77].

In most cases, however, the metal semiconductor contact will not be a clean ohmic contact. The interface properties will change the electrical behavior of the metal/semiconductor heterostructure. These electrical characteristics are normally designed by changing the electronic properties of the semiconductor using doping and band-gap engineering such that a tunnel barrier, an ohmic contact, or a Schottky barrier is formed. An uncontrolled interface due to phase separation or severe intermixing leads to unpredictable changes in the device performance. The structural and magnetic information on the ferromagnetic/semiconductor interface is quite substantial, but detailed electrical characterization is rather limited. For spin-injection there is recent consensus based on experimental and theoretical [78] results that a tunnel injector is the best alternative. In spin-injection using tunneling, vacuum barriers [79–81], Al_2O_3 barriers [82,83] and Schottky barriers [84,85] have been used. From a device perspective, the vacuum barrier is not very practical and the Schottky barrier might not be very stable. Our preference goes to the fabrication of a stable Al_2O_3 oxide barrier such as used in magnetic tunnel junctions [86–88].

4.2. Al_2O_3: a good tunnel barrier for spin-injection

We recently applied our expertise in fabricating magnetic tunnel junctions to the fabrication of spin-injection structures for realizing spin-injection components. The advantages of this approach are that the magnetic properties of the contact can be well controlled at the metal/insulator interface, and this interface will be more stable over time and with temperature than direct metal/semiconductor heterostructures. Although a Schottky barrier contact can act as a tunnel injector, recent reports show 2% spin injection efficiency at room temperature [84], such devices may suffer from the above stated problems. The fabrication of the tunnel-injector includes the epitaxial growth of a semiconductor heterostructure that should allow the observation of spin-injection. Since the spin-injection efficiency will be assessed through the optical response of the structure, surface emitting

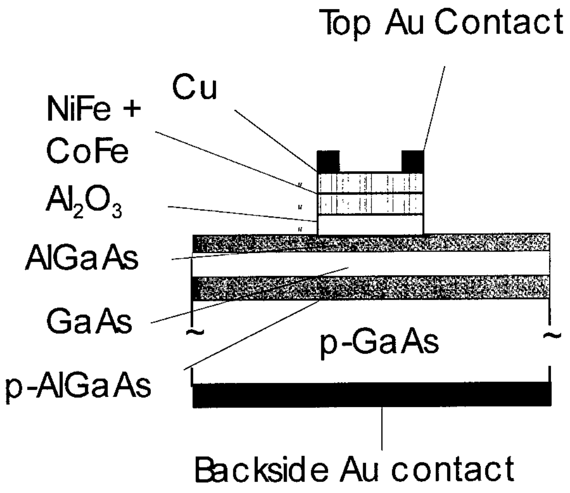

Fig. 9. Schematic cross-section of an LED structure with Al_2O_3 tunnel barrier injector.

LED components were fabricated (see Fig. 9). GaAs/AlGaAs heterostructures were grown by MBE consisting of the active region, interface control, carrier confinement and contact layers for good LED operation. The sample was unloaded from the MBE and transferred to the sputtering tool to fabricate a 1.9-nm-thick Al_2O_3 layer. First an Al layer was deposited which was subsequently oxidized in a controlled O_2 ambient of 100 torr. As a magnetic top contact we sputtered NiFe or CoFe layers. The *I–V* characteristic show that the tunnel-injector allows to inject electrons in the conduction band of the GaAs active region of the LED. The structure of the Al_2O_3 was not optimized and first attempts were made to deposit the Al for the barrier in the MBE system, without success so far. Using an appropriate optical assessment technique [89] we recently found evidence of spin injection exceeding 8% at 80 K using this type of LED. This is a promising development that may find further improvement if the barrier structure can be optimized, possibly using a full epitaxial structure. The advantage of the oxide barrier approach for the tunneling is, furthermore, that Si-based spintronic structures become possible.

Besides the use of the magnetic contacts to realize spin-injection, moderate spin-injection efficiencies have been obtained using GaMnAs as a spin-injector [74]. The possibility to incorporate the ferromagnetic semiconductors in tunnel structures [90], 2-DEG structures [71] and Schottky barriers [91] and to control the magnetism with voltage [92], makes them highly attractive for future spintronic components. Recent reports on the spin-polarized tunneling from the valence band of GaMnAs to the conduction band of GaAs in a p+-GaMnAs/n+GaAs reverse biased Esaki-type diode [93,94] brings another degree of freedom to the design of FMS-based semiconductor structures.

5. Conclusion

Molecular beam epitaxy is an extremely powerful tool for the exploration of new devices, as proven once more in the field of spintronics. Through the expertise gained in the epitaxy of magnetic thin films on semiconductors and the realization of magnetic semiconductor materials, the progress in spintronic devices using III–V heterostructures has been rapid over the past few years. This paper has highlighted a few areas of research and some of the basic challenges for realizing spin-transport devices.

Acknowledgments

The authors gratefully acknowledge the collaboration with A. Kumar, R. Jansen, R. Vlutters and C. Lodder on the spin-valve transistor; with A. Filip and B. van Wees on the spin injection, with A. Twardowski on the Squid measurements on AlMnAs. Professor V.I. Safarov is acknowledged for his contribution in the assessment of the spin-injection of the tunnel-barrier device [89]. We further thank W. van de Graaf for III-V MBE growth. Parts of this work was funded under the EC contracts: SPIDER, FENIKS (G5RD—CT2001—00535) and SPINOSA. KD acknowledges financial support from the I.W.T. (Belgium). W.V.R. acknowledges financial support as a Postdoctoral Fellow of the Fund for Scientific Research Flanders-Belgium (F.W.O.).

References

[1] T. Sands, C.J. Palmstrøm, J.P. Harbison, V.G. Keramidas, N. Tabatabaie, T.L. Cheeks, R. Ramesh, Y. Silverberg, Mater. Sci. Rep. 5 (1990) 99–170.
[2] J.G. Zhu, C.B. Carter, C.J. Palmstrom, K.C. Garrison, Appl. Phys. Lett. 55 (1990) 39.
[3] J.G. Zhu, C.J. Palmstrøm, C.B. Carter, J. Appl. Phys. 77 (1995) 4312–4320.
[4] D.E. Brehmer, K. Zhang, C.J. Schwarz, S.-P. Chau, S.J. Allen, J.P. Ibbetson, J.P. Zhang, C.J. Palmstrom, Appl. Phys. Lett. 67 (1995) 1268.
[5] T. Sands, J.P. Harbison, N. Tabatabaie, W.K. Chan, H.L. Gilchrist, T.L. Cheeks, L.T. Florez, V.G. Keramidas, Surf. Sci. 228 (1990) 1–8.
[6] S.J. Allen, N. Tabatabaie, C.J. Palmstrom, G.W. Hull, T. Sands, F. DeRosa, H.L. Gilchrist, K.C. Garrison, Phys. Rev. Lett. 62 (1989) 2309.
[7] J.G. Zhu, C.B. Carter, C.J. Palmstrom, S. Mounier, Appl. Phys. Lett. 56 (1990) 1323.
[8] M. Tanaka, M. Tsuda, T. Nishinaga, C.J. Palmstrøm, Appl. Phys. Lett. 68 (1996) 84–86.
[9] G.A. Prinz, Phys. Rev. Lett. 54 (1985) 1051–1054.
[10] G.A. Prinz, Science 250 (1990) 1092.
[11] J.A.C. Bland, B. Heinrich (Eds.), Ultrathin Magnetic Structures, I and II, Springer), Berlin, 1994.
[12] M. Gester, C. Daboo, R.J. Hicken, S. Gray, A. Ercole, J.A.C. Bland, J. Appl. Phys. 80 (1996) 347.
[13] B.T. Jonker, H. Abad, J.J. Krebs, J. Appl. Phys. 76 (1994) 6294.

[14] E. Kneedler, P.M. Thibado, B.T. Jonker, B.R. Bennet, B.V. Shanabrook, R.J. Wagner, L.J. Whitman, J. Vac. Sci. Technol. 14 (1996) 3193.

[15] J.M. Florczak, P.J. Ryan, J.N. Kuznia, A.M. Wowchak, P.I. Cohen, R.M. White, G.A. Prinz, E.D. Dahlberg, Mater. Res. Soc. Symp. Proc. 300 (1989) 213.

[16] A.Y. Liu, D.J. Singh, J. Appl. Phys. 73 (1993) 6189–6191.

[17] G.A. Prinz, J. Magn. Magn. Mater. 100 (1991) 469.

[18] S.J. Blundell, M. Gester, J.A.C. Bland, C. Daboo, E. Gu, M.J. Baird, A.J.R. Ives, J. Appl. Phys. 73 (1993) 5948.

[19] J.A.C. Bland, R.D. Bateson, P.C. Riedi, R.G. Graham, H.J. Lauter, J. Penfold, C. Schackleton, J. Appl. Phys. 69 (1991) 4989.

[20] C.J. Gutierrez, J.J. Krebs, G.A. Prinz, Appl. Phys. Lett. 61 (1992) 2476.

[21] C.J. Gutierrez, J.J. Krebs, M.E. Filipkowski, V.G. Harris, W.T. Elam, J. Magn. Magn. Mater. 126 (1993) 232.

[22] J. Dekoster, E. Jedryka, C. Meny, G. Langouche, J. Magn. Magn. Mater. 121 (1993) 69.

[23] J.P. Jay, E. Jedryka, M. Wojcik, G. Langouche, P. Panissod, Zeit. Physik B 101 (1996) 329.

[24] C.D. England, B.N. Engel, C.M. Falco, J. Appl. Phys. 69 (1991) 5310.

[25] J. De Boeck, W. Van Roy, C. Bruynseraede, A. Van Esch, H. Bender, G. Borghs, Microelectronics J. 27 (1996) 383–392.

[26] M. Tanaka, J.P. Harbison, M.C. Park, Y.S. Park, T. Shin, G.M. Rothberg, J. Appl. Phys. 76 (1994) 6278–6280.

[27] M. Tanaka, J.P. Harbison, G.M. Rothberg, J. Cryst. Growth 150 (1995) 1132–1138.

[28] M. Wojcik, E. Jedryka, S. Nadolski, Z. Liu, K. Dessein, G. Borghs, J. De Boeck, J. Magn. Magn. Mater. 226-230 (2001) 1588–1590.

[29] H. Akinaga, K. Tanaka, K. Ando, T. Katayama, J. Cryst. Growth 150 (1995) 1144–1149.

[30] H. Akinaga, S. Miyanishi, W. Van Roy, L.H. Kuo, Appl. Phys. Lett. 70 (1997) 2472–2474.

[31] T. Sands, J.P. Harbison, M.L. Leadbeater, S.J. Allen, G.W. Hull, R. Ramesh, V.G. Keramidas, Appl. Phys. Lett. 57 (1990) 2609–2611.

[32] W. Van Roy, J. De Boeck, H. Bender, C. Bruynseraede, A. Van Esch, G. Borghs, J. Appl. Phys. 78 (1995) 398–404.

[33] M. Tanaka, J.P. Harbison, J. De Boeck, T. Sands, B. Philips, T.L. Cheeks, V.G. Keramidas, Appl. Phys. Lett. 62 (1993) 1565–1567.

[34] K.M. Krishnan, Appl. Phys. Lett. 61 (1992) 2365–2367.

[35] M. Tanaka, J.P. Harbison, T. Sands, B. Philips, T.L. Cheeks, J. De Boeck, L.T. Florez, V.G. Keramidas, Appl. Phys. Lett. 63 (1993) 696–698.

[36] C. Bruynseraede, J. De Boeck, W. Van Roy, G. Lauhoff, H. Bender, A. Van Esch, R. Mertens, J.A.C. Bland, G. Borghs, MRS Symp. Proc. 384 (1995) 85–90.

[37] G. Lauhoff, C. Bruynseraede, J. De Boeck, W. Van Roy, J.A.C. Bland, G. Borghs, Phys. Rev. Lett. 79 (1997) 5290.

[38] J. De Boeck, C. Bruynseraede, H. Bender, A. Van Esch, W. Van Roy, G. Borghs, J. Cryst. Growth 150 (1995) 1139.

[39] H. Van Leuken, A. Lodder, M.T. Czyzyk, F. Springelkamp, R.A. de Groot, Phys. Rev. B 41 (1990) 5613–5626.

[40] A. Sakuma, J. Phys. Soc. Jpn. 63 (1994) 1422–1428.

[41] R.A. de Groot, F.M. Mueller, P.G. van Engen, K.H.J. Buschow, Phys. Rev. Lett. 50 (1983) 2024–2027.

[42] K.E.H.M. Hanssen, P.E. Mijnarends, Phys. Rev. B 34 (1986) 5009–5016.

[43] K.E.H.M. Hanssen, P.E. Mijnarends, L.P.L.M. Rabou, K.H.J. Buschow, Phys. Rev. B 42 (1990) 1533–1540.

[44] W. Van Roy, J. De Boeck, B. Brijs, G. Borghs, Appl. Phys. Lett. 77 (2000) 4190–4192.

[45] L. Castelliz, Z. Metallkde 46 (1955) 201.

[46] W. Van Roy, M. Wojcik, E. Jedryka, S. Nadolski, O. Richard, B. Brijs, G. Borghs, J. De Boeck, JEMS 01, Grenoble, France (2001) to be presented.

[47] M. Wojcik, E. Jedryka, S. Nadolski, W. Van Roy, G. Borghs, J. De Boeck@ J. Magn. Magn. Mater. (2001) submitted.

[48] Y. Ji, G.J. Strijkers, F.Y. Yang, C.L. Chien, J.M. Byers, A. Anguelouch, Xiao Gang, A. Gupta, Phys. Rev. Lett. 86 (2001) 5585.

[49] W. Van Roy, H. Akinaga, S. Miyanishi, K. Tanaka, L.H. Kuo, Appl. Phys. Lett. 69 (1996) 711.

[50] W.H. Butler, X.-G. Zhang, X. Wang, J. van Eck, J.M. MacLaren, J. Appl. Phys. 81 (1997) 5518.

[51] S.S. Kang, G.J. Jin, X.N. Xu, H.R. Zhai, S.S. Jiang, Y. Chen, W.R. Zhu, G.S. Dong, S.M. Zhou, X. Jin, J.W. Feng, Appl. Phys. Lett. 69 (1996) 3923–3925.

[52] K. Matsuyama, H. Asada, T. Saeki, Y. Sawamoto, K. Tanaguchi, J. Appl. Phys. 51 (1997) 5449.

[53] D.J. Monsma, J.C. Lodder, T.J.A. Popma, B. Dieny, Phys. Rev. Lett. 74 (1995) 5260–5263.

[54] D.J. Monsma, R. Vlutters, J.C. Lodder, Science 281 (1998) 407–409.

[55] K. Dessein, H. Boeve, P.S.A. Kumar, J. De Boeck, J.C. Lodder, L. Delaey, G. Borghs, J. Appl. Phys. 87 (2000) 5155–5157.

[56] K. Dessein, A.P.S. Kumar, L. Lagae, J. De Boeck, L. Delay, G. Borghs, J. Magn. Magn. Mater. 226-230 (2001) 2081–2083.

[57] H. Bender, A. Van Esch, W. Van Roy, R. Oesterholt, J. De Boeck, G. Borghs, Structural characterization of InMnAs and GaMnAs epitaxial magnetic films grown by MBE on GaAs, IOP Publishing, 1995, pp. 293–296.

[58] H. Ohno, A. Shen, F. Matsukura, A. Oiwa, A. Endo, S. Katsumoto, Y. Iye, Appl. Phys. Lett. 69 (1996) 363–365.

[59] J. De Boeck, R. Oesterholt, A. Van Esch, H. Bender, B.C.C. Van Hoof, G. Borghs, Appl. Phys. Lett. 68 (1996) 2744.

[60] H. Shimuzu, et al., Appl. Phys. Lett. 74 (1999) 398.

[61] A. Shen, et al., Appl. Phys. Lett. 71 (1997) 1540.

[62] E. Matsukura, et al., Phys. Rev. B 57 (1998) 2037.

[63] T. Dietl, H. Ohno, F. Matsukura, J. Cibert, D. Ferrand, Science 287 (2000) 1019–1022.

[64] J. Koenig, H.-H. Lin, A.H. MacDonald, Phys. Rev. Lett. 84 (2000) 5628.

[65] A. Oiwa, et al., Physica B 249 (1998) 775.

[66] T. Omiya, et al., Physica E 7 (2000) 976.

[67] S. Von Molnar, et al., Phys. Rev. Lett. 51 (1983) 706.

[68] T. Story, et al., Phys. Rev. Lett. 56 (1986) 777.

[69] T. Dietl, A. Haury, Y. Merle d'Aubigne, Phys. Rev. B 55 (1997) R3347.

[70] C. Zener, Phys. Rev. 440 (299) (1950) 81–83.

[71] Z. Liu, V.V. Moshchalkov, G. Borghs, J. De Boeck (2001) in press.

[72] S. Datta, B. Das, Appl. Phys. Lett. 56 (1990) 665–667.

[73] R. Fiederling, M. Keim, G. Reuscher, W. Ossau, G. Schmidt, A. Waag, L.W. Molenkamp, Nature 402 (1999) 787–790.

[74] Y. Ohno, D.K. Young, B. Beschoten, F. Matsukura, H. Ohno, D.D. Awschalom, Nature 402 (1999) 790–792.

[75] G. Schmidt, D. Ferrand, L.W. Molenkamp, A.T. Filip, B.J. van Wees, Phys. Rev. B 62 (2000) R4790–R4793.

[76] F.G. Monzon, M.L. Roukes, J. Magn. Magn. Mater. 198-199 (1999) 632–635.

[77] A.T. Filip, B.H. Hoving, F.J. Jedema, B.J. van Wees, B. Dutta, G. Borghs, Phys. Rev. B 62 (2000) 9996–9999.

[78] E.I. Rashba, Phys. Rev. B 62 (2000) R16267–R16270.

[79] S.F. Alvarado, P. Renaud, Phys. Rev. Lett. 68 (1992) 1387–1390.

[80] S.F. Alvarado, Phys. Rev. Lett. 75 (1995) 513–516.

[81] C.J. Hill, X. Cartoixa, R.A. Beach, S.D.L., T.C. McGill, Cond-Mat/0010058 (2000).

[82] M.J.W. Prins, H. van Kempen, H. van Leuken, R.A. de Groot, W. Van Roy, J. De Boeck, J. Phys.: Condens. Matter 7 (1995) 9447–9464.

[83] V. Motsnyi, W. Van Roy, J. Das, E. Goovaerts, G. Borghs, J. De Boeck, in: Ferromagnetic Metal/Tunnel Barrier/Semiconductor Devices for Optical Detection of Spin-Polarized Current Injection into a Semiconductor, Grenoble, France (2001) submitted.

[84] H.J. Zhu, M. Ramsteiner, H. Kostial, M. Wassermeier, H.-P. Schonherr, Phys. Rev. Lett. 87 (2001) 016601.

[85] A. Hirohata, Y.B. Xu, C.M. Guertler, J.A.C. Bland, J. Appl. Phys. 87 (2000) 1–3.

[86] J.S. Moodera, L.R. Kinder, T.M. Wong, R. Meservey, Phys. Rev. Lett. 74 (1995) 3273–3276.

[87] J. De Boeck, G. Borghs, Phys. World 12 (1999) 27–32.

[88] K.-M.H. Lenssen, G.J.M. Dormans, R. Cuppens, ''Expectations of MRAM in Comparison with Other Non-volatile Memory Technologies, Arlington, VA, USA, 2000.

[89] V.F. Motsnyi, V.I. Safarov, J. De Boeck, J. Das, W. Van Roy, E. Goovaerts, G. Borghs, Appl. Phys. Lett. (2002) in press.

[90] M. Tanaka, Y. Higo, J. Appl. Phys. 89 (2001) 6745–6747.

[91] Z. Liu, H. Boeve, W. Van Roy, S. Nemeth, V.V. Moshchalkov, G. Borghs, J. De Boeck, J. Cryst. Growth 227/228 (2001) 867–873.

[92] H. Ohno, D. Chiba, F. Matsukura, T. Omiya, E. Abe, T. Dietl, Y. Ohno, K. Ohtani, Nature 408 (2000) 944–946.

[93] M. Kohda, Y. Ohno, K. Takamura, F. Matsukura, H. Ohno, Jap. J. Appl. Phys. 40 (2001) 1274–1276.

[94] E. Johnston-Halperin, D. Lofgreen, R.K. Kawakami, D.K. Young, L. Coldren, A.C. Gossard, D.D. Awschalom, Phys. Rev. B 65 (2002) 041306.

ELSEVIER

Thin Solid Films 412 (2002) 14–23

thin solid films

www.elsevier.com/locate/tsf

Size effects in epitaxial films of magnetite

J. Korecki[a,b,*], B. Handke[a,b], N. Spiridis[a], T. Ślęzak[b], I. Flis-Kabulska[c], J. Haber[a]

[a]*Institute of Catalysis and Surface Chemistry, Polish Academy of Sciences, Niezapominajek 8, 30-239 Kraków, Poland*
[b]*Faculty of Physics and Nuclear Techniques, University of Mining and Metallurgy, Al. Mickiewicza 30, 30-059 Kraków, Poland*
[c]*Institute of Physical Chemistry, Polish Academy of Sciences, Kasprzaka 44/52, 01-224 Warszawa, Poland*

Abstract

Resent results concerning epitaxial $Fe_3O_4(001)$ films grown by reactive deposition on MgO(001) substrates as well as obtained by oxidation of epitaxial Fe(001) films are reviewed. Conversion electron Mössbauer spectroscopy (CEMS) performed in and ex situ was used to check the stoichiometry and electronic properties with monolayer resolution. Size effects were reflected in reduction of the Verwey temperature for the film thickness less than 50 nm. With further decrease in thickness, the films showed strong deviation from the bulk properties due to formation of a magnesium rich phase near the MgO/Fe_3O_4 interface. Surface oxidation to γ-Fe_2O_3, which can be reversed by annealing, was found using CEMS. The atomic scale surface characterization was accomplished for the first time in situ by the scanning tunneling microscopy, which revealed details of the surface reconstruction and termination. © 2002 Elsevier Science B.V. All rights reserved.

Keywords: Magnetite; Thin epitaxial films; Conversion electron Mössbauer spectroscopy; Scanning tunneling microscopy; Surface reconstruction

1. Introduction

Transition-metal oxides are a subject of intensive research for their interesting physical phenomenology [1] and technological importance as catalysts [2], anticorrosives [3] and magnetic materials [4]. Magnetite (F_3O_4), as a strongly correlated material, combines the full spin polarization on the Fermi level with a high Curie temperature and has potential industrial application in magnetic recording or spin electronics [5] and also as a catalytic support [6]. Magnetite shows native conductivity, being one of a few exceptions among simple metal oxides and therefore can be easily studied with the scanning tunneling microscopy (STM), a powerful method in the model catalyst studies. The model catalyst studies with oxide materials have often faced numerous problems connected with the preparation of reproducible and well-characterized single crystal surfaces [7]. Difficulties in preparation of that type, reported also for magnetite [8], can be overcome by the thin film technology enabling to grow a high quality Fe_3O_4 surface by the reactive molecular beam epitaxy (MBE). Epitaxial magnetite films are also important for spin dependent transport devices, as the mobile electrons may be 100% polarized. However, many features of structural, electronic and magnetic properties of thin films are still under debate [9–11]. Size and surface effects lead to strong deviations from bulk properties, which additionally depend on the sample thickness and stoichiometry varying for different technological parameters of the growth process. Additionally, the stoichiometry and structure of the surface and interface layers may differ from that of the film interior. Few atomic layers forming the phase boundary are often crucial with regard to the phenomena of the interest. This is just the case of the catalytic reactions or tunneling, which are typical surface/interface processes.

Magnetite crystallizes in the cubic inverse spinel structure. The oxygen ions form a closed packed cubic structure with Fe ions localized in two different sites, octahedral and tetrahedral. The tetrahedral sites (A) are occupied by trivalent Fe ions. Tri- and divalent Fe ions occupying the octahedral sites (B) are randomly arranged at room temperature because of an electron hopping. Below $T_V \sim 125$ K the electron hopping ceases and the Fe ion charge undergoes a long range ordering. This leads to a metal–insulator transition known as the Verwey transition. The transition concerns not only

---

*Corresponding author. Faculty of Physics and Nuclear Techniques, University of Mining and Metallurgy, al. Mickiewicza 30, 30-059 Kraków, Poland. Tel.: +48-12-617-2911; fax: +48-12-634-1247.
E-mail address: korecki@uci.agh.edu.pl (J. Korecki).

0040-6090/02/$ - see front matter © 2002 Elsevier Science B.V. All rights reserved.
PII: S0040-6090(02)00306-1

electric properties but can be also seen in the heat capacity [12] or magneto-resistance measurements [13], and has a strong manifestation in the hyperfine interactions probed by the Mössbauer spectroscopy, which has been widely used in bulk magnetite studies [14]. At room temperature, when the electron hopping process is fast, the Mössbauer spectrum is characterized by two sextets. The one with the hyperfine magnetic field B_{hf}= 48.8 T and the isomer shift IS=0.27 mm/s relative to α-Fe corresponds to the Fe_A^{3+} ions at the tetrahedral A-sites. The second one with B_{hf}=45.7 T and IS=0.65 mm/s is the $Fe_B^{2.5+}$-like average signal from the cations at the octahedral B sites. Fe_B^{+2} and Fe_B^{3+} are indistinguishable due to a fast electron transfer (electron hopping), which is faster ($\tau \sim 1$ ns) than the ^{57}Fe excited state lifetime (98 ns). The magnetite unit cell contains eight Fe_A^{3+} ions and eight Fe_B^{2+} and Fe_B^{3+} ions, 16 in total at the B sites, therefore, the intensity ratio $\beta = I(B)/I(A)$ of the two spectral components is a sensitive measure of the stoichiometry. Assuming that the room temperature ratio of the recoil-free fractions f_B/f_A for the B and A sites is 0.97 [15], the intensity ratio β for perfect stoichiometry should be 1.94. In non-stoichiometric magnetite, under an excess of oxygen, cation vacancies at the B sites are created. The vacancies screen the charge transfer and isolate the hopping process. For each vacancy, five Fe^{3+} ions in octahedral sites become trapped. In the Mössbauer spectrum these trapped Fe^{3+} ions at the octahedral sites and Fe^{3+} ions at tetrahedral sites are indistinguishable without applying an external magnetic field. Therefore, in the spectrum of non-stoichiometric magnetite, intensity transfer from the $Fe_B^{2.5+}$ to Fe_A^{3+}-like components is observed. Therefore, the intensity ratio β decreases markedly with the oxidation process, until the stoichiometry reaches the γ-Fe_2O_3 phase, which is represented by a single unresolved Zeeman component, close to that characteristic of the Fe_A^{3+} site in magnetite.

Below T_V the Mössbauer spectrum becomes complicated and difficult to interpret, comprising a superposition of at least five components. Any impurities and vacancies screen the hopping process, lowering the transition temperature and changing the character of the transition. The sharp first order Verwey transition in stoichiometric magnetite becomes smoother and more second order-like.

Electronic transport in magnetite is determined by the short-range interactions between the nearest neighbors that are the iron ions in the octahedral sites. Thus, in the case of the systems with reduced dimensionality, a strong influence on the phase transition, coming from the film microstructure and the surface or interface related phenomena, is expected. It is difficult to distinguish between intrinsic size effects and effects related to deviation from the stoichiometry at the interface and surface. In the present paper we discuss Mössbauer results, which partially solve this problem by an analysis of the surface and interface stoichiometry of thin epitaxial magnetite films.

The conversion electron Mössbauer spectroscopy (CEMS) has numerous advantages when applied to thin films. Contrary to most of the surface sensitive methods, CEMS has an ability to probe buried layers and interfaces with the monolayer sensitivity for films made of a pure Mössbauer isotope [16]. The method gives the atomic scale local characterization of chemical, structural and magnetic properties, simultaneously. The CEMS measurements are ultra high vacuum compatible, which gives the possibility of in situ investigations of clean surfaces in a wide temperature range. Exceptional sensitivity of our CEMS measurements (below one monolayer of ^{57}Fe) and a strong radiation source allowed us to collect high quality Mössbauer spectra also for thinnest films.

A controversial problem faced in many magnetite studies is surface termination and reconstruction. The surface structure of (001) oriented magnetite is usually discussed considering the bulk unit cell as composed of eight atomic sublayers, which contain either only tetrahedral iron atoms in A sites (so called A layer) or oxygen and octahedral B iron ions (so called B layer). The distance between A or B layers is approximately 0.2 nm, whereas the smallest interlayer spacing (A–B) is approximately 0.1 nm. Neither of the bulk terminated Fe_3O_4(001) surfaces (A nor B) is charge compensated and the charge neutrality condition of the polar Fe_3O_4(001) is the driving force of the reconstruction, which, although intensively studied with different methods for single crystals [17,18] as well as for epitaxial films [10,11,19–22], is still not fully understood and explained. Moreover, the valence-band spectra taken from an epitaxial film differ considerably from those of cleaved Fe_3O_4 samples and the surface spin polarization is smaller than expected [23].

In this paper we present resent results concerning Fe_3O_4(001) films grown by reactive deposition on MgO(001) substrates [24,25] as well as obtained by a post-preparation oxidation of epitaxial Fe(001) films [26]. Combination of STM and CEMS studies applied in situ at ultra high vacuum conditions, resulted in the atomic scale characterization of the film surface as well as the film bulk and buried interfaces.

2. Experimental details

The experiment was performed using a multi-chamber UHV system (base pressure 1×10^{-10} mbar) which was described previously [27]. The preparation chamber contains a miniature MBE system, consisting of metal vapor sources and quartz monitors to control the evaporation rate and a four-grid LEED/AES spectrometer. The CEMS chamber is dedicated to the in situ measure-

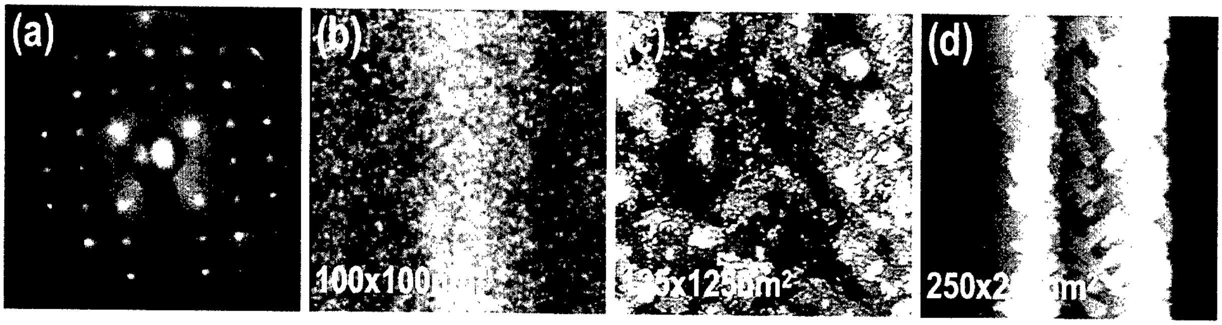

Fig. 1. (a) LEED pattern at the electron energy of 70 eV for the ($\sqrt{2}\times\sqrt{2}$)R45° reconstructed surface of the 20 nm Fe_3O_4(001) film on MgO(001) and STM topographic scans: (b) for the as-deposited surface-deposition temperature 520 K, (c) after 1 h annealing at the deposition temperature and (d) after 1 h annealing at 820 K.

ments of the Mössbauer effect by detection of the conversion electrons using a large opening channeltron. The sample was mounted to a cold finger of a stationary liquid nitrogen cryostat, which allowed to perform the measurements in the temperature range between 80 K and 500 K.

A second UHV system was used for in situ STM, equipped with a similar technological facility as the one described above.

All discussed samples were prepared on MgO(001) substrates cleaved in N_2 atmosphere prior to the introduction into the UHV system. The substrates were then annealed for 1 h at 900 K in UHV and after this procedure the MgO(001) surface showed atomic cleanness and perfect structural order as checked with AES and LEED. Magnetite was grown by the Fe-vapor deposition at the rate of approximately 1 nm/min, in the presence of oxygen. Oxygen was provided, using a precision leak valve, from a nozzle placed 1 cm from the substrate to achieve a relatively high local O_2 pressure avoiding contamination of the whole chamber. For the Mössbauer experiments ^{57}Fe isotope was used. The small lattice spacing mismatch (0.3%) between magnetite and the MgO substrate in the (001)-plane provides favorable conditions for the epitaxial growth, which helps in reaching the thermodynamic equilibrium. The magnetite phase could be stabilized in a broad range of the O_2 partial pressure ($1\times10^{-7}\div1\times10^{-6}$ hPa), as controlled by a quadrupole mass spectrometer, for the substrate held at 520 K. For all sample ranging from 500 nm down to 3 nm thickness, LEED (Fig. 1a), displayed a ($\sqrt{2}\times\sqrt{2}$)R45° reconstruction relative the primitive surface bulk unit cell of magnetite. This type of reconstruction is typical for the (001) bulk magnetite surface [17] as well as for the surface of epitaxial magnetite films on MgO(001) [19–22]. Decreasing the film thickness below 5 nm caused an increase of a diffused background accompanied by spot broadening, leaving the pattern symmetry unchanged.

Ex situ STM studies of magnetite film require ion bombardment/annealing treatment for restoring the surface cleanness [19–22]. We were able to study the surfaces of the as-prepared films in situ and to examine the influence of annealing as shown in Fig. 1b–d for 20 nm films. When the films were cooled down to the room temperature immediately after the deposition is completed, the STM picture revealed grainy structures with a nanometer lateral size, which by the height analysis can be identified as monoatomic terraces spaced by approximately 0.2 nm (Fig. 1b). The overall height amplitude in the presented area was <1 nm, which means that no more than five monoatomic levels were exposed. Annealing the films for 1 h at the preparation temperature resulted in an increase of the terrace size up to several nanometers (Fig. 1c). Rising the annealing temperature up to 800 K produced large flat areas with the lateral dimensions of 20–50 nm (Fig. 1d) but AES analysis indicated the presence of magnesium, which had diffused from the substrate, as it was observed previously [28].

3. Electronic and magnetic properties vs. film thickness

Mössbauer spectra were measured in situ for the films from 430 nm down to 3 nm thickness at the temperature range between 80 and 300 K. A selection of the spectra for the 430 nm and 10 nm samples at three different temperatures is presented in Fig. 2 [24].

The 430 nm sample represents the bulk stoichiometric magnetite behavior. The hyperfine magnetic field B_{hf}, the isomer shift IS and the quadrupole splitting QS are in a good agreement with the literature values for the bulk material. The component with larger B_{hf} and smaller IS corresponds to trivalent Fe ions located at the tetrahedral A sites, while the other one is interpreted as the average signal from Fe^{3+} and Fe^{2+} ions at the octahedral B sites, seen effectively due to the electron hopping as $Fe^{2.5+}$ ions. By lowering temperature, the effect of the Verwey transition can be observed in the Mössbauer spectra. The Verwey transition, as seen by our CEMS analysis, is a multistage process. When T_V

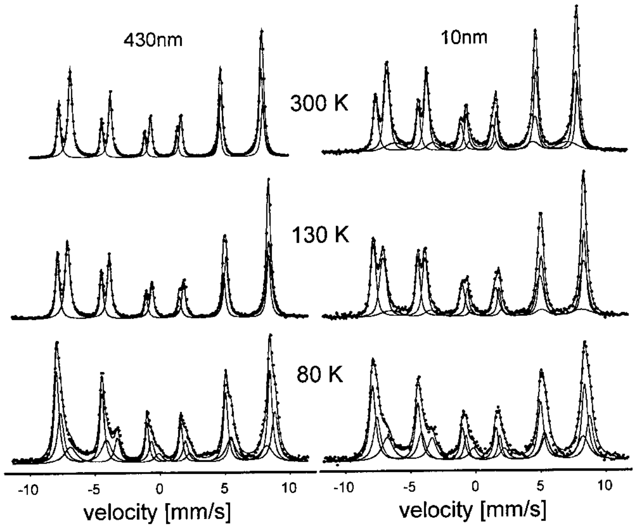

Fig. 2. Selection of CEMS results for 430 nm and 10 nm epitaxial $Fe_3O_4(001)$ films at different temperatures [24].

is approached going from high temperatures, at first the components associated with the A and B sites gradually reverse their intensity, the effect being particularly strong below 130 K for the 430 nm sample. The change of the intensity is accompanied by a broadening of the lines. This phenomenon, which is probably due to the dynamic effects connected with the electron hopping, remains not fully explained even for the bulk magnetite, indicating a highly diffuse charge dynamics. In the narrow temperature range, close to T_V, the Mössbauer spectrum undergoes drastic changes connected with the charge ordering. The electron hopping freezes, which means that the Fe^{3+} and Fe^{2+} ions at the B site differentiate in the Mössbauer spectrum. It is manifested by new components that appear in the spectrum. Eventually, in the third transition stage, which proceeds down to the lowest applied temperature (80 K), the new hyperfine pattern becomes more distinct and the lines - narrower. At 80 K, a reasonable fit with three spectral components, corresponding to Fe^{3+} at the A site, Fe^{3+} at the B site and Fe^{2+} at the B site was possible. Magnetite spectra below T_V are rather complex because of twinning, which means that there is a dipolar field distribution leading to broad and weakly resolved spectra [14]. The component corresponding to the Fe^{2+} ions at the B site is the most complex due to the characteristic high value of the quadrupole splitting QS. This is the reason why the apparent distribution of the ions at the B site between Fe^{3+} and Fe^{2+} deviates considerably from the expected 1:1 ratio.

The spectra for the 10 nm sample are similar to those for the 430 nm one (comp. Fig. 2). However, besides the slightly lowered values of B_{hf} for the component A and B, there is one remarkable difference at the room temperature. A third component with a relatively broad distribution of B_{hf} has to be added to the fitted spectrum. We interpret this component as the one coming from the interface, where diffusion of Mg and Fe cations takes place, as suggested earlier for annealed magnetite films [28]. The contribution of the interfacial component to the spectrum reaches 15%. Taking into account that the contribution of the A site for the 10 nm spectrum remains unchanged with respect to a bulk and it amounts to 1/3, it is obvious that the interfacial component originates from the octahedral sublattice, in which the Fe ions have been replaced by Mg ones. By this assumption, from the relative area ratio of the spectral components, the thickness of the interface zone is estimated as 2.0 nm. At the low temperature (80 K), the spectral component from the Mg rich phase and the B site Fe^{2+} ions cannot be resolved due to an intricate character of the spectra below the Verwey transition. Our observation contradicts the earlier CEMS studies of the Fe_3O_4/MgO interface using ^{57}Fe probe layer [29], where no deviation from the magnetite stoichiometry was observed. However, it has to be noted that the broad interfacial component could be detected only thanks to high spectrum statistics and quality. Even more intriguing, is that the ultra thin magnetite layers in Fe_3O_4/MgO multilayers, were found to be compositionally uniform [30,31].

Around T_V, the interpretation of the Mössbauer spectra is difficult but the Verwey transition can be followed using a spectrum parameter, which is independent on the applied spectrum model. Our analysis is based on the observation of the total amplitude ratio of the outermost line groups at the positive and negative velocities. For stoichiometric magnetite, well below the Verwey transition, the '1/6 ratio' parameter (defined by the inset in Fig. 3) is very close to 1. The plots of '1/6 ratio' vs. temperature (Fig. 3) clearly reveal a complicated character of the transition reflected in the Mössbauer spectra. For the 10 nm sample the transition is much broader than for the 430 nm one. The first transition stage observed as a gradual intensity reversal

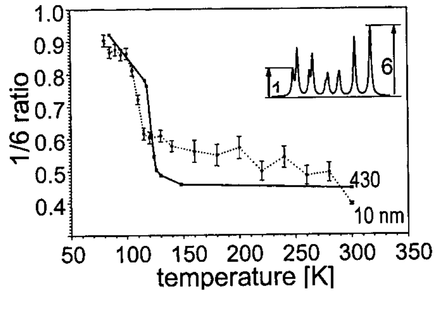

Fig. 3. '1/6 ratio' parameter plotted vs. temperature for the 430 nm (■) and the 10 nm (O) thick samples (error bars for the 430 nm sample are less than the size of points). '1/6 ratio' is defined in the inset [24].

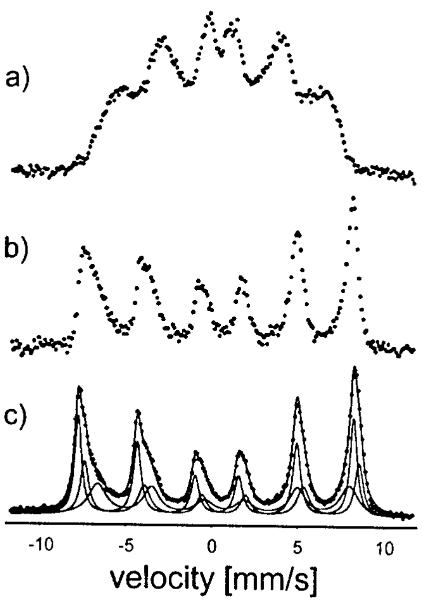

Fig. 4. CEMS spectra for the 3 nm epitaxial $Fe_3O_4(001)$ film at 300 K (a), 130 K (b) and 80 K (c) [24].

of the components A and B has its onset for the thin sample just below the room temperature, whereas for the thick sample this transition stage is nearly completely suppressed. Similarly, at low temperatures, the transition region for the thin sample is much broader than for the thick one. This is an indication that the transition may change from the first order to the second order when the sample becomes thinner. The reason of the change in the transition character may be either lattice strains due to the lattice mismatch with the substrate or the natural doping with Mg coming from the substrate.

The value of T_V is the important information source concerning the magnetite stoichiometry. T_V varies from 125 K (for δ close to 0) to approximately 100 K for highly non-stoichiometric samples ($\delta = 0.02$) [33]. From Fig. 3 T_V for the 430 nm film is estimated as 122 K indicating nearly perfect stoichiometry, whereas the 10 nm sample undergoes the transition at approximately 110 K.

The spectra for the thinnest studied sample, which was 3 nm thick, are shown in Fig. 4. At 300 K a typical relaxation character of the spectra is obvious (Fig. 4a). Similar behavior observed for magnetite films on sapphire [32] and for Fe_3O_4/MgO multilayers [34] was attributed to superparamagnetism. Superparamagnetism in ultrathin magnetite films originates from the nucleation of the Fe_3O_4 films on MgO(001) [34]. The lower symmetry of the inverse spinel structure and the larger unit cell compared to the MgO substrate mean that the magnetite islands can nucleate in eight different ways and coalescence of different islands leads to a formation of antiphase boundaries, which are a perturbation for the exchange interaction. The relaxation character of the spectrum at room temperature does not allow to conclude about the chemical composition and the electronic properties. However, by lowering the temperature, the superparamagnetic relaxation is blocked and below 200 K the spectra reveal their static character. From low temperature measurements (Fig. 4b,c) it is clear that the 3 nm sample shows the behavior which differs considerably from the bulk magnetite-like one. The most important observation is that the spectra resemble those for magnetite below the Verwey transition, at least in the whole temperature range where the superparamagnetic relaxation is slow enough to give a static magnetic spectrum with a well-resolved hyperfine pattern, i.e. between 80 and 200 K. It could mean that the Verwey transition in the ultrathin magnetite films is shifted to higher temperatures (or completely suppressed). An alternative explanation involves formation of a magnesium rich inverse spinel, which is structurally isomorphic with magnetite and then indistinguishable by diffraction methods (LEED, RHEED or X-rays). Our films were grown at the temperature (520 K) at which, massive Mg surface diffusion through a thick film cannot be expected, but the formation of a magnesium rich spinel phase at the interface occurs as it is seen for the 10 nm sample. James et al. [35] concluded that no magnesium ferrite is formed in Fe_3O_4/MgO multilayers but the result is based on superparamagnetic spectra and in our opinion is not proved sufficiently. Summarizing, we suggest that the suppression of the Verwey transition in ultrathin magnetite films (thinner than 5 nm) originate from their chemical composition (high concentration of magnesium impurities) and that the structure and composition of ultrathin magnetite films, and at the Fe_3O_4/MgO interface, differ strongly from those of a bulk. This observation remains in direct contradiction with the previous results [29–31,34,35].

4. Surface and interface seen by CEMS and STM

In magnetite films, composition inhomogeneities are expected not only at the film/substrate interface, as mentioned above but also at the surface. This problem was addressed by Fuji et al. [29] who used depth-selectivity of CEMS to probe surface layers with a sub-nanometer ^{57}Fe probe layer embedded in ^{56}Fe samples. Minor depth-dependent changes were confined to a few outermost atomic layers but the essential electronic bulk features, including a rapid electron hopping, were retained at the surface and also at the Fe_3O_4/MgO interface. This observation contrasts strongly with the scanning tunneling microscope images of a clean magnetite (001)-surface interpreted in terms of a Verwey-type charge ordering in the surface layer at room temperature [8]. A possible explanation for this discrepancy is oxidation and contamination of the magnetite surface, which is unavoidable during ex situ CEMS

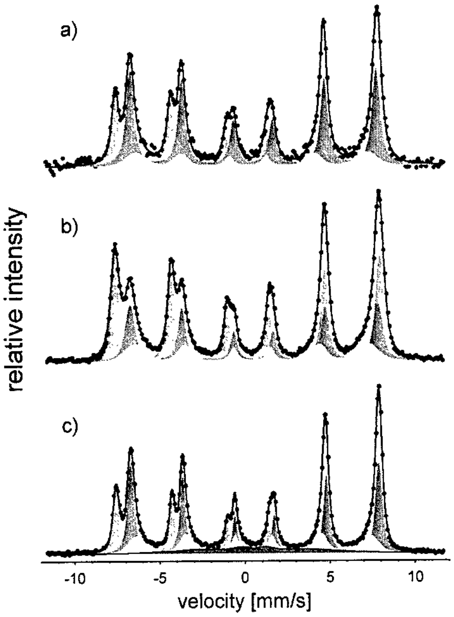

Fig. 5. Room temperature CEMS spectra of the 10 nm epitaxial magnetite film: as-grown (a), oxidized in air (b) and annealed for 1 h at 600 K at UHV (c) [25].

measurements, although, generally magnetite is thought to be stable against room temperature oxidation [32]. To clarify this problem the CEMS measurements were done for the 10 nm Fe_3O_4(001) film after 1-month exposure to the atmosphere and then again at UHV condition, after being annealed in vacuum for 1 h at 600 K [25]. The measured spectra are collected in Fig. 5, together with the spectrum in the as-prepared state (Fig. 5a) repeated for a direct comparison from Fig. 2.

After an exposure of the sample to a clean air at the atmospheric pressure a drastic change in relative intensities of spectral components are clearly seen (Fig. 5b) but the hyperfine parameters of the fitted components (except the area ratio) did not change markedly. The obvious reason of the observed changes is surface oxidation. The thickness of the modified layer may be estimated based on the hypothesis of the cation vacancies formation at the octahedral sites. Assuming, for simplicity, that the oxidized phase has a homogeneous composition of γ-Fe_2O_3, the thickness of the oxidized surface layer was found to be 1.5 nm. Annealing the sample at 600 K for 1 h at UHV restored the spectra of the 'as-prepared' state (Fig. 5c). The UHV condition is strongly reducing and reverses the oxidation. Annealing also has an effect on the MgO/Fe_3O_4 interface as seen by the appearance of an additional component with a broad B_{hf} distribution at approximately 25 T. The large IS and low B_{hf} values indicate that the new component should be related to a Mg rich phase. It is formed when Fe diffuses into MgO, finally forming a $Fe_{1-x}O$ wustite-type oxide with the cubic structure of MgO [36]. For further investigation of this process an additional 60-nm-thick sample was prepared. By increasing the sample thickness, the interdiffusion process could be studied in a broader temperature range. The final effect of the annealing cycles is shown in Fig. 6. After the last annealing cycle at 1000 K, a Mg-doped magnetite phase component and a wustite-like doublet (IS = 1.04 mm/s, QS = 0.33 mm/s) can be identified unambiguously in the Mössbauer spectrum. The deeply buried wustite layer could not be detected by other methods [37]. By comparison with the spectra of the Mg-doped magnetite single crystals [38], the average Mg concentration x in the formula $Mg_xFe_{3-x}O_4$ is estimated to be 0.10–0.15. From the intensity of the spectral components, the thickness of the wustite layer formed in the MgO substrate is found to be approximately 5 nm.

Because of the observed oxidation, surface sensitive studies of magnetite require in situ measurements. In Fig. 7 we show in situ CEMS spectra with the $^{57}Fe_3O_4$-probe layer deposited on top of 20 nm $^{56}Fe_3O_4$ films. When the probe layer is 2.4 nm thick a bulk-like magnetite CEMS spectrum is observed (Fig. 7a). For the films analyzed in Fig. 7b,c, a 0.8 nm probe layer is used to follow electronic surface properties of films displaying different surface reconstruction: $(\sqrt{2}\times\sqrt{2})$R45° (Fig. 7b) or (1×1) (Fig. 7c). The surface structure of magnetite will be discussed in more detail below, in relation to STM measurements. Here we want only to stress the obvious difference between the both spectra. For the $(\sqrt{2}\times\sqrt{2})$R45° reconstruction, the spectrum retained many features of bulk magnetite. The spectral components of the A and B sites can be identified unambiguously although, judging from the $Fe^{3+}/Fe^{2.5+}$ component intensity ratio, the number of the Fe ions occupying perfect octahedral sites is reduced compared with the bulk stoichiometry. The 0.8 nm probe layer containing ^{57}Fe corresponds to eight ideal atomic layers of the A- and B-type. From the intensity of the three Zeeman components, which were indispensable to fit the spectrum it could be concluded that the ^{57}Fe atoms of the probe layer form approximately three

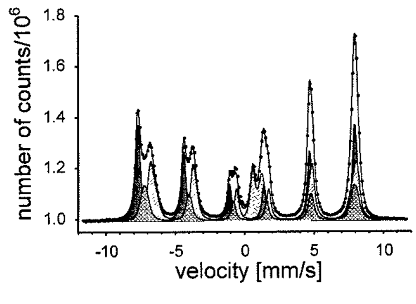

Fig. 6. CEMS spectrum after 1 h annealing cycles between 500 and 1000 K, with 100 K steps, for the 60 nm epitaxial magnetite film [25].

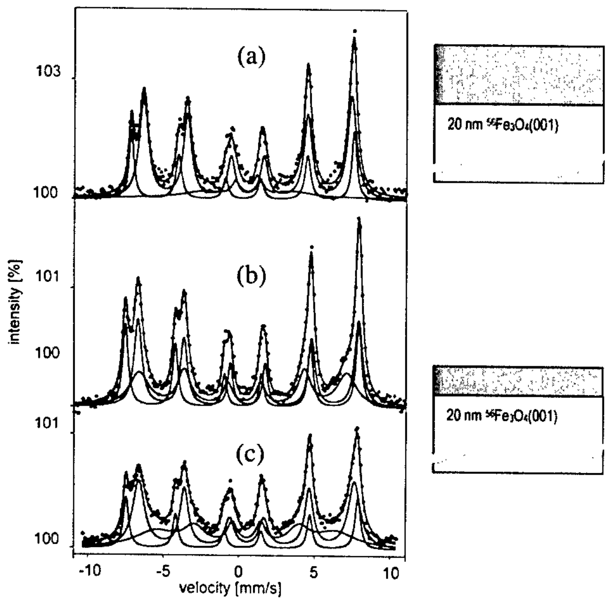

Fig. 7. Room temperature CEMS spectra of the 20 nm $^{56}Fe_3O_4(001)$ sample with $^{57}Fe_3O_4(001)$ probe layers: (a) 2.4 nm, (b) and (c) 0.8 nm with $(\sqrt{2}\times\sqrt{2})R45^\circ$ or (1×1) reconstruction, respectively.

stoichiometric A–B layer pairs. The remaining ^{57}Fe atoms, in amount equivalent to four A or two B ideal layers, give rise to the Zeeman component with broadened lines, the reduced hyperfine magnetic field $B_{hf}=42.9(5)$ T and the isomer shift $IS=0.45(5)$ mm/s, which lies between the values for the A and B sites. Such component was observed also by Fuji et al. [29] and interpreted as coming from Fe^{3+} ions. From our analysis of the hyperfine parameters we favor the interpretation that it is due to all Fe ions in two or three topmost layers, which are subjected to relaxation and reconstruction.

Fig. 7c shows the CEMS spectrum for a sample displaying (1×1) reconstruction. The surface structure is very sensitive to the preparation condition and a small variation of the oxygen partial pressure during preparation, deposition temperature or post-preparation annealing may induce an irreproducible change of the surface reconstruction from $(\sqrt{2}\times\sqrt{2})R45^\circ$ to (1×1). From the CEMS spectrum it becomes obvious that such a change is connected with a pronounced relaxation of the surface layer from the ideal spinel structure. As compared to the $(\sqrt{2}\times\sqrt{2})R45^\circ$ reconstruction, the spectral components attributed to the surface layers are more intense and much broader. There is also a clear reduction of the Fe ion number contributing to the ideal A-type layers. It might be the indication that the (1×1) reconstruction corresponds to the surface terminated with the A-type layer.

The surface termination and interlayer relaxations of the $(\sqrt{2}\times\sqrt{2})R45^\circ$ surface are being the subject of an intensive debate [9]. It is the most typical reconstruction for MBE grown films monitored in situ by LEED or RHEED [19–22]. However, surprisingly, in situ diffraction experiments were never combined with in situ STM studies. It is commonly believed that autocompensation is a necessary, but insufficient, condition for the correctness of any particular surface structural model [9]. The most natural way to achieve an autocompensated $Fe_3O_4(001)$ surface that possesses the observed $(\sqrt{2}\times\sqrt{2})R45^\circ$ symmetry is to terminate it with a half tetrahedral Fe^{3+} monolayer. However, autocompensation can also be achieved by terminating the surface with a B-type layer, in which the number of oxygen vacancies or/and the Fe^{3+} to Fe^{2+} ratio is varied. Many different reconstruction models based on A- or B-type layer termination were proposed and discussed in the literature—the most recent review can be found in the paper of Mijiritskii and Bjorma [11]. Some authors believe that both types of termination are possible, but there is the consensus that they do not occur simultaneously on one surface. Such a conclusion comes from the STM images, in which the smallest step height observed on the $Fe_3O_4(001)$ surface (see Fig. 1) is approximately 0.2 nm, which corresponds to the interplanar spacing of the A–A or B–B layers, whereas for the mixed A/B termination 0.1 nm steps are expected. Indeed, our topographic large scan STM images shown in Fig. 1 led to the same result. However, it is not necessarily true passing to the atomically resolved patterns presented in Fig. 8. The image taken at the sample bias 1 V (Fig. 8a) has a similar character to the one presented by Stanka et al. [22], which was interpreted as coming from the octahedral Fe termination with characteristic rows which are Fe ions in octahedral sites. The height histogram (below), constructed from the data in the white frame area, clearly reveals that two monoatomic terraces are spaced by 0.2 nm. Situation changes entirely for the bias voltage lowered to 0.75 V, as seen from Fig. 8b. Already, from a visual inspection, it becomes obvious that the surface structure is more complicated and diversified than it could be expected from a simple model assuming a homogenous octahedral or tetrahedral termination. The apparent step height depends on the tunneling conditions. The height histogram for the same area shows now a broad distribution without any pronounced features of steps. We were also able to demonstrate that by changing the bias to negative values the image symmetry changes completely, indicating tetrahedral termination [39]. Consequently, we postulated a mixed octahedral/tetrahedral termination, assuming that different atoms or atomic planes are imaged at different sample biases.

5. Magnetite by oxidation of Fe(001) epitaxial films

Annealing improves the surface quality (lateral size of terraces) but it inevitably leads to the diffusion of

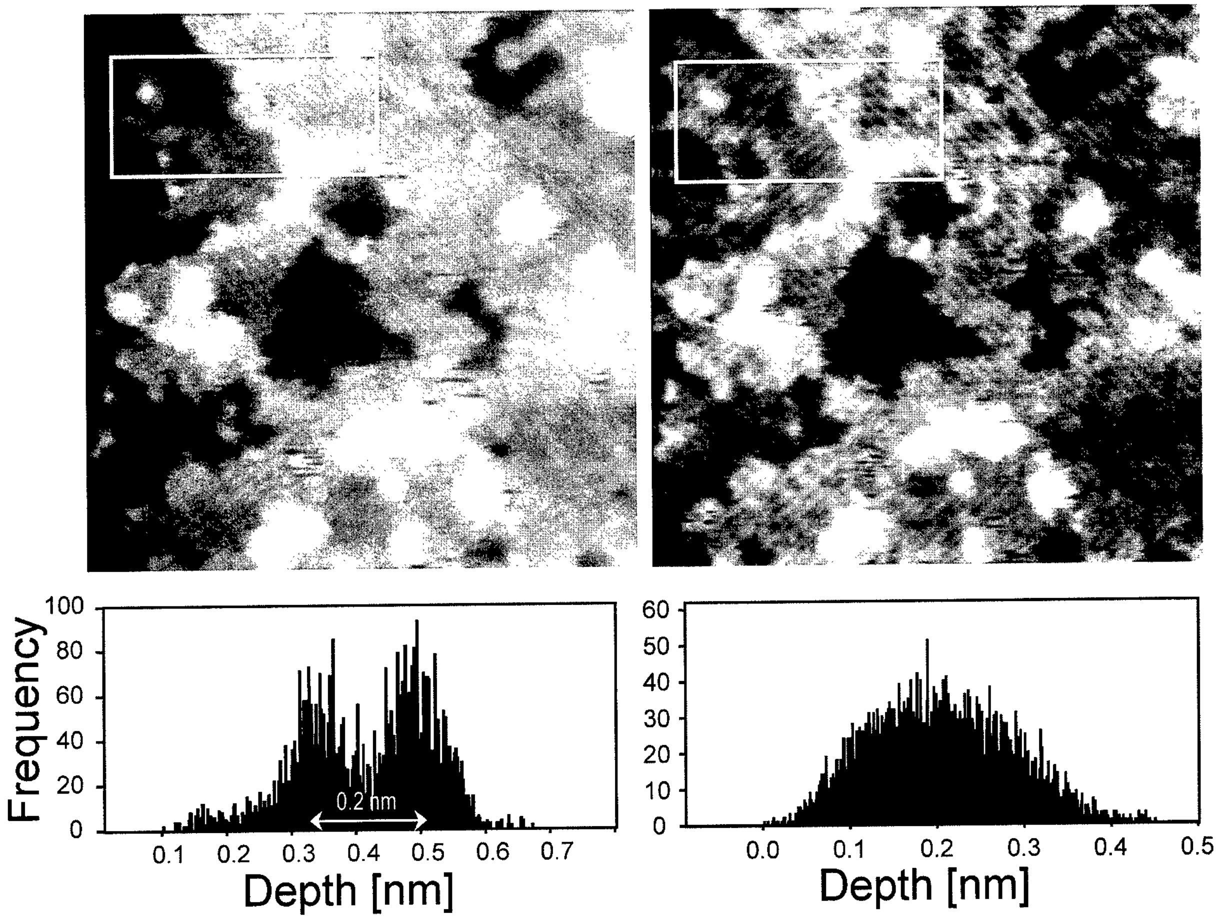

Fig. 8. Atomically resolved 30×30 nm^2 STM images of the 20 nm Fe_3O_4(001) film on MgO(001) taken at different sample biases: 1 V (left) and 0.75 V (right). Below: height histograms from the marked areas.

magnesium into the magnetite film. This phenomenon sets a temperature limit for the growth of Fe_3O_4(001) on MgO(001) by the reactive deposition of Fe. An alternative preparation procedure, used for the Fe_3O_4(111) growth on metallic substrates is oxidation of epitaxial ultrathin Fe films [40,41]. We have used a similar preparation technique for oxidizing an epitaxial Fe(001) film on MgO(001) [42]. To enable further studies with the Mössbauer spectroscopy, the iron isotopes ^{57}Fe and ^{56}Fe were used to enhance the surface sensitivity and a typical sample was engineered by placing the 5 nm ^{57}Fe probe layer on top of the 20 nm ^{56}Fe film. Iron was evaporated from thermal sources on polished MgO(001) substrates at an elevated temperature that was optimized for a flat growth [42]. Fe grows on MgO(001) with epitaxial relations: Fe(001)//MgO(001) and Fe[110]//MgO[100], i.e. by the 45° rotation of the (001) surface unit cell. A flat growth is reported for Fe on MgO at elevated temperatures [42] but to prevent an island-type growth nucleation should proceed at low temperature (e.g. 300 K) and then temperature can be raised gradually up to 620 K at a final thickness. Fig. 9a documents the surface topography of the 20 nm film obtained according to the above receipt. An oxide layer was formed on the Fe(001) surface by annealing the film for 15 min at 550 K in 10^{-4} Pa O_2 partial pressure. The oxidation resulted in the formation of a new epitaxial phase observed in a LEED pattern (Fig. 9b). The pattern symmetry indicated that the layer could be a magnetite. The STM image showed distinct changes of the film topography (Fig. 9c). Small irregular grains transformed after annealing to monoatomic terraces with atomically resolved structures characteristic for magnetite [22], as shown in the inset in Fig. 9c. Unambiguous identification of the layer formed is given by a CEMS measurement shown in Fig. 10. The spectrum could be fitted with four components. Components (A) and (B) come from magnetite representing Fe ions in tetrahedral and octahedral sites, respectively. Component (M) is due to a metallic iron. Apparently, the oxidation affected only a part of the top ^{57}Fe layer. Component (I) comes probably from an interfacial layer formed between Fe_3O_4 and metallic iron. Neglecting differences in recoilless fractions, the thickness of the oxide layer can be estimated by comparing the relative intensity of the spectral components,

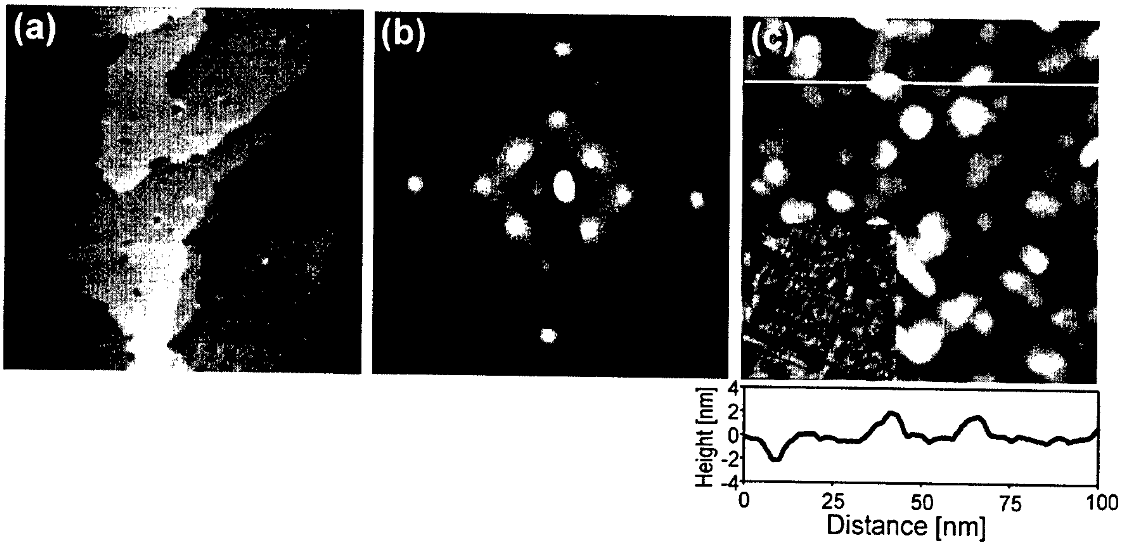

Fig. 9. Oxidized 20 nm-^{56}Fe/5 nm-^{57}Fe epitaxial film on MgO(001) as characterized by LEED and STM: (a) 100×100 nm^2 topographic STM image of the Fe(001) surface before oxidation, (b) LEED pattern at 94 eV after oxidation and (c) 100×100 nm^2 topographic STM image after oxidation. Inset on (c) shows the 12.5×12.5 nm^2 atomically resolved scan of the film annealed at 750 K.

which indicated that the magnetite layer formed on the epitaxial Fe(001) film is 3 nm thick. The Fe_3O_4(001) layer obtained in this way could be subjected to a high temperature annealing for improving the structure because the remaining Fe layer sets an effective barrier for Mg diffusion.

6. Conclusions

Highly sensitive in situ CEMS measurements gave us precise structural and magnetic characterization of epitaxial magnetite films grown on MgO(001). By lowering the film thickness down to the 10 nm range, the electronic film properties reflected in the Verwey transition are modified considerably: T_V decreases, the transition becomes broader. We attributed these changes to the MgO/Fe_3O_4 interface, at which a magnesium rich phase is postulated based on the CEMS results. The surface electronic properties seen by a probe layer correlate with the surface reconstruction. Modifications of the surface hyperfine pattern for the $(\sqrt{2}\times\sqrt{2})R45°$ reconstruction are weaker than for the (1×1) one.

In situ STM shed some light on the surface termination of the Fe_3O_4(001) films. By the analysis of the STM images at different bias voltages, we suggest that a mixed A- and B-type termination can occur on a one surface.

Preparation of Fe_3O_4(001) films by oxidizing epitaxial Fe(001) films gives a promising perspective for growing layers with unique structural and magnetic properties.

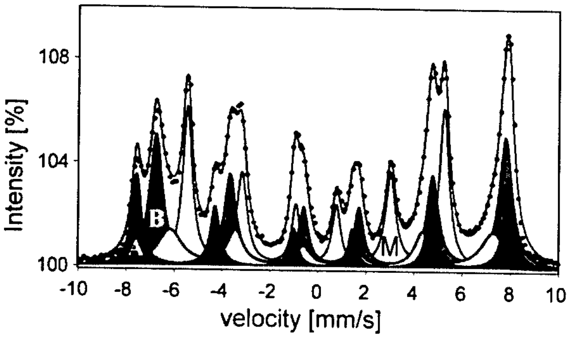

Fig. 10. In situ CEMS spectrum of the oxidized 20 nm-^{56}Fe/5 nm-^{57}Fe epitaxial film on MgO(001).

Acknowledgments

This work was partially supported by the Polish State Committee for Scientific Research, grant no. 7 T08A 002 20.

References

[1] V.E. Henrich, P.A. Cox, The Surface Science of Metal Oxides, Cambridge University Press, Cambridge, 1993.
[2] H.H. Kung, Transition Metal Oxides: Surface Chemistry and Catalysis, Elsevier, Amsterdam, 1989.
[3] P. Marcus, V. Maurice, in: K.E. Heusler (Ed.), Passivation of Metals and Semiconductors, Trans Tech, Switzerland, 1994, p. 221.
[4] G.A. Prinz, Phys. Today 48 (1995) 58.
[5] P.J. van der Zaag, P.J.H. Bloemen, J.M. Gaines, R.M. Wolf, P.A.A. van der Heijden, R.J.M. van de Veerdonk, W.J.M. de Jonge, J. Magn. Magn. Mater. 211 (2000) 301.
[6] C.H.F. Peden, G.S. Herman, I.Z. Ismagilov, B.D. Kay, M.A. Henderson, Y.-J. Kim, S.A. Chambers, Catal. Today 51 (1999) 513.

[7] U. Diebold, in: A.W. Czanderna, C.J. Powell, T.E. Madey (Eds.), Specimen Handling, Preparation, and Treatments in Surface Characterization, Kluwer Academic, New York, 1998.
[8] J.M.D. Coey, I.V. Shvets, R. Wiesendanger, H.-J. Güntherodt, J. Appl. Phys. 73 (1993) 6742.
[9] S.A. Chambers, Surf. Sci. Rep. 39 (2000) 105.
[10] F.C. Voogt, Ph.D. Thesis, Departments of Chemical Physics and Nuclear Solid State Physics, University of Groningen, Netherlands, 1998.
[11] A.V. Mijiritskii, D.O. Boerma, Surf. Sci. 486 (2001) 73.
[12] J.P. Schepherd, J.W. Koenitzer, R. Aragón, C.J. Sandberg, J.M. Honig, Phys. Rev. B 31 (1985) 1107.
[13] G.Q. Gong, A. Gupta, G. Xiao, W. Qian, V.P. Dravid, Phys. Rev. B 56 (1997) 5096.
[14] R.S. Hargrove, W. Kündig, Solid. State Commun. 8 (1970) 303.
[15] D.T. Margulies, F.T Parker, M.L. Rudee, F.E. Spada, J.N. Chapman, P.R. Aitchison, A.E. Berkowitz, Phys. Rev. Lett. 79 (1997) 5162.
[16] J. Korecki, U. Gradmann, Phys. Rev. Lett. 55 (1985) 2491.
[17] G. Tarrach, D. Burgler, T. Schaub, R. Wiesendanger, H.-J. Güntherodt, Surf. Sci. 285 (1993) 1.
[18] C. Seoighe, J. Naumann, I.V. Shvets, Surf. Sci. 440 (1999) 116.
[19] J.M. Gaines, P.J.H. Bloemen, J.T. Kohlhepp, C.W.T. Bulle-Lieuwma, R.M. Wolf, A. Reinders, R.M. Jungblut, P.A.A. van der Heijden, J.T.W.M. van Eemeren, J. aan de Stegge, W.J.M. de Jonge, Surf. Sci. 373 (1997) 85.
[20] S.A. Chambers, S.A. Joyce, Surf. Sci. 420 (1999) 111.
[21] S.A. Chambers, S. Thevuthasan, S.A. Joyce, Surf. Sci. 450 (2000) L273.
[22] B. Stanka, W. Hebenstreit, U. Diebold, S.A. Chambers, Surf. Sci. 448 (2000) 49.
[23] H.-J. Kim, J.-H. Park, E. Vescovo, Phys. Rev. B 61 (2000) 15288.
[24] B. Handke, T. Slezak, M. Kubik, J. Korecki, J. Radioanal. Nucl. Chem. 246 (2000) 27.
[25] B. Handke, J. Haber, T. Slezak, M. Kubik, J. Korecki, Vacuum 63 (2001) 331.
[26] I. Flis-Kabulska, B. Handke, N. Spiridis, J. Haber, J. Korecki, Surf. Sci., in press.
[27] J. Korecki, M. Kubik, N. Spiridis, T. Slezak, Acta Phys. Polonica A 97 (2000) 129.
[28] J.F. Anderson, M. Kuhn, U. Diebold, K. Shaw, P. Stoyanov, D. Lind, Phys. Rev. B 56 (1997) 9902.
[29] T. Fuji, M. Takano, R. Katano, Y. Isozumi, Y. Bondo, J. Magn. Magn. Mater. 130 (1994) 267.
[30] C.L. Chang, G. Chern, Y.R. Chean, C.L. Chen, Appl. Surf. Sci. 161 (2000) 448.
[31] G.J. Strijkers, J.T. Kohlhepp, P.A.A. van der Heijden, H.J.M. de Jonge, J.M. Gaines, J. Appl. Phys. 85 (1999) 5294.
[32] T. Fuji, M. Takano, R. Katano, Y. Bondo, Y. Isozumi, J. Appl. Phys. 66 (1989) 3168.
[33] J.M. Honig, J. Alloys Comp. 229 (1995) 24.
[34] F.C. Voogt, T.T. Palstra, L. Niesen, O.C. Rogojanu, M.A. James, T. Hibma, Phys. Rev B 57 (1998) R8107.
[35] M.A. James, F.C. Voogt, L. Niesen, O.C. Rogojanu, T. Hibma, Surf. Sci. 402–404 (1998) 332.
[36] A. Perez, G. Marest, B.D. Sawicka, J.A. Sawicki, T. Tyliszczak, Phys. Rev. B 28 (1983) 1227.
[37] K.A. Shaw, E. Lochner, D.M. Lin, J. Appl. Phys. 87 (2000) 1727.
[38] J.L. Dormann, T. Merceron, P. Renaudin, V.A.M. Brabers, J. Phys. (Paris) Colloq. 41 (C1) (1980) 177.
[39] N. Spiridis, J. Korecki, in preparation.
[40] G.H. Vurens, M. Salmeron, G.A. Somorjai, Surf. Sci. 201 (1988) 128.
[41] W. Weiss, M. Ritter, Phys. Rev. B 59 (1999) 5201.
[42] S.M. Jordan, J.F. Lawler, R. Schad, H. van Kempen, J. Appl. Phys. 84 (1998) 1499.

ELSEVIER

Thin Solid Films 412 (2002) 24–29

thin solid films

www.elsevier.com/locate/tsf

Shadow mask technology

T. Schallenberg*, C. Schumacher, S. Gundel, W. Faschinger

Physikalisches Institut, EP III, Universität Würzburg, Am Hubland, D-97074 Würzburg, Germany

Abstract

We investigate molecular beam epitaxy (MBE) regrowth through shadow masks developed from AlGaAs/GaAs layers on GaAs [001] substrates. Adjusting the directions of the molecular beams relative to the masks results in in situ lateral structuring. This enables us to modify doping and composition within one layer, to shift it laterally, and even to split it or to reduce its width relative to the mask's aperture. The resolution of this selective area epitaxy (SAE) technique is restricted by half shadows and surface diffusion. With diaphragms and thin masks it is possible to decrease half shadows to a few nanometers. However, diffusion mainly is a material parameter. We have investigated III–V and II–VI semiconductors. In the latter case it is extremely dependent on the crystal orientation. Along $[1-10]$ diffusion lengths are very short. This is in agreement with ab initio calculations in our group. Thus lateral structuring with a resolution of a few nanometers is achieved. We discuss the degrees of freedom, which arise from different chamber geometries and mask concepts. With simple striped masks complex structures such as stacked three colour detectors or selective contacts to embedded 2DEGs can be realised. Three novel mask concepts will be presented. Deeply underetched masks serve as elastic substrates for misfit layers over the critical thickness without plastic relaxation. Second, as an analogy to cleaved edge overgrowth, we use masks developed from AlGaAs/GaAs superlattices. Finally interconnected structures with lateral periodicity of a few micrometers have been realised with grid masks.

Keywords: Molecular beam epitaxy; Shadow masks; Selective area epitaxy; Superlattices

1. Introduction

Mechanical shadow masking is, generally speaking, an obsolete method of patterning vacuum deposited films. However, when its limitations are unimportant, one may exploit its several advantages over modern lithographic techniques. Being an in situ technique it helps to improve device characteristics [1]. Devices, which are not feasible by post-processing or ex situ techniques, have been realised by in situ lateral structuring [2,3]. Also large-scale integration of devices has been demonstrated [4].

Usually removable mechanical masks made of refractory materials (W, Ta, Mo, and Si) are used for selective area epitaxy (SAE) [5]. Shadow masks with small apertures are realised by anisotropic etching of pyramidal shaped holes through thin (001) Si wafers (50 μm thick) [6]. Alternatively a p^+-Si or silicon nitride membrane is prepared and openings are structured by conventional lithography [7]. Both kinds of masks are used in contact mode, which means that the aperture defining side is in contact with the substrate. In this way the partial shadow width, which is proportional to the residuary shadowing distance, is minimised. Selective growth of patterned GaAs/AlGaAs such as with a width as narrow as 1 μm has been demonstrated [6]. However, when using an in situ mask fixture, which is necessary for multi-step masking, the worse contact (increased shadowing distance) causes a minimum 5–7 μm width of the mesa edges [5]. By using a relative motion between the mask and the substrate during deposition a controlled lateral variation of chemical composition in the epitaxial layer structure can be realised. The smallest width of lines written in this way is approximately 10 μm [8]. For using different in situ masks absolute positioning is an unsolved problem. In ultra-high vacuum environment a resolution of the order of several micrometers has not been realised. Due to this limited resolution and alternative SAE techniques, which realise in situ growth of small dimensional structures by means of self-assembling techniques, shadow growth with removable shadow masks has lost its importance for semiconductor technology.

---

*Corresponding author.

0040-6090/02/$ - see front matter © 2002 Elsevier Science B.V. All rights reserved.
PII: S0040-6090(02)00307-3

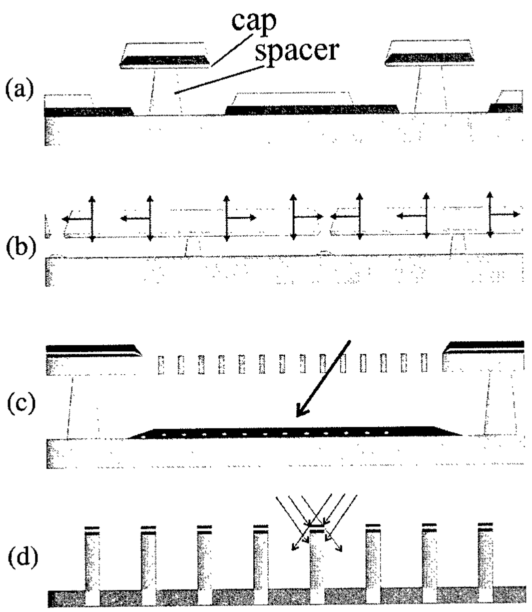

Fig. 1. (a) Growth into T-shape masks for lateral structuring. (b) Growth onto deeply underetched T-masks. The elasticity of the mask is used in order to increase the critical thickness of a misfitted layer. (c) Grid masks enable the growth of coherent structures with lateral periodicity. (d) An analogy to cleave edge overgrowth. Selectively etched SL.

2. Stationary shadow masks

We investigate molecular beam epitaxy (MBE) regrowth through shadow masks developed from AlGaAs/GaAs layers on GaAs [001] substrates (see Fig. 1a). First the GaAs cap layer is structured lithographically and subsequently underetched by hydrofluoric acid, which selectively attacks the AlGaAs spacer layer and uncovers the atomically smooth substrate surface. In this way sub-micrometer apertures and an MBE-precise distance of the shadow edge from the substrate is realised. Döhler et al. have first considered the alignment of such stationary masks relative to the incidence angles of the material sources [2,9,10]. By synchronising mask rotation with shutter operation they achieved selective doping.

2.1. Spatial resolution

Without diffusion the resolution of lateral structuring is limited only by the extend of partial shadows Δx. These are due to the finite aperture y of the oven's orifice (see Fig. 2c). For the RIBER 32 MBE (chamber geometry sketched in Fig. 2) with standard effusion cells the angular spread of the molecular beams is approximately 10°. This is minimised by an increased sample–source distance d and by using small apertures in front of the ovens. In the latter case hot-lip cells or separate heatings are required to prevent accruing of the apertures. Since the width of partial shadows Δx below the mask is proportional to the distance t from the shadow edge, we have reduced the thickness of the spacer layer in order to reduce the width of partial shadows to the order of 10 nm.

In such small dimensions controlled deposition is interfered by diffusion dynamics. For MBE of III–V semiconductors diffusion lengths of the order of several micrometers limit the shadow growth resolution. Submicrometer resolution is only realised with weak-diffusing components like Si or Al. However, dynamics are effectively reduced at low substrate temperatures (LT). Therefore magnetic III–V semiconductors, which are regularly LT-grown, are ideally suited for in situ nanostructuring with the shadow growth technique. Another important class of materials, which is ideally suited to be structured by shadow growth, is wide-bandgap II–VI semiconductors. In this case we have observed an extremely anisotropical diffusion behaviour. When ZnSe (Se-rich) is deposited through stripe-masks oriented along the [1−10] direction faceting of the mesa edges due to self-assembly is observed. In contrast to this a round-shape profile of the edges is observed in the perpendicular [110] orientation. This shape is due to the flux-gradient of the partial shadow. From these experiments we conclude that the preferential diffusion-direction is along [110] with diffusion lengths of the order of 1 μm, while in the perpendicular [1−10] direction diffusion lengths are only of the order of 10 nm. This can be understood by results obtained from density functional calculations in the local density approxima-

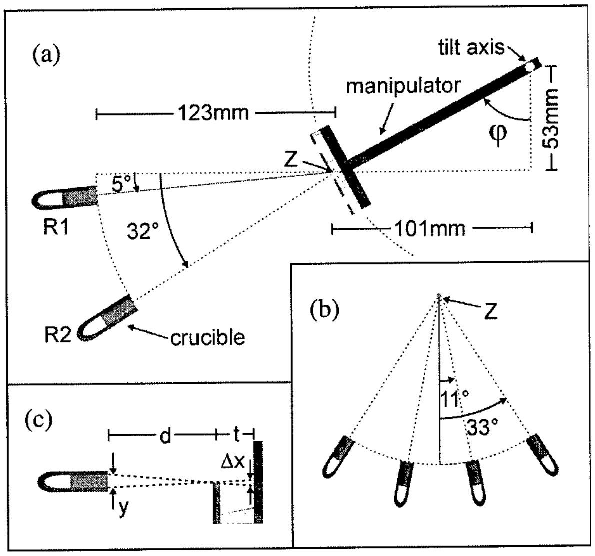

Fig. 2. (a) Sketch of the RIBER 32 chamber geometry with the manipulator in standard position (tilt angle $\varphi = 62°$). The effusion cells (not scaled) are aligned in two angles from the horizontal plane. (b) Their horizontal separation is 22°. (c) The partial shadow Δx is due to the finite aperture y of the oven's orifice.

tion. For these calculations the total energy of a single zinc atom on top of an otherwise perfect selenium-rich (2×1) surface was calculated as a function of position in order to obtain a map of the surface potential for zinc [11]. The result shows that for diffusion in $[1\bar{1}0]$ direction the zinc atoms have to overcome barriers of approximately 640 meV resulting from the selenium dimer rows, whereas similar barriers in the [110] direction are only of the order of 180 meV. A more detailed discussion of diffusion dynamics during the growth of ZnSe will be given in a later contribution.

2.2. Degrees of freedom

Compared with shadow growth with removable masks, the degrees of freedom for lateral structuring with only one stationary mask are somewhat reduced. In order to compensate this deficiency we have done intense basic investigations and developed techniques, which further expand the degrees of freedom of this technique.

These are lateral layer offset, size-control, selective doping, secondary shadowing, and composition modification. Lateral layer offset is realised by changing the angle of incidence of parallel molecular beams relative to the shadow mask. In our MBE chamber pivoting the sample manipulator does this. For a shadow mask of thickness t and an incidence angle φ the absolute layer offset x is given by $x=t\,\tan(\varphi)$. Size control is due to enhanced compound-sticking. At the growth temperature the single elements reevaporate from the surface where they cannot find their compound partners. With non-parallel incident molecular beams growth is restricted mainly to the overlap of the molecular beams. This option depends on the sticking coefficients (material properties), and is not effective with most III–Vs (e.g. gallium does not evaporate and forms droplets where no arsenic is incident). Selective doping is realised by varying the incidence directions of the acceptor and donator molecular beams. In the same way composition modifications of mixed crystals are achieved by adding the mixing components with different angles. Finally secondary shadowing enables the deposition of laterally separated layers. By means of secondary shadow effects in situ grown steep edges can also be used instead of extremely thin shadow masks. In this way it is also possible to integrate shadow edges of different height into one structure.

With all these many degrees of freedom controlled deposition of complex nanostructures in three dimensions is realised. Structures, which demonstrate the potential of this technique, include the nipi band filling modulator (selective contacts to doping-superlattices first realised by Döhler et al. [2]), selective deposition of sub-micrometer in situ contacts to embedded layers (stapled three colour detectors or selective contacts to embedded 2DEGs can be realised in this way [12]), homogeneous ZnSe quantum-wires embedded in MgZnSSe [13], and ZnSe-embedded CdSe quantum-dots arrayed in a single line [14]. These structures have in common that they cannot be realised by any other method.

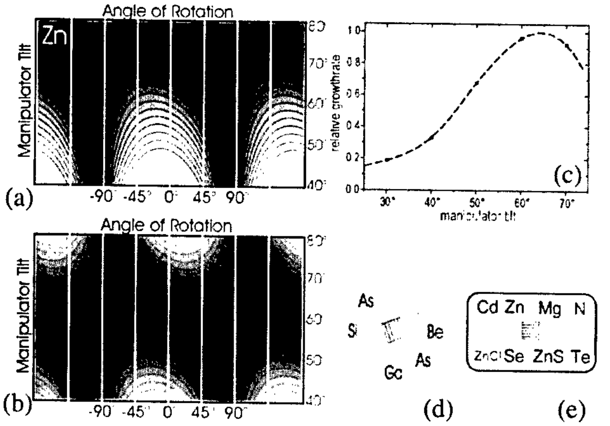

Fig. 3. Angles of incidence φ (relative to a stripe mask) dependent from manipulator tilt and rotation angles [(black) $0°\leq \text{abs}(j)\leq 50°$ (white)]. (a) Zn effusion cell (R1; left inner cell). (b) Se effusion cell (R2; left inner cell). (c) Growth rates of AlGaAs/GaAs-SLs (R2 cells) dependent on the manipulator tilt angle. (d) Center-symmetric arrangement of the effusion cells. (e) Alignment of the effusion cells in two lines.

2.3. Chamber geometry

For the design of new devices with the above stated degrees of freedom some restrictions, which are due to the MBE chamber geometry have to be considered. As has been discussed before the resolution limiting angular spread of the molecular beams is effectively reduced with diaphragms, which minimise the apertures of the sources. Therefore the crucial restrain of the degrees of freedom is the inability to freely vary the directions of the molecular beams. In a standard MBE chamber geometries there are only two co-ordinates (manipulator-tilt and -rotation; see Fig. 3a,b) defining the possible alignments of the sample holder relative to a stationary array of elemental cells. Therefore the residual freedoms critically depend on the cells' arrangement. Chambers with a source alignment in two lines, and the center symmetrical type are commonly used (see Fig. 3d). In the second case it is not possible to align a stripe-mask in the way that more than two molecular beams are incident parallel (with respect to the stripes). Therefore uniform mixed crystals are only achieved by continuously rotating the samples, or by mixing the binary compounds digitally. This severely constrains the freedom to choose whatever material. However, in our RIBER 32 MBE chamber (see Fig. 2a,b) the sources are aligned in two lines with each four elemental cells

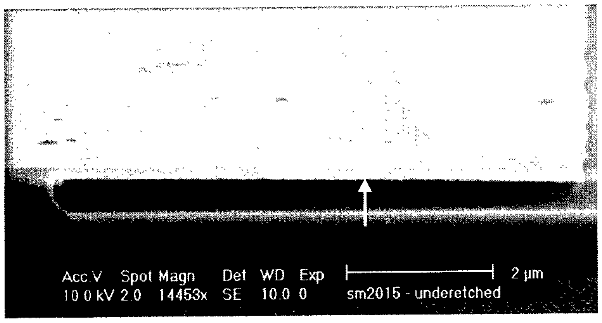

Fig. 4. Elastic mask: a deeply underetched GaAs-layer.

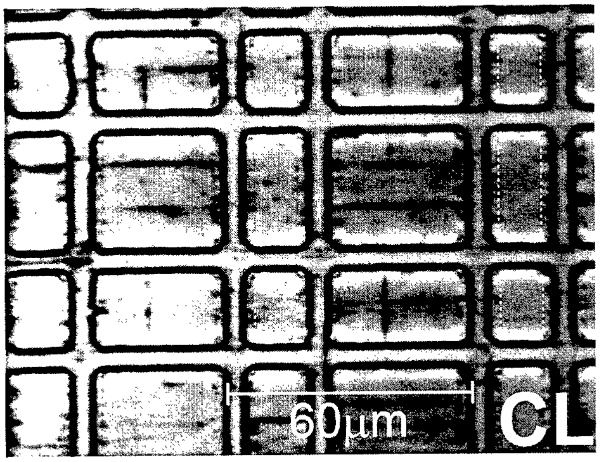

Fig. 5. Cathodo-luminescence micrograph of an overgrown elastic masks. The dashed boxes indicate not underetched areas of elastic fields, which are free of dark-line and point-defects.

(Fig. 3d). In this configuration the growth of uniform quaternary layers is possible. Pivoting the sample manipulator does offsetting the mixed-crystal layers. And non-parallel incidence of the molecular beams is possible in a wide range of the (two-dimensional) manipulator positions. Therefore a large variety of complex structures can be grown. Usage of multi-crucible cells, compound sources, or an UHV transfer system, which interconnects several MBE chambers, further expands the possibilities. In the Würzburg MBE cluster six MBE chambers plus an in situ metallization chamber are connected together in this way.

For a further improvement of the chamber geometry for directed molecular beam epitaxy the possibility to manipulate the sources' arrangement in situ is the main task. Simple solutions to this problem are valved cells with kinked line cracking zones lapping into the chamber. In situ manipulation of the outlets' position can be arranged by rotating this extension. Valved cells are generally important for this technique since the effective flux rates vary with manipulator tilt. The consequences of this are variations of the growth rates (see Fig. 3c), the composition of mixed crystals, and the critical flux-ratio of compounds (p_{II}/p_{VI}, and p_{III}/p_{V}, respectively) from the stoichiometric value. The final task that is important for the chamber geometry is the position of the tilt-axis. This should cross the sample, since otherwise flux variations tend to be more complex (as in the RIBER 32 MBE; see Fig. 2a).

3. Mask concepts

The interesting properties of AlGaAs/GaAs shadow masks (selectively etchable, pseudomorphic, strong, and elastic) have inspired us for the following three novel mask concepts.

3.1. Elastic mask

The first mask is based on the extreme strength and elasticity of deeply underetched GaAs-cap layers. Thin layers are even stable if the free-standing parts drag out 50 times the layer thickness h_b (Fig. 4). Such fine structures can be used as elastic substrates (see Fig. 1b). Lo [15] has calculated that the effective critical thickness t_{eff} (for the generation of misfit dislocations) of films deposited on ideal elastic substrates approaches infinity ($t_{\mathrm{eff}}^{-1}=t_c^{-1}-h_b^{-1}$) as the substrate thickness h_b is reduced to below the critical thickness t_c (with inelastic substrate). For $t_c<h_b<2t_c$ Lo also supposed that threading dislocation free heteroepitaxy could still be achieved, since threading dislocations tend to be pushed into the thin substrate due to the effect of image force. However, selective area epitaxy on plain substrates also expands critical thicknesses. This is due to lateral elastic relaxation of selectively deposited layer, if the thickness to width ratio $h/2l$ is high. Jain et al. have performed finite element calculations for this case, and found that for the ratios $h/2l=0.05$, and 0.1 stresses in the middle of an elastically relaxed stripe are reduced by 26%, and 40%, respectively [16]. We have defined fields on a shadow mask by opening narrow aperture stripes along [110] and [1−10] direction. The edges of these fields have been underetched on a width of 2 µm, serving as elastic substrates. The residuary area of the 10–30 µm wide fields is based on the thick AlGaAs spacer layer and is free to relax laterally in order to reduce strain in layers, which are grown above it. We have overgrown such elastic fields. A 50 nm thin GaAs buffer and 750 nm ZnSe (overcritical) were deposited under standard MBE conditions. With an optimised mask preparation defects due to leavings on the mask (as those observed in Fig. 4) could be avoided. Results obtained by means of high-resolution X-ray diffraction (HRXRD) indicate that the thick ZnSe layer on the elastic mask is only partially relaxed. The degree of plastic relaxation is only $\gamma=0.53$. Additionally a triangle shaped diffuse scattering signal is observed in the 115 reciprocal space maps. This is probably due to the existence of pseudomorphic

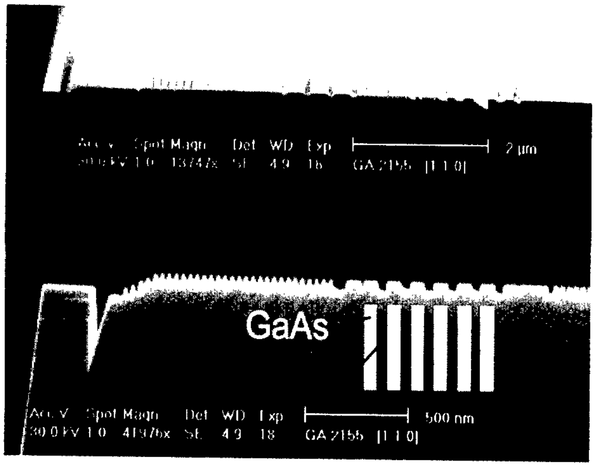

Fig. 6. Scanning electron micrographs from selectively etched AlGaAs/GaAs-superlattices.

fields, which are free of treading dislocations (see Fig. 5). Evaluation of cathodoluminescence micrographs shows a significant reduction of the defect density with the size of the fields. On most of the small fields (edge lengths >10 µm) no defects have been found.

3.2. Analogy to cleaved edge overgrowth

The second mask concept (see Fig. 1d) is analogous to cleaved edge overgrowth (CEO). GaAs/AlGaAs superlattices (SLs) were cleaved and subsequently dipped in hydro-fluoric acid (HF). This selectively etches the AlGaAs layers, and leaves free-standing GaAs lines (see Fig. 6). The smallest line widths realised in this way are as small as 10 nm (35 nm high). The idea is to overgrow these pattern-lines (the combined use of shadow techniques is optional). Since two MBE processes define thickness and width, it should be possible to realise homogeneous nanowires in this way. In contrast to CEO in situ cleaving is not required since the growth area is spatially separated from aluminium–composite layers. In the first experiments we have overgrown such pre-patterned cleave edges with III–V materials (see Fig. 7). Self-assembly of smooth facets has been observed when the nominal thickness of grown layers was of the order of the width of the GaAs-stripes (Fig. 7b). With only thin GaAs/InGaAs layers deposited onto the mask the homogeneity of the etched GaAs-lines was not affected (Fig. 7a). In order to reproducibly realise homogeneous nanowires with this mask concept improved processes for the preparation of the terminated [110] GaAs interfaces (oxide-, or hydrogen-), and for a proper desorption (substrate temperature is critical) have to be developed.

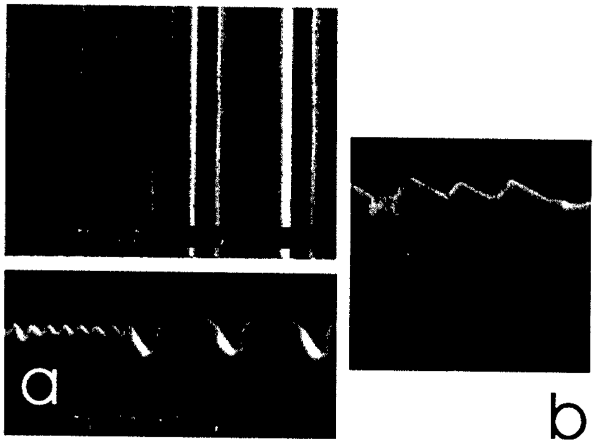

Fig. 7. Scanning electron micrograph of overgrown etched superlattices. (a) Thin layers. (b) Thick layer.

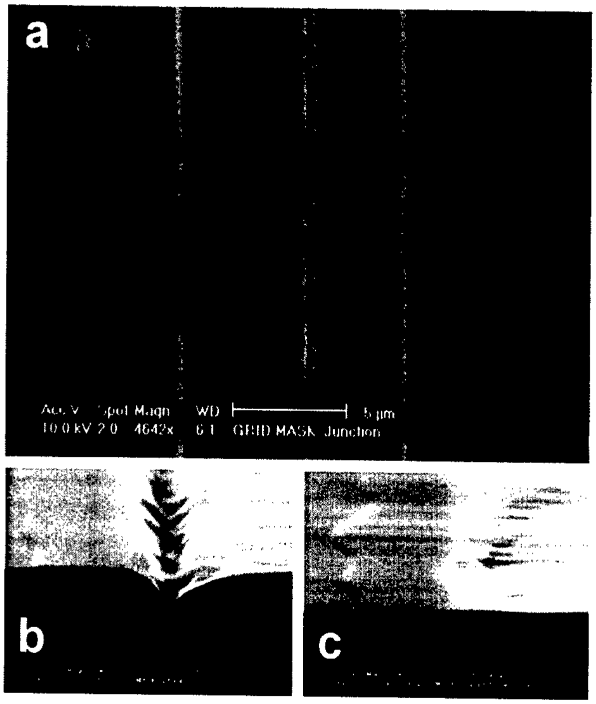

Fig. 8. (a) Scanning electron micrographs from AlGaAs and GaAs stripes, which have been deposited through a 10 µm periodic grid mask with 4.6 µm apertures. (b) A groove between the AlGaAs and the GaAs stripe. (c) Widened apertures level the groove, and coherent periodic arrays of stripes are realised.

3.3. Grid mask

The final mask concept (see Fig. 1c) presented in this contribution is a real two-dimensional mask. A grid mask was structured by etching arrays of aperture stripes (4.5–5.5 µm×150 µm) with 10 µm lateral periodicity into the 1-µm-thick GaAs cap layer. Finally the residual GaAs grid was completely underetched. In this way large areas of the substrate are uncovered, with only the free hanging grid above them. Bending of the grid stripes due to gravity is small. In a first experiment we have deposited AlGaAs and GaAs layers through the grid with absolute layer offsets of 2.5 μm, and −2.5 μm, respectively (see Fig. 8a). Consequently the growth areas meet in the middle of the aperture lines and in the centre below the free-hanging GaAs grid lines. Dependent on the width of the aperture-lines separate stripes (with grooves; see Fig. 8b), and alternatively interconnected structures with lateral periodicity of 10 μm have been realised (see Fig. 8c). The potential of grid masks is the possibility to perform in situ structuring of lateral-periodic structures with the same many degrees of freedoms that have been discussed above.

4. Conclusion

In summary, directed shadow growth through stationary shadow masks is an in situ technique suited for nanostructuring. Since its high resolution is based on weak diffusion dynamics it addresses especially those materials, which are not well suited for self-assembling techniques. These are LT:III–V (important magnetic semiconductors) and most II-VI semiconductors (group VI-rich growth). We have developed several techniques, which make up the many degrees of freedom of this technique. These are lateral layer offset, size-control, (selective doping,) secondary shadowing, and composition modifications. By this growth of complex nanostructures in three dimensions is realised. Shadow growth also avoids restrictions, which are due to layer-by-layer growth. Therefore unusual materials combinations (e.g. relaxed with pseudomorphic structures) and new devices can be realised.

We have discussed restrictions due to the MBE chamber geometry as the angular spread of the molecular beams, the fixed arrangement of effusion cells, and variations of the fluxes. Possible solutions for these problems have been presented.

Three novel mask concepts were presented. Homogeneous quantum-wires can be realised by overgrowing selectively etched superlattices. In contrary to CEO in situ cleaving is not required. Secondly we have demonstrated that overgrowing elastic masks increases critical thicknesses. Finally we have presented a first two-dimensional stationary shadow mask, the grid mask. This enables the growth of interconnected structures with lateral periodicity.

Acknowledgments

This work is granted by the 'Deutsche Forschungsgemeinschaft' (SFB 410, project A1).

References

[1] D.C. Streit, T.R. Block, A. Han, M. Wojtowicz, D.K. Umemoto, K. Kobayashi, A.K. Oki, P. Liu, R. Lai, G.I. Ng, J. Vac. Sci. Technol. B 13 (1995) 771.

[2] X. Wu, K.H. Gulden, M. Thomas, G. Wilson, J. Walker, G.H. Döhler, J.R. Whinnery, J.S. Smith, J. Cryst. Growth 127 (1993) 896.

[3] A. Lorke, J.H. English, A.C. Gossard, P.M. Petroff, J. Appl. Phys. 77 (1995) 3578.

[4] H. Saito, I. Ogura, Y. Sugimoto, K. Kasahara, Appl. Phys. Lett. 66 (1995) 2466.

[5] Y. Luo, A. Cavus, M. Tamargo, J. Wan, F.H. Pollak, J. Vac. Sci. Technol. B 16 (1998) 1312.

[6] W.T. Tsang, M. Ilegems, Appl. Phys. Lett. 31 (1977) 301.

[7] G. Kaminsky, J. Vac. Sci. Technol. B 3 (1985) 741.

[8] W.T. Tsang, A.Y. Cho, Appl. Phys. Lett. 32 (1978) 491.

[9] K.H. Gulden, X. Wu, J.S. Smith, P. Kiesel, A. Höfler, M. Kneissel, P. Riel, G.H. Döhler, Appl. Phys. Lett. 62 (24) (1993) 3180.

[10] G. Hasnain, D. Mars, G.H. Döhler, M. Ogura, J.S. Smith, Appl. Phys. Lett. 51 (1987) 832.

[11] S. Gundel, Doctoral Dissertation, Physikalisches Institut, Universität Würzburg, 2001.

[12] T. Schallenberg, C. Schumacher, W. Faschinger, Physica E, Proc. MSS 10 (2001).

[13] T. Schallenberg, M. Obert, G. Bacher, V. Türck, C. Schumacher, W. Faschinger, in press.

[14] T. Schallenberg, V. Türck, C. Schumacher, W. Faschinger, in press.

[15] Y.H. Lo, Appl. Phys. Lett. 59 (1991) 2311.

[16] S.C. Jain, A.H. Harker, A. Atkinson, K. Pinardi, J. Appl. Phys. 78 (1995) 1630.

ELSEVIER

Thin Solid Films 412 (2002) 30–33

www.elsevier.com/locate/tsf

Trions as a probe of spin injection through II–VI magnetic/non-magnetic heterointerface

M. Ghali[a,*], J. Kossut[a], E. Janik[a], M. Kutrowski[a], Ł. Kłopotowski[b], M. Potemski[c], F. Teran[c]

[a]*Institute of Physics, Polish Academy of Sciences, Al. Lotników 32/46, 02-668 Warsaw, Poland*
[b]*Institute of Experimental Physics, Warsaw University, ul. Hoża 69, 00-81 Warsaw, Poland*
[c]*Grenoble High Magnetic Laboratory, F-38042 -Cedex 9, Grenoble, France*

Abstract

We report on an efficient injection of spin polarized electrons from CdMgMnTe diluted magnetic semiconductor to non-magnetic CdMgTe quantum well structure. The electron spins were able to diffuse keeping their polarization memory for distances larger than 2000 Å. Study of the optical properties of trions is shown to be a new, highly sensitive detection tool of spin injection.

PACS: 78.55.Et; 78.55.-m; 73.90.+f

Keywords: Diluted magnetic semiconductors; Trions; Spin injection

1. Introduction

Manipulation of electron spins is a basic ingredient of the new field of spintronics. The ability to exploit these spins in semiconductors promises new devices with enhanced functionality, such as high speed spin-polarized field effect transistors or logic gates in the emerging field of quantum computation [1]. This new class of devices involves injection of spin-polarized electrons through a magnetic/non-magnetic interface, with the spins being able to maintain the memory of their polarization during the transport in the non-magnetic semiconductor. At the present stage of development a sensitive spin polarization detection is, moreover, essential. Recently, efficient spin injection into semiconductors has been achieved utilizing either diluted magnetic [2] or ferromagnetic semiconductors [3] even in lattice-mismatched structures [4,5]. In all these cases spin polarized carriers have been injected into GaAs non-magnetic semiconductor structures due to the large spin coherence length observed in these materials [6]. The detection of those coherently transmitted spins has been recorded by observing polarized excitonic luminescence from non-magnetic quantum well QW utilized as spin injection detector.

In this work we study transmission of spin-polarized electrons in CdMgTe non-magnetic semiconductor where spins originated from a diluted magnetic CdMgMnTe spin injector. Moreover, the main feature of this study is that we use negatively charged excitons X^- as a new probe for spin detection. Negatively charged excitons or trions in two-dimensional systems have been evidenced experimentally in 1993 [7] and have been the subject of very intensive studies [8–10] since then. Here we exploit the unique properties of trions that are due to their highly sensitive spin dependent formation character.

2. Experiment

The structure under study consists of a CdTe/$Cd_{0.92}Mg_{0.08}Te$ heterostructure with type I band alignment grown by molecular beam epitaxy on (100) oriented SI-GaAs substrate. A relatively wide CdTe quantum well (QW) with 150 Å width (assuring narrow lines in luminescence spectra) is confined between an abrupt band gap $Cd_{0.92}Mg_{0.08}Te$ barrier in one side. On the other side, a graded band gap barrier of $Cd_{1-x}Mg_xTe$, x ranging between 0.08 to 0.25, has been grown using the digital alloy method [11]. On the top of the latter barrier, a 380-nm-thick quaternary compound layer of $Cd_{0.72}Mg_{0.25}Mn_{0.02}Te$ diluted magnetic semiconductor (DMS) was grown, which serves as a source of spin

---

*Corresponding author. Tel.: +48-22-843-1331; fax: +48-22-843-1331.
E-mail address: mohsen@ifpan.edu.pl (M. Ghali).

0040-6090/02/$ - see front matter © 2002 Elsevier Science B.V. All rights reserved.
PII: S0040-6090(02)00308-5

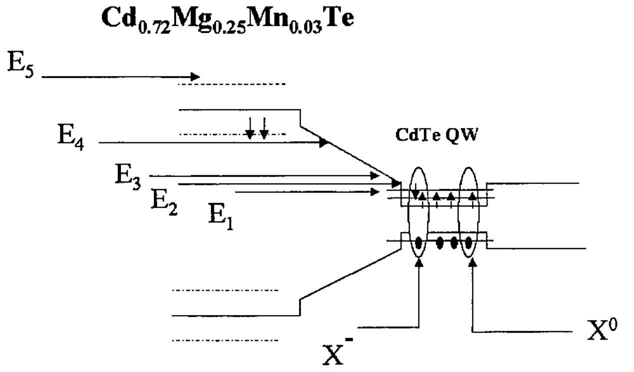

Fig. 1. A schematic diagram of the band alignment of the sample structure. Thick long arrows indicate absorption into different regions using different excitation energies. Dashed lines show the giant Zeeman splitting of CdMgMnTe bands.

polarized carriers. Fig. 1 shows a schematic diagram of the band alignment of the entire structure. The structure was intentionally undoped. However, due to residual impurities we may expect present of excess electrons in the QW of approximately 10^{10} cm^{-2}. The graded band gap spacer barrier between the QW and the spin injector was intended to enhance carrier diffusion into the QW.

Magneto-photoluminescence experiments were carried out on this structure in magnetic fields up to 13 T at the temperature of 1.8 K. Selective excitations in the QW, in the non-magnetic barrier and close but above the magnetic layer band gap have been performed using Ti:sapphire, He–Ne and Kr^+ lasers, respectively. Care was taken to keep the exciting power for each excitation line to precisely 1 mW. Auxiliary photoreflectivity experiments have been performed.

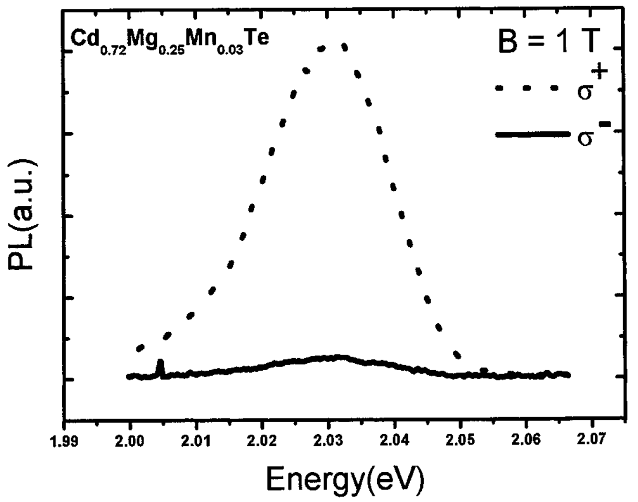

Fig. 2. Circular polarized PL of $Cd_{0.72}Mg_{0.25}Mn_{0.02}Te$ spin injector material under excitation by 2.18 eV in both (a) σ^+ and (b) σ^- detections in magnetic field 1T.

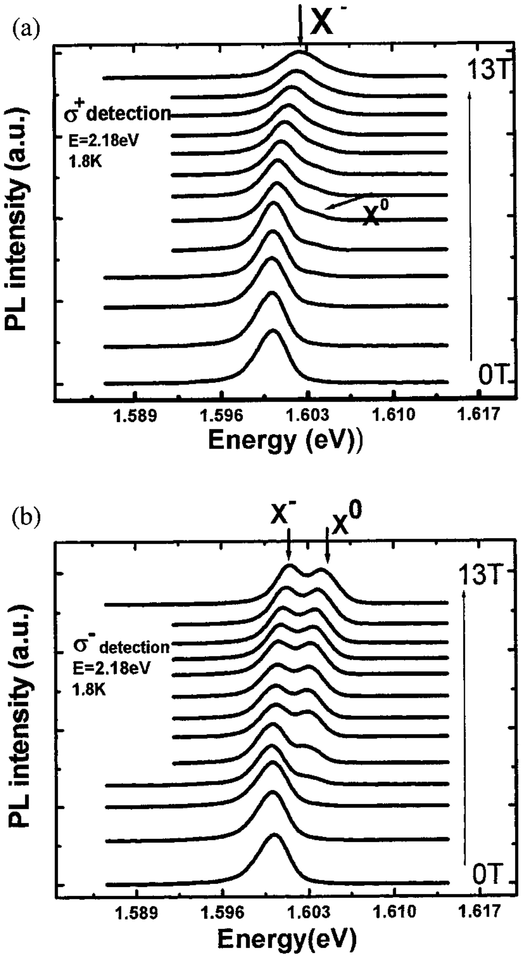

Fig. 3. PL spectra from the CdTe QW under excitation with 2.18 eV in different magnetic fields (from Zero till 13T). The detection was analyzed in both (a) σ^+ and (b) σ^-. Neutral exciton (X^0) is clearly pronounced at high magnetic fields starts from 3.6 T. The lower energy satellite peak is assigned to X^- trion. Note that both X^0 and X^- are circularly polarized in reversed directions.

3. Results and discussions

First, we confirmed by the reflectivity and PL measurements that the $Cd_{0.72}Mg_{0.25}Mn_{0.02}Te$ layer indeed shows a large Zeeman splitting (~35 meV at 5 T) between the spin-up ($m_j = 1$) and spin down ($m_j = -1$) excitons (i.e. it displays a giant spin splitting characteristics of DMS). Fig. 2 shows the photoluminescence from $Cd_{0.72}Mg_{0.25}Mn_{0.02}Te$ in σ^+ and in σ^- detection at 1T. As we can see, all optically pumped electrons in this layer relax to the lower Zeeman level producing a system of completely polarized excitons and, therefore, really completely polarized electrons [12]. This effect arises due to the presence of Mn^{2+} in the material that greatly facilitate the spin-flip processes. This feature, in fact, makes CdMgMnTe as an efficient spin injecting system. Fig. 3a,b shows the evolution of the PL spectra from the 150 Å CdTe QW at 1.8 K as a function of a

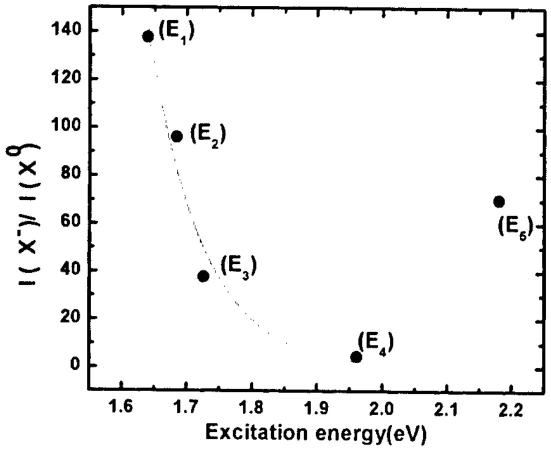

Fig. 4. The density ratio between X^- trion and neutral exciton (X^0) when photo-absorption occurs inside the QW (E_1), in the non-magnetic barrier (E_2, E_3, E_4) and above the spin aligner band gap (E_5). The decay of the ratio is clearly seen when the absorption is being in the non-magnetic regions (barrier and QW) while a re-enhancement of the ratio occurs when absorption occurs in the magnetic layer (the spin injector). Symbols represent data points while line is a guide to eyes.

magnetic field B in both σ^+ and σ^- detection, respectively. In these experiments unpolarized laser light with energy 2.18 eV has been used to excite the structure close to but above the CdMgMnTe band gap. As we can see, at $B=0$, the spectra are dominated by a strong peak at 1.600 eV with a small satellite ~3.4 meV at a higher energy. This satellite becomes gradually more pronounced with an increasing magnetic field in the σ^- polarization. This polarization behavior is confirmed in additional photoreflectivity measurements (not shown here). We assign the high-energy peak to neutral exciton recombination (X^0) while the lower one to a negatively charged exciton (X^-). The details of X^- identification will be shown elsewhere. The presence of trions in our intentionally undoped structure, showing their clear signature in the optical properties, can be ascribed to background n-type impurities in the structure. This effect has been observed in other recent studies in GaAs [13], CdTe [14] and ZnSe [15] structures. We estimate from the dissociation energy of the trions in our structures that the excess background electrons in the QW to be $\sim 3\times 10^{10}$ cm^{-2} [16]. The intense X^- peak at zero fields indicates the high probability of X^- formation. Fig. 4 shows the integrated intensity ratio of X^- to that of exciton (which we assume to be proportional to the densities of X^- and X^0, respectively) under different excitation energies: above, in the non-magnetic barrier, and inside the QW in the magnetic field of 0.5 T.

Let us discuss first what happens when the excitation energy does not exceed the band gap of the magnetic layer (2.03 eV in the absence of the magnetic field). In Fig. 4—under various excitation energies, E_1, E_2, E_3, E_4—it is clearly seen that the X^-/X^0 intensity ratio decays with the excitation energy increasing gradually from the QW band edge. This behavior implies a reduction of the excess electrons in the QW. This is, in turn, related to the fact that most of the absorption events occur in the non-magnetic barrier region when excitation is above the QW edge [17]. As in intentionally n-type doped GaAs-AlGaAs QWs, the internal electric fields created both by the ionized donors and the excess electron charges in the well tend to separate the photo-created electron–hole pairs excited in the barrier [18]. It is suggested that the holes are swept into the well where they can recombine with the excess electrons in the QW, while the photo-excited electrons are trapped by the ionized impurities in the barrier [19]. Those electrons that, nevertheless, enter into the well have a 'wrong' spin (i.e. the same spin with $m_j=+1/2$ corresponding to the lowest Zeeman component of spin splitting conduction band in the non-magnetic material) as those already present in the well, therefore, not being able to form a stable trion in a singlet state.

Let us now see what happens when the absorption of the exciting light occurs in the magnetic layer (the spin injector in our structure). With excitation energy E_5, we notice in Fig. 4 a significant increase of the X^- to X^0 intensity ratio. We have to keep in mind that there is a reversal of sign of the g-factor of the photoexcited electrons in this magnetic regions ($g<0$ for the CdMgTe barrier and CdTe QW) while $g>0$ for CdMgMnTe magnetic spin aligner. The formation probability of X^- trion is proportional, specifically, to the number of spin-down ($m_j=-1/2$) electrons in the QW system. These can be easily supplied if there is an efficient and spin preserving transfer of electrons from the spin injector to the QW layers. This leads to an important conclusion that this enhancement of X^-/X^0 density ratio is due to spin polarized electrons diffusing, in the spin down state, from the magnetic spin aligner (CdMgMnTe) to the CdTe QW via 2000 Å of graded band gap non-magnetic CdMgTe spacer. These polarized electron spins, which are in the 'correct' spin state; $m_j=-1/2$; (i.e. reversed in direction to those contained already in the CdTe QW) are captured by confined electron–hole pairs (excitons) inside the QW increasing the formation probability of X^- trions.

In conclusion, we have shown possibility of optically injecting electron spins from II–VI magnetic semiconductor to non-magnetic CdTe QW using a non-ordinary probe (negatively charged exciton). The trion X^- can be efficiently used as a highly sensitive spin detector due to its spin dependent formation character.

Acknowledgments

This work has been partially supported by center of Excellence CELDIS under contract ICA1-CT-2000-70018.

References

[1] G. Prinz, Phys. Today 48 (1995) 58.
[2] R. Fiederling, M. Keim, G. Reuscher, W. Ossau, G. Schmidt, A. Waag, L. Molenkamp, Nature 402 (1999) 787.
[3] Y. Ohno, D. Young, B. Beschoten, F. Matsukura, H. Ohno, D. Awschalom, Nature 402 (1999) 790.
[4] B. Jonker, Y. Park, B. Bennett, H. Cheong, G. Kiseoglou, A. Petrou, Phys. Rev. B 62 (2000) 8180.
[5] M. Ghali, J. Kossut, E. Janik, K. Reginski, L. Klopotowski, Solid State Commun. 119 (6) (2001) 371.
[6] J. Kikkawa, D. Awschalom, Nature 397 (1999) 139.
[7] K. Kheng, R. Cox, Y. Merlr d'Aubigne, F. Bassani, K. Saminadayar, S. Tatarenko, Phys. Rev. Lett. 71 (1993) 1752.
[8] Th. Taliercio, P. Lefebvre, V. Calvo, D. Scalbert, N. Magnea, H. Mathieu, J. Allegre, Phys. Rev. B 58 (1998) 15408D.
[9] D. Brinkmann, J. Kudrna, P. Gilliot, B. Honerlage, A. Arnoult, J. Cibert, S. Tatarenko, Phys. Rev. B 60 (1999) 4474.
[10] F. Munteanu, Y. Kim, C. Perry, D. Rickel, J. Simmons, J. Reno, Phys. Rev. B 61 (2000) 4731.
[11] A. Gossard, H. Sundaram, P. Hopkinse, in: A. Gossard (Ed.), Epitaxial Microstructures, Academic, Boston, 1994.
[12] J. Furdyna, J. Kossut, Diluted Magnetic Semiconductors, Semiconductors and Semimetals, 25, Academic Press, New York, 1998.
[13] J. Osborne, A. Shields, M. Pepper, F. Bolton, D. Ritchie, Phys. Rev. B 53 (1996) 13002.
[14] C. Hu, W. Ossau, P. Tan, T. Wojtowicz, G. Karczewski, J. Kossut, Phys. Rev. B 63 (2000) 045313.
[15] O. Homburg, K. Sebald, P. Michler, J. Gutowski, H. Wenisch, D. Hommel, Phys. Rev. B 62 (2000) 7413.
[16] V. Huard, R. Cox, K. Saminadayar, A. Arnoult, S. Tatarenko, Phys. Rev. Lett. 84 (2000) 187.
[17] A. Shields, M. Pepper, D. Ritchie, M. Simmons, Adv. Phys. 44 (1995) 47.
[18] I. Kukushkin, V. Klitzing, K. Ploog, V. Kirpichev, A. Shepelet, Phys. Rev. B 40 (1989) 4179.
[19] G. Finkelstien, H. Shtrikman, I. Bar-Joseph, Phys. Rev. Lett. 74 (1995) 976.

ELSEVIER

Thin Solid Films 412 (2002) 34–37

thin solid films

www.elsevier.com/locate/tsf

The growth modes of epitaxial Au/Co/Au sandwiches

A. Wawro[a,]*, L.T. Baczewski[a], P. Pankowski[a], M. Kisielewski[b], I. Sveklo[b], A. Maziewski[b]

[a]*Institute of Physics Polish Academy of Sciences, Al. Lotników 32/46, 02-668 Warsaw, Poland*
[b]*Laboratory of Magnetism, Institute of Physics, University of Bialystok, ul. Lipowa 41, 15-424 Bialystok, Poland*

Abstract

Optimum growth conditions of epitaxial Au/Co/Au sandwiches with a strong perpendicular magnetic anisotropy have been investigated. The thermally induced evolution of the sandwich morphology, which determines its magnetic properties, was studied by means of reflection high-energy electron diffraction and Auger electron spectroscopy. The roughness of Au and Co surfaces, affected by the sample annealing, was evaluated from the length-dependent variance of topography acquired by atomic force microscopy.

Keywords: Surface roughness; Epitaxy; Gold; Cobalt

---

1. Introduction

Magnetic properties of surfaces and interfaces have been one of the most important topics in modern magnetism. They have been mostly studied in structures with lowered dimensionality like thin magnetic sandwiches or multilayers. A perpendicular magnetic anisotropy, being of great interest from both basic research and practical applications (e.g. for magnetic storage media) points of view, is one of the results of the presence of interfaces in such structures. Therefore, the Co/Au system has been widely studied since the first announcement of such property in 1986 [1]. The thin Co layer exhibits a magnetisation perpendicular to the film plane, which similarly to other features, such as coercivity, magnetic domain structure, magnetisation reversal and Curie temperature [2–12], is film thickness dependent. Above a certain critical thickness a second order phase transition takes place resulting in the magnetisation reorientation to the in-plane direction.

The earliest studies of these phenomena were based on the assumption that the interfaces were morphologically smooth. However, the existence of interface roughness in real films might affect substantially their magnetic properties. Shape and interface anisotropy is strongly dependent on the film structure and the interface roughness due to appearance of non-compensated magnetic poles. Imperfections of the interfaces may act as pinning centres for domain walls, modifying mechanisms of magnetisation reversal. Therefore, an understanding of a correlation between the film morphology and magnetic properties is of great importance.

In this paper we analyse the growth conditions of Au and Co layers as a function of the type of substrates. On the basis of reflection high-energy electron diffraction (RHEED) and Auger electron spectroscopy (AES) analyses, supported by the topography measurements at various scan sizes, performed by use of atomic force microscopy (AFM), the thermally-induced evolution of the Au/Co/Au sandwich structure is described.

2. Experimental details

The Au/Co/Au sandwiches were grown in a molecular beam epitaxy (MBE) system with the vacuum level in the range of 10^{-10} torr. Glass and sapphire wafers with orientation (11–20) buffered with a Mo layer were used as substrates. Co and Mo were evaporated from electron guns and Au from effusion cells at the rates lower than 0.5 Å/s. All deposition processes were performed at room temperature (RT). The bottom Au layer, 200-Å-thick, was grown either directly on the glass substrate or on the Mo buffer (200 Å) covering a sapphire substrate. The shape of the Co layer was either flat or wedge-like (obtained with the use of a linear motion of the shutter) depending on a specific magnetic measurement purpose. Its thickness range was between 0 and 25 Å. The top Au layer was kept at 80 Å in

---

*Corresponding author.
E-mail address: wawro@ifpan.edu.pl (A. Wawro).

0040-6090/02/$ - see front matter © 2002 Elsevier Science B.V. All rights reserved.
PII: S0040-6090(02)00309-7

Table 1
Roughness σ and correlation length ξ parameters for Au and Co layers annealed at various temperatures

T (°C)	200-Å Au on glass		200-Å Au on Mo buffer		8-Å Co on Au		15-Å Co on Au	
	σ (nm)	ξ (nm)	σ (nm)	ξ (nm)	σ (nm)	ξ (nm)	σ (nm)	ξ (nm)
RT	4.30	87.1	0.46	64.2	0.18	86.3	0.20	169.2
170	3.75	83.7	0.17	125.0				
200	5.13	121.2	0.19	126.6				
250					0.21	83.3	0.14	138.9
300	6.50	101.3	0.27	124.8				

thickness. The crystalline structure of all grown layers was characterised in situ by RHEED. The AES analysis was carried out to check the chemical composition of the layers and to estimate diffusion processes due to the sample annealing. Ex situ AFM measurements (Nanoscope III) in the Tapping mode were performed for surface roughness investigations.

3. Results and discussion

The growth mode of the bottom Au layer is strongly influenced by the substrate type. Au layers deposited on glass wafers are polycrystalline, whereas the epitaxial growth is obtained for sapphire (11–20) substrates. In the latter case the RHEED pattern exhibits clear streaks for all layers, typical of monocrystalline structure. The Mo buffer deposited on the sapphire substrate has (110) orientation. Such a buffer favours the growth of the Au (111) layer. In spite of a large lattice mismatch, approximately 14%, the Co layer deposited on Au exhibits coherent growth in (0001) orientation. On the basis of our analysis it is impossible to distinguish whether its structure is fcc or hcp type. The top Au layer grows also in the (111) orientation—the same as the bottom Au layer. The following relations between in-plane directions of the constituent layers are found: sapphire (11–20)/Mo(110): [0001]||[1-1-1], Mo(110)/Au(111): [001]||[1–10], Au(111)/Co(0001): [1–10]||[11–20], Co(0001)/Au (111): [11–20]||[1–10]. The RHEED streaks for Mo ([001], [1–10] and [1–11] directions) and Au surfaces ([1–12] and [1–10] directions) are sharp with distances between them as for the bulk. These layers are relaxed and no strains on their surface are present. In contrast, the Co layer behaves in a different way. The RHEED streaks along [11–20] and [1–100] directions are blurred and the lattice constant, determined from the distance between them, varies with the Co layer thickness. Due to a remained coherence and large lattice mismatch in Co layers grown on Au the existence of expanding strains is observed. Even for 15-Å-thick Co layer the lattice constant is 3% higher than for the bulk. The annealing of Co layers at 250 °C leads to substantial strain relaxation. This phenomenon is discussed further in the paper.

Because of the strong influence of the layer morphology, determined by the growth conditions, on magnetic properties, an unambiguous characterisation of the surface roughness is required. For this purpose the scaling theory for self-affine fractal surfaces was applied [13,14]. The analytic form of a function for roughness analysis is given as:

$$g(R)=2\sigma^2[1-\exp(-(R/\xi)^{2H})]$$

where R is a linear dimension of the analysed area; σ, calculated surface roughness; ξ, correlation length; and H, Hurst dimension. For $R \ll \xi$ the value of the correlation function varies as $g(R) \sim R^{2H}$. Above the correlation length ($R \gg \xi$) the value of the function g no longer scales with R and saturates at $2\sigma^2$. The value of the parameter ξ may be attributed to the linear dimension of islands.

The roughness dependence on the length scale was investigated on the base of the AFM topography measurements. The microscopic images, recorded with the resolution 512×512 pixels, were divided consecutively by 4, 16, 64, 256, 1024 and 4096 non-overlapping square tiles, covering the whole scanned area. The value of $g(R)$ was taken as the mean value calculated over all tiles.

The calculated surface roughness σ and the correlation length ξ are shown in Table 1. As mentioned earlier, the growth mode was determined by the type of substrate. Au layers deposited on a glass substrate are polycrystalline. Typical three-dimensional growth occurs. As a consequence the surface is very rough. Consecutive annealing at temperatures in the range from 170 to 350 °C shows that the roughness has a tendency to increase, similarly to the trend shown by the correlation length, leading to the wider and higher islands of the deposited material.

The quality of the Au layer morphology is substantially improved by using the sapphire substrate buffered with Mo. The deposition at RT results in Stranski–Krastanov mode growth, typical of the (111) plane. Atomically flat islands, approximately 80 nm in diameter, with sixfold symmetry are observed (Fig. 1). The fluctuation of the surface height is of the order of double

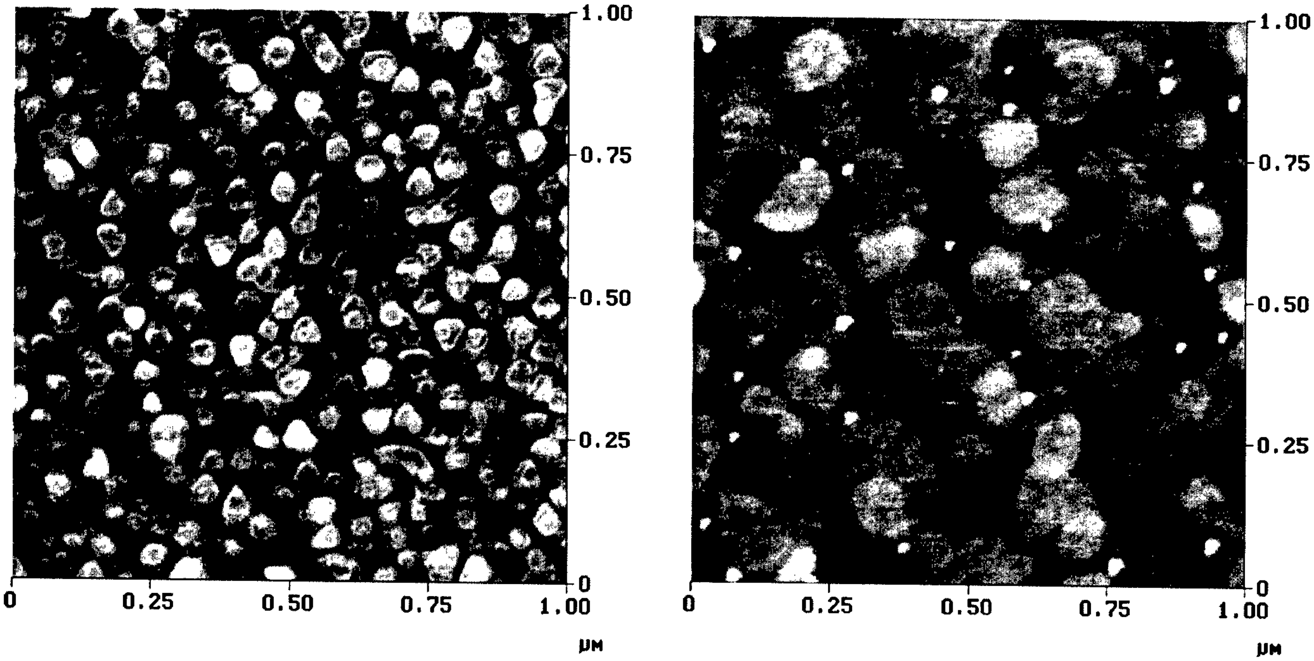

Fig. 1. AFM image of the Au 200-Å-thick layer as-deposited on the Mo buffer (left) and after annealing at 200 °C (right). The range of the grey scale is 2 nm.

(111) plane spacing. Contrary to Au growth on glass, the vacuum annealing of the Au layer deposited on the Mo buffer improves significantly its morphology. The temperature of 170 °C is high enough to reduce the roughness more than twice (fluctuation of the surface height is suppressed to single monolayer step height) and increase the diameter of atomically flat islands by the same factor. The annealing at higher temperatures up to 600 °C does not affect the topography markedly. It is worth to mention that even a small miscut of a sapphire wafer might change the growth of the Au bottom layer from the island-like to terrace-like mode.

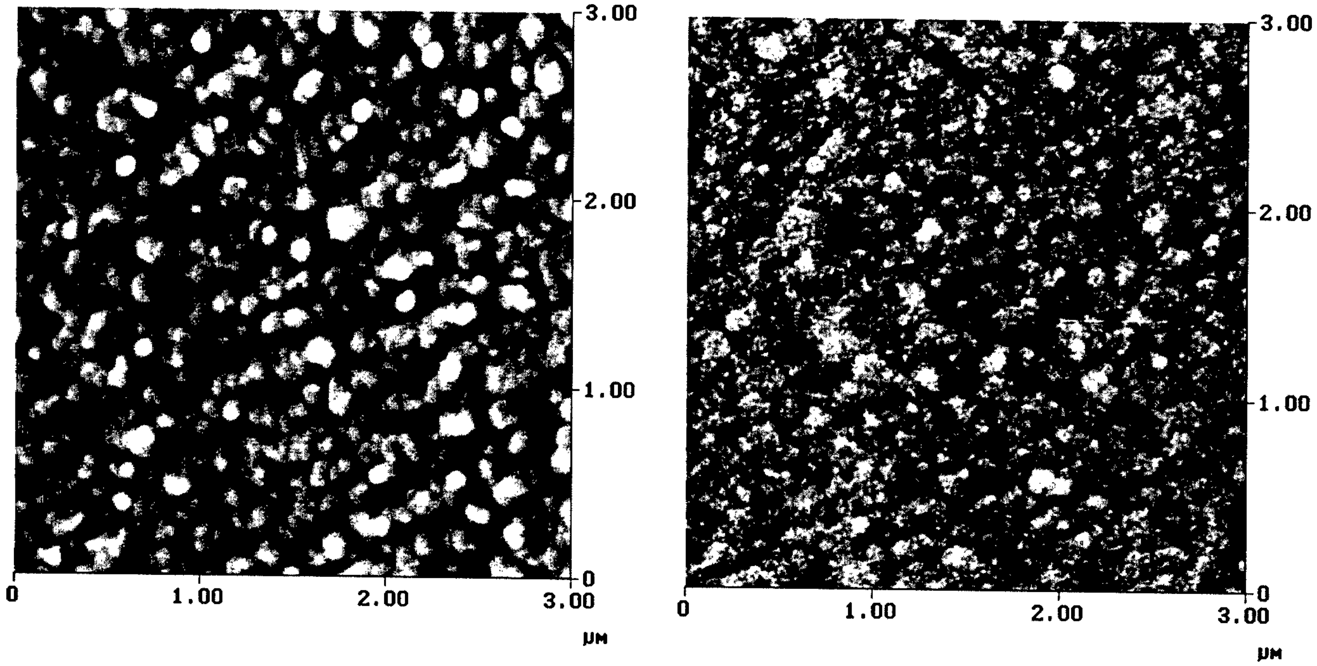

Fig. 2. AFM image of the Co 15-Å-thick layer as-deposited on the Au layer (left) and after annealing at 250 °C (right). The range of the grey scale is 4 nm.

Fig. 3. RHEED streaks acquired on as-deposited (left) and after annealing at 250 °C (right) 8-Å-thick Co layers. Before annealing streaks are blurred, but single and correspond to the lattice constant 2.72 Å. After annealing they are split revealing the lattice parameter 2.59 Å and 2.83 Å for outer and inner, respectively.

The evaporation of Co layers was performed at RT on the bottom Au layer, previously annealed at 200 °C. The surface of the as-deposited Co layer has the island-like structure, similar to that for the annealed Au layer (Fig. 2). Additionally, a weak structure of the island surface is visible in the AFM image. The Co surface roughness is comparable to that of the annealed Au layers, but the correlation length takes different values as the Co layer thickness changes. For an 8-Å-thick Co film the parameter ξ oscillates around 90 nm, whereas for a thicker layer (15 Å) it increases up to 170 nm. Annealing at 250 °C for 45 min causes smearing of the surface island structure. Their contours, although still visible in the AFM image, are much less pronounced. The annealing process does not affect markedly the roughness of the thin Co layer whereas for the thicker one it results in the surface smoothening as reported in Speckmann et al. [4].

The RHEED pattern observation allows to investigate the existence of strains due to the lattice mismatch of both components of the sandwich. The surface lattice parameter of the as-deposited 8-Å Co layer is substantially enhanced up to the value of 2.72 Å, in comparison to 2.51 Å for the bulk. In a 15-Å-thick Co layer the strain relaxation is stronger, revealing the value of 2.59 Å. Annealing of the Co layer performed at 250 °C evidently affects its crystalline structure. For an 8-Å-thick Co film the splitting of the RHEED streaks occurs (Fig. 3), being a proof of the lattice constant relaxation to the values of 2.54 Å and 2.84 Å for Co and Au, respectively. Surprisingly, such splitting is not observed for 15-Å Co layers. For this sample the lattice parameter after annealing, measured by the distance between the RHEED streaks, is equal to 2.83 Å—very close to the Au bulk value (2.88 Å). On the basis of AES spectra comparison from both as-deposited and annealed 15-Å Co layers, it is evident that Au behaves as a surfactant giving rise to an increase of the AES signal for Au and a suppression of the respective signal for Co.

Since Au and Co are mutually insoluble, the reverse diffusion may take place after the annealing. Most probably, due to the diffusion activated by annealing, a non-continuous Au film appears on the surface of the thin Co layer, whereas in the case of the thick Co film, it is fully covered with Au. Moreover the coherence between Au and Co layers is lost, giving rise to the relaxation of strains. This is compatible with the evolution of Co surface morphology, monitored changes in the RHEED pattern and the Auger electron spectrum after the annealing of the samples. Thus it is reasonable to expect that the annealing lowers substantially magnetoelastic contribution to the magnetic properties of Co layers. Magneto-optical measurements are in progress and will be published soon.

4. Conclusions

The sapphire substrate buffered with Mo is ideal for growth of smooth Au/Co/Au sandwiches. The annealing above 170 °C improves the flatness of the Au surface—atomically smooth areas of a few hundred nanometers in diameter occur. In the as-deposited Co layers the expanding strains should result in the significant magnetoelastic contribution to magnetic properties. The thermal treatment releases strains and the lattice parameter relaxes. The Au acts as a surfactant appearing on the top of the Co layer after annealing at 250 °C.

Acknowledgments

This work was supported by the Polish State Committee for Scientific Research (Grant No. 2PO3B06515) and ESF NANOMAG project.

References

[1] C. Chappert, K. Le Dang, P. Beauvillain, H. Hurdequint, D. Renard, Phys. Rev. B34 (1986) 3192.

[2] C. Chappert, P. Bruno, J. Appl. Phys. 64 (1988) 5736.

[3] P. Bruno, G. Bayureuther, P. Beauvillain, C. Chappert, G. Lugert, D. Renard, P. Renard, J. Seiden, J. Appl. Phys. 68 (1990) 5759.

[4] M. Speckmann, H.P. Oepen, H. Ibach, Phys. Rev. Lett. 75 (1995) 2035.

[5] M. Henh, S. Padovani, K. Ounadjela, P. Bucher, Phys. Rev. B54 (1996) 3428.

[6] H.P. Oepen, Y. Millev, J. Kirschner, J. Appl. Phys. 81 (1997) 5044.

[7] U. Rüdiger, J. Yu, L. Thomas, S.S. Parkin, A.D. Kent, Phys. Rev. B59 (1999) 11914.

[8] A. Murayama, K. Hyomi, J. Eickmann, C.F. Falco, Phys. Rev. B60 (1999) 15245.

[9] C. Train, R. Mégy, C. Chappert, J. Magn. Magn. Mater. 202 (1999) 321.

[10] C.M. Schneider, P. Bressler, P. Schuster, J. Kirschner, J.J. de Miguel, R. Miranda, Phys. Rev. Lett. 64 (1990) 1059.

[11] F. Huang, M.T. Kief, G.J. Mankey, R.F. Willis, Phys. Rev. B49 (1994) 3962.

[12] R. Zhang, R.F. Willis, Phys. Rev. Lett. 86 (2001) 2665.

[13] G. Palasantzas, J. Krim, Phys. Rev. B 48 (1993) 2873.

[14] G. Palasantzas, Phys. Rev. B 48 (1993) 14472.

ELSEVIER

Thin Solid Films 412 (2002) 38–43

thin solid films

www.elsevier.com/locate/tsf

Polarity selection process and polarity manipulation of GaN in MOVPE and RF-MBE growth

A. Yoshikawa[a,b,*], K. Xu[a]

[a]*Center for Frontier Electronics and Photonics, Chiba University VBL, Chiba, Japan*
[b]*Department of Electronics and Mechanical Engineering, Chiba University, Chiba, Japan*

Abstract

The polarity-controlled growth of GaN on a sapphire substrate by metalorganic vapor phase epitaxy (MOVPE) and molecular beam epitaxy (MBE) was demonstrated. The mechanisms for polarity reversion of GaN by TMAl preflow in MOVPE growth and high-temperature deposited AlN intermediate layers in MBE growth were discussed based on the 'two monolayers of Al' model. The kinetic process of GaN polarity selection on a sapphire substrate, Al layers, and AlN surface was investigated by RF-MBE growth. Reversing Ga polarity to N polarity could also be realized by nitridation of the deposited Al layers. These results provided a comprehensive understanding of the effects of surface stoichiometry, growth temperature and N source species (ammonia or N plasma) on GaN polarity. It was concluded that GaN tended to grow with Ga polarity which was kinetically favorable on thermally cleaned sapphire substrates and Al-covered surfaces, the polarity conversion of GaN by TMAl preflow, AlN intermediate layer or Al insertion layers relied on the fact that they provided an Al platform on which the subsequent epilayer prefers to grow with Ga polarity. © 2002 Elsevier Science B.V. All rights reserved.

Keywords: Metalorganic vapor phase epitaxy; Molecular beam epitaxy; GaN; Polarity

1. Introduction

One of the main characteristics of GaN is its polarity due to absence of symmetry center in the [0001] direction. The morphologies and properties of the films grown with Ga polarity and N polarity are quite different because of the different growth mechanisms predominant on the two polar surfaces [1,2]. The large piezoelectric and spontaneous polarization fields existing in nitride devices allow a significant tailoring of the carrier dynamics and optical properties. These effects can further be used, for instance, to generate two-dimensional carriers gases without modulation doping, and polarization enhanced Shottky barriers [3]. Theoretical calculation predicted that the polarity inversion domain boundaries (IDBs) would not affect the near band gap luminescence due to the absence of midgap electronic states, and it was very recently observed that the photoluminescence of IDBs was one order magnitude higher than that of bulk GaN [4]. To explore fully the potential functions and applications of III-nitrides, it is necessary to understand and play with polarities.

Due to these interesting important features, intensive research works have been conducted on the growth behaviors of GaN with different polarities. Many factors were reported to influence the epilayer polarities, such as growth methods, buffer layer types, buffer layer temperature, substrate nitridation, surface stoichiometry, growth rate and so on [5–12]. So far, the related mechanisms are not understood well. The effects of polarity on GaN growth behaviors and properties, as well as the factors controlling the polarity selection process must be investigated in order to provide the knowledge necessary for further improvement of film crystal quality, and device performances.

Recently, we demonstrated polarity-controlled MOVPE growth of GaN by using trimthyl-aluminum (TMAl) preflow [2], and developed a 'three-step growth method' based on the polarity-control [6]. In this paper, we present our extensive studies on the polarity selection processes of GaN grown sapphire substrate by MOVPE and RF-MBE. The related mechanisms for polarity manipulation both in MOVPE and MBE growth are discussed based on the 'two monolayers of Al' model. Realization of polarity manipulation is the first important

---

*Corresponding author. Center for Frontier Electronics and Photonics, Chiba University VBL, Chiba, Japan. Tel.: +81-43-290-3990; fax: +81-43-290-3991.

E-mail address: yoshi@cute.te.chiba-u.ac.jp (A. Yoshikawa).

PII: S0040-6090(02)00310-3

step toward exploring the super-functional optoelectronic devices by utilizing the polarization effects of III-nitrides.

2. Experimental

MOVPE growth of GaN was conducted at a chamber pressure of 200 torr [2]. The substrate was first thermally cleaned in H_2 ambient at 1100 °C for 10 min and then nitrided in the ammonia gas flow of 1500 sccm for 90 s. Prior to the deposition of a GaN buffer layer on the nitridated sapphire substrate, a TMAl preflow was introduced to cover the surface with at least two monolayers of Al at 550 °C, required to reverse the film polarity. Then, a 20-nm-thick GaN buffer layer and 2.5-μm-thick GaN epilayer were grown on nitrided sapphire substrate at 550 and 1080 °C, respectively.

RF-MBE growth of GaN was carried out in a system with attached coaxial ion collision impact scattering spectroscopy (CAICISS) system. Active N was supplied from Applied EPI Uni-bulb RF plasma cell. To investigate the polarity selection process and polarity conversion mechanisms of GaN, Al insertion layers and AlN intermediate layers were used to manipulate the polarity. The detailed growth process can be seen in Xu et al. [7].

Polarities of GaN films were characterized by using RHEED and CAICISS. The polarity of GaN as well as the Ga/N polarity ratio was determined by comparing the experimental spectra and the theoretically simulated ones. The simulated CAICISS spectra with different N/Ga polarity percentages are shown in Fig. 1. The polar angle is defined as the one between incident ion beam and sample surface.

3. Results and discussions

3.1. Polarity manipulated growth of GaN by MOVPE

The CAICISS spectra of the samples grown without and with the TMAl preflow supplied for 2 s, 5 s, and 10 s prior to the low temperature buffer layer deposition are shown in Fig. 2a–d, respectively. GaN epilayer polarity can be identified by comparison of the measured spectra with the simulated spectra. It is shown that GaN films grown on the nitrided sapphire without TMAl preflow have N polarity, whereas GaN films grown using a TMAl preflow above 5 s possess Ga polarity. The sample with 2-s TMAl preflow time was mainly N-polar and a few-percentage of Ga-polar, i.e. mixed polarities. Anyway, it was found that TMAl flow prior to buffer layer deposition could dramatically convert the film from N polarity to Ga polarity.

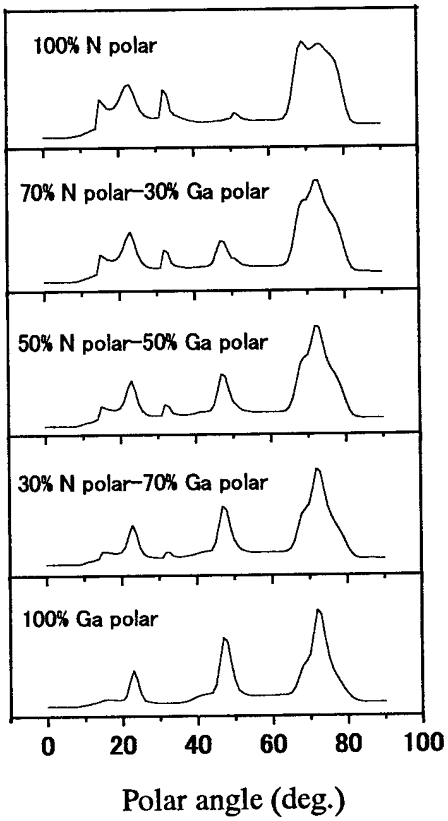

Fig. 1. Simulated CAICISS spectra of GaN with different Ga polar and N polar percentage. The spectra are Ga signal intensity dependence on the incident angle of He ion in $GaN_{[11\bar{2}0]}$ azimuth, the accelerated voltage is 2 kV, penetration depth is 10 A.

Surface morphologies of the samples grown with different TMAl preflow time are shown in Fig. 3. The surface of GaN film with 2-s TMAl preflow showed still the hexagonal facets likewise the sample without TMAl preflow (0 s). However, the morphology of GaN films with TMAl preflow exceeding 5 s was dramatically changed into a flat surface.

The correlation of the TMAl preflow time and the resulting Al layer thickness is crucial to understand above experiment results. We have grown AlN by the MBE method. With very good reproducibility, after 400 cycles of growth at 1100 °C with the TMAl supply time of 2 s and a flow rate of 5 μmol/min, cross-sectional field-emission scanning electron microscopy (FE-SEM) measurement showed that AlN layer thickness was approximately 90–105 nm. Since one monolayer of AlN is 0.2489 nm, 2-s TMAl supply with a flow rate of 5 μmol/min corresponded to a monolayer AlN growth. In Fig. 3, Al layer thickness formed by 5-s TMAl preflow in a flow rate of 5 μmol/min was estimated approximately at 2–2.5 monolayers. The polarity inversion structure was schematically shown in Fig. 4. We termed it as a model of 'two monolayers of Al'. From the point of view of structure, two monolayers of Al are necessary and also sufficient to complete the conversion from N polarity to Ga polarity. The kinetic process of

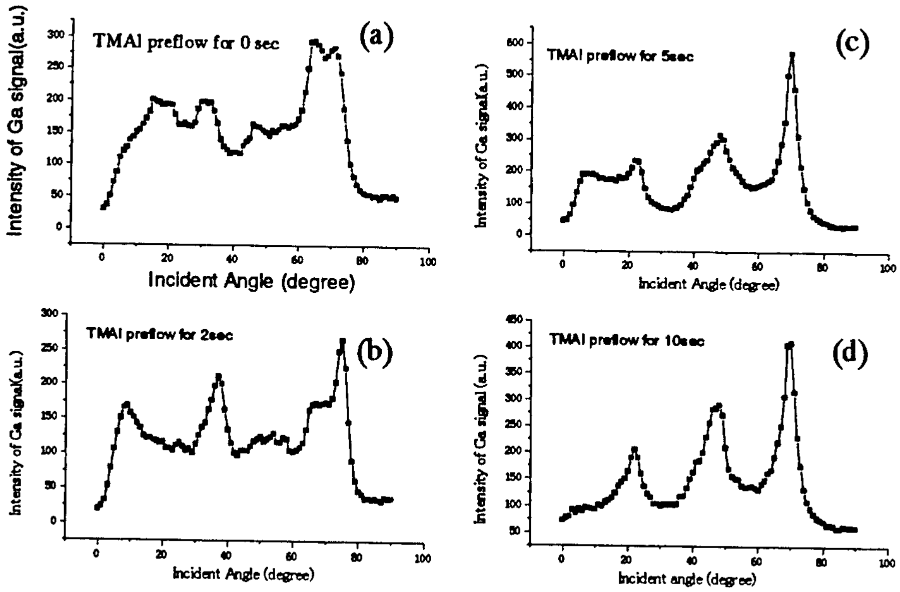

Fig. 2. CAICISS spectra of MOVPE grown GaN with different TMAl preflow times. Ga signal intensity dependence on the incident angle of He^+, were recorded in $GaN_{[11\bar{2}0]}$ azimuth: (a) grown without TMAl preflow, N polarity; (b) with TMAl preflow of 2 s, mixed polarity; (c) TMAl preflow of 5 s, Ga polarity; and (d) TMAl preflow of 10 s, Ga polarity.

GaN polarity selection with Al insertion layers will be discussed in Section 3.3.4.

3.2. A new three-step method MOVPE growth for high-quality GaN epilayers based on polarity manipulation

A new three-step method has been developed to grow high-quality GaN epilayers based on polarity manipulation. The first step consists of substrate nitridation and growth of a thin AlN layer by the migration enhanced epitaxy method. Up to date, a number of experimental studies have been conducted to understand the nitridation processes. AlN could be formed on sapphire substrate during nitridation, with the thickness of a nanometer scale depending on temperature and N sources. This will greatly improve the alignment of GaN or AlN crystal axis orientation on sapphire substrate, and decrease the relative rotations and tilts of crystal axis inside the nucleation layer. The thin, MBE-grown AlN layer was expected to inherit the sapphire substrate crystallinity and extend the high crystallinity from the nitridated sapphire substrate into the GaN layer.

Afterwards, the TMAl preflow and buffer layer were introduced to solve cracking and improve the surface morphology; this is the second step. TMAl was intentionally introduced to reverse the N polarity of AlN to

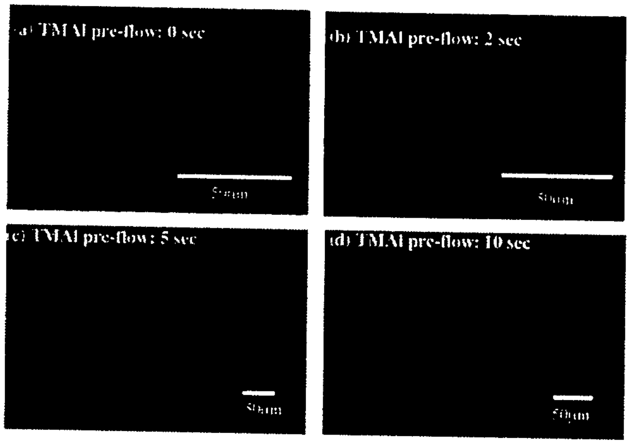

Fig. 3. Nomarski optical photographs of GaN films grown for different TMAl preflow times: (a) 0 s, (b) 2 s, (c) 5 s and (d) 10 s. The surface morphology of GaN films was changed into a flat surface by TMAl preflow periods exceeding 5 s.

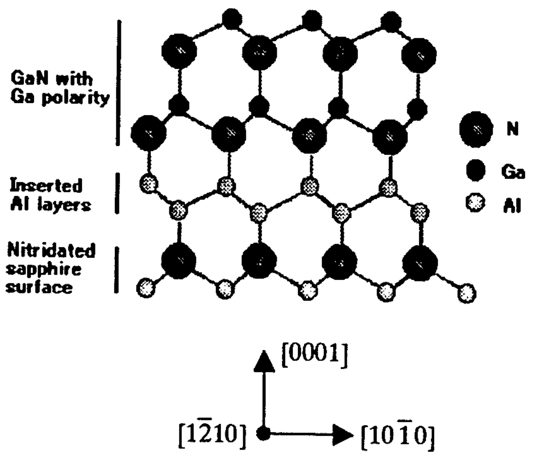

Fig. 4. A schematic model to illustrate the effect of TMAl preflow on GaN polarity.

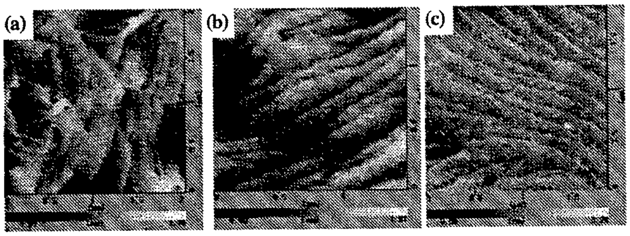

Fig. 5. AFM images of Ga polar epilayers grown with three different methods: (a) with conventional two steps, (b) with nitridation and TMAl preflow, and (c) grown with the three-step method.

the Ga polarity of GaN. The GaN buffer layer thickness was 20 nm.

The third step is epilayer growth at high temperature of 1080 °C. The ramping process from buffer deposition temperature to epitaxial temperature was executed in two steps, first with lower ramping rate below 900 °C, and higher ramping rate from 900 to 1080 °C.

The detailed mechanisms about the three-step growth, have been discussed in Yoshikawa and Takahashi [6]. As a comparison with the other growth methods, we show typical AFM images of GaN grown under the identical conditions but different methods in Fig. 5. Fig. 5a shows the sample grown by the conventional two-step method. The dark points correspond to the threading dislocations with a screw-type Burgers vector (pure screw or mixed), they reveal higher degree of relative tilts among the column structures. After applying nitridation to the sapphire substrate, the alignment of GaN columns on the substrate was improved, as shown in Fig. 5b, resulting in lower density of dark points. The Ga polar growth of this sample was realized by introducing TMAl preflow before low-temperature buffer layer deposition. Fig. 5c is the typical morphology of the GaN epilayer grown by the three-step method. Long growth steps without termination was observed, indicating a significant improvement to epilayer quality.

3.3. GaN polarity selection process and polarity manipulation in RF-MBE growth

3.3.1. Polarity of GaN grown on sapphire substrate

CAICISS spectra of GaN grown by RF-MBE on nitridated and non-nitridated sapphire substrates are shown in Fig. 6a,b. By comparing with the simulated results, we knew the film grown on extensively nitridated sapphire substrate was not 100% N polarity, but the estimated Ga polarity was below 5%; while the GaN epilayer grown on non-nitridated sapphire substrate was of well-defined Ga polarity. This result showed that, even the chemical activity of N supplied from RF plasma was very high, Ga polarity was favorable on the thermally-cleaned sapphire surface regardless of source supply order. Therefore, we could not simply refer RF-MBE grown GaN as N polarity.

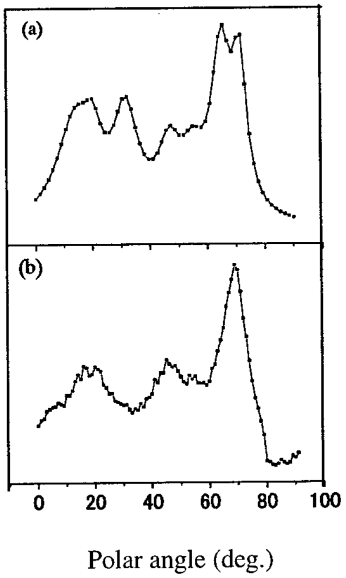

Fig. 6. CAICISS spectra of GaN grown by RF-MBE: (a) on extensively nitridated sapphire substrate; and (b) on non-nitridated sapphire substrate.

The thermally-cleaned sapphire substrate was usually terminated by Al in an ultra-high vacuum. In following, we investigated the effect of Al deposition on GaN polarities.

3.3.2. GaN polarity manipulation by Al insertion layer during RF-MBE growth

Fig. 7a shows the CAICISS spectrum of the GaN film which was grown on nitridated sapphire substrate but with 1-ML Al insertion during the epilayer growth. The signal is very complicated at a low angle. This may

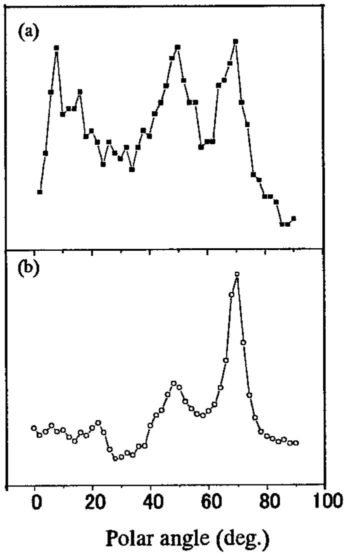

Fig. 7. CAICISS spectra of GaN: (a) 1-ML Al deposition during epitaxy; (b) 2-ML Al deposition for two times during epilayer growth.

be caused by the excess Ga coverage on the real surface. According to the peak shape from 60 to 80° in Fig. 7a, it was found the film was mixed-polarity, and the spectrum was close to the simulated one assuming 30% Ga polarity. For the sample grown with 2-ML Al deposition, the measured CAICISS spectrum was similar to Fig. 7a, but the Ga polarity percentage increased to approximately 70%. Following this, we tried the 2-ML Al deposition two times during the epitaxy. After 20-nm GaN growth on the first 2 ML of Al, the second deposition of 2-ML Al was done. The corresponding CAICISS spectrum is shown in Fig. 7b, it is clear that polarity of the epilayer was completely changed to the Ga one. Thus it has been confirmed that 2-ML Al coverage is necessary and also enough to reverse N polarity to Ga polarity. Logically, if 2 ML is not enough, the polarity will not be changed regardless of the deposition times. The yield of approximately 30% Ga polarity by 1-ML Al deposition is thought due to 2-ML Al islands formation. The yield of approximately 70% Ga polarity was attributed to the fact that the surface was not fully covered by 2-ML Al uniformly even the mean thickness of deposited Al layer was 2 ML.

We have also tried to reverse Ga polarity to N polarity by using Al insertion layer. It was shown that a much thicker Al layer and much stronger N plasma are necessary to complete the polarity conversion. Thus, 80% N polarity was yielded after 5-min nitridation to the 30-ML-thick Al layer with a N plasma condition of 500-W RF-power and 1.2 sccm N_2 flow rate. Evidently, the selection of N polarity on the surface featured with metal-like bonds was kinetically unfavorable.

3.3.3. RF-MBE growth investigation on GaN polarity inversion mechanism by high-temperature deposited AlN intermediate layer

In the third group experiment, GaN polarity selection on the AlN intermediated layer was investigated. The N-polarity GaN epilayer was grown at 820 °C with N plasma condition of 300-W RF-power and 0.8 sccm N_2 flow rate, corresponding GaN growth rate was 0.7 μm/h. Under this N plasma condition, a Ga flux as high as 2.5 A/s was needed to realize the pseudo-two-dimensional growth and this was also the upper limit for the Ga flux to avoid the Ga droplet. The AlN intermediate layer was grown by different methods. As stated above, the Al flux was fixed at 0.5 A/s for all experiments in this paper. We could switch GaN growth to AlN intermediate layer growth by simply closing the Ga shutter and open the Al shutter while keeping the N plasma condition the same. Accordingly, AlN was grown under the N-rich condition by this method. The CAICISS spectrum of GaN with a 20-nm-thick AlN intermediate layer grown under the N-rich condition is shown in Fig. 8a; it is a well-defined N-polarity spectrum. In situ RHEED monitoring confirmed that 20 nm of AlN can completely cover the GaN surface under the above growth condition. This result shows that the AlN intermediate layer grown under a N-rich condition will not change the polarity of the GaN epilayer.

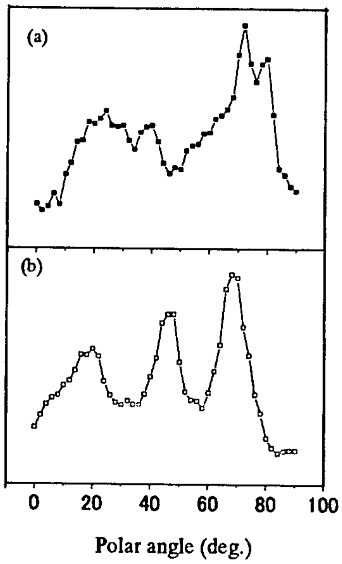

Fig. 8. CAICISS spectra of GaN: (a) GaN grown on AlN without N shutter modulation, i.e. under N-rich condition; (b) GaN grown on AlN with N shutter modulation.

Therefore, it has been found that the high-temperature deposited AlN layer itself could not convert N polarity GaN to Ga polarity. The surface stoichiometry of AlN during the growth is a critical point.

As a further investigation, even though both Al and N flux are kept the same as stated above, if the N shutter is modulated during AlN growth while the Al shutter is kept open, the Al/N ratio is adjusted to above unity. The polarity of the GaN epilayer grown under this condition could be perfectly changed to Ga polarity, as shown in Fig. 8b. In this growth method, the N shutter operation was modulated by 4 s open and 6 s close. The 6-s close of the N shutter allowed approximately 1.1 ML of Al deposition. In order to investigate why the Al/N ratio affects the polarity of GaN grown latter on, we examined the effect of AlN surface stoichiometry on GaN polarity. In the case that the AlN intermediate layer was grown under the same nitrogen-rich condition mentioned above, we did excess Al deposition before starting GaN growth on AlN at 820 °C. The Al deposition time was 12 s, corresponding to 2.2-ML coverage. The resulting GaN epilayer was proven to be Ga-polarity. The experimental results suggest that excess Al coverage on the AlN intermediate layer was crucial to reverse N polarity to Ga polarity by the AlN high-temperature intermediate layer.

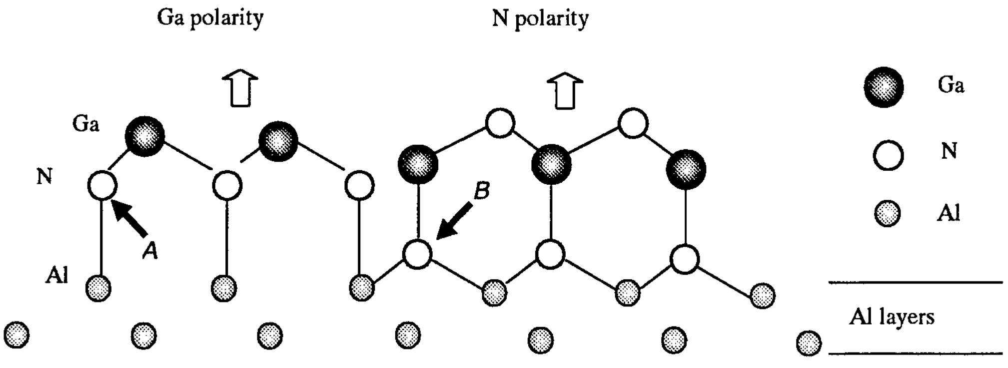

Fig. 9. Polarity selection process of GaN on the Al layer.

3.3.4. Kinetic process of GaN polarity selection on the Al layer

The GaN polarity selection process is schematically shown in Fig. 9. Since bonding energy between Al and N is higher than that between Ga and N, the polarity of GaN grown on the Al covered surface depends on bonding configuration among Al and N when Ga and N species arrive at the surface. If the N atom takes position A, Ga polarity occurs; if the N atoms take position B, N polarity occurs. STM characterization and theoretical calculation showed that Ga atoms in the GaN surface would form metallic bonds which were only slightly weaker than those formed in bulk Ga, coherently, we think the Al adlayer on the GaN surface may form much stronger metallic bonds than Ga atoms. For N atoms entering position B, it needs the cooperation among three Al atoms, therefore, N polarity is kinetically unfavorable on the Al covered surface. However, due to the high ionicity of III-nitrides, the growing epilayer tends to keep its polarity. To reverse Ga polar to N polar, much thicker Al-layer coverage and stronger N-plasma irradiation are necessary, which will be reported later.

4. Conclusions

Polarity manipulation of GaN on sapphire substrates both in MOVPE and MBE growth has been demonstrated. Polarity selection processes of GaN on nitrided, non-nitrided sapphire substrates, Al layers, and AlN intermediate layers were investigated. Results showed that, Ga polarity was kinetically favorable on thermally cleaned sapphire substrates and Al covered surfaces. Polarity conversion from N polarity to Ga polarity could be seen by Al insertion layers, and vice versa. GaN polarity reversing mechanism by AlN was also clarified. It is suggested that the polarity conversion of GaN by AlN or Al relies on the fact that they provide an Al platform on which the subsequent epilayer preferred to grow with Ga polarity.

Acknowledgments

This work was partly supported by the ‘Research for the Future Program’, Japan Society for the Promotion of Science (JSPS-RFTF 96R16201) and the Grants-in-Aid for Scientific Research (B) #13450121, Japan Society for the Promotion of Science.

References

[1] R. Held, G. Nowak, B.E. Ishug, S.M. Seutter, A. Parkhonmovsky, A.M. Dabiran, P.I. Cohen, I. Grzegory, S. Porowski, J. Appl. Phys. 85 (1999) 7697.
[2] A. Yoshikawa, D.H. Lim, K. Xu et al., Japan–Korea Joint Workshop, Short-wavelength Semiconductor Optoelectronic Devices and Materials, 2000, p. 9.
[3] E.T. Yu, X.Z. Dang, L.S. Yu, D. Qiao, P.M. Aspeck, S.S. Lau, G.J. Sullivan, K.S. Boutros, J.M. Redwing, Appl. Phys. Lett. 73 (1998) 1880.
[4] P.J. Schuck, M.D. Mason, R.D. Grober, O. Ambacher, A.P. Lima, C. Miskys, R. Dimtrov, M. Stutzmann, Appl. Phys. Lett. 79 (2001) 952.
[5] D.H. Lim, K. Xu, Y. Taniyasu K. Suzuki, S. Arima, B.L. Liu, K. Takahashi, A. Yoshikawa, IPAP-CS1 (2000) 150–153.
[6] A. Yoshikawa, K. Takahashi, Phys. Stat. Sol. 228 (2001) 523.
[7] K. Xu, N. Yano, A.W. Jia, A. Yoshikawa, K. Takahashi, International Conference on Nitride Semiconductors, Denver, to be published in Physic Status Solidi b 188 (2001).
[8] K. Xu, N. Yano, A.W. Jia, A. Yoshikawa, K. Takahashi, J. Crystal Growth 237–239 (2002) 1003.
[9] T. Zywietz, J. Neugebauer, M. Scheffler, J. Northrup, C.G. Van de Walle, MRS Internet J. Nitride Semicond. Res. 3 (1998) 26.
[10] A.R. Smith, R.M. Feenstra, D.W. Greve, J. Neugebauer, J.E. Northrup, Phys. Rev. Lett. 79 (1997) 3934.
[11] A. Kikuchi, T. Yamada, S. Nakamura, K. Kusakabe, D. Sugihara, K. Kishino, Jpn. J. Appl. Phys. 39 (2000) L330.
[12] X.Q. Shen, T. Ide, S.H. Cho, M. Shimizu, S. Hara, H. Okumura, S. Sonoda, S. Shimizu, J. Cryst. Growth 218 (2000) 155.

ELSEVIER

Thin Solid Films 412 (2002) 44–49

thin solid films

www.elsevier.com/locate/tsf

SiGe(C) epitaxial technologies—issues and prospectives

T.J. Grasby*, T.E. Whall, E.H.C. Parker

Department of Physics, University of Warwick, Coventry CV4 7AL, UK

Abstract

Epitaxial layers of SiGe(C) have entered mainstream Si processing—forming base regions in heterojunction bipolar transistors. There are also exciting prospects that SiGe(C) could impact MOS technologies. In both cases heteroepitaxial layers enable very significant performance enhancements at device and circuit level. A related area and a familiar hot-potato is silicon epitaxy for device active regions in MOS technologies—where tightly controlled doping distributions can be incorporated to facilitate device function at deep submicron channel lengths. CVD is a preferred epitaxy deposition technique for production—currently LP-CVD and UHV-CVD dominate. Each of these techniques demand much of the technology and have their respective strengths and weaknesses. Issues regarding matrix and doping control, uniformity, blanket and selective area growth and throughput (a sensitive area) will be addressed. Also in the CVD portfolio is LEPE-CVD—a recent contender for the production arena which has the facility of being able to access very high deposition rates as required for example in depositing relaxed buffer layer material required as 'virtual substrates' for higher Ge content layers. SS-MBE, traditionally the favourite technique for research, also has distinct possibilities for development as a production tool. Here the issues relate primarily to throughput and system design, and (surprisingly) matrix profile control. These techniques will be outlined and reviewed along with issues which determine their development as the competition hots up in epitaxy, and as more complex and high Ge content structures are needed to progress Si technology to new performance heights and application areas.

Keywords: SiGe epitaxy; Layer growth techniques; Device technologies

1. Introduction

Epitaxy is playing an increasingly significant role in Si microelectronics. CMOS integrated circuits (ICs) are fabricated in Si 'epi' and advanced bipolar junction transistors (BJTs) have epitaxial base regions. An important recent development has been the entry of the SiGe heterojunction bipolar transistors (HBT) into the production arena—devices which significantly outperform Si BJTs, and which demand much of the epitaxy process, with z control of matrix and dopant concentrations down to nanometre dimensions. The addition of C to the base region to suppress B diffusion adds a further dimension on epitaxy growth and control.

The SiGe devices are fabricated using near conventional Si processing techniques, and crucially, in the case of SiGe BiCMOS, have to be processed alongside Si CMOS circuitry, again putting demands on the epi process. There is also an intriguing possibility that SiGe can similarly be used to enhance MOSFET device performance, and epitaxy may also find a role in defining high resolution dopant structures required in advanced sub 100 nm CMOS technologies.

In this paper we review the approaches being made in production environments to fabricate SiGe(C) epitaxial device structures and consider what further developments are possible in this exciting and challenging area.

2. Chemical vapour deposition

Chemical vapour deposition (CVD) is currently being used, almost exclusively, by process engineers as the growth technology for SiGe(C) heterojunction device material. CVD has been used for over two decades for Si epitaxial growth—generally a few micrometres of material for CMOS ICs. CVD techniques have been developed over this time to yield today's sophisticated single-wafer tool, currently operating with 8 inch wafers but a 12-inch capability exists.

CVD depends on thermally-induced chemical interactions at the Si wafer surface as a means of depositing epitaxial material (see Fig. 1). Suitable mixtures of so-called precursors (source gases) containing atoms of interest are carried (usually with H_2 carrier gas) over the Si wafer [1]. Crucial operating parameters include

---

*Corresponding author.

E-mail address: t.j.grasby@warwick.ac.uk (T.J. Grasby).

0040-6090/02/$ - see front matter
PII: S0040-6090(02)00311-5

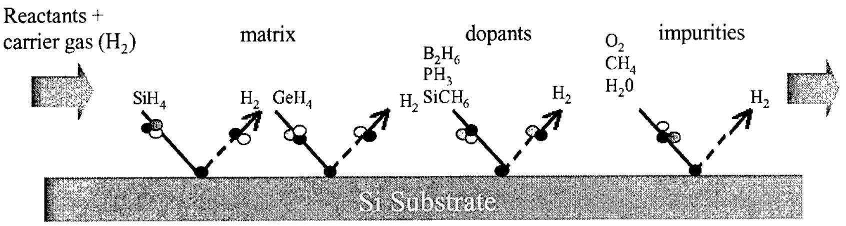

Fig. 1. Schematic representation of the thermally activated chemical decomposition of incident precursors, leading to growth of SiGe:C by the LP-CVD process. Impurities shown are unintentional but can influence growth at low temperatures.

wafer temperature, pressure and flow rate and purity of the gaseous mixture. The challenges presented by Si heterostructures require additionally the ability to incorporate very abrupt compositional changes in this process and over the last decade this has led to the cold-walled low pressure (LP)-CVD variant being developed where pressures are reduced typically from 100s to 10s of torr pressure, and growth temperatures from typically 950–650 °C.

2.1. SiGe(C) LP-CVD

$Si/Si_{1-x}Ge_x$ is essentially a strained layer technology and this requires lower growth temperatures than used in Si homoepitaxy to preserve strain and to suppress development of elastic relaxation processes, enabling highly planar structures to be grown. Temperatures of approximately 650 °C are used for the growth of $x=0.2$ structures. In this regime the growth rate becomes temperature limited (see Fig. 2), allowing source gas (typically SiH_4 and GeH_4) pressures to be reduced and to thereby minimise disruption in the growth arising from turbulence. However, because sharp interfaces are generally required high flow rates (carrier gas + source gases) are used to enable rapid changes in the composition of the gas over the wafer to be achieved.

Operating in this regime, however, has a downside. Growth rates are low with implications on throughput and because we are acting with an activated decomposition process, growth rate depends critically on temperature (see Fig. 2). At 650 °C a change of 1 °C will alter the deposition rate by ~10%—well outside the specification demanded by process engineers! The wafer temperature therefore has to be highly reproducible and highly uniform across the wafer-demanding complex heater technology designed just to heat the wafer and its holder (susceptor), sophisticated temperature measurement system and operational procedures. Temperature measurements down to these low temperatures have proved to be difficult, and currently wafer temperature is monitored (rather than directly measured) by either pyrometers or thermocouples mounted in the susceptor

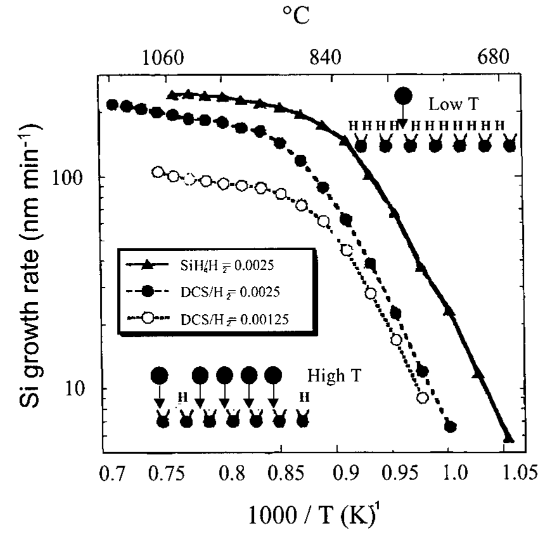

Fig. 2. Temperature dependence on the Si growth rate for different precursors/gas flow rates during the LP-CVD process, indicating an activated decomposition process for growth temperatures (T_G) < 800 °C. The insets show flow rate limited growth at high T_G and temperature limited growth at low T_G.

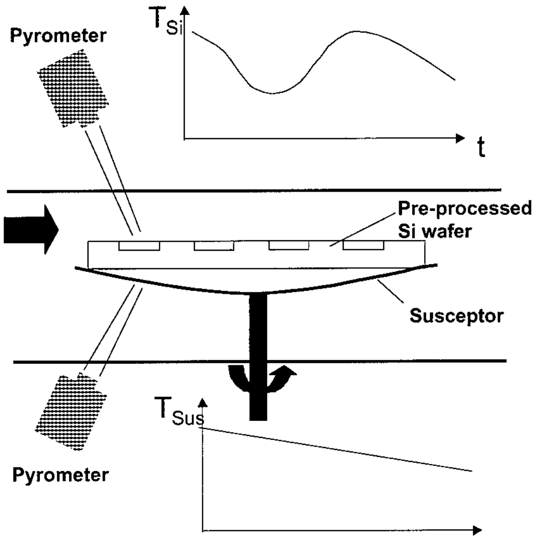

Fig. 3. Schematic representation of the sample susceptor, showing differences in susceptor to wafer temperature with time, due to coating of the susceptor and emissivity changes and possible temperature variations in the reactor.

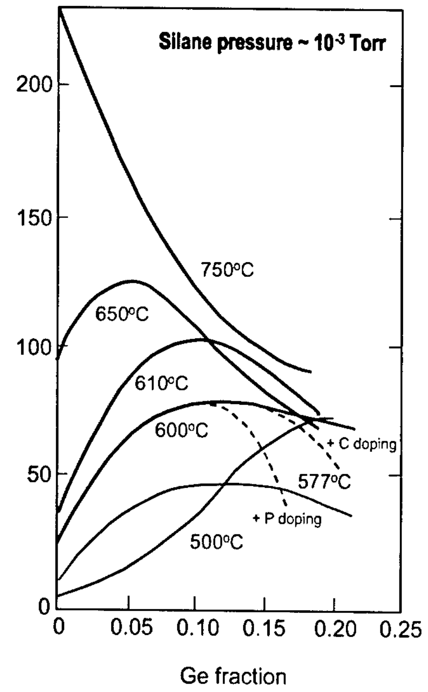

Fig. 4. Interdependence of growth rate and Ge fraction—further complicated in the presence of dopants for various deposition temperatures.

which holds the wafer (see Fig. 3). As all heating is accomplished by radiation, changes in the emmisivity of the wafer holder and surrounding infrastructure which can occur during deposition, means that this is at best only an indicator of wafer temperature. This situation is further complicated by actual temperature changes on the surface of the grown layer-induced by emmisivity changes produced by compositional changes in the growing layer or changes in surface topography or arising from any pre-processing carried out on the wafer.

It is thus evident that a considerable amount of process development is required in LP-CVD reactors—very iterative in nature—to yield a prescribed heterostructure design. These procedures are further complicated by the interdependence of the deposition rates at the surface-for example, deposition rates of 650 °C are reduced by Ge for x up to 0.05 and then decrease quite dramatically with increasing value of x (see Fig. 4). It is a tribute therefore that Osten and co-workers at IHP have developed a process involving source gas methyl/silane, to yield C concentrations of 10^{19}–10^{20} cm^{-3} in a B-doped SiGe base of the HBT, to suppress B diffusion [2].

Also as growth temperatures are reduced it becomes increasingly difficult to maintain clean deposition conditions. Water and oxygen (especially) in the background ambient produce oxidation followed by desorption as volatile SiO. As temperatures are reduced significant reductions in background contamination pressures are required to maintain an oxide-free surface, so procedures have to be developed which minimise such oxidation (Fig. 5). This is especially difficult at the wafer cleaning stage, which involves a high temperate bake (between 700 and 900 °C) usually in the presence of hydrogen to generate a clean surface, and exposure to the background ambient before growth can be commenced leads to some oxidation of the surface.

Process development is the 'Achilles heel' of the LP-CVD process, especially as there is always pressure to keep throughput (wafers per hour) at acceptable levels. Wafer cleaning procedures are being developed to increase throughput and maintain wafer cleanliness prior to epi deposition. With wafer temperature excursions (e.g. cleaning → deposition) time has to be allowed for wafer temperatures to settle with obvious penalties on throughput. Good practise in LP-CVD also entails cleaning the reactor before the next wafer is introduced-involving pushing HCl through the system, again with throughput implications. This leaves the system cleansed of previously deposited material to facilitate reproducible temperature measurement and eliminate memory doping problems. However, once the entire process has been developed, LP-CVD reactors offer the industry very reliable and reproducible 'blanket' (i.e. covering the entire wafer) SiGe(C) layer growth, with long campaign lengths, a material quality second to none and with layer thickness control demonstrated down to ~1 nm for $x \approx 0.2$ (see Fig. 6).

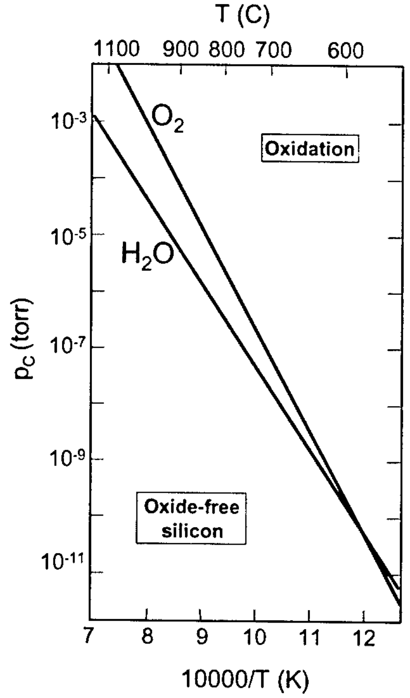

Fig. 5. Temperature dependence of H_2O and O_2 pressures required to maintain an oxide free surface.

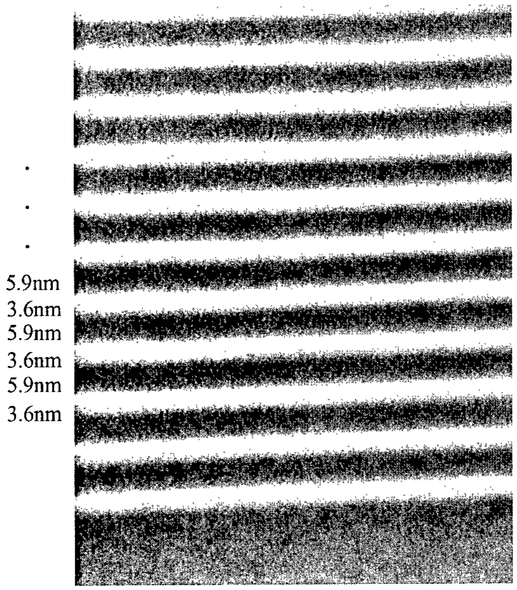

Fig. 6. Bright field cross-sectional (XTEM) micrograph of multiple quantum well (QW) structure for Ge fraction $(x)=0.2$ grown by LP-CVD (showing 'state of the art' highly planar (1 nm resolution) interfaces).

Selective epi growth (SEG) in silicon 'windows' defined usually by SiO_2 patterns is a very challenging adaptation of the LP-CVD process—but can have significant processing advantages. This is achieved by adding gaseous HCl to the gas mixture, but selectively imposes further limitation of the process 'window'. SEG is a hot research topic in several large institutions.

2.2. UHV-CVD

In the late 1980s Berni Meyerson of IBM developed a radical new approach to the growth of Si/SiGe heterostructures. The underlining philosophy was that since very close control of heterointerfaces is required to yield high resolution compositional profiles, slow growth rates are indeed desirable, so that low temperature deposition must be confronted [3]. Meyerson chose 550 °C as the temperature, giving Si growth rates of ~0.3 nm/min, with wafers immersed in a hot-walled (wafer temperature–wall temperature) furnace, giving highly uniform temperature across the wafer (Fig. 7). The growth pressure is also an important parameter to be considered, bearing in mind that in order to meet acceptable throughput levels, batch processing was essential with a large number of wafers (up to 35) required to meet throughput demands. The growth (total) pressure was reduced to very low levels—10^{-3} torr to reduce unwanted silane chemistry reactions and crucially, to ensure a uniform material supply to the closely spaced wafers through molecular transport processes that occur at these pressures. Two other developments are necessary to reduce background gas pressures to UHV levels so that clean surface and deposition conditions could be ensured. An ex-situ wafer cleaning process was also developed involving H termination of surface bonds to dramatically reduce oxidation, and enable the generation of clean surfaces at 550 °C.

UHV-CVD technology is used primarily by IBM and yields exceedingly high quality and highly uniform heterostructure layers with throughput acceptable to a BiCMOS production line at IBM.

2.3. LEPE-CVD

With HBT devices the strained heterolayers are grown directly on the Si wafer. However, full exploitation of the Si/SiGe technology requires substrate templates with lattice constants between Si and Ge to set the strain condition and also allow higher Ge content structures to be grown. Such substrates are termed 'virtual substrates' (VSs) and are fabricated by growing fully relaxed SiGe layers on the Si wafer. There have been several approaches to produce optimum VSs and the most studied is to gradually grade the Ge composition from 0 up to the desired value (y) over several microns of material—this produces a well relaxed VS. However, a cross-hatch topographical structure usually develops on the surface as a consequence of dislocations interacting and is detrimental to the overgrowth of high quality active structures. Recently CMP processes have been developed which smooth out the VS.

A very recent development in CVD especially relevant to VS production, is low energy plasma-enhanced (LEPE-CVD) [4]. With this version of the CVD process, deposition takes place on a wafer immersed in an argon plasma and where with the biasing is such that argon ions impinging the substrate do no significant damage. The ions, however, modify the surface reaction chemistry to yield dramatically increased deposition rates—

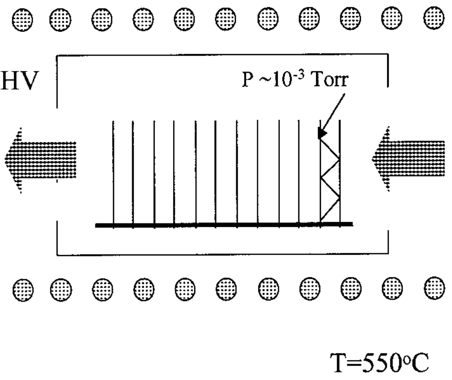

Fig. 7. Schematic of the 'hot wall' UHV-CVD reactor. The low pressure of gases ensures uniform material supply over the wafers by molecular flow.

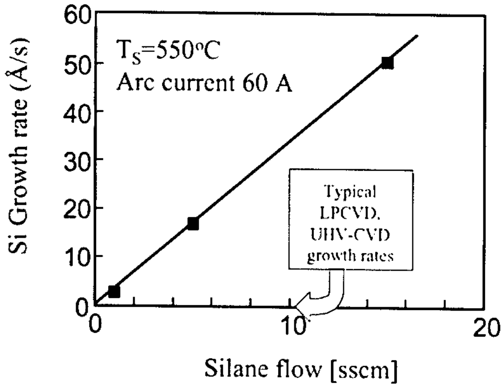

Fig. 8. Si growth rate dependence on the Silane flow for LEPE-CVD using a plasma arc current of 60 A at a growth temperature of 550 °C—indicating dramatic enhancement compared to conventional CVD.

approximately 100 times faster than conventional CVD at 550 °C (see Fig. 8).

LEPE-CVD has been able to produce high quality VS structures with very smooth surfaces in ~10 min as opposed to ~hours needed in LP-CVD, with corresponding economic implications. This opens up the possibility of using VS as the starting wafer (possibly with CMP) and with growth of the active heterostructures by another technique (e.g. LP-CVD). A further intriguing development by von Kanel at ETH (Zurich) has been to reduce (by deflection) the plasma density at the substrate and thereby back-off the deposition rate in LEPE-CVD to approximately 0.1 nm/s, allowing active layer (~8 nm thick) deposition on the freshly grown VS. Already, very high quality Si p-channel MOSFET device structures have been fabricated in material grown using such an approach (Fig. 9).

2.4. Role of SS-MBE

The question arises, particularly pertinent to this conference, does solid source (SS)-MBE have any significant role to play in Si/SiGe heterostructure production? MBE is viewed by the Si industry as a good research tool, but with its UHV operating conditions, and the limited source supply (re e-beam evaporation sources), the industry considers that it is not process-friendly or able to reach throughputs levels needed in production.

As the growth temperatures in CVD are reduced, however, to accommodate strain layer growth, deposition rates quickly fall off and the 6–30 nm/min available in SS-MBE start to look respectable. In addition, because MBE is a physical deposition process the deposition rate of all components and deposition temperature are decoupled. This is certainly a considerable attribute when developing processes, and unlike CVD, MBE is easily capable of delta layer deposition and also of high Ge content ($0.4<x<1$) layers (e.g. see Fig. 10) which may well be needed in future HBT devices and SiGe MOSFETs. Mechanical flux shutters allow for exceedingly precise control of deposited material. The demands placed on substrate temperature are much less stringent

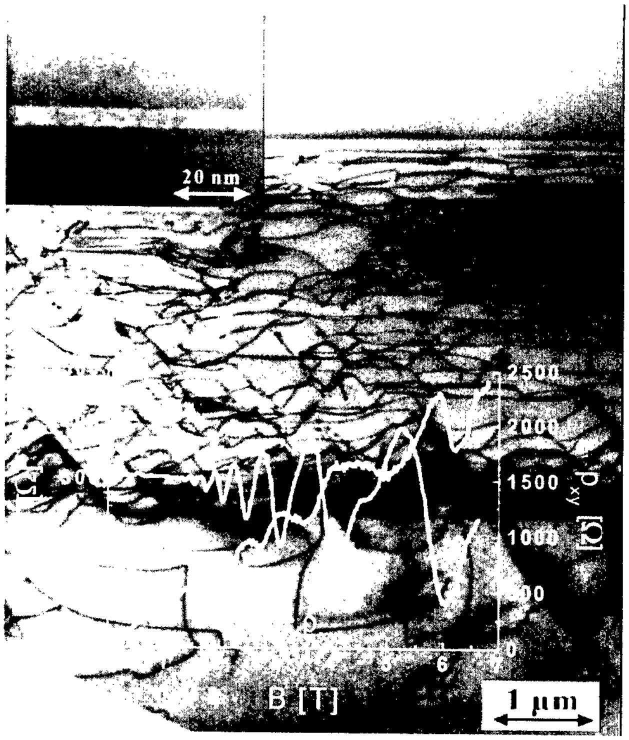

Fig. 9. Cross-sectional (XTEM) dark field micrograph of a p-channel MOSFET structure grown by LEPE-CVD. The virtual substrate (VS) was grown at a high deposition rate (~15 min)—plasma density reduced for channel region to obtain high interfacial definition.

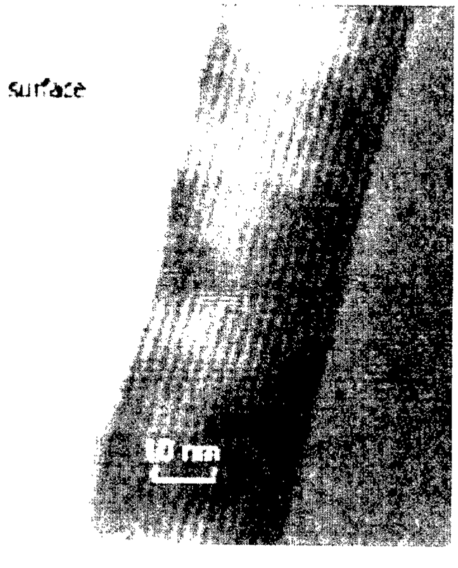

Fig. 10. Cross-sectional (XTEM) bright field micrograph of a SiGe superlattice grown by SS-MBE showing alternate 1 nm Si–Ge layers.

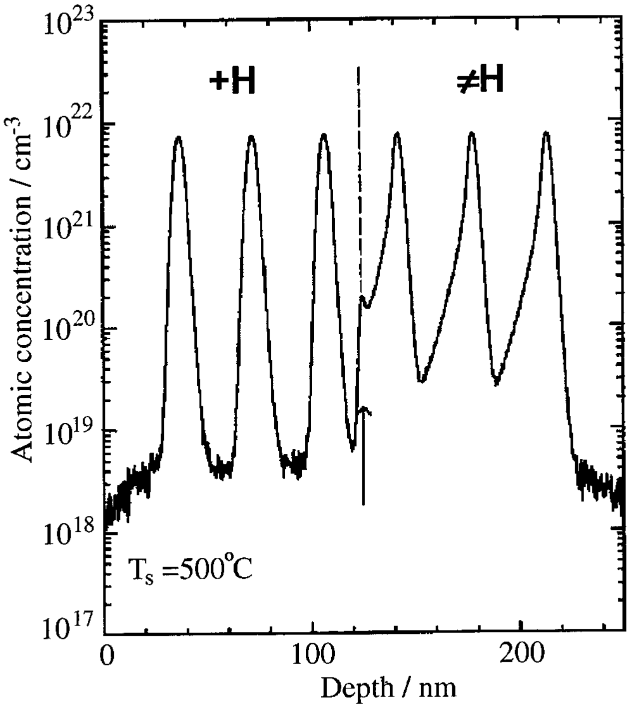

Fig. 11. Ge secondary ion mass spectroscopy (SIMS) profiles showing how H^+ surfactants can be used to suppress Ge segregation in SS-MBE.

than in CVD, leading to a much simpler heater system and temperature stabilisation regimes. However, there are some growth temperatures where segregation of matrix and dopant species (Ge, B, Sb) can be more prevalent than in CVD and this could be restrictive, although procedures are being developed which reduced segregation to CVD levels [5] (Fig. 11). A further issue is that with the current technology only approximately 15% of the evaporated Si and Ge fluxes are used for layer growth on the wafer, the remainder deposited over the system infrastructure. This excess material then would require proper management if it is not to lead to particle contamination of the system and the wafer [6].

3. Conclusions

In this review we have attempted to address the critical issues for epitaxy technologies as epitaxy becomes an exceedingly significant process in Si microelectronics. Without doubt variants of the CVD process seem to have a secure future. Once the process has been developed it really comes into its own—with long-term campaign times, high reproducibility and high material quality. In LP-CVD, the principal tool in the field, the critical dependence of deposition rates on growth temperature, means that careful management of the system is required to maintain reliability of layer specifications. UHV-CVD, with its hot-wall reaction chamber allows wafers to be immersed in a thermal enclosure giving excellent uniformity and quality. However, great demands are placed on both these techniques as new structures are needed to continually improve device performance. It is possible that new precursors will become available to improve deposition rates at low temperature. LEPE-CVD, a relative newcomer to the field, may well prove to be of great significance for low temperature deposition and a full appraisal of these techniques is eagerly awaited. Some radical developments in SS-MBE technology will be needed before that could be considered to enter the production arena.

References

[1] D.W. Greve, Mater. Sci. Eng. B 18 (1993) 22–51.
[2] H.J. Osten, H. Rücker, J.P. Liu, B. Heinemann, Micro. Eng. 56 (2001) 209–212.
[3] B.S. Meyerson, IBM J. Res. Dev. 44 (6) (2000) 132–141.
[4] M. Kummer, C. Rosenblad, A. Dommann, T. Hackbarth, G. Höck, M. Zeuner, E. Müller, H. von Känel, EMRS (Strasbourg) Conference (2001) in press.
[5] T.J. Grasby, in press.
[6] T.J. Grasby, in press.

ELSEVIER

Thin Solid Films 412 (2002) 50–54

thin solid films

www.elsevier.com/locate/tsf

Influence of covering on critical thickness of strained $In_xGa_{1-x}As$ layer

Agata Jasik*, Kamil Kosiel, Włodzimierz Strupiński, Marek Wesołowski

Institute of Electronic Materials Technology, Ul. Wólczyńska 133, 01-919 Warsaw, Poland

Abstract

We examined the critical layer thickness (CLT) of mismatched epitaxial layers and strained heterostructures. Samples consisting of $In_xGa_{1-x}As$/InP and $In_{0.52}Al_{0.48}As/In_xGa_{1-x}As/In_{0.52}Al_{0.48}As$/InP were grown on InP substrates by metalorganic vapour phase epitaxy (MOVPE). The atomic force microscopy (AFM) was used to observe misfit dislocation generation. When the layer is buried in the heterostructure, its critical layer thickness increases. Our investigations have shown how many times this value may be exceeded in chosen technological conditions. A model was proposed, which explains difference between CLT of InGaAs with free surface and CLT of buried InGaAs. Heterostructures mentioned above were employed for producing InAlAs/InGaAs/InP HEMT transistors. © 2002 Elsevier Science B.V. All rights reserved.

Keywords: Metalorganic chemical vapour deposition; Atomic force microscopy; Lattice parameters; Stress

1. Introduction

Ternary alloys are of increasing interest for both electronic and optical devices, such as heterojunction bipolar transistors, high electron mobility transistors, high-speed switching lasers, solar cells. Much work has focussed on the $In_{0.53}Ga_{0.47}As$ alloy because it can be grown lattice matched to the InP substrate. The use of mismatched epitaxial layers allows much greater freedom in designing heterostructure devices with desired characteristics.

If the lattice mismatch between the epilayers and substrate is small and the layer is thin, the mismatch is accommodated by strain in layer. In the case, when the mismatch or the layer thickness is increasing, the formation of misfit dislocation at substrate–layer interface is energetically favourable. However, lattice relaxation via misfit dislocation degrades the structural, electrical and optical epitaxial layer quality.

The point at which misfit dislocation starts to form is called the critical layer thickness (CLT), d_C. Although several theories have been proposed to predict critical value [1,2] in their work most authors [3,4] based on Matthews and Blakeslee model. Following equation arises from their model and it describes critical layer thickness [5]:

$$d_C=\left(\ln\frac{d_C}{b}+1\right)\frac{b(1-\nu\cos^2\alpha)}{2\pi\frac{\Delta a}{a}(1+\nu)\cos\lambda} \quad (1)$$

where: $b=\frac{a}{\sqrt{2}}$ is Burgers vector, a is the lattice constant, ν is the Poisson ratio, α is the angle between the dislocation lines and its Burgers vector, λ is the angle between the slip direction and that direction in the layer plane which is perpendicular to the line of intersection of the slip plane and the interface, and $\frac{\Delta a}{a}=\frac{a_W-a_P}{a_P}$ is the lattice mismatch.

Several groups [6,7], however, reported exceeding of the critical value obtained from Eq. (1). Besides, it follows from a strain compensation technique, which is often used to reduce net strain [8], that critical layer thickness with free surface has to be smaller than the CLT of the buried one. Experimental investigations of these differences were realised.

We studied critical thickness of covered layer and layer with free surface using atomic force microscopy as a characterization tool. In this paper we show that $In_xGa_{1-x}As$ layer with 1.3% lattice-mismatch in spite of

---

*Corresponding author.

E-mail address: jasik_a@sp.itme.edu.pl (A. Jasik).

0040-6090/02/$ - see front matter © 2002 Elsevier Science B.V. All rights reserved.
PII: S0040-6090(02)00312-7

exceeding the critical layer thickness defined by Mathews and Blakeslee, can be used as a pseudomorphic channel layer in HEMT structures. We measured, by the Van der Pauw method, not only the channel layer lattice relaxation but also electrical parameters of HEMT structures with different channel thickness.

2. Experiment

Heterostructures were grown by low pressure metalorganic vapour phase epitaxy LP-MOVPE on semi-insulating (100) InP:Fe substrates. A horizontal quartz reactor (AIX 200) and IR heated graphite susceptor were used. Trimethylgallium (TMGa), trimethylindium (TMIn), trimethylaluminum (TMAl) and arsine AsH_3, phosphine PH_3 were used as III and V group elements precursors with palladium-purified hydrogen carrier gas. During the structure growth, the reactor pressure and temperature were maintained at 100 mbar and at 650 °C, respectively. The V/III ratio was unchanged and amounted to 172. Samples were divided in to two groups (there were four samples with different InGaAs thicknesses in these groups): with free surface and covered by InAlAs layer. The first group consisted of (from bottom to top) an undoped InP buffer on InP:Fe substrate and an $In_xGa_{1-x}As$ strained layer ($x=65\%$). The second group of samples consisted of HEMT structures. An undoped InP buffer layer was first grown on InP:Fe substrate. A 10 period $In_{0.53}Ga_{0.47}As/In_{0.52}Al_{0.48}As$ superlattice and 10 nm $In_{0.52}Al_{0.48}As$ layer were subsequently deposited as the buffer. Finally, an $In_{0.65}Ga_{0.35}As$ channel layer (with different thickness' between samples), 4 nm $In_{0.52}Al_{0.48}As$ spacer, delta-doping Si donor layer and 20 nm $In_{0.52}Al_{0.48}As$ Schottky layer terminated the structure growth. In order to measure electrical parameters of these structures by the Van der Pauw method, the contact layer was not deposited. Growth interruptions of approximately 10 s were used at the interfaces between the $In_{0.65}Ga_{0.35}As$ channel and $In_{0.52}Al_{0.48}As$ layers to provide sufficient time for the growth surface of the channel layer to become smooth. It resulted in an improvement of interfaces quality and high electron mobility [9].

The growth rate of mismatched layer is equal to $r=$ 5.87 Å/s. It was determined by two techniques: secondary ion mass spectrometry (SIMS) to record the Ga element depth profile and a profilometer to measure of this value.

The structural properties of an $In_{0.65}Ga_{0.35}As$ mismatched layer with free surface and covered by an $In_{0.52}Al_{0.48}As$ layer were investigated by atomic force microscopy (AFM). AFM observations were made in air at room temperature with a Digital Instruments Nanoscope III using large field head. The investigation of sample surfaces allowed us to notice the onset of misfit dislocation generation, which correspond to the experimental critical layer thickness.

3. Results and discussion

3.1. Samples with free surface of $In_{0.65}Ga_{0.35}As$ layer

The $In_{0.65}Ga_{0.35}As$ layers with various thickness (23.4 Å, 70.2 Å, 103.4 Å, 125 Å) were characterised by AFM. Fig. 1 shows AFM images of strained (a) and relaxed (c) $In_{0.65}Ga_{0.35}As$ layers surfaces with different thicknesses (intermediate variant was missing).

The surface of the strained $In_{0.65}Ga_{0.35}As$ layer has a regular and straight monolayer step (two-dimensional growth mode). The average interstep distance is 200 nm and surface roughness is 3.5 Å (Fig. 1a). With increasing layer thickness, two-dimensional islands growth mode succeeded in two-dimensional growth, what is shown on the grown surface (Fig. 1b). As the thickness increases further, the elastic strain energy builds up to the point, where it becomes energetically favourable to form misfit dislocation at the interface. Finally, at a thickness of 125 Å, misfit dislocation lines can be seen on the layer surface (Fig. 1c). Hence the experimental critical layer thickness is equal to 100 Å for $In_{0.65}Ga_{0.35}As$ layer, while the critical value evaluated from Mathews and Blakeslee Eq. (1) is 68 Å. It is approximately 1.5 times greater than theoretically predicted, but it is too small to use this layer as an active range in HEMT structure (because of carrier confinement) with various thickness of $In_{0.65}Ga_{0.35}As$ channel (60 Å, 120 Å, 180 Å, 235 Å, 470 Å). However, several authors [9,10] have reported excellent properties of electronic devices from heterostructures with $In_xGa_{1-x}As$ and InAlAs layers exceeding Mathews and Blakeslee limit and experimentally determined the value. To investigate these discrepancy, HEMT structures with various thickness $In_{0.65}Ga_{0.35}As$ layer as a channel were grown.

3.2. Samples with covered $In_{0.65}Ga_{0.35}As$ layer

Surfaces of HEMT structures with various thicknesses of $In_{0.65}Ga_{0.35}As$ channel (60 Å, 120 Å, 180 Å, 235 Å, 470 Å) were observed using AFM. Selected images are shown in Fig. 2.

In Fig. 2a,b a strained heterostructure case is shown. The thickness of channel layer is above the Mathews and Blakeslee limit and is equal to 180 Å. Straight, parallel terraces with width and step high of 342 nm and 4.3 Å (in measured point), respectively, are shown on this sample. Surface roughness is approximately 1.5 Å. The relaxed structure with a 235 Å channel InGaAs layer is shown in Fig. 2c. Misfit dislocations appeared at the interface and dislocation lines can be seen on the

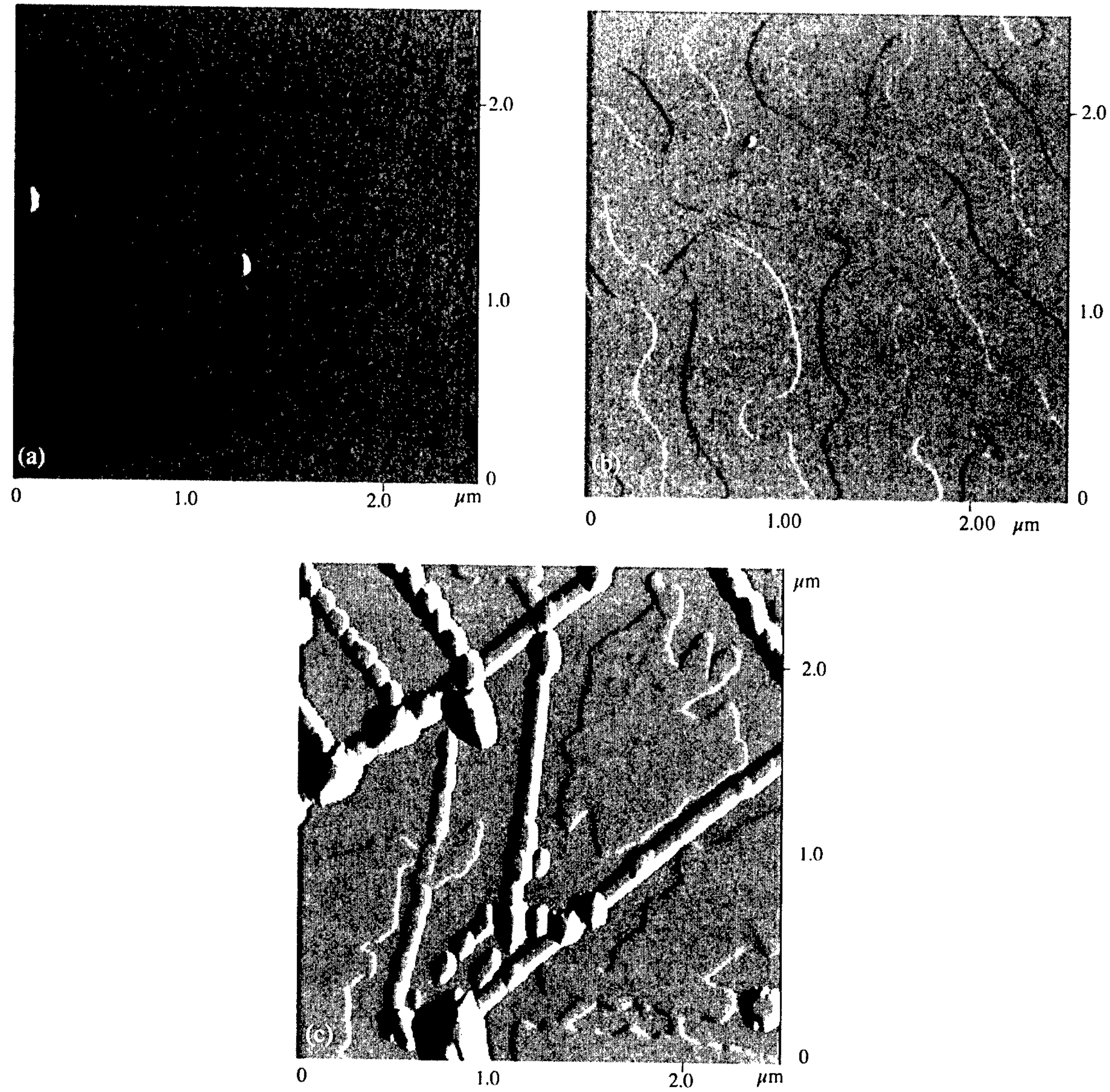

Fig. 1. AFM image of $In_{0.65}Ga_{0.35}As$ layers surface with their different thickness: (a) 23.4 Å, (b) 103.4 Å, (c) 125 Å.

sample surface. The critical channel thickness covered by InAlAs layer was determined as an average value between thicknesses in strained and relaxed cases. It equals 200 Å and it is three times greater than the value predicted by Mathews and Blakeslee theory and twice greater than experimentally specified thickness of strained InGaAs layer with free surface. To explain these discrepancy, a model, schematically presented in Fig. 3, was proposed.

Elementary cells of strained $In_xGa_{1-x}As$ layer mismatched to the InP lattice, covering InAlAs layer and InP substrate are illustrated by different size squares.

In a non-distorted state (Fig. 3II), the lattice parameter of a covered InAlAs layer a_{cap} equals to one of substrate (buffer) a_S and it is smaller than lattice constant of a strained $In_{0.65}Ga_{0.35}As$ layer.

In a coherent lattice state, in heterostructure layers interact forces, which are proportional to their thickness. We make an assumption that the lattice substrate does not deform because of its greater thickness than one layer.

The interaction between the covering layer and the mismatched one boils to the extent of covering materials lattice and to compress net of the mismatched layer (Fig. 3II). As a result of this interaction, lattice mismatch between a substrate InP lattice and strained $In_{0.65}Ga_{0.35}As$ layer covered and compressed by $In_{0.52}Al_{0.48}As$ layer results in being smaller than lattice mismatch one without covering $In_{0.52}Al_{0.48}As$ layer, (Fig. 3III and I). It is known that decreasing of a strain in a material lattice, the critical layer thickness is increasing.

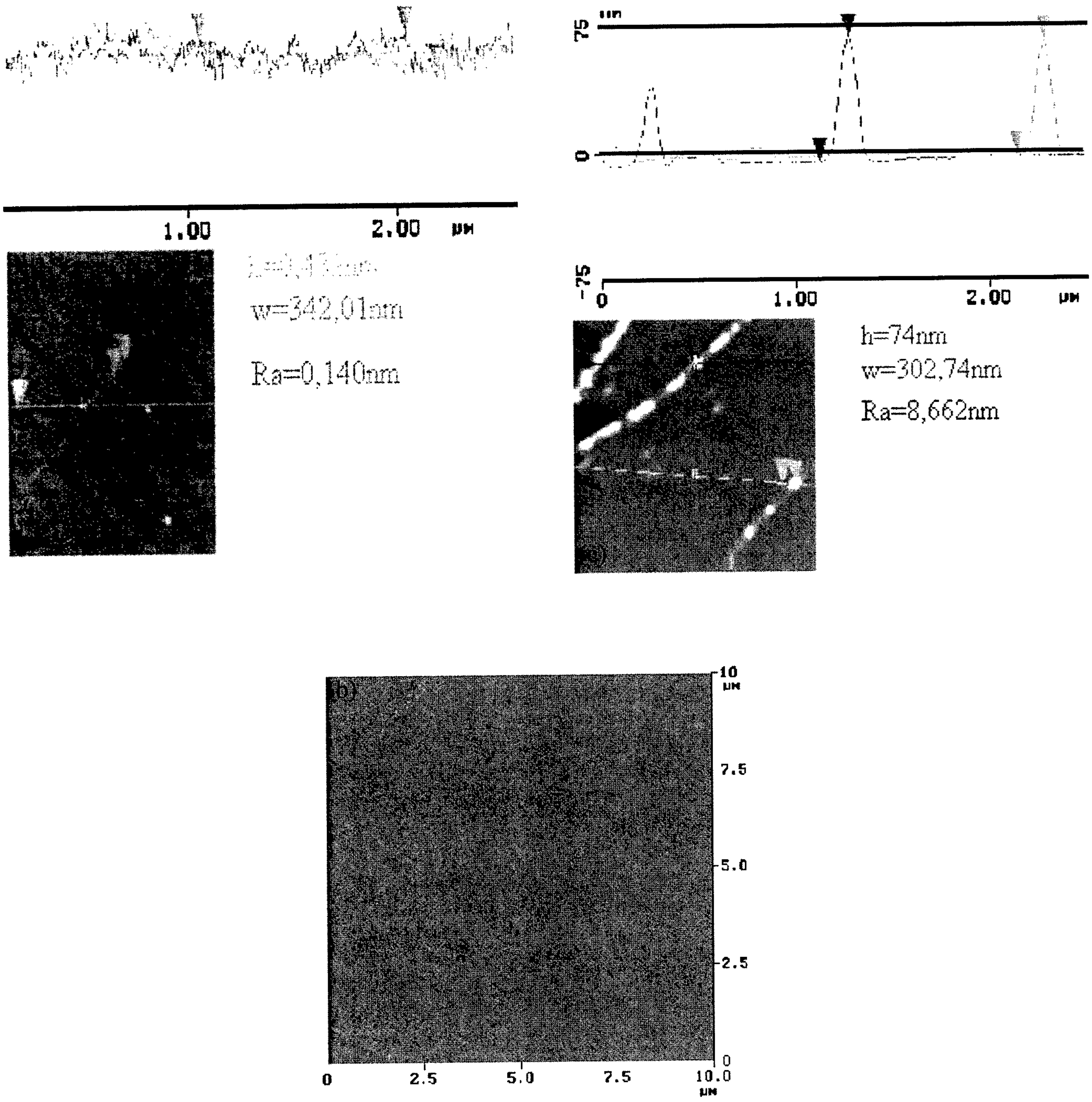

Fig. 2. AFM images of HEMT surfaces with different channel thickness: (a) 180 Å, (b) 180 Å, (c) 235 Å.

This model is working correctly beyond some thickness of covering layer. Above this value, $In_{0.52}Al_{0.48}As$ become to be an undeformable material.

Electrical parameters of HEMT structures were obtained by Van der Pauw measurements and placed in Table 1.

To make a comparison parameters of pseudomorphic HEMT structures to parameters of HEMT with a matched $In_{0.53}Ga_{0.47}As$ channel, the structure 955 was grown. Not fully carrier confinement to an active region is the reason for reduction of parameters beyond the thickness of 18 nm. Degradation of lattice correctness and larger contribution of an interface roughness in carrier scattering cause decreasing electron mobility with going up channel thickness. A 1090 HEMT structure with the channel thickness equal to 18 nm has the best electrical parameters. Above heterostructures were applied for producing InAlAs/InGaAs/InP HEMT tran-

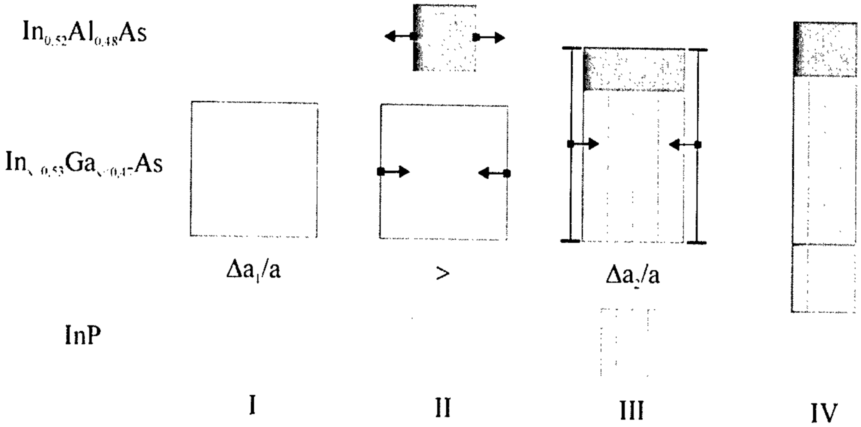

Fig. 3. Schematic diagram describing the decrease of lattice mismatch as a result of interacting a strain layer with a covering layer.

Table 1
Electrical parameters of HEMT structures

N°P	x (%)	Thickness (nm)	Electrical parameters of HEMT structures			
			n_{300K} (cm^{-2})	μ_{300K} (cm^2 Vs^{-1})	n_{77K} (cm^{-2})	μ_{77K} (cm^2 Vs^{-1})
955	53	20	2.22×10^{12}	8179	2.37×10^{12}	37 898
1599	65	6	5.1×10^{11}	2170	6.1×10^{11}	18 998
1606	65	12	2.7×10^{12}	6667	2.2×10^{12}	43 211
1090	65	18	1.9×10^{12}	9998	2.1×10^{12}	55 100
1607	65	23.5	3.3×10^{12}	5805	2.9×10^{12}	41 001
1608	65	47	2.1×10^{12}	4059	2.0×10^{12}	28 756

Table 2
The critical thickness of strained $In_{0.65}Ga_{0.35}As$ layer

Layer	The critical thickness of strained $In_{0.65}Ga_{0.35}As$ layer (nm)			
	d_{MB}	d_{FS}	d_{CS}	d_{CS}/d_{MB}
$In_{0.65}Ga_{0.35}As$	6.8	10.34	20.0	2.94

sistors. Their characteristics are presented in Nawz et al. [10].

4. Conclusion

We have investigated the impact of covering InAlAs layer on the critical thickness of strained InGaAs layer grown by MOVPE on InP substrate. Using AFM, we determined the critical thickness of InGaAs layer with free surface and covered by a 25-nm InAlAs layer and we compared with the Mathews and Blakeslee limit. Obtained parameters are shown in Table 2.

The critical thickness of the strained $In_{0.65}Ga_{0.35}As$ layer covered by InAlAs is approximately three times greater (2.94 times) than the value obtained from the Mathews and Blakeslee formula. To explain this discrepancy, a model was proposed. The findings were applied to growth of pseudomorphic InGaAs/InAlAs/InP HEMT.

References

[1] A. Bradley, A. Fox, A. William, A. Jesser, J. Appl. Phys. 68 (1990) 2801.
[2] A. Snyder, R.C. Cammarata, J. Electron. Mater. 26 (1997) 966.
[3] P. Roura, S.A. Clark, J. Bosch, F. Peira, A. Cornet, J.R. Morante, J. Appl. Phys. 77 (1995) 4018.
[4] X. Zhang, O. Briot, B. Gil, R. Aulombard, J. Appl. Phys. 78 (1995) 5490.
[5] J.W. Matthews, A.E. Blakeslee, J. Cryst. Growth 27 (1974) 118.
[6] T. Okada, G.C. Weatherly, J. Cryst. Growth 179 (1997) 339.
[7] W.A. Jasser, X. Kuhlman, D. Wilsdorf, Phys. Stat. Sol. 19 (1967) 95.
[8] M. Ogasawara, H. Sugiura, M. Mitsuhara, M. Yamamoto, M. Nakao, J. Appl. Phys. 84 (1998) 4775.
[9] R.G. Pereira, B. Yavich, L.C.D. Gonçalves, P.L. Souza, A.B. Henriquues, Electr. Lett. 34 (1998) 2173.
[10] M. Nawaz, H. Zirath, E. Choumas, S.H.M. Persson, A. Jasik, W. Strupinski, Microelec. Reliabil. 39 (1999) 1765.

ELSEVIER

Thin Solid Films 412 (2002) 55–59

www.elsevier.com/locate/tsf

MOVPE technology and characterisation of silicon δ-doped GaAs and $Al_xGa_{1-x}As$

B. Ściana[a,*], D. Radziewicz[a], B. Paszkiewicz[a], M. Tłaczała[a], M. Utko[b], P. Sitarek[b], G. Sęk[b], J. Misiewicz[b], R. Kinder[c], J. Kováč[c], R. Srnanek[c]

[a]*Faculty of Microsystem Electronics and Photonics, Wrocław University of Technology, Janiszewskiego 11/17, 50-372 Wrocław, Poland*
[b]*Institute of Physics, Wrocław University of Technology, Wybrzeże Wyspiańskiego 27, 50-370 Wrocław, Poland*
[c]*Department of Microelectronics, Faculty of Electrical Engineering and Information Technology, Slovak University of Technology, Ilkovičova 3, 81219 Bratislava, Slovak Republic*

Abstract

This work presents the investigation of MOVPE growth of silicon δ-doped GaAs and $Al_xGa_{1-x}As$ epilayers and different methods used for their characterisation. The influence of the growth temperature, SiH_4 flow rate and $Al_xGa_{1-x}As$ composition on δ-doping characteristics is discussed. Properties of the Si δ-doped structures were examined using capacitance–voltage (*C–V*) measurements, photoreflectance spectroscopy, micro-photoluminescence, micro-Raman and photocurrent spectroscopies. © 2002 Elsevier Science B.V. All rights reserved.

Keywords: MOVPE technology; δ-doping; C-V profiling; PR spectroscopy; μ-RS; μ-PL; PC spectroscopy

1. Introduction

Delta-doping is a novel doping method which spatially confines the dopant atoms to one or a few atomic layers. This type of incorporation of dopant atoms into crystalline structure of semiconductor material modifies its electronic structure by bending the conduction or valence band edges to form a V-shaped potential well. The electrons (or holes) confined in this potential well are regarded as a two-dimensional electron or hole gas. Delta-doping is very attractive for application in advanced semiconductor devices, such as HEMTs, HBTs, resonant tunnelling diodes, quantum well infrared photodetectors, homo- and hetero-nipi doped superlattices, modulators. Most of the delta-doped epitaxial structures are deposited by molecular beam epitaxy (MBE) due to the low growth temperatures. On the other hand, MBE growth of δ-doped structures above 600 °C results in large dopant profile broadening caused by the Fermi-level pinning-induced segregation [1,2]. This effect is not observed in δ-doped layers grown by MOVPE, although the growth temperatures are usually between 650 °C and 750 °C, what is explained by hydrogen surface passivation [1–3]. This work presents results of Si δ-doping of GaAs and $Al_xGa_{1-x}As$ structures grown by MOVPE and discusses different methods used for their characterisation.

2. Experimental details

The following epitaxial test structures (type A, type B) were grown by MOVPE on semi-insulated or n-Si-doped GaAs substrates using an atmospheric pressure AIX200 R&D Aixtron reactor:

A. Si δ-doped GaAs sample consisted of a 900-nm of GaAs buffer layer followed by Si δ-layer and a 150÷160-nm GaAs cap layer; and
B. Si δ-doped $Al_xGa_{1-x}As$ (or AlAs) sample consisted of a 250-nm GaAs buffer layer followed by a 200-nm undoped $Al_xGa_{1-x}As$ (or AlAs) in the middle of which the Si δ-layer was placed and a 32÷45-nm GaAs oxidise protection layer.

The TMGa, TMAl, AsH_3 and SiH_4 (20 ppm in H_2) were used as the growth and dopant precursors. High purity H_2 was employed as a carrier gas. The substrate temperature (T_g) was in the range of 670÷760 °C for δ-doped GaAs and 760 °C for δ-doped $Al_xGa_{1-x}As$ ($x=0.29$, 0.34, 0.35, 0.46, 0.6) and δ-doped AlAs samples. The SiH_4 flow rate was changed from 10 to 100 ml/min. A basic δ-doping procedure 'purge-doping-

---

*Corresponding author.
E-mail address: sciana@wenif.pwr.wroc.pl (B. Ściana).

PII: S0040-6090(02)00313-9

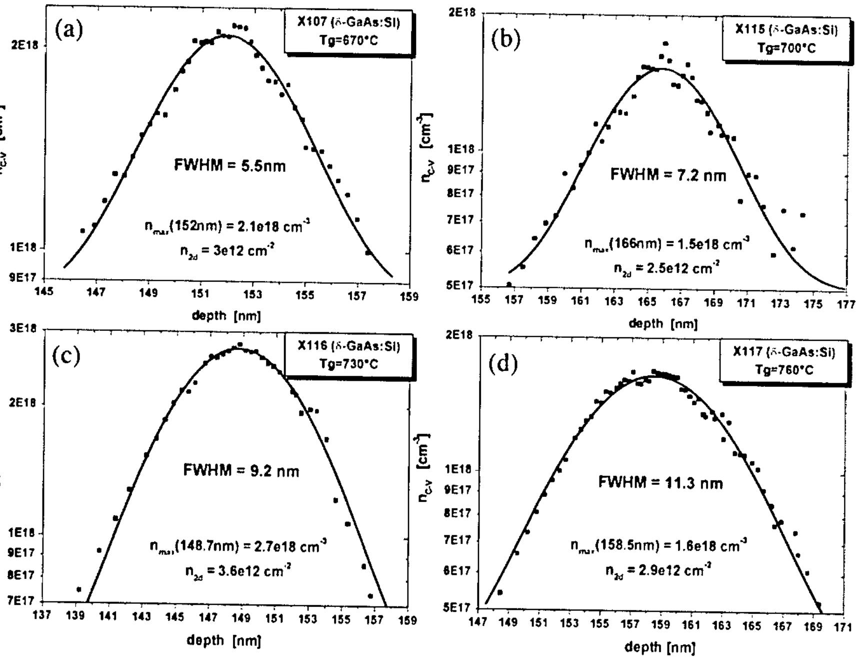

Fig. 1. The C–V profiles of Si δ-doped GaAs grown at: (a) 670 °C, (b) 700 °C, (c) 730 °C, (d) 760 °C.

purge' was applied [1,2,4]. The obtained structures were examined by C–V measurements using a mercury probe and a HP 4192A impedance analyser (5 Hz ÷ 13 MHz). Also photoreflectance, micro-photoluminescence, micro-Raman and photocurrent spectroscopies were applied.

3. Results and discussion

3.1. Influence of the growth temperature and SiH_4 flow rate on the sheet electron density and the width of C–V profiles of Si δ-doped GaAs epilayers. Results of C–V measurements

The influence of the growth temperature and SiH_4 flow rate on the properties of Si δ-doped GaAs epilayers was investigated. The main method used for determination of the electron concentration and broadening of the dopant distribution in the obtained structures was C–V measurement done at frequencies below 100 kHz. The C–V profiles, presented in Fig. 1, were measured for Si δ-doped GaAs epilayers (type A) grown at 670 °C, 700 °C, 730 °C and 760 °C (samples X107, X115, X116 and X117, respectively). The SiH_4 flow rate was 100 ml/min for the all structures. The best results were obtained for the Si δ-doped GaAs grown at 670 °C (sample X107, Fig. 1a).

For this layer no diffusion broadening of the profile was observed. The width of the C–V profile, $\text{FWHM}_{C-V} \approx 5.5$ nm (determined by applying Gaussian approximation) is comparable to the spatial extent of the ground-state wave function $z_0 \approx 5.5$ nm, calculated from the following equation [1,2,5]:

$$z_0 = 2\sqrt{\frac{7}{5}}\left(\frac{4}{9}\frac{\varepsilon\hbar^2}{e^2 n_{2d} m^*}\right)^{1/3} \qquad (1)$$

where, ε is the semiconductor permittivity, e is the elementary charge, n_{2d} is the sheet electron density, m^* is the electron effective mass. Fig. 2 shows the dependence of the sheet electron density and the C–V profile widths of Si δ-doped GaAs (type A) on the SiH_4 flow rate. The growth temperature was 670 °C, SiH_4 flow rate was changed from 10 to 100 ml/min. The values of z_0, calculated from Eq. (1) for sheet electron concentrations above 10^{12} cm^{-2}, are also included.

For high values of SiH_4 flow rate (>40 ml/min) saturation of the electron density is observed. It can be explained by establishment of the equilibrium between adsorption and desorption process of the active Si species, autocompensation caused by incorporation of Si atoms into As sites and/or formation of Si clusters [2]. The values of FWHM_{C-V} are in a good agreement with the calculated values of z_0. The C–V profile widths obtained for Si δ-doped AlAs and $Al_{0.35}Ga_{0.65}As$ were broad (FWHM_{C-V} = 12.4 and 29.6 nm, respectively) due to the influence of thermal diffusion at high growth temperature (760 °C) which was required for improving the material quality.

3.2. Photoreflectance spectroscopy

Photoreflectance spectroscopy (PR) was applied to the investigation of Si δ-doped epilayers. The experi-

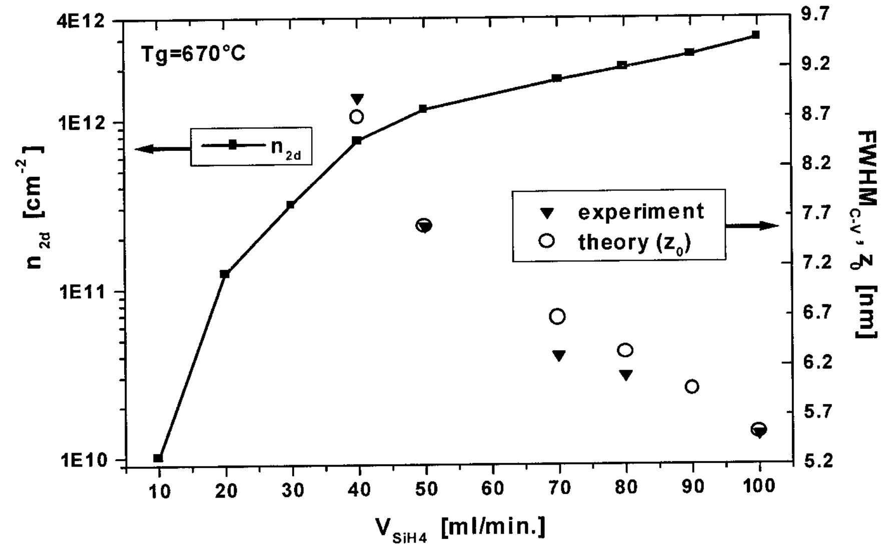

Fig. 2. Dependence of the sheet electron density and the $FWHM_{C-V}$ of Si δ-doped GaAs on SiH_4 flow rate.

mental set-up for these measurements has been described previously [6]. The PR spectrum of Si δ-doped GaAs (type A) is presented in Fig. 3. A lot of distinguished Franz–Keldysh oscillations (FKOs) above the band gap energy are seen, demonstrating the existence of a strong uniform electric field in the very high quality epitaxial layer. The observation of FKOs and application of fast Fourier transform (FFT) allowed to determine the internal electric field F and the potential barrier height V_B between the surface and the δ-doped region [7].

The following values were obtained for the investigated Si δ-doped epilayers:

$F=53$ kV/cm, $V_B=0.74$ V for GaAs (type A, $T_g=670$ °C, $V_{SiH4}=100$ ml/min); and
$F=68$ kV/cm, $V_B=0.94$ V for $Al_{0.35}Ga_{0.65}As$ and $F=110$ kV/cm; $V_B=1.57$ V for AlAs (type B, $T_g=760$ °C, $V_{SiH4}=100$ ml/min.).

3.3. Micro-photoluminescence and micro-Raman spectroscopy

Micro-photoluminescence (μPL) and micro-Raman spectroscopy (μRS) were used for determination of a δ-layer position and its spreading in Si δ-doped GaAs structures. A beam of He–Ne laser ($\lambda=632.8$ nm) was scanned at room temperature along the bevelled structure, and change of PL (at $\lambda=870$ nm) and the ratio of intensities of transversal optical phonon (TO) and longitudinal optical phonon (LO) was detected. The diameter of the spot was $1\div2$ μm and 10 μm for RS and PL, respectively. The bevels were prepared by chemical etching [8], the bevel angle was approximately 6×10^{-5} rad. Fig. 4a presents dependence of PL along the bevelled Si δ-doped GaAs structure (sample X105). The presence of δ-layer makes the PL signal to increase between 135 nm (point U) and 160 nm (point L) below the surface. This is a spreading of the Si dopant. Position of the middle point of δ-layer (145 nm from surface, point D) corresponds to an inflex point of the dependence. Based on the obtained characteristic we could determine a dimension of a δ-layer, much like as in the case of $FWHM_{C-V}$ in $C-V$ profiling. The half width of a δ-layer (HWD) is defined as a distance between point D on the bevel and the point, where PL intensity decreases to 10% of the intensity in point D. The PL intensity in the buffer layer (point L) is defined as zero. The estimated value of HWD for sample X105 is 9 nm. This sample was also examined by Raman spectroscopy (Fig. 4b). The change of TO/LO ratio on the bevelled structure is similar to the PL dependence in the bevel length range $3\div3.5$ mm, where δ-layer is located. In this case, the same procedure (as for the PL measurements) of determination of HWD was applied and the identical value of 9 nm was obtained. The position and spreading of the δ-layer, determined by RS and PL for sample X105, are in good coincidence with the values obtained for this structure by the $C-V$ measurements (n_{max} placed 157 nm from the surface, $FWHM_{C-V}=8.6$ nm).

3.4. Photocurrent spectroscopy

Photocurrent (PC) measurements were realised on Au–Schottky contacts by illumination from the surface side. The Schottky contacts were evaporated through the metal mask. The diameter of the circular Schottky contacts and distance between them was 830 and 185 μm, respectively. The ohmic contacts were prepared before Schottky contacts deposition on one side of the sample. Photocurrent spectroscopy of δ-doped samples

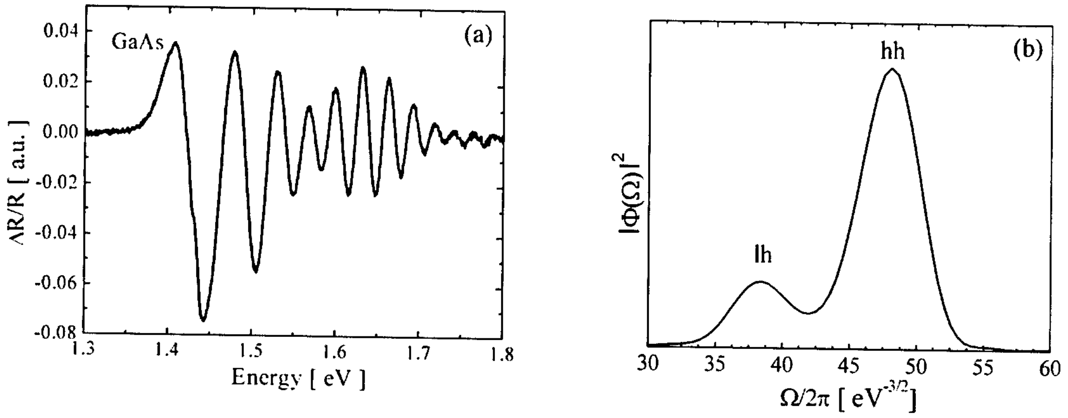

Fig. 3. The PR spectrum (a) and its fast Fourier transform (b) for the Si δ-doped GaAs.

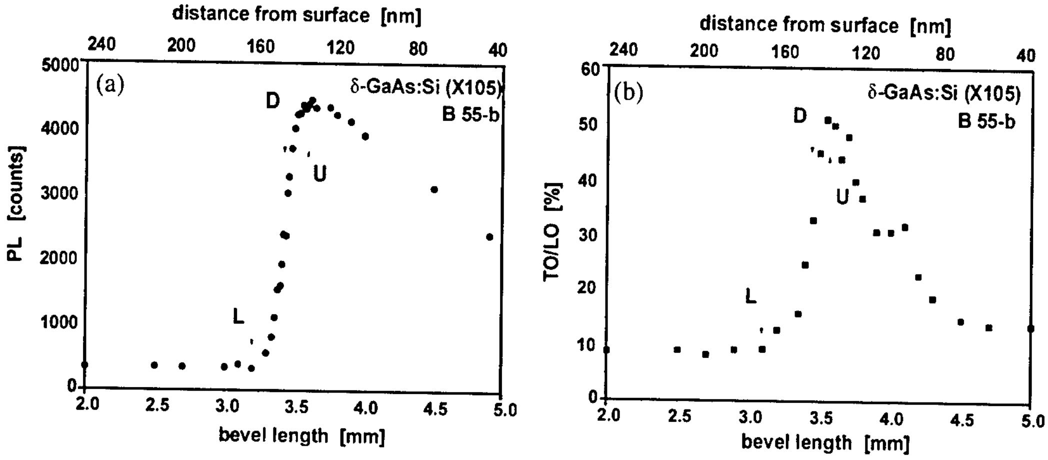

Fig. 4. Change of PL intensity (a) and of TO/LO ratio (b) on the bevelled structure X105.

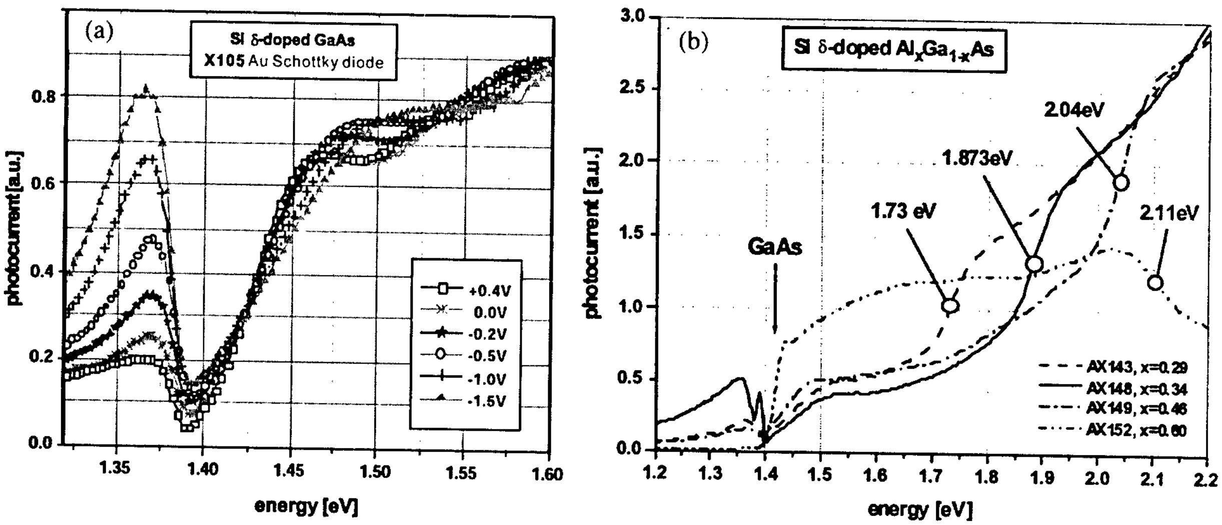

Fig. 5. Photocurrent vs. energy for: (a) Si δ-doped GaAs for different Schottky contact bias; and (b) Si δ-doped $Al_xGa_{1-x}As$ with different Al content.

is influenced by the electrical field introduced by a δ-doped layer resulting in oscillation of the PC signal above the band gap energy and by the interface on GaAs substrate side (peak at 1.37 eV). The PC spectrum of Si δ-doped GaAs (sample X105) is shown in Fig. 5a. The minimum of oscillations at 1.5 eV, corresponding to δ-layer, shifts the position under bias voltage due to the change of the electric field inside the structure. In the case of the PC measurements of homogeneous n-doped GaAs Schottky diodes, only the shift of the low energy edge under bias voltage was observed.

The PC spectra of the Si δ-doped $Al_xGa_{1-x}As$ epilayers with different Al content are shown in Fig. 5b (type B structure; $x=0.29$, 0.34, 0.46, 0.6 for sample AX143, AX148, AX149 and AX152, respectively). The presented spectra show $Al_xGa_{1-x}As$ absorption edge and GaAs absorption in the GaAs interface layer. The oscillations of the PC signal above the band gap energy are not so pronounced as in the case of Si δ-doped GaAs (Fig. 5a).

4. Conclusions

MOVPE technology and characterisation of the fabricated Si δ-doped GaAs and $Al_xGa_{1-x}As$ are described. The best results were obtained for Si δ-doped GaAs structures grown at 670 °C, what was confirmed by $C-V$, PR and PC measurements. These layers have the narrowest $C-V$ profiles ($FWHM_{C-V}\sim 5.5$nm), comparable to the calculated spatial extent of the ground-state wave function z_0. They exhibit also the best PR spectra and distinct oscillations of the photocurrent above the band gap energy. The $C-V$ profiles obtained for Si δ-doped $Al_xGa_{1-x}As$ and AlAs are broader caused probably by the thermal diffusion at high growth temperature (760 °C). The calculated values (based on PR spectra) of the potential barrier heights V_B for Si δ-doped GaAs, $Al_{0.35}Ga_{0.65}As$ and AlAs suggest that the Fermi level is pinned at the middle of the band gap of the investigated epilayers, what is in good agreement with previous reports [9]. Micro-Raman spectroscopy and micro-photoluminescence were successfully used for determination of δ-layer position and its spreading in Si δ-doped GaAs structures. The obtained results are in good coincidence with $C-V$ measurements. The presented investigations are important for optimisation of MOVPE technology of advanced semiconductor devices utilising Si δ-doped $Al_xGa_{1-x}As/GaAs$ heterostructures as the active regions. The study helped to evaluate suitable characterisation methods such as $C-V$ and PR measurements, allowing fast, precise and non-destructive examination of δ-doped device structures.

Acknowledgments

This work was partly supported by the Polish Scientific Research Committee, Grants: 8T11B00618, 8T11B05718, by Advanced Materials and Nanotechnology Centre of Wroclaw University of Technology; by the Slovak Grant Agency (VEGA) from Grants No. 1/7613/20, 1/7600/20 and by the Polish–Slovak project pol/slov/11.

References

[1] E.F. Schubert, J. Vac. Sci. Technol. A 8 (1990) 2980.

[2] G. Li, C. Jagadish, Solid-State Electron. 41 (1997) 1207.

[3] G.M. Yang, S.G. Park, K.S. Seo, B.D. Choe, Appl. Phys. Lett. 60 (1992) 2380.

[4] B. Ściana, D. Radziewicz, M. Tłaczała, G. Sęk, M. Nowaczyk, J. Misiewicz, Proc. of the 3rd Intern. EuroConference ASDAM 2000, Slovakia, Oct. 2000, p. 281.

[5] E.F. Schubert, R.F. Kopf, J.M. Kuo, H.S. Luftman, P.A. Garbinski, Appl. Phys. Lett. 57 (1990) 497.

[6] J. Misiewicz, K. Jezierski, P. Sitarek, P. Markiewicz, R. Korbutowicz, M. Panek, B. Ściana, M. Tłaczała, Adv. Mater. Opt. Electron. 5 (1995) 321.

[7] M. Nowaczyk, G. Sęk, J. Misiewicz, B. Ściana, D. Radziewicz, M. Tłaczała, Thin Solid Films 380 (2000) 243.

[8] R. Srnanek, R. Kinder, B. Ściana, D. Radziewicz, D.S. McPhail, S.D. Littlewood, I. Novotny, Appl. Surf. Sci. 177 (2001) 139.

[9] H. Shen, M. Dutta, J. Appl. Phys. 78 (1995) 2151.

ELSEVIER

Thin Solid Films 412 (2002) 60–63

thin solid films

www.elsevier.com/locate/tsf

Explanation of the initial phase change vs. incident angle of the RHEED intensity oscillation

Ákos Nemcsics*

Hungarian Academy of Sciences, Research Institute for Technical Physics and Materials Science, P.O. Box 49, H-1525 Budapest, Hungary

Abstract

Reflection high-energy electron diffraction, which is a very widely used monitoring technique of molecular-beam-epitaxial growth processes, has still some unexplained features. An interesting example of these, the so-called $t_{3/2}/T$ phenomenon, is investigated in this work. The first period of the intensity oscillations of reflection high-energy electron diffraction shows a singular behaviour. An interpretation for the initial change of the phase and of the period duration dependence on the incident angle of the electron beam using the notion of surface coherence length is given here. This particular phenomenon is satisfactorily explained in the case of a GaAs (001) surface. © 2002 Elsevier Science B.V. All rights reserved.

Keywords: Reflection high-energy electron diffraction; Molecular beam epitaxy; $t_{3/2}/T$ phenomenon; GaAs

1. Introduction

Reflection high-energy electron diffraction (RHEED) is a widely used monitoring technique during molecular-beam-epitaxial (MBE) growth. The reconstruction and roughness of the surface can be observed by the RHEED pattern. The intensity of the RHEED pattern oscillates under appropriate conditions during the growth process. One period of these oscillations corresponds to the growth of one single monolayer (ML) in a layer by layer mode.

RHEED patterns and its oscillations of intensity are very complex phenomena. These effects can be used as a versatile tool for in-situ monitoring of the epitaxial layer growth, in spite of the fact that we do not know many details of its nature. Several mechanisms of the behaviours of RHEED oscillations are not yet understood. For example, some of these problems involve different phases of the specular and non-specular RHEED beams [1], or differences in behaviour of the oscillations in the case of III–V and II–VI materials [2]. The description of these phenomena was attempted by several authors. A thoroughly review of these models is given in Joyce et al. [3]. The anomalies of the initial phase of the RHEED oscillations, the so-called $t_{3/2}/T$ phenomena, are investigated in this work. Making use of computer simulations we provide an explanation for the initial phase shift.

2. The $t_{3/2}/T$ phenomenon in experiments

The initial period and the amplitude of RHEED oscillations differ from what follows those seen after a prolonged observation. Except for the first period, the measured decay of the oscillations fits well to an exponential function [4]. The incident electron beam impinges on the surface with an angle between 0.7° and 3°. If the incident or the azimuthal angle are changed, then the initial phase of the oscillations also changes. The measured 'rocking' data for the specular spot according to Resh et al. [1] and Joyce et al. [3] are shown in Fig. 1. Data points were obtained by measuring the time to the second minimum, so-called $t_{3/2}$, and normalising with respect to the period at a steady state, T. These data are obtained vs. incident angle at two different azimuthal directions for the GaAs (001) surface. The temperature of substrate during growth was 600 °C [1] and 580 °C [3], respectively. The electron beam energy (12.5 keV) was mentioned only in the second reference [3].

3. Results and discussion

3.1. The notion of the surface coherence length

The simple kinematic theory [1] does not predict the phase shift of the oscillations, which would additionally

---

*Tel.: +36-1-392-2222 ext 3178; fax: +36-1-392-2235.
E-mail address: nemcsics@mfa.kfki.hu (Á. Nemcsics).

PII: S0040-6090(02)00314-0

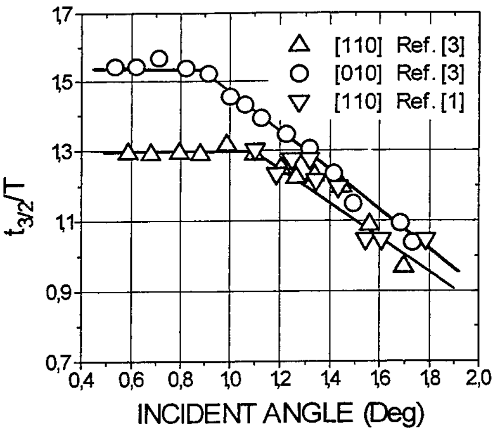

Fig. 1. The experimental 'rocking' data of RHEED oscillation, that is the ratio of $t_{3/2}/T$ as a function of the incident angle of the electron beam in [110] and [010] azimuthal directions of a GaAs (001) surface. The data values originate from Resh et al. [1] and Joyce et al. [3]. The lines serve only as guides to the eye.

depend on the condition of the incidence of the electron beam. The contribution of inelastic processes, such as Kikuchi scattering, to the phase shift phenomenon is not completely taken into account in this approach [1]. The RHEED phenomenon is partly reflection-like and partly diffraction-like. The effect of the phase shift is described by noting the exact positions of the minima of the oscillations. The detailed behaviour of the minima and maxima of the oscillations can be explained also using a geometrical picture, which will be employed also in the present paper. Because the specular spot is not a reflected beam, the interaction of the electron beam and the target surface must be described quantum mechanically. The glancing-incidence angle electron beam interacts with the surface over a relatively large area. However, the reflected–diffracted information obtained does not come from the whole of this area. The interaction between the surface and the electron beam occurs only under special conditions, therefore, we need to consider the notion of surface coherence length (w). Beeby [5] introduced the quantum mechanics definition of this quantity. Here we briefly point the major steps introducing this quantity.

However, now we have supposed that the surface coherence length w is of the same order as the coherence length (Λ) of the beam [6]. In the above-mentioned experiments the energy of the electron beam is in the order of $E=10$ keV, corresponding to de Broglie wavelength $\lambda=12.2\times10^{-12}$ m. The coherence length of the electron beam Λ can be determined as [7]:

$$\Lambda=\frac{\lambda}{2\beta\sqrt{1+(\Delta E/E)^2}}$$

where β and ΔE are the angular spread and the thermal width (i.e. the energy spread) of the electron energy of the incident beam, respectively. The beam divergence ranges usually between 10^{-4} and 10^{-5} rad and the energy spread is approximately 0.5 eV [8]. The spatial width for the wave packet for highly collimated beam can be estimated, to extend by: $\Lambda_0=6.1$ nm with these values. Another estimate of the wave packet from interference investigations gives 300 λ [9]. In this way we can obtain similar value of $\Lambda_0=3.7$ nm for the wave packet.

The spot size of the illuminating electron beam on the surface (L) in the incident direction depends strongly on the incident angle (α). If the cross-section of the illuminating electron beam is b then the touching area dependence on incident angle can be expressed by the following simple trigonometrical function $L=b/\sin\alpha$. This dependence is very strong in the vicinity of an incident angle of 1°. Therefore, we can suppose that the surface coherence length depends on the incident angle and is described by a similar function ($\Lambda=w/\sin\alpha$) [6].

3.2. The size of characteristic growth terraces

The relation between the domain size (s) and the surface coherence length (w) in the case of a polycrystalline surface was investigated in Beeby [5]. This concept can be applied in our case if we consider, instead of domains, identically oriented growth units (or growth terraces). An estimate of the characteristic dimension of a growth terraces can be made from experimental data. The terrace average width (s) and the migration length of Ga (l) depend on the substrate temperature. The RHEED oscillations are present if $l\leq s$ and absent if $l\geq s$. In our case the migration length is 7 nm because the substrate temperature is 580 °C [3].

The binding energy on the (001) surface in the directions [110] and [$1\bar{1}0$] is different, which can be explained with the different dangling bonds in different directions [4]. This anisotropy is manifested in the different growth rates. The growth rate in the [110] direction is larger than that in the perpendicular direction [10]. This anisotropy is apparent not only in the growth of the crystal but also in the etching (i.e. during decomposition of the crystal). This factor can be estimated with the help of etch-pit shapes (see Fig. 4 in Nemcsics et al. [11]), where the ratio of the sides of the rectangle shaped pits is a factor of approximately 2.4. Here is supposed that the growth rates in the [110] and [$1\bar{1}0$] directions differ by a similar amount (see Fig. 2).

3.3. Initial phase dependence on the incident angle

It is supposed that the surface coherence length and the average terrace width have similar dimensions at glancing-incidence angles ($w\approx s$), because the touching length of the electron beam (assumed to be the same

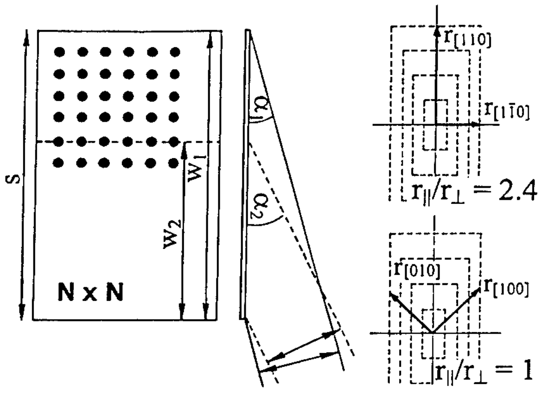

Fig. 2. The left side of the figure shows view of one island with lattice nodes in the growth model consisting of islands of $P \times P$ ($P = 4$) terraces of $N \times N$ ($N = 36$) lattice sites, where the relation between the terrace dimension and surface coherence length is illustrated. The right side illustrates the ratio of $r_{\parallel}/r_{\perp}$, if the observation direction changes towards [110] and [010].

as the surface coherence length) changes very abruptly at angles less than 1° and in this region the function $t_{3/2}/T$ is constant, since $w > s$ (see Fig. 1). The relation of the surface coherence length and average terrace width is changed with the changes of the incident angle. If the incident angle increases, the surface coherence length becomes smaller than the average terrace width ($w < s$), so and thus the reflected–diffracted information comes from only a part of the average terrace.

The polynuclear growth model in the two-dimensional case was used for our calculations [12]. The simplified picture takes into consideration diffraction contributions only from the topmost ML and the RHEED intensity is taken as proportional to the smooth part of the surface top layer [4]. The computing model assumes $N \times N$ lattice sites in a $P \times P$ growth terrace (Fig. 2) [1,6]. The relation between the terrace size and the area of the surface coherence is shown in left side of Fig. 2. It is clear that the information supplied about the probed surface area decreases with an increasing incident angle of the beam. The different crystallographic directions mean different growth rates. Here the ratio of $r_{[110]}/r_{[1\bar{1}0]}$ are estimated to be 2.4. The oscillations were computed for two different ratios of $r_{\parallel}/r_{\perp}$, where $r_{\parallel}$ and $r_{\perp}$ are the growth rates for the observation direction parallel to the electron beam and perpendicular to it, respectively. Thus, the assumed value of the ratio in the case of the beam along [110] is 2.4. The ratio in the [010] direction taken as 1 (see right side of Fig. 2). The calculated oscillations in the case of both ratios can be seen in Fig. 3. Perfect layer-by-layer growth was assumed in the calculation, so only the actual top monolayer was investigated. The calculated function of $t_{3/2}/T$ vs. the azimuthal angle in the two different directions is plotted in Fig. 4. The growth time for one complete ML in the two different directions is the same (T), but the phase is different ($t_{3/2}$) because of the anisotropic growth rate. These curves correspond very well to the measured 'rocking' data in Fig. 1. If the surface coherence length is larger than the average terrace width then the $t_{3/2}/T$ ratio remains constant (with the value is determined by the $r_{\parallel}/r_{\perp}$ ratio). If the surface coherence length is smaller than the average terrace width, then the $t_{3/2}/T$ ratio decreases also.

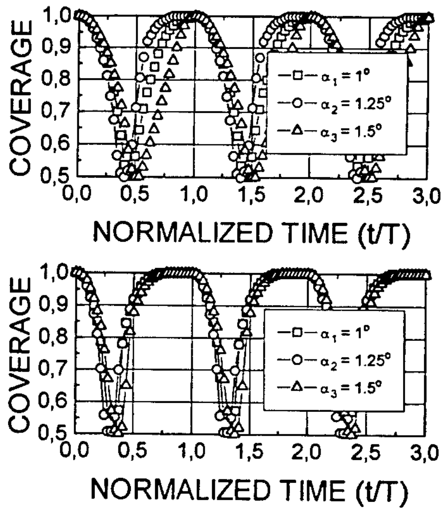

Fig. 3. The computed oscillations at different incident angles. The symbols □, ○ and △ mean incident angles of 1°, 1.25° and 1.5°, respectively. The change of incident angle means that the reflected-diffracted information comes from 100%, 80% and 60% of the terrace area, respectively. The upper part of the figure shows the case of $r_{\parallel}/r_{\perp} = 2.4$ and the lower part shows $r_{\parallel}/r_{\perp} = 1$.

The behaviour of $t_{3/2}/T$ vs. incident angle was investigated for glancing-incidence angles, under 1.8°. Our model describes the incident angle dependence of $t_{3/2}/T$ in this range only. In real situations, the diffracted–reflected electron beam gets information not only from the topmost ML, but a larger incident angle causes also a larger penetration depth. The description of this phenomenon at larger incident angles probably can be

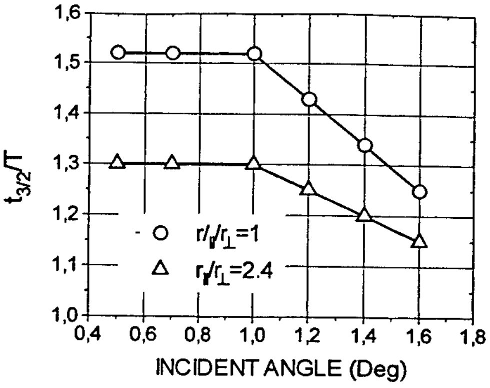

Fig. 4. The computed $t_{3/2}/T$ ratio vs. incident angle in different crystallographic directions (in the case of $r_{\parallel}/r_{\perp} = 2.4$ and $r_{\parallel}/r_{\perp} = 1$).

improved by considering more MLs below the surface during the growth process.

4. Conclusion

The phenomenon of the initial phase variation of the RHEED intensity oscillation is explained here with the help of the concept of the surface coherence length. The surface coherence length corresponds to the surface area probed by a coherent beam, which changes with the incident angle of the beam. A geometrical description was used for the interpretation. Our explanation is demonstrated by a computer simulation. The demonstration was carried out in two different crystallographic directions, where a realistic estimation was made concerning the ratio of the crystal growth rates. The calculations were carried out with a discrete lattice node arrangement. The topmost ML was taken into account. The calculated curves for the decay of the oscillations correspond very well with the measured 'rocking' data in the investigated range.

Acknowledgments

This work was supported by Hungarian National Scientific Foundation (OTKA) through Grant T 030426.

References

[1] J.S. Resh, K.D. Jamison, J. Strozier, A. Bensaoula, A. Ignatiev, Phys. Rev. B 40 (1989) 799.
[2] J. Griesche, N. Hoffmann, M. Rabe, K. Jacobs, Prog. Cryst. Growth Character. Mater. 37 (1998) 103.
[3] B.A. Joyce, J.H. Neave, J. Zhang, P.J. Dobson, in: P.K. Larsen, P.J. Dobson (Eds.), Reflection High-Energy Electron Diffraction and Reflection Imaging of Surfaces, NATO ASI Series B: Physics, 188, Plenum Press, New York, 1987, p. 397.
[4] Á. Nemcsics, J. Olde, M. Geyer, R. Schnurpfeil, R. Manzke, M. Skibowski, Phys. Stat. Sol. (a) 155 (1996) 427.
[5] J.L. Beeby, Surf. Sci. 80 (1979) 56.
[6] Á. Nemcsics, J. Cryst. Growth 217 (2000) 223.
[7] O. Brümmer, J. Heydenreich, K.H. Krebs, H.G. Schneider (Eds.), Festkörperanalyse mit Elektronen, Ionen und Röntgenstrahlen, Deutscher Verlag der Wissenschaften, Berlin, 1980.
[8] H. Lüth, Surfaces and Interfaces of Solid Materials, third ed, Springer, Berlin, 1995.
[9] O. Klemperer, Electron Physics, Butterworths, London, 1958.
[10] Y. Horikoshi, H. Yamaguchi, F. Briones, M. Kawashima, J. Cryst. Growth 105 (1990) 326.
[11] Á. Nemcsics, L. Petrás, K. Somogyi, Vacuum 41 (1990) 1012.
[12] Y. Ishibashi, J. Phys. Soc. Jpn. 60 (1991) 3215.

ELSEVIER

Thin Solid Films 412 (2002) 64–75

thin solid films

www.elsevier.com/locate/tsf

Laterally overgrown structures as substrates for lattice mismatched epitaxy

Z.R. Zytkiewicz

Institute of Physics, Polish Academy of Sciences, Al. Lotnikow 32/46, PL-02-668 Warsaw, Poland

Abstract

This article provides a general review of the epitaxial lateral overgrowth (ELO) technology and of application of ELO layers as substrates with adjustable value of lattice constant. In particular, the issues of ELO growth mechanism, substrate defect filtration during ELO procedure and strain in ELO layers will be addressed. Recent literature data on MOVPE ELO growth of GaN on sapphire and our results on lateral overgrowth of GaAs on GaAs and Si substrates by LPE are used as examples. Finally, other lateral overgrowth techniques (growth of lattice mismatched bridge layers and pendeo-epitaxy) will be presented and compared with the conventional ELO technique. © 2002 Elsevier Science B.V. All rights reserved.

Keywords: Lateral overgrowth; Lattice mismatched epitaxy; Epitaxial lateral overgrowth; Pendeo-epitaxy

1. Introduction

Very often there are no suitable substrates for lattice-matched epitaxy of semiconductor structures. In such case a buffer layer with graded or abrupt composition profile is usually deposited on available substrate to obtain the layer with required value of lattice constant. However, despite sophisticated methods of buffer layer engineering, density of dislocations threading to the surface of the buffer from its interface with a lattice mismatched substrate is often too high for device applications. Therefore, the lateral growth techniques have been developed to avoid propagation to the epilayer of dislocations present in the buffer layer. Epitaxial lateral overgrowth (ELO) is a method of epitaxial growth on a partially masked substrate [1]. Prior to the ELO procedure a suitable relaxed buffer layer is grown on the substrate. Then, the structure is covered by a thin masking film and patterned by conventional photolithography to form on its whole area a grating of mask-free seeding windows (Fig. 1a). Finally, an epitaxial layer is deposited on such substrate. The epilayer nucleates selectively on the seeds and the growth proceeds in the direction normal to the substrate. As soon as the crystallisation front exceeds the top surface of the mask, the growth in lateral direction over the masking film starts (Fig. 1b). The adjacent ELO stripes coalesce to form a continuous epilayer if enough growth time is given. The main advantage of this approach is that the buffer dislocations are blocked by the masking film and can propagate to the ELO layer through a narrow window in the mask, only. Therefore, the laterally grown parts of ELO layers ('wings') should be nearly defect-free despite a high density of threading dislocations (marked as TD in Fig. 1) in the underlying structure. As will be presented below, there are many experimental data showing high efficiency of defect filtration in epitaxial laterally overgrown semiconductor structures. Thus, the ELO method, when combined with well elaborated techniques of buffer layers engineering, is a promising tool to grow high quality epilayers on available lattice mismatched substrates. Then, required value of lattice constant is obtained by controlling composition of the buffer, while dislocations introduced during relaxation of its lattice mismatch with the substrate are filtered during subsequent homoepitaxial lateral overgrowth. In this way new semiconductor substrates with lattice constant different from that of available bulk III–V crystals can be generated allowing for epitaxy of a new class of high quality semiconductor structures required by modern opto- and microelectronics. The recent breakthrough in development of long lifetime GaN/InGaN blue lasers, being due to the high efficiency of defects filtration during lateral growth, is the most

---

E-mail address: zytkie@ifpan.edu.pl (Z.R. Zytkiewicz).

0040-6090/02/$ - see front matter © 2002 Elsevier Science B.V. All rights reserved.
PII: S0040-6090(02)00315-2

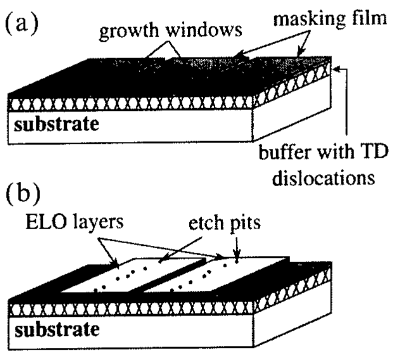

Fig. 1. Principle of ELO procedure: (a) growth of relaxed buffer layer followed by deposition of an amorphous masking film, photolithography and etching of mask-free seeds ('growth windows'); (b) growth of ELO layers starts selectively from the seeds. Then, the ELO layers spread laterally over the masking film. TD are the dislocations threading to the surface of the buffer. The respective etch pits are visible on ELO surface over the seeds, only.

spectacular recent achievement of the ELO technique [2].

Two main fields of interest can be easily distinguished in the published reports on ELO research. These are lateral overgrowth of GaN epilayers on sapphire or SiC substrates and ELO of 'traditional' III–V compounds (e.g. GaAs or InP) on silicon substrates. This choice apparently results from the market demand for novel, low cost semiconductor devices. Therefore, vapour phase growth of ELO GaN and liquid phase epitaxial lateral overgrowth of GaAs will be used as examples in this review to illustrate the basic phenomena that take place in ELO structures. It will be shown that some general rules for growing of thin and wide layers, efficient filtration of defects threading from underlying buffer and impact of this process on structural and optical quality of overgrown material, interaction of ELO layers with the mask leading to downward wings tilt and the ways this tilt can be reduced, relaxation of thermal stress via wing tilting—all these phenomena are similar in both cases despite fundamental differences between the growth techniques used and different properties of materials grown. This clearly means that they are not specific attributes of a particular ELO case but must originate directly from the principle of the ELO technique. Presentation of such general features of epitaxial lateral overgrowth is the aim of this article. In the following sections the issues of ELO growth mechanism, substrate defects filtration during ELO procedure and strain in ELO layers will be addressed. Finally, some other techniques of lateral overgrowth will be presented and compared with the conventional ELO technique.

2. Mechanism of growth of ELO layers

Efficient ELO procedure requires large growth rate anisotropy, i.e. the growth conditions are necessary at which lateral growth of the layer is much faster than that in the direction normal to the substrate. To benefit from a natural growth anisotropy of various crystal faces the ELO process should proceed at low supersaturation [3]. Therefore, equilibrium growth techniques as liquid phase epitaxy (LPE) or vapour phase epitaxy (VPE) should be chosen, if possible, for lateral overgrowth. Indeed, the ELO layers with the value of the aspect (wing width/thickness) ratio as large as 70 are actually grown from a liquid phase. Solution or melt growth of group III nitrides is extremely complicated due to low solubility of nitrogen in liquid metals. Therefore, metalorganic VPE (MOVPE) or hydride VPE (HVPE) are commonly used nowadays to grow ELO structures of these compounds. However, large supersaturation at the growing face makes control of growth anisotropy difficult, so lateral structures of GaN with an aspect ratio up to 4 are obtained by MOVPE, only. Molecular beam epitaxy (MBE) growth of ELO layers is even more complicated as deposition of polycrystalline material on the mask is hard to avoid [4,5]. Sophisticated systems with molecular beams oriented at low angle to the substrate, low growth rate and precise temperature control [6] or special substrate preparation and growth procedures [7] are necessary to get growth started selectively from the seed. There is no significant gas phase diffusion during MBE growth, so lateral overgrowth must rely on the surface mobility of adatoms, only. Therefore, even if growth selectivity is obtained, the MBE grown ELO layers are usually very narrow which makes their application in devices production difficult.

Much is known already about the mechanisms active during growth of ELO layers (see Nishinaga [3] and Zytkiewicz [8] for a review). It has been shown that shape of cross-section and the aspect ratio of the layers can be efficiently controlled by choice of seeds orientation. The basic idea is to find such orientation of the seeding lines for which the side walls of the ELO layer are covered by fast-growing planes, while the slowly grown facet is formed on the upper surface. Then, the requirement of large ratio of lateral to vertical growth rates can be fulfilled [3]. For GaN on sapphire ELOs the seeding windows are usually aligned along the ⟨11−20⟩ or the ⟨1−100⟩ directions of GaN [9]. For LPE growth of ELO layers on (100) GaAs or InP substrates seeding lines with directions slightly rotated relative to the ⟨110⟩ are commonly used [3]. Steps on the surface supplied by substrate miscut or dislocations enhance the vertical growth of ELO [8,10]. Therefore, additional restriction for seeds direction appears on off-oriented substrates. Then, from the optimal seed directions the one must be chosen for which density of misorientation steps inside the seeding area is the smallest [10]. For the same reason dislocation density in the buffer must be as low as possible to obtain ELO layers with a large

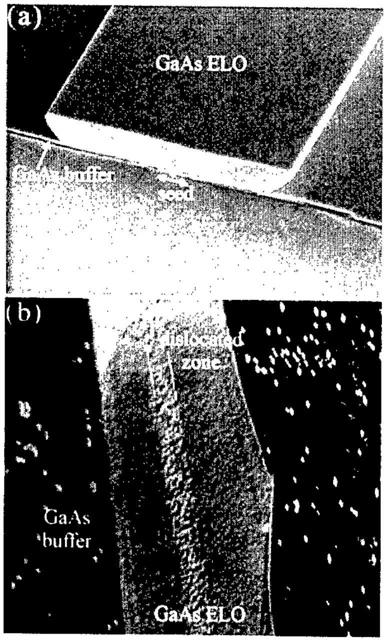

Fig. 2. Scanning electron microscopy image of LPE grown GaAs on Si ELO structure (a) and its plane view after etching in KOH to reveal etch pits distribution (b).

value of the aspect ratio. Doping has been found as an useful way by which the vertical growth rate can be reduced, leading to thin and wide ELO layers. Indeed, we have reported a significant increase of the width/thickness ratio for heavily Si doped GaAs ELO layers grown by LPE [11]. The effect has been explained as being due to impurity induced retardation of surface steps flow on the upper surface of ELO. A similar phenomenon has also been found for Mg-doped GaN ELO layers grown by MOVPE [12].

3. Filtration of substrate defects in ELO structures

Fig. 2a shows a scanning electron microscopy (SEM) image of a cross-section of a GaAs ELO layer deposited on silicon substrate. The structure consists of Si(100) substrate with MBE grown 2-μm-thick GaAs buffer on which the SiO_2 masking film has been sputtered. The GaAs ELO layer was grown by LPE. Its width and thickness are 85 μm and 11 μm, respectively. Other growth details can be found elsewhere [13]. Fig. 2b shows the plane view of the same layer after revealing of etch pits by etching in molten KOH. It is noteworthy that the density of etch pits on the buffer surface is very high ($\sim 10^8$ cm^{-2}). On the contrary, in the ELO layer only the dislocations threading from the buffer are observed. As shown in Fig. 2b, these dislocations are confined in a very narrow area above the seed. The rest of the ELO layer is nearly dislocation free, which has been additionally proved by studies of the layers with the use of synchrotron X-ray topography technique [14]. This finding shows that the mechanism of substrate defects filtration active during ELO procedure is very efficient. Similar phenomenon is commonly observed in all laterally overgrown semiconductor structures [3,15–17].

The question arises if all the dislocations originally present in the seeding area do reach surface of ELO layer. Studies of GaN ELO structures by transmission electron microscopy have shown that a large part of dislocations threading from the buffer through opening in the mask change their direction inside the ELO material, so they propagate parallel to the substrate [18]. This change of the propagation direction prevents the dislocations from crossing the film. Consequently, only a part of dislocations from the buffer reach surface of ELO layer. This phenomenon, together with blocking of dislocations by the mask, results in much lower dislocation density in ELO structures as compared with that in planar buffer layers. The mechanism of bending of TD dislocations in ELO layers is not fully understood yet, although there are suggestions that the bending may be closely related to the change of the growth front and appearance of crystal facets at the very beginning of lateral overgrowth [19]. Probably, stress present during growth of the layers may play its role as well. Some of dislocations threading from the buffer propagate through the ELO without any change of their direction, so they create a defected zone on the surface above the seed as that visible on Fig. 2b. In GaN those dislocations are aligned parallel to the *c*-axis (i.e. perpendicular to the surface), so width of the defected zone does not change significantly with the layer thickness. In many cases, however (e.g. the case of GaAs on Si), TD dislocations are of 60° type. Then, the defected zone width is proportional to the layer thickness and, hence, the lateral growth rate must be increased at expense of vertical growth to obtain a large dislocation-free area of the layer [20].

High crystallographic quality of ELO wings results in their better optical properties than those of planar buffers. As example, Fig. 3 shows a plane view of the GaAs on Si ELO structure similar to that from Fig. 2a, in panchromatic mode of cathodoluminescence (CL).

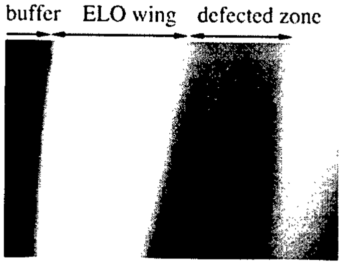

Fig. 3. Cathodoluminescence image of LPE grown GaAs on Si ELO structure from Fig. 2.

Higher CL intensity from the wing as compared to that coming out from the material grown vertically above the seed, and even much higher than that coming out from the buffer, is clearly visible. This is what should be expected, as dislocations are known to behave like centres of effective non-radiative recombination of excited carriers. Similar distribution of cathodoluminescence intensity has also been observed across surface of GaN on sapphire ELO structures [21].

An advantage of using ELO layers for epitaxial device structures was first demonstrated by Nakamura et al., who reported in 1997 a multiquantum well InGaN/GaN laser diode having a life-time longer than 1000 h when deposited on GaN/sapphire ELO substrate [22]. Since then the life-time of these diodes has been significantly increased, so they are commercially available at present. For a comparison, the same InGaN/GaN diodes made on conventional sapphire substrates had worked for 300 h, only [23]. This remarkable improvement was due to significant reduction of the threshold current density of the laser diodes fabricated on low dislocation density ELO substrates. Kozodoy et al. have shown directly that the use of lateral overgrowth to eliminate dislocations leads to better electrical properties of GaN p–n junctions [24]. Reverse-bias leakage current was reduced by three orders of magnitude for the diodes located on low-dislocation density ELO wings. Moreover, large reduction of dark current and sharper cut-off have been found for AlGaN solar-blind detectors fabricated on ELO substrates [25]. The examples presented above are the best evidence that application of ELO technology leads to significant progress in development of high performance semiconductor devices made of lattice mismatched epitaxial structures.

4. Strain in ELO structures

ELO layers are of much higher quality than the reference planar structures but they are not free of strain. In particular, there is a question about strain induced by the mask itself and/or its possible interaction with the overgrown layer. Moreover, the lattice mismatch and thermal strain induced by different thermal expansion coefficients of subsequent layers and the substrate may result in large deformations of the layers. Although in real heteroepitaxial ELO structures all these phenomena are present together, for clarity of presentation in the next section problem of interaction of ELO layers with the mask underneath will be discussed first. Then, the issue of thermal strain in ELO structures will be addressed.

X-Ray diffraction and topography techniques are commonly employed when studying strain in laterally overgrown structures. Fig. 4 shows the typical geometry used for measurements of X-ray rocking curves of ELO layers. First, the rocking curve is measured for the sample position in which the scattering plane (defined by incident and diffracted wave vectors) is perpendicular to the seeding line direction. This corresponds to the axis of sample rotation during the ω scan being parallel to the seeds ($\varphi=0$). Next, the sample is rotated around the substrate normal and the rocking curve is measured again for the scattering plane parallel to the seeds (i.e. for $\varphi=90°$). As will be shown later, this procedure allows to determine the most characteristic features of the strain field in the samples.

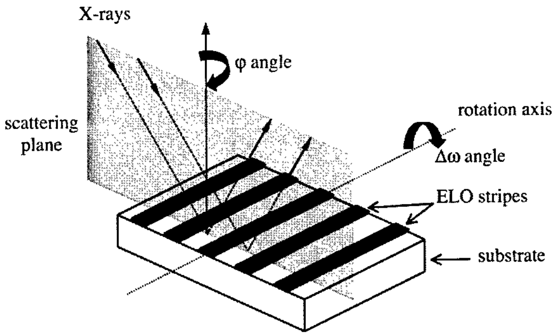

Fig. 4. Schematic of geometry used for measurements of X-ray rocking curves of ELO samples. The scattering plane is defined by incident and diffracted wave vectors. φ is the angle between direction of the seeds and the sample rotation axis during the ω scan; $\varphi=0°$ for the geometry shown.

4.1. Mask induced strain in ELO layers

Fig. 5 shows X-ray rocking curves of GaAs layer grown by LPE on SiO_2 masked GaAs substrate (see the source article for growth details) [26]. Both, the as-grown sample and that cut from the same wafer and etched to remove selectively the SiO_2 mask have been studied. The rocking curves presented in Fig. 5a,b have been measured with the $\varphi=0°$ and $\varphi=90°$ sample orientation, respectively. As it can be seen from Fig. 5a the rocking curve of the as-grown sample is very broad. However, it becomes much narrower after the SiO_2 mask has been removed. On the contrary, for $\varphi=90°$ the rocking curve is quite narrow and etching causes only a slight change of its shape (Fig. 5b). It is worth mentioning that during rocking curve measurements the X-ray diffraction is sensitive mainly to the distortion of the (100) crystal planes in the scattering plane. Therefore, the large width of the rocking curve shown in Fig. 5a indicates that a significant deformation of the as-grown ELO takes place in the cross-section plane perpendicular to the seeds. In principle, similar broadening of the rocking curve could also be caused by lattice mismatch and/or composition gradients inside the structure. However, an analysis of reciprocal space maps collected during diffraction experiments of the same sample has ruled out such possibilities in our case [27].

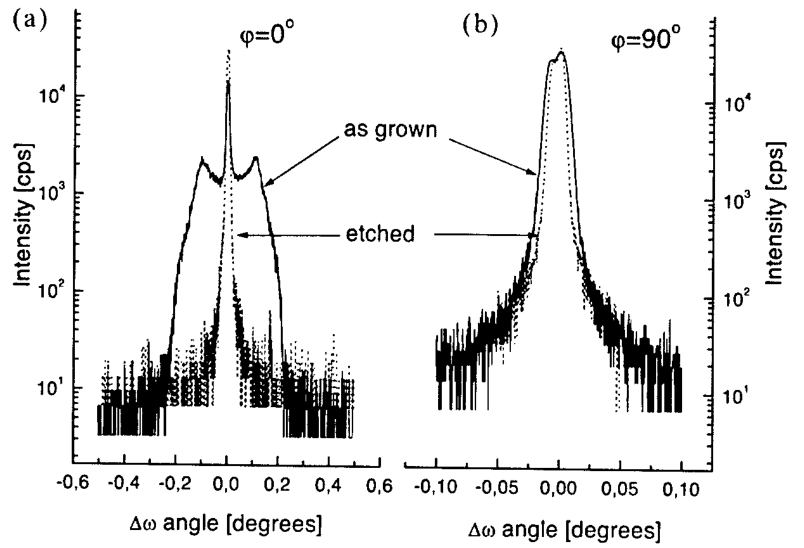

Fig. 5. Rocking curves of (400) CuKα_1 reflection from the as-grown (solid line) and etched (dotted line) GaAs ELO layers on the SiO$_2$-covered GaAs substrate measured with the ω axis parallel (a) and perpendicular (b) to the seeding lines.

We have postulated the following picture of strain in GaAs ELO layers grown by LPE on GaAs substrates [26]: the layers are under stress due to interaction of ELO wings with the SiO$_2$ mask. This stress is below the plastic flow threshold and accompanied strain, responsible for downward tilt of ELO wings visible in Fig. 6a, disappears when the SiO$_2$ mask is removed by selective etching (Fig. 6b). Let us to point out that from the shape of the rocking curve alone it is impossible to say whether the ELO wings tilt upwards or downwards, so additional experiments are needed to determine unambiguously the tilt direction. In our case, we did a series of diffraction experiments in which a very narrow X-ray beam was precisely moved in small steps across a wide GaAs ELO layer [28]. Thus, measurements of rocking curves from precisely defined regions of the single ELO stripe were possible. By analysing the order in which the side maxima appear while the beam is moved across the stripe we have proved that the wings tilt towards the mask surface. Moreover, the data obtained by scanning X-ray diffraction experiments were used to explain the origin of all the features visible on the rocking curve in Fig. 5a. In particular, we have proved that the side maxima are due to diffraction from the edges of the ELO stripe. Therefore, the misorientation of ELO crystal planes must be the largest there. Consequently, half of the angular separation of the side peaks on the rocking curve can be used as a good measure of the maximum tilt angle $\Delta\Theta_{\max}$ of ELO lattice planes (see Fig. 6a).

We have studied the homoepitaxial GaAs ELO layers by synchrotron X-ray reflection and transmission topography techniques [14,29–31]. The data obtained fully confirm the picture of strain in ELO structures shown in Fig. 6. The topographs together with appropriate numerical simulations have also been used to determine quantitatively how the misorientation of ELO lattice planes varies with position across the ELO stripe [30]. This procedure has led us to the conclusion that misorientation of the ELO lattice planes increases much faster near the centre of the ELO stripe than at the edges. In other words, the curvature radius of (100) lattice planes increases towards the edges of the ELO layer, which is in very good agreement with the measured shape of the ELO surface. Such analysis of ELO lattice planes curvature has allowed us to postulate that bending of the ELO stripes starts at the very beginning of growth when the laterally overgrown parts are thin and flexible. Then, the bent crystal planes might be reproduced during subsequent growth, although still retaining their shape [30]. As will be shown later, this is exactly the behaviour observed experimentally.

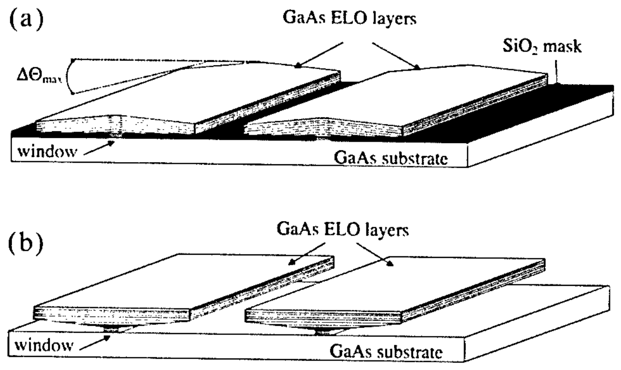

Fig. 6. Schematic drawing of the GaAs on GaAs ELO cross section. The bending is shown in the as-grown state (a). The deformation of crystal planes disappears when the SiO$_2$ mask is removed by etching (b). $\Delta\Theta_{\max}$ is the tilt of (100) crystal planes between the edge and central part of ELO.

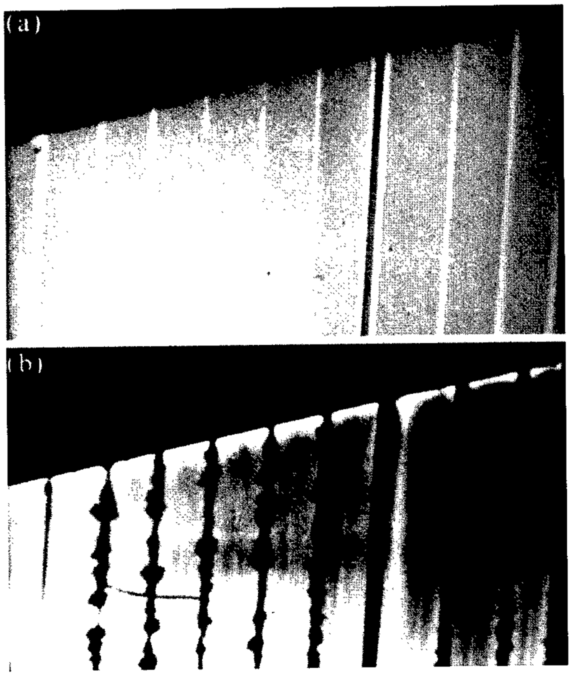

Fig. 7. SEM (a) and CL (b) images of fully overgrown GaAs on GaAs ELO structure. Defects are created at the coalescence fronts where ELO stripes tilted in opposite directions merge.

Very broad X-ray rocking curves similar to that shown in Fig. 5a are very often observed in various ELO systems, which shows that tilting of ELO wings towards the mask is a common problem in laterally overgrown structures. In some cases (e.g. in GaN on sapphire ELO structures) the values of the tilt angle $\Delta\Theta_{max}$ in excess of 2° are reported [32]. So large tilts cannot be accommodated elastically, i.e. by the mechanism we have observed in our GaAs/GaAs samples (see Fig. 5a and Fig. 6). Indeed, cross-sectional transmission electron microscopy studies of GaN on sapphire ELO structures have revealed characteristic defects in the overgrown region, which consisted of arrays of dislocations running along the seed direction [33]. These defects, originating from the bent TD dislocations propagating laterally in the ELO layer, create low-angle tilt boundaries above the edges of the SiO_2 mask.

Tilting of wings caused by their interaction with the mask underneath creates significant problems for coalescence of neighbouring stripes as they tilt in opposite directions (see Fig. 6a). For example, Fig. 7a,b shows, respectively, SEM and CL images of surface of fully overgrown GaAs ELO layer deposited by LPE on SiO_2 masked GaAs substrate. Creation of new defects at the front of coalescence of tilted wings is visible. Similar behaviour has been also observed for GaN on sapphire fully overgrown ELO structures [33]. The image presented in Fig. 7b clearly shows how serious degradation of ELO quality can be caused by tilting of laterally overgrown parts of the layers. Therefore, there is a widespread discussion in the literature on the origin of tilting of the ELO wings and on the way it can be reduced by controlling the growth parameters.

Fini with co-workers were the first who used X-ray diffraction to observe the time evolution of lattice planes bending in GaN on sapphire ELO layers [34]. The scans in reciprocal space through the (10−13) diffraction peak of GaN obtained in situ, during growth of the structures by MOVPE are shown for various growth times in Fig. 8a. Prior to epitaxy the central peak being due to the diffraction from the GaN buffer is visible, only. Emergence of the side maximum is evident for the growth times ~100 s, and by ~300 s, distinct side peaks have evolved indicating the wings tilt ~0.9°. Post growth SEM studies of layer cross-sections have shown that a significant lateral overgrowth started just at that moment. The wing peak narrows during subsequent

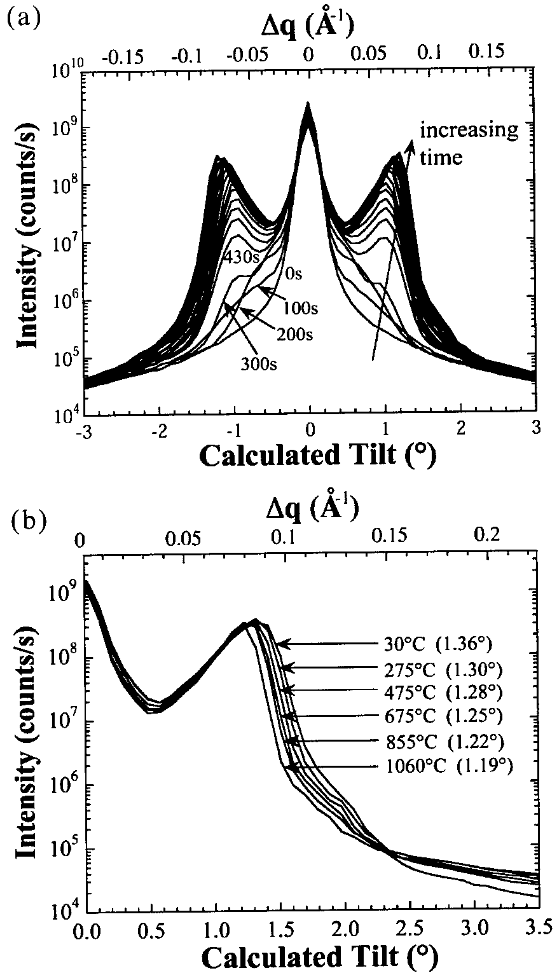

Fig. 8. Scans in reciprocal space through the (10-13) X-ray diffraction peak obtained for various growth times during MOVPE growth of GaN on sapphire ELO structures (a) and on cooling to room temperature (b). The scans in (b) are shown over half of the range measured (from Fini et al. [34]).

growth while its position slightly changes, reaching a tilt of ~1.19° after 3600 s of growth. The data collected during this elegant experiment are direct evidence that wing tilt must be due to interaction of the wing with the mask and that it starts at the very beginning of lateral overgrowth, in agreement with our earlier suggestion [30].

Keeping this in mind, the following recipe for the reduction of the mask-induced bowing of ELO layers can be proposed: the initial vertical growth rate of ELO must be increased to start the lateral overgrowth at some microscopic distance from the upper surface of the mask [28]. Then, the chance of ELO wings capture by attractive force and their interaction with the mask should be reduced. We have found several examples that this recipe efficiently works in practice. In particular, we have shown that the GaAs ELO layers grown on SiO_2 coated substrates are strain-free if their wings hang over without any contact with the underlying mask [35]. In the other cases, tilting of the wings can be efficiently tailored by controlling the ratio of vertical to lateral growth rates at the beginning of ELO growth. This has been achieved by growing the GaAs ELO layers on SiO_2-coated GaAs substrates with increasing density of dislocations. Then, the ratio of vertical to lateral growth rates at the beginning of the growth was increased due to the higher density of surface steps, which in turn led to reduction of the mask-induced tilt of ELO wings [28,35]. In the limiting case of heavily dislocated GaAs substrates, namely on GaAs-coated Si substrates, the vertical growth of GaAs ELO was so fast that air-bridged structures without any interaction with the mask were obtained [13]. Similarly, Fini et al. have shown that the quality of coalescence of adjacent ELO GaN stripes can be improved by forcing vertical development of ELO stripes at the beginning of the growth, followed by change of growth conditions and fast lateral overgrowth of the structure [36]. This is exactly the same recipe we have proposed.

Replacement of commonly used dielectric films by other mask materials seems to be a promising way of reduction of mask induced wing tilt. In particular, we have found that that bending of the GaAs ELO layers grown by LPE is negligible when the SiO_2 mask is replaced by a thin graphite film [26]. We have explained this finding by delayed start of lateral growth caused by the change of the shape of the melt in the corner between the side wall of the ELO layer and the mask when the SiO_2 is replaced by graphite film not wetted by the gallium melt [35]. Similarly, tungsten has been found as promising mask material for MOVPE growth of GaN ELO structures with very low tilt of the wings [37]. In principle, however, it is difficult to predict a priory the mask material that would be the most suitable for each particular ELO case. Therefore, the most natural way to eliminate the mask induced strain would be to grow the ELO structures with their wings having no direct contact with the mask surface. The GaN air-bridged ELO structures grown by Kidoguch et al. [38] or our GaAs ELO layers with wings hanging over the mask [35] are the best examples that this goal can be achieved. Unfortunately, quite often the growth conditions required for reproducible growth of such structures are difficult to find.

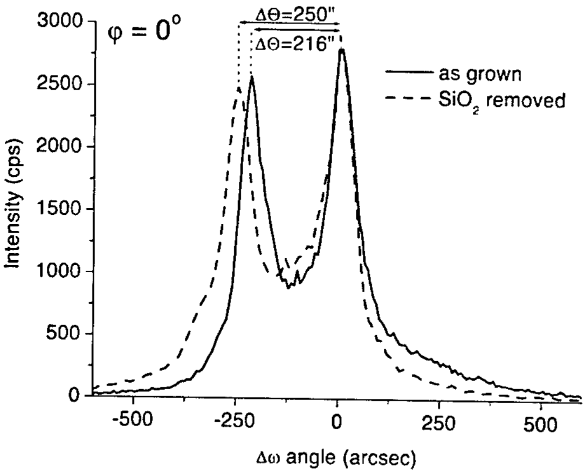

Fig. 9. Rocking curves of (400) CuKα_1 reflection for the as-grown (solid line) and etched (dotted line) GaAs ELO layer on the GaAs-coated Si substrate measured with the ω axis parallel to the seeding lines.

4.2. Thermal strain in ELO structures

Additional deformation of ELO lattice planes may arise when the sample, due to the different thermal expansion coefficients of its components, experiences a large stress upon cooling from the growth to room temperature. This effect is commonly observed in planar heterostructures. As will be shown below, in ELO structures this strain can be relaxed via additional tilting of ELO wings while still preserving their high quality.

Fig. 9 shows the (400) CuKα_1 rocking curve of the GaAs ELO layer on the GaAs-coated Si substrate [13]. The scattering plane was set perpendicular to the seeds in this experiment. As it is seen, the rocking curve consists of two peaks which are separated by $\Delta\Theta = 216$ arcsec. The whole rocking curve is so wide that presence of ELO deformation similar to that observed by us for GaAs ELO layer on GaAs substrate could be suspected. For the GaAs on GaAs ELO system we attributed broadening of the rocking curve to the bending strain induced by ELO stripes adhesion to the SiO_2 mask. Then, the tilt of wings disappeared after the mask had been removed. As seen in Fig. 9, the situation is quite the opposite for the ELO GaAs on Si-the separation of the peaks increases ($\Delta\Theta = 250$ arcsec) after removal of the mask by selective etching. Moreover, analysis of

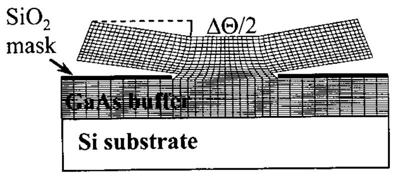

Fig. 10. Schematic drawing of cross-section of the as-grown GaAs ELO layer on Si substrate. The tilt of (100) ELO wings crystal planes equals $\Delta\Theta/2$, where $\Delta\Theta$ is angular separation of diffraction peaks in Fig. 9.

layer cross-sections with the use of an optical microscope has revealed a microscopic gap between the ELO and the masking film. Thus, the mask induced bending of lattice planes cannot explain the data obtained.

We have performed X-ray diffraction experiments with a narrow X-ray beam moved across the single ELO stripe to show that two peaks visible in Fig. 9 are due to the diffraction from the wings [13]. It is noteworthy that the full width at half maximum of each peak equals to 94 arcsec only, which is much smaller than that of the MBE grown GaAs buffer (435 arcsec). This result, together with an analysis of CL intensity (Fig. 3) and etch pits density (Fig. 2b) distributions, confirms very high crystallographic quality of laterally grown GaAs on Si substrates. By using the X-ray diffraction technique with the beam scanned across the ELO layer we have proved also that the wings tilt upward in the GaAs on Si case [13], which is just the opposite behaviour to that observed in the GaAs/GaAs ELO system. All these results have allowed us to create a model of bending of the GaAs ELO layer on Si substrate as illustrated in Fig. 10. A biaxial tensile strain caused by different thermal contraction of epilayer and substrate is commonly observed in GaAs layers on Si substrates [39]. This strain disappears when the GaAs/Si structure is heated to a temperature of ~500 °C [40], which is close to our LPE growth temperature. Therefore, the GaAs ELO layer grows essentially stress free. At room temperature, the basal plane of the ELO should have the same tensile deformation as the upper surface of the buffer GaAs. Since the ELO layer stands free and does not adhere to the mask, unrestricted strain relaxation and free contraction of vertically grown volume of ELO should take place in its upper part. This, in turn, must lead to the upward bending of ELO wings (as shown in Fig. 10). The thermal tensile strain in the seeding area is partially compensated by the mask induced compression [27]. Therefore, deformation of ELO at its base, and consequently the ELO wings tilt angle, increase when the SiO_2 mask is removed. This leads to increase of angular separation of X-ray reflections as shown in Fig. 9. Let us compare the rocking curves of the GaAs ELO layers grown on GaAs and GaAs-coated Si substrates shown in Fig. 5a and Fig. 9, respectively. The rocking curve from Fig. 5a is very broad which indicates some distribution of strain along the interface between the wing and the mask. On the contrary, in the GaAs on Si structure strain is localised in the seeding area only and the main part of the wings is strain free, so the wing peaks are very sharp. In this way, the different shapes of the rocking curves directly reflect different mechanisms responsible for deformation of ELO lattice planes in both cases.

It is worth noting that our model of thermal strain relaxation in ELO layers predicts that the direction of wing tilt must be correlated with the sign of the strain in the buffer. In particular, downward wings tilt should be observed if the buffer layer is under compressive thermal stress (e.g. in GaN on SiC or sapphire substrates). This is exactly the behaviour presented in Fig. 8b for the GaN on sapphire ELO system. At the growth temperature GaN ELO wings are tilted downward due to their interaction with the mask. Upon cooldown to room temperature position of the wing peak changes from 1.19° to 1.36°, which means that additional downward tilt induced by thermal stress has occurred. Qualitatively, the same phenomenon can be inferred from recent simulations via finite element analysis of strain in ELO structures [41].

5. Related techniques of lateral overgrowth

The most characteristic feature of the ELO process presented so far is the change of the predominant growth direction—from vertical in the growth window to lateral in the regions over the masking film. In principle, however, it is possible to start lateral overgrowth from the seeds oriented perpendicular to the substrate surface, so change of the growth direction is not necessary. If the substrate (bare substrate or substrate covered by a suitable buffer layer) is etched to create on its surface a pattern of ridges or elongated columns oriented similar to that of windows in ELO, conditions are provided such that the side walls of the columns provide the crystallographic template for lateral growth. Fig. 11a shows geometry of silicon substrate used for LPE lateral overgrowth of Si from ridge seeds [42,43]. A thin SiO_2 mask has been deposited in the trenches to avoid direct epitaxy on the substrate. During LPE the growth starts from the side walls of the ridges and proceeds laterally over the mask. The top surface of the ridge is the dislocation-free Si(111) facet, so it contains no step sources. Therefore, under proper growth conditions the vertical growth is completely eliminated and the layer grows laterally without any change of its thickness. As the thickness of the layer is determined by the ridge height, it can be easily controlled. However, very thin layers are difficult to obtain. When the thickness of the layer decreases the radius of curvature of its side wall decreases as well (see Fig. 11a). This leads to increase

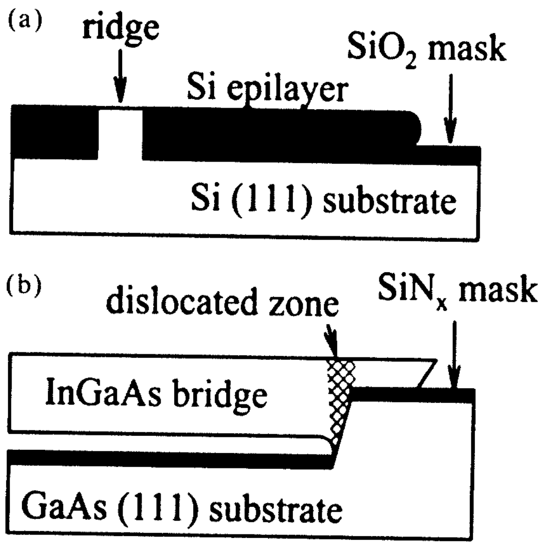

Fig. 11. Schematic illustration of cross sections of Si epilayer grown by LPE on (111) Si substrate from a ridge seed (a) and of InGaAs bridge layer grown by LPE on GaAs substrate (b).

of the equilibrium concentration of the solute around this wall due to the Gibbs–Thomson effect. Therefore, higher melt supersaturation must be used to grow thinner layers. Then, however, vertical growth may be initiated if the supersaturation is large enough for two-dimensional nucleation at the top surface of the ridge. Using this technique as thin as 0.23 μm Si layers with an aspect ratio up to 82 have been grown laterally upon SiO_2-coated Si substrates by LPE [42].

On the contrary to the case of homoepitaxy, in lattice mismatched heterostructures the top surface of the columns is not dislocation-free and must be covered by an additional mask to avoid excessive vertical growth. Fig. 11b shows schematically how this approach has been applied by Iida et al. to grow by LPE InGaAs bridge layers on GaAs substrates [44]. First, the substrate covered by the SiN_x mask has been processed by photolithography and etching to fabricate on its surface a pattern of deep circular trenches. Then, $In_xGa_{1-x}As$ ($x \sim 0.06$) layer has been grown on such substrate by LPE. It is noticing worthy that no InGaAs buffer is used in this case. The layer grew inwards from the side wall of the trench forming a bridge over the trench. Some growth over the mask outside the trench area was observed as well. Analysis of the layer surface revealed presence of dislocated zone with etch pits density $\sim 10^6$ cm^{-2} only above the small area where the layer was in direct contact with the GaAs substrate. The rest of the layer, having the diameter above 1 mm, was of very high quality with dislocation density below 10^4 cm^{-2}, so it could be used as substrate for further deposition of device layers. Unfortunately, the technology presented has been tested only for very low In concentrations (and for very high In content when InAs instead of GaAs was used as the substrate [45]). Thus, more research is needed to study how this procedure would work for the heteroepitaxial structures with large lattice mismatch. Moreover, the question about quality of coalescence of the layers grown from the opposite walls of the trench seems still to be open. Despite that, the technology of LPE growth of bridge layers over the trenches seems to be very promising due to its simplicity, very high efficiency and high quality of layers produced.

Finally, let us present the method of lateral overgrowth that has received much attention recently, namely the pendeo- (from the Latin: to *hang* or to be *suspended*) epitaxy (PE). To grow PE GaN layers, a thin AlN wetting layer and GaN buffer are grown first on an available substrate as shown in Fig. 12a. Next, trenches deep enough to reach the substrate surface (or even slightly deeper) are etched in the structure. The bottoms of trenches and top surfaces of GaN columns are then

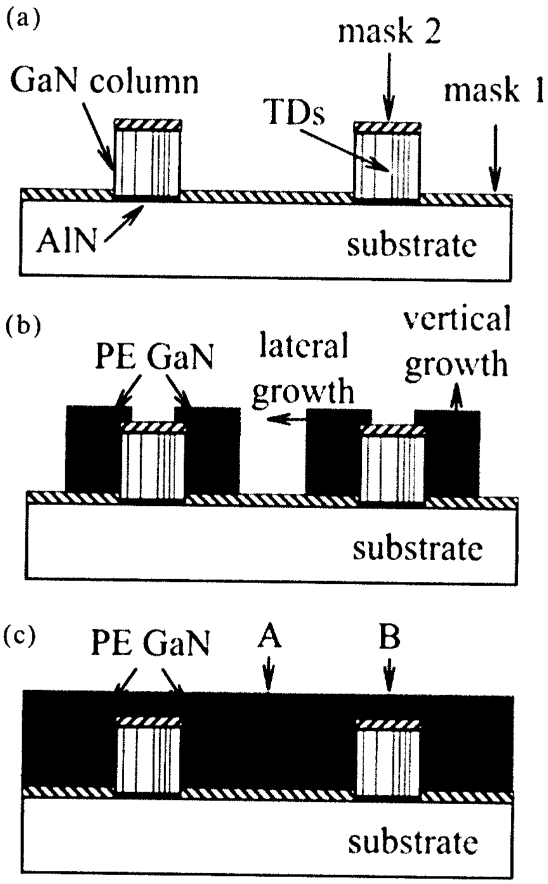

Fig. 12. Schematic of the process steps for pendeo-epitaxy of GaN: (a) etching of elongated columns in GaN buffer layer followed by masking of the substrate (mask 1) and the top column surfaces (mask 2); (b) epitaxial growth of GaN starts from exposed side walls of GaN columns and proceeds laterally to fill the trenches; also some vertical growth occurs; (c) PE layers merge over the trenches (seam A) and over the capped GaN columns (seam B), so continuous PE GaN film is formed. TDs are the dislocations threading to the surface of the GaN column.

covered by a suitable masking film, so GaN column side walls are the only surfaces exposed for subsequent GaN regrowth. During pendeo-epitaxy the GaN layers overflow the trenches growing laterally from the column side walls (see Fig. 12b). Also some vertical growth takes place followed by lateral growth over the mask covering the top of GaN mesas. If long enough growth time is given the PE layers starting from adjacent seeds merge at the fronts marked 'A' and 'B' in Fig. 12c, so a continuous PE GaN layer is formed. As mentioned before, dislocations thread in the GaN buffer mainly along the *c*-axis (i.e. perpendicular to the surface). Thus, only a very small part of them intersect the side wall of GaN columns and propagate into PE GaN layer. Therefore, the regrown material contains four to five orders of magnitude lower density of dislocations than that in the buffer [46]. Moreover, in contrary to the ELO case, also the dislocations originally present in the buffer (marked as TDs in Fig. 12) are prevented from reaching the PE layer if the GaN columns are capped by the mask. Thus, in principle, the density of dislocations should be reduced over the whole area of the substrate and the need to locate devices only in the laterally overgrown parts of the structures (as it was in the case of ELO-see Section 3) could be eliminated.

The PE technique in its version shown in Fig. 12 has been used by Chen et al. to grow by MOVPE GaN layers on SiO_2 masked sapphire substrates [47]. Studies of the layers with the use of transmission electron microscopy have proved that laterally overgrown parts of the layers are nearly dislocation-free. However, new dislocations have been found at the fronts (marked as 'A' and 'B' in Fig. 12) where the layers merge as well as over the edges of masked GaN columns. In the light of what has been written in Section 4.1 above, this finding is not surprising. Most probably, interaction of the laterally overgrown parts of the layers with the SiO_2 mask has occurred leading to their relative misorientation and defects creation at the coalescence fronts. Thus, this is the same phenomenon as we have discussed already and which is illustrated in Fig. 7.

These results, as well as the whole discussion in Section 4 of this review, clearly show that properties of laterally overgrown layers are strongly influenced by the presence of a mask. In particular, the strain introduced by the mask and 'poisoning' by impurities diffusing out from the mask at high temperature have negative impact on quality of the layers. Therefore, the processes are needed in which layers could be grown laterally without any masking film. It is important to note that each mask requires additional technological steps. Thus, a maskless version of selective epitaxy would result in significant simplification of the whole procedure, which is especially important if the growth process under development is to be applied on industrial scale. Zheleva et al. have found that under proper MOVPE conditions neither GaN nor free Ga do accumulate on 6H-SiC (0001) surface [46]. Thus, the pendeo-epitaxy of GaN without mask between the GaN columns (mask 1 in Fig. 12) became possible by replacement of sapphire by SiC. As before, PE growth started from the side walls of the GaN columns and proceeded laterally at some distance from the SiC surface. Transmission electron microscopy showed that neither tilting nor low angle tilt boundary were present at the coalescence boundary over the trench (seam 'A' in Fig. 12c). However, tilting of 0.2° and defects at the seam 'B' were still found in the portion of the coalesced GaN layer, which interacted with the mask covering the GaN column [48]. This tilt can be further eliminated if completely mask-free PE process (i.e. without masks 1 and 2) is employed as has been reported for GaN [46] and AlGaN [49] on SiC systems. Then, defect-free coalescence can be obtained at both coalescence fronts [46]. The price paid for that, however, is enhanced vertical growth of the PE layer and free propagation into regrown GaN of TD dislocations originally present in the GaN buffer.

The next step towards commercialisation of pendeo-epitaxy of GaN would be to replace SiC substrates, which are expensive and available with low diameters, by large area silicon wafers. However, direct epitaxy of GaN on Si is difficult and usually results in polycrystalline films, most likely due to the prior formation of the SiN_x film on the Si surface. Therefore, Davis et al. have employed the procedure in which Si(111) substrates are first covered by an epitaxial film of SiC, followed by their transfer to the MOVPE system for deposition of an AlN wetting layer and a GaN buffer [48]. Next, they could make use of the process route elaborated earlier for PE of GaN on bulk SiC, namely, substrate etching to define GaN columns and PE regrowth. The quality of the GaN layers they obtained was quite similar to that on bulk SiC substrates. The problem, however, was the thermal stress arising due to large difference of thermal expansion coefficients between subsequent layers, which resulted in cracking of the structures on cooling if the SiC transition layer was too thin.

6. Summary

Review of the epitaxial lateral overgrowth technology and of application of ELO layers as substrates with an adjustable value of lattice constant is provided. The main idea behind lateral overgrowth techniques is selective epitaxy of a homoepitaxial layer on a relaxed buffer having the required value of lattice parameter. The seeds can be defined by patterning of the mask covering the buffer layer (ELO) or the growth starts from the exposed side walls of ridges etched in the buffer (PE). Selective nucleation of the layer in the narrow seeds allows to pass through information on buffer lattice spacing, while blocking all (or main part of) defects created due to lattice misfit between the buffer and its substrate. We have shown numerous examples that this procedure works efficiently. Usually, practical realisation of the idea above depends on the system considered. Quite often specific properties of materials and of growth technique used determine the way in which laterally overgrown structures are produced (eg. the maskless pendeo-epitaxy of GaN on SiC). There are, however, some basic phenomena typical for all laterally overgrown structures. These include some general rules that should be followed to obtain wide and thin laterally overgrown layers (i.e. choice of optimal direction of the seeds, high quality of the buffer, low growth rate, use of doping to enhance lateral growth, etc.). Efficient filtration of dislocations originally present in the buffer is well evidenced in all laterally overgrown structures. Tilt of wings caused by their interaction with the mask underneath is commonly observed both in ELO and PE layers independently on the growth technique used. If the tilt angle is small the accompanied strain can be accommodated elastically (eg. in GaAs on GaAs ELOs). Otherwise, arrays of dislocations creating low angle boundaries appear above the mask edges (eg. the case of GaN ELO structures). Tilting of laterally grown parts of the layer leads to generation of new defects at the coalescence front where two layers grown from neighbouring seeds and having opposite tilt directions merge. Growing the layers standing free above the mask seems to be the best way to improve quality of the coalescence front, although there are no general recipes how to grow such structures. Thermal strain being due to different expansion coefficients of subsequent layers is also commonly found in laterally overgrown heterostructures. However, if the layer is attached to the buffer through the narrow seeds only, this strain is usually much smaller than in reference planar structures.

It is difficult to predict how the lateral overgrowth technology will develop in the future. From scientific point of view there are still many questions to be answered. In particular, understanding of microscopic interaction of ELO wings with the mask, identification of mechanisms leading to bending of dislocations threading through the seed in ELO and many other issues require further work. Basic crystal growth research is needed to increase width of laterally overgrown layers, to improve the quality of coalescence fronts, to develop technology of lateral overgrowth of ternary layers on binary substrates and to simplify the whole growth procedure according to industrial standards. Application of laterally overgrown layers will depend on progress of these studies. Growth technology must be significantly simplified for wide application of laterally overgrown substrates. Market demands for novel semiconductor devices will decide if and which techniques of lateral epitaxy find their permanent position in industrial practice. Nowadays there is a large demand for group III nitrides substrates, so lateral overgrowth of these compounds is mostly studied in many laboratories worldwide. Probably, the importance of lateral overgrowth of 'traditional' III–V ternary substrates will increase in the near future.

Acknowledgments

The author thanks D. Dobosz for her assistance in the LPE growth of the GaAs ELO structures and J. Domagala and M. Godlewski for XRD and CL, respectively, analysis of the GaAs ELO samples. Contributions of T. Tuomi, R. Rantamaki, P.J. McNally, and D. Danilewsky to synchrotron X-ray topography experiments are highly appreciated. Moreover, permission for the use of the data shown in Fig. 8 granted by P. Fini from the University of California in Santa Barbara is highly appreciated. This work is partly supported by the Polish Committee for Scientific Research under the grant No. 7T08A 007 20.

References

[1] L. Jastrzebski, J.F. Corboy, R. Soydan, J. Electrochem. Soc. 136 (1989) 3506, and references therein.
[2] S. Nakamura, M. Senoh, S. Nagahama, N. Iwasa, T. Yamada, T. Matsushita, H. Kiyoku, Y. Sugimoto, T. Kozaki, H. Umemoto, M. Sano, K. Chocho, Jpn. J. Appl. Phys. 36 (1997) L1568.
[3] T. Nishinaga, Cryst. Prop. Prep. 31 (1991) 92.
[4] R.J. Matyi, H. Shichijo, T.M. Moore, H.-L. Tsai, Appl. Phys. Lett. 51 (1987) 18.
[5] J.T. Torvik, J.I. Pankove, E. Iliopoulos, H.M. Ng, T.D. Moustakas, Appl. Phys. Lett. 72 (1998) 244.
[6] G. Bacchin, T. Nishinaga, J. Cryst. Growth 208 (2000) 1.
[7] H. Tang, J.A. Bardwell, J.B. Webb, S. Moisa, J. Fraser, S. Rolfe, Appl. Phys. Lett. 79 (2001) 2764.
[8] Z.R. Zytkiewicz, Cryst. Res. Technol. 34 (1999) 573.
[9] K. Hiramatsu, A. Usui, in: J.H. Edgar, S. Strite, I. Akasaki, C. Wentzel (Eds.), GaN and Related Semiconductors, EMS Datareview Series No. 23 INSPEC, IEE, London, 1999, p. 440.
[10] S. Sakawa, T. Nishinaga, J. Cryst. Growth 115 (1991) 145.
[11] Z.R. Zytkiewicz, D. Dobosz, M. Pawlowska, Semicond. Sci. Technol. 14 (1999) 465.
[12] B. Beaumont, S. Haffouz, P. Gibart, Appl. Phys. Lett. 72 (1998) 921.
[13] Z.R. Zytkiewicz, J. Domagala, Appl. Phys. Lett. 75 (1999) 2749.
[14] R. Rantamäki, T. Tuomi, Z.R. Zytkiewicz, D. Dobosz, P.J. McNally, J. Phys. D 32 (1999) A114.
[15] B-Y. Tsaur, R.W. McClelland, J.C.C. Fan, R.P. Gale, J.P. Salerno, B.A. Vojak, C.O. Bozler, Appl. Phys. Lett. 41 (1982) 347.
[16] P.O. Hanson, A. Gustafsson, M. Albrecht, R. Bergmann, H.P. Strunk, E. Bauser, J. Cryst. Growth 121 (1992) 790.
[17] T.S. Zheleva, O-H. Nam, M.D. Bremser, R.F. Davis, Appl. Phys. Lett. 71 (1997) 2472.
[18] T.S. Zheleva, O.-H. Nam, R.F. Davis, in: J.H. Edgar, S. Strite, I. Akasaki, C. Wentzel (Eds.), GaN and Related Semiconductors, EMS Datareview Series No. 23 INSPEC, IEE, London, 1999, p. 447.

[19] A. Sakai, H. Sunagawa, A. Usui, Appl. Phys. Lett. 71 (1997) 2259.

[20] S. Sakawa, T. Nishinaga, Jpn. J. Appl. Phys. 31 (1992) L359.

[21] Z. Yu, M.A.L. Johnson, T. Mcnulty, J.D. Brown, J.W. Cook, J.F. Schetzina, MRS Internet J. Nitride Semicond. Res. 3 (1998) 6,

[22] S. Nakamura, M. Senoh, S. Nagahama, N. Iwasa, T. Yamada, T. Matsushita, H. Kiyoku, Y. Sugimoto, T. Kozaki, H. Umemoto, M. Sano, K. Chocho, Jpn. J. Appl. Phys. 36 (1997) L1568.

[23] S. Nakamura, M. Senoh, S. Nagahama, N. Iwasa, T. Yamada, T. Matsushita, Y. Sugimoto, H. Kiyoku, Jpn. J. Appl. Phys. 36 (1997) L1059.

[24] P. Kozodoy, J.P. Ibbetson, H. Marchand, P.T. Fini, S. Keller, J.S. Speck, S.P. DenBaars, U.K. Mishra, Appl. Phys. Lett. 73 (1998) 975.

[25] G. Parish, S. Keller, P. Kozodoy, J.P. Ibbetson, H. Marchand, P.T. Fini, S.B. Fleischer, S.P. DenBaars, U.K. Mishra, E.J. Tarsa, Appl. Phys. Lett. 75 (1999) 247.

[26] Z.R. Zytkiewicz, J. Domagala, D. Dobosz, J. Bak-Misiuk, J. Appl. Phys. 84 (1998) 6937.

[27] Z.R. Zytkiewicz, J. Domagala, D. Dobosz, J. Bak-Misiuk, J. Appl. Phys. 86 (1999) 1965.

[28] Z.R. Zytkiewicz, J. Domagala, D. Dobosz, Mater. Res. Soc. Symp. Proc. 570 (1999) 273.

[29] R. Rantamäki, T. Tuomi, Z.R. Zytkiewicz, D. Dobosz, P.J. McNally, D. Danilewsky, Mater. Res. Soc. Symp. Proc. 570 (1999) 181.

[30] R. Rantamäki, T. Tuomi, Z.R. Zytkiewicz, J. Domagala, P.J. McNally, D. Danilewsky, J. Appl. Phys. 86 (1999) 4298.

[31] R. Rantamäki, T. Tuomi, Z.R. Zytkiewicz, P.J. McNally, D. Danilewsky, J. X-Ray Sci. Technol. 8 (2000) 277.

[32] P. Fini, H. Marchand, J.P. Ibbetson, S.P. DenBaars, U.K. Mishra, J.S. Speck, J. Cryst. Growth 209 (2000) 581.

[33] A. Sakai, H. Sunakawa, A. Usui, Appl. Phys. Lett. 73 (1998) 481.

[34] P. Fini, A. Munkholm, C. Thompson, G.B. Stephenson, J.A. Eastman, M.V. Ramana Murty, O. Auciello, L. Zhao, S.P. DenBaars, J.S. Speck, Appl. Phys. Lett. 76 (2000) 3893.

[35] Z.R. Zytkiewicz, J. Domagala, D. Dobosz, J. Appl. Phys. 90 (2001) 6140.

[36] P. Fini, L. Zhao, B. Morgan, M. Hansen, H. Marchand, J.P. Ibbetson, S.P. DenBaars, U.K. Mishra, J.S. Speck, Appl. Phys. Lett. 75 (1999) 1706.

[37] H. Miyake, M. Yamaguchi, M. Haino, M. Motogaito, K. Hiramatsu, S. Nambu, Y. Kawaguchi, N. Sawaki, Y. Iyechika, T. Maeda, I. Akasaki, MRS Internet J. Nitride Semicond. Res. 5S1 (2000) W2.3,

[38] I. Kidoguchi, A. Ishibashi, G. Sugahara, Y. Ban, Appl. Phys. Lett. 76 (2000) 3768.

[39] S.F. Fang, K. Adomi, S. Iyer, H. Morkoc, H. Zabel, C. Choi, N. Otsuka, J. Appl. Phys. 68 (1990) R31, and references therein.

[40] N. Lucas, H. Zabel, H. Morkoc, H. Unlu, Appl. Phys. Lett. 52 (1988) 2117.

[41] T.S. Zheleva, W.M. Ashmawi, K.A. Jones, Phys. Stat. Sol. (a) 176 (1999) 545.

[42] Y. Suzuki, T. Nishinaga, Jpn. J. Appl. Phys. 29 (1990) 2685.

[43] I. Silier, A. Gutjahr, N. Magel, P.O. Hansson, E. Czech, M. Konuma, E. Bauser, F. Banhart, R. Kohler, H. Raidt, B. Jenichen, J. Cryst. Growth 166 (1996) 727.

[44] S. Iida, Y. Hayakawa, T. Koyama, M. Kumagawa, J. Cryst. Growth 200 (1999) 368.

[45] K. Balakrishnan, S. Iida, M. Kumagawa, Y. Hayakawa, 13th International Conference on Crystal Growth, Kyoto, 30 July–4 August 2001, 2001.

[46] T.S. Zheleva, S.A. Smith, D.B. Thomson, K.J. Lithicum, P. Rajagopal, R.F. Davis, J. Electron. Mater. 28 (1999) L5.

[47] Y. Chen, R. Schneider, S.Y. Wang, R.S. Kern, C.H. Chen, C.P. Kou, Appl. Phys. Lett. 75 (1999) 2062.

[48] R.F. Davis, T. Gehrke, K.J. Lithicum, E. Preble, P. Rajagopal, C. Ronning, C. Zorman, M. Mehregany, J. Cryst. Growth 225 (2001) 335.

[49] R.F. Davis, T. Gehrke, K.J. Lithicum, T.S. Zheleva, E.A. Preble, P. Rajagopal, C.A. Zorman, M. Mehregany, J. Cryst. Growth 225 (2001) 134.

ELSEVIER

Thin Solid Films 412 (2002) 76–83

www.elsevier.com/locate/tsf

Monitoring epiready semiconductor wafers

D.A. Allwood, S. Cox, N.J. Mason*, R. Palmer, R. Young, P.J. Walker

Physics Department, Clarendon Laboratory, University of Oxford, Parks Road, OX1 3PU Oxford, UK

Abstract

GaAs wafers are often sold by the manufacturers as 'epiready', meaning the substrates can be used with no further treatment. However, there is no clear agreement what epiready means, although one manufacturer recommends that they be used within 3 months of purchase. However, many growers find they are unable to obtain good growth results from their processes with untreated wafers and have to resort to long-established etching procedures. With the increase in multi-wafer molecular beam epitaxy (MBE) and metal organic vapour phase epitaxy (MOVPE) reactors, this approach is no longer viable. This work investigates the ageing of GaAs wafers stored, both under a variety of conditions [e.g. temperatures of 200 °C, room temperature and −20 °C] and assessed by atomic force microscopy (AFM) after various procedures had been performed, including annealing in molecular hydrogen using a MOVPE reactor. The primary source of ageing on an epiready GaAs wafer has been found to be the transfer oxidation from the native As_2O_3 (present at time = 0) to Ga_2O_3 (present after 24 h, 3 months and 2 years, respectively, at the storage temperatures mentioned above). This transfer oxidation does not occur across the whole surface but in discrete areas that may be associated with the step edges on the substrate surface. This is the cause of deterioration of an epiready substrate, but it can be slowed by storing the GaAs wafers at −20 °C. Storage in a domestic freezer has allowed even 2-year-old GaAs wafers to be used without any further preparation. © 2002 Elsevier Science B.V. All rights reserved.

Keywords: Monitoring epiready; Semiconductor; Wafers

1. Introduction

Epitaxial techniques such as MBE and MOVPE rely on the perfection of the surface of the substrate to give a template that allows further growth of high quality semiconductor crystals. Semiconductor substrates are manufactured from boules of material grown from a melt by various processes [1]. The substrates are then sawn from the boule and chemo-mechanically polished. All these stages can introduce defects into the substrate: the thermal strain from growing the boule can result in dislocations in the final substrate [1], cutting can introduce 'saw-damage' into the substrate whilst polishing can leave the final surface non-stoichiometric, e.g. with an excess of one element (usually group III) over the other.

The provision of a perfect, stoichiometric surface used to be the responsibility of the grower who had to prepare the wafer before use [involving degreasing, etching (to remove saw-damage), rinsing and drying]. Now, however, there is a choice and the term 'EpiReady' has been registered as a trademark of Wacker-Chemitronic GmbH [2]. This new approach was made possible by low metal contamination in the polishing and by producing a final surface whose carbon and oxide layers were removable by in situ cleaning in a MOVPE reactor. Now, many other substrate vendors are offering substrates 'epiready' but there is no strict definition of the term. The responsibility for the provision of a perfect surface is now a partnership, the wafer manufacturer supplying an epiready surface and the grower finding conditions where this can be successfully deoxidised and annealed in the equipment before growth [3,4]. With increasing wafer numbers in multi-wafer reactors, this partnership is the only realistic choice for most industrial reactors.

A study of InP substrates [5] and GaAs substrates [3] have both found and an increase of the oxide thickness with time but no data was presented showing how this affected the epireadyness. Although one manufacturer recommends that GaAs wafers are used within 3 months of purchase, there is no information in the literature about what occurs over this period of time to leave the GaAs surface unepiready nor under what storage conditions this degradation occurs.

---

*Corresponding author. Tel.: +44-1865-855167; fax: +44-1865-371090.

E-mail address: nigel.mason@kamelian.com (N.J. Mason).

0040-6090/02/$ - see front matter © 2002 Elsevier Science B.V. All rights reserved.
PII: S0040-6090(02)00316-4

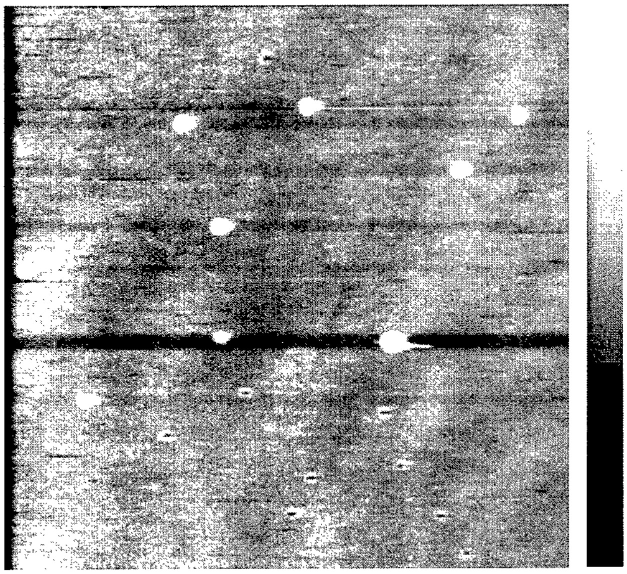

Fig. 1. Atomic force microscope image (6-μm square) of an on-axis GaAs surface after heating to 550 °C, holding and cooling. The grey scale represents 10 nm in height.

We have used a variety of techniques to study the ageing of GaAs wafers; the loss of epireadiness and the provision of best storage conditions and the results are reported here.

2. Experimental

The wafers used in this work were obtained from AXT, Freiberger, and Wafer Technology and were on-axis. We neither observed any measurable difference between any of the manufacturers nor between doped and undoped wafers under the conditions used here. The wafers were stored in a domestic freezer (−20 °C) a domestic fridge (0 °C) normal clean room ambient (20 °C) whilst remaining in their original polyethylene packing and inert gas filled metallised-polyester bag. For elevated-temperature storage (200 °C) the wafers were removed from the packing and placed in a clean, covered Petri dish in a muffle furnace. Care was taken to ensure the door of the furnace remained open for as short a time as possible when adding and removing samples, to ensure a stable temperature regime for the storage trial.

The reactor conditions used have been outlined before [6] but to reiterate briefly a flow of 16 l/min of hydrogen at atmospheric pressure was used in these experiments. The samples were usually ramped up to 550 °C at 40 °C/min, held at temperature for 15 min, and cooled at the same rate.

Homoepitaxial growth was achieved at 660 °C using trimethylgallium (−9 °C) and tertiarybutylarsine (5 °C).

The HCl/water dip involved submerging the wafer in a 50% HCl/water solution for 30 s and then rinsing for 1 min in de-ionised water and then drying using filtered nitrogen.

The atomic force microscopes (AFM), used in this study were either a Burleigh Metris or Thermomicroscope M5 and results were similar in either case.

3. Results and discussions

Fig. 1 is an AFM image of a GaAs wafer heated up to 550 °C, held, and cooled, under molecular hydrogen. We were establishing conditions for the growth of InSb quantum dots on GaAs substrates directly (no buffer layer) and in order to avoid contaminating the InSb with arsenic, were heating up the GaAs wafers with no group V species present. Since InSb grows best at 400 °C, it seemed unlikely that the GaAs would decompose, even if heated to 550 °C before growth to de-oxidise it as we had previously established conditions for the deoxidation of GaAs using optical monitoring [6,7]. When we checked that this was correct we observed the islands in the AFM image, which are present even though nothing has been deposited. An obvious possibility was that there was some decomposition of the GaAs surface, so we undertook a series of experiments. First, we tried fresh wafers, straight from the manufacturer (Fig. 1 was obtained using a 3-month-old wafer) and no islands were observed. Secondly we treated the older wafers with an HCl dip (it is known that this dip only removes As_2O_3 and Ga_2O_3 from the wafer [8–10]) again no islands were observed. Then we varied the temperature of anneal between 450 °C and 650 °C and the features only changed in their size and number

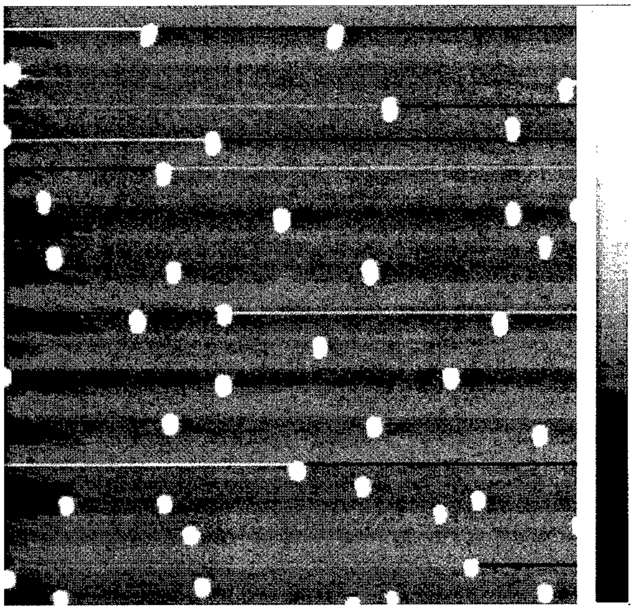

Fig. 2. Atomic force microscope image (6-μm square) of an on-axis GaAs surface after heating to 450 °C, holding and cooling. The grey scale represents 30 nm in height.

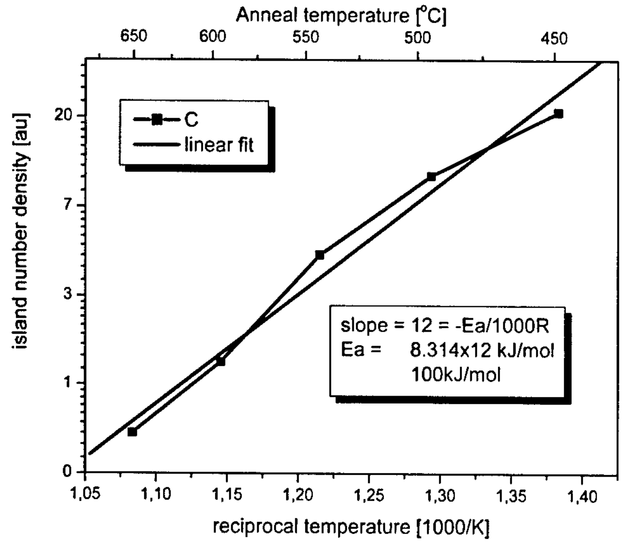

Fig. 3. Logarithmic plot of island number density vs. reciprocal absolute temperature. The grey line is a linear fit to the data.

density. As an example, Fig. 2 shows the results of heating to 450 °C and annealing.

Such a change in the number density and size of these features is indicative of a kinetically controlled surface diffusion phenomenon. In order to check this, the island area and number density are measured and calculated over multiple AFM images using analysis and counting software to give statistically sound data. A scan size of 30 μm square was initially investigated and if this proved to be free of defects and damage the area was divided into nine 10-μm squares and the number density was statistically assessed to give a mean and standard deviation, this allowed for accurate comparisons to be made between various experimental conditions and an assessment of errors and standard deviations. Fig. 3, shows the log of the number density plotted against the reciprocal absolute temperature. The linear nature of this plot means that the island growth is a kinetically controlled surface phenomenon and an activation energy of 100 kJ/mol can be calculated from the fitted data in Fig. 3. Such a value suggests that the islands grow by a surface diffusion process and we would suggest that they are islands of gallium but not due to incongruent decomposition of the GaAs, for the following five reasons:

1. The value of 100 kJ/mol (1.2 eV) is similar to that obtained (1.1 eV) from the diffusion of Ga atoms on GaAs in a MBE study [11,12].
2. An AFM study [13] involving heating GaAs wafers in a MBE chamber with no arsenic overpressure showed very similar island size and number density and was able to chemically confirm the islands as being composed only of gallium by X-ray photoelectron spectroscopy.
3. The temperature of the 450 °C anneal is well below that for incongruent evaporation of GaAs (650 °C) [14].
4. The islands are absent when we anneal the wafers under tertiarybutylarsine that can pyrolyse at temperatures as low as 450 °C.
5. The islands are considerably softer (when measured by lateral force microscopy, an adjunct of AFM) compared to similar sized GaSb islands.

These results were obtained, both on the traditional horizontal single wafer reactor and on our newer vertical reactor (similar to a close spaced reactor [15]) so it seems unlikely that there is some artefact from the transfer of any species from a hot susceptor upstream of the sample in the horizontal reactor.

The results suggest that age, storage, and treatment have a considerable effect on GaAs wafers when annealed under molecular hydrogen. An explanation for this lies in the nature of the native oxide present on any GaAs wafer suggested over 20 years ago [16]. Initial oxidation of a fresh GaAs wafer takes place on the arsenic sites and is indicated by the following equation:

$$4\mathrm{GaAs} + 3\mathrm{O}_2 \rightarrow 2\mathrm{As}_2\mathrm{O}_3 + 4\mathrm{Ga} \qquad (1)$$

This very rapid surface reaction quickly becomes passivated as the diffusion of oxygen through the oxide layer slows down after the growth of a few monolayers of oxide. After a few days the thickness of As_2O_3 has reached 1–2 nm (a similar thickness to that seen for oxides growing on aluminium or titanium or other self-passivating oxide systems). Subsequently, a much slower solid-state reaction takes place in between the As_2O_3 and the bulk GaAs:

$$2\mathrm{GaAs} + \mathrm{As}_2\mathrm{O}_3 \rightarrow 4\mathrm{As} + \mathrm{Ga}_2\mathrm{O}_3. \qquad (2)$$

This reaction occurs very slowly, as a typical bulk solid-state reaction, over a period of months. It occurs even if the wafer is stored in its original inert gas filled, metallised polyester bag, because the As_2O_3 is present on the wafer surface before the bag is sealed.

In order to examine the morphological implications of Eq. (2), a 2-year-old wafer, expected to have had a considerable amount of Ga_2O_3 formed, was examined in the AFM after an HCl/water dip. As mentioned above, the dip is expected to remove only the oxide. Fig. 4 shows a high magnification AFM of such a wafer. Significant, features are observed in an otherwise flat, amorphous surface. The features are approximately 100 nm across and 4 nm deep. We suggest that these features are the result of the removal of Ga_2O_3 that had developed from Eq. (2). This idea is supported by our observation that a similar HCl/water dip on a freshly supplied substrate shows a flat amorphous surface of

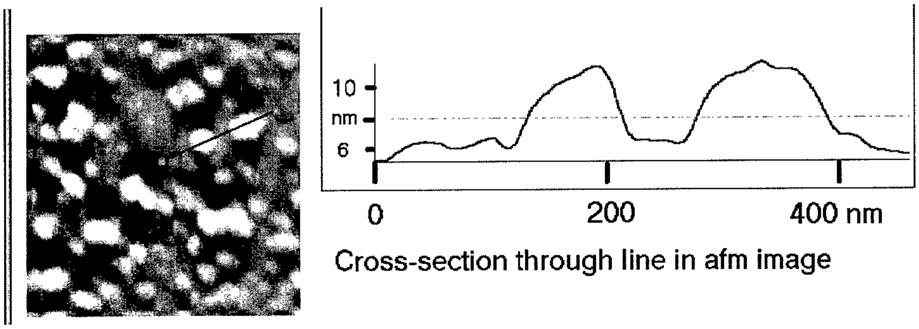

Fig. 4. Atomic force microscope image of an on-axis GaAs surface after an HCl/water dip. The image is a 1-μm square and the grey scale represents 12 nm with a line roughness of 1.9 nm.

roughness 0.5 nm. As no localised Ga_2O_3 is expected on a fresh wafer this confirms that the features in Fig. 4 are indeed from localised oxidation via Eq. (2). Fig. 5 shows a low-magnification image from the same surface as in Fig. 4. Here the pits seen in Fig. 4 are seen to be coalesced in lines running down the image. The spacing between these lines is of the order of 600 nm which is very similar to that expected for the separation of step edges on the on-axis GaAs surface used in these studies suggesting that the oxidation is somehow influenced by the step edges. Fig. 6 shows a schematic of what we propose is happening over a period of some months and after a subsequent HCl/water dip. That the features are possibly initiated at the step edges is reasonable from an energetic point-of-view as kink sites on step edges would be favourable as places for reactions to occur. The change of the wafer surface from an atomically flat surface covered in a thin uniform layer of As_2O_3 to a much rougher surface with a thicker oxide over a period of months is in good agreement with previous X-ray diffraction and ellipsometric studies [7,17,18]. It is also likely to affect the quality of growth of any epitaxial layer. There is also the possibility that if arsine is used in the deoxidation stage before epitaxy, then the lack of pyrolysis of arsine

Fig. 5. Atomic force microscope image of an on-axis GaAs surface after an HCl/water dip. The image is a 10-μm square and the grey scale represents 8 nm with a line roughness of 1.2 nm.

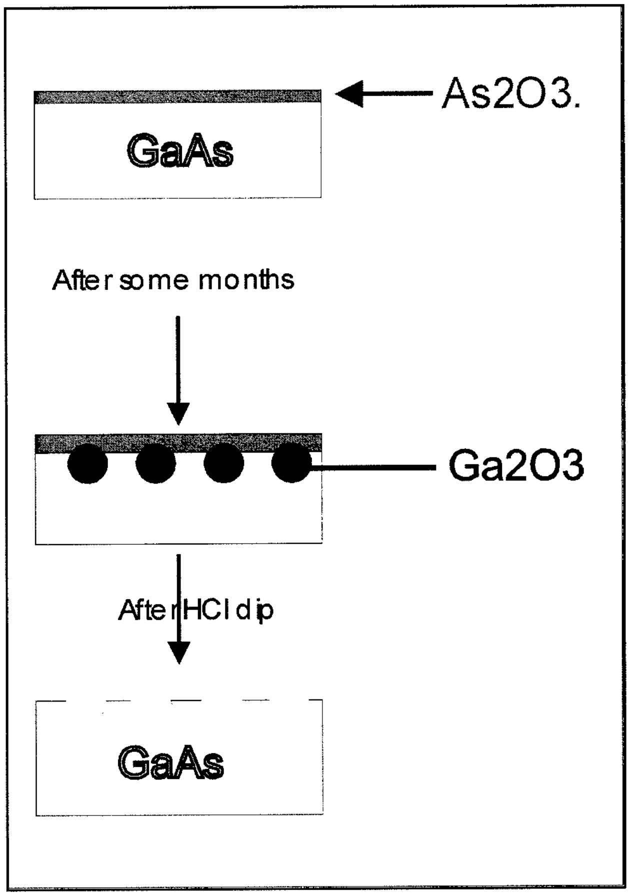

Fig. 6. Schematic of GaAs oxidation [Eqs. (1) and (2)] and subsequent surface after HCl/water dip.

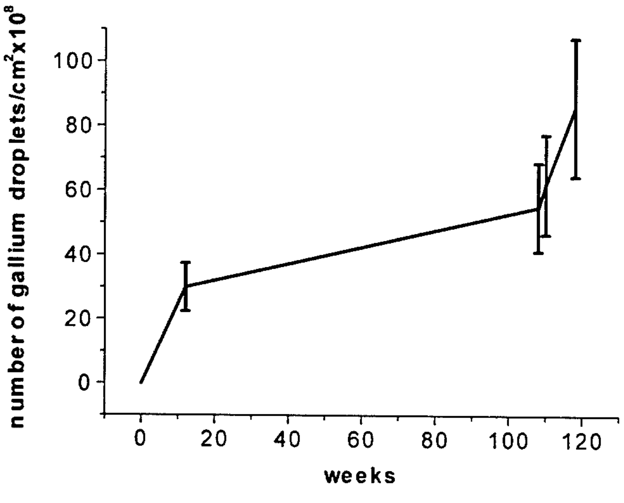

Fig. 7. Plot of number density of gallium droplets/cm^2 vs. time since polishing (in weeks).

at the temperatures where these islands are observed might lead to them forming before sufficient arsenic is present to mop up the gallium. This would lead to large islands of GaAs forming at the higher temperatures when the arsenic is present from pyrolysis and is absorbed into the gallium droplets. Such a surface would lead to subsequent growth having very poor morphology. Either of these morphological issues might be the reason why GaAs is only given a 3-month certificate of conformity to an epiready state. To study this aspect of ageing we instigated an ageing trial with wafers stored under ambient conditions and then examined them using both annealing (as above) and homoepitaxial growth.

3.1. Ageing trial

The full ageing trial is currently on going and will be reported later. Initial results confirm that the number density of the gallium droplets found under similar conditions to those used to produce Fig. 1 follow a trend that supports our above hypothesis that they are indicative of a surface that has been aged beyond 3 months. Fig. 7 shows the number density with respect to time. The error bars are quite large and we are still investigating the source of this variation but, overall, the graph agrees well with our hypothesis that even over the first month after polishing the wafer has an increasing amount of Ga_2O_3 which gradually changes the surface from epiready to unepiready, the actual time when this would manifest itself as poor growth will depend on the conditions used during the bakeout (arsine or tBAs). To show this we have used two different conditions to grow homoepitaxial GaAs as part of the ageing trial. Growth 1 is a set of typical conditions with tBAs switched into the reactor during both the heat-up and cool-down as well as during the homoepitaxy. Growth 2 is a set of conditions that attempt to mimic arsine whilst using tBAs. To do this we have only switched the tBAs into the reactor at a temperature (500 °C) to mimic the pyrolysis of arsine [19]. When we use Growth 1 on wafers that are 0 and 4 weeks old we get atomically flat terraces (average roughness 0.1 nm) in the AFM similar to those seen Fig. 8. On a 12-week-old wafer the homoepitaxial layer no longer grows in step flow to give atomically flat terraces but in an island growth mode giving a very much rougher surface (average roughness 1.5 nm) seen in Fig. 9. This change is also seen in Growth 2 but the rougher, island growth occurs at week 4 not week 12. This would suggest that the length of time a wafer is epiready is determined by the precursors used and perhaps the reactor geometry and there is no specific time limit that covers all possible conditions.

Eq. (2) suggests that it might be possible to increase the rate of gallium oxidation by increasing the temperature. In order to test various post-polishing treatments we wished to develop a way of ageing GaAs over a suitable period (days) to be able to predict the results over longer periods (months). We have stored wafers at various elevated temperatures to determine if this can accelerate the ageing discussed above. We have been able to accelerate the reaction occurring in Eq. (2) by storage of the wafers at elevated temperatures for quite short periods and Table 1 shows the results. Clearly, storage at 200 °C gives similar results, in terms of gallium island density to storage at room temperature at

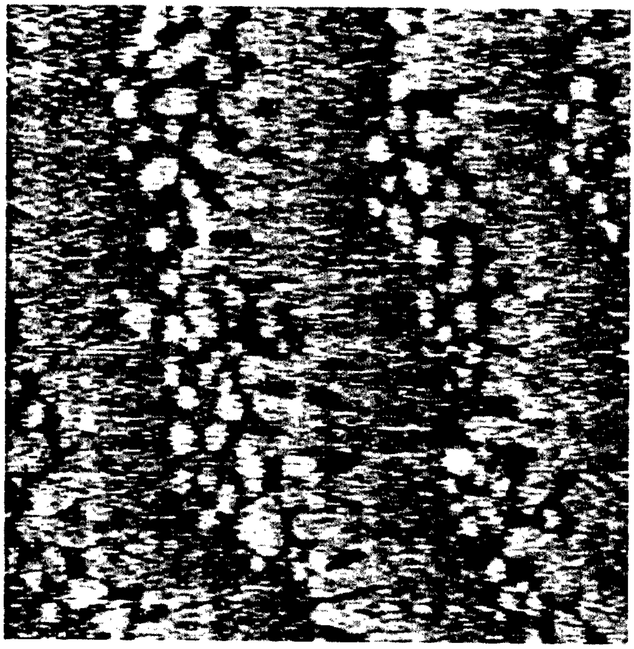

Fig. 8. Atomic force microscope image of a fresh on-axis GaAs surface after homoepitaxial growth. The image is a 3-μm square and the grey scale represents 1 nm with a line roughness of 0.1 nm.

Fig. 9. Atomic force microscope image of older on-axis GaAs surface after homoepitaxial growth. The image is a 3-μm square and the grey scale represents 10 nm with a line roughness of 1.5 nm.

20 °C for over 2 years. This facility will enable us to test rapidly any surface treatments that might be expected to improve the ageing properties of a GaAs wafer (e.g. by modifying the oxide). The results presented here are also supported by XPS measurements made at 200 °C where the reaction in Eq. (2) is observed directly [20] as a change in the peak intensities of the two oxides, the arsenic oxide diminishing and the gallium oxide increasing over a period of a few hours. This suggests quantitatively at least that temperature will play an important role in wafer storage.

An alternative, quantitative, technique for studying the progress of Eq. (2) is to use Raman scattering to monitor the signal obtained from elemental arsenic precipitated from the GaAs when it is oxidised by the As_2O_3. The arsenic peak is easily identifiable in Raman spectra of GaAs at 260 cm^{-1} [21]. A typical GaAs Raman spectra LO phonon at 295 cm^{-1} is shown in Fig. 10, together with the spectra taken after high-temperature annealing in air for various times. As expected, the arsenic content of oxide layers increased with anneal time. However, surprisingly, when the ambient of the furnace was changed from oxygen to dry nitrogen, elemental arsenic content initially increased to that seen after 1 h in Fig. 10, and stopped increasing. It seems that the As_2O_3 present on the surface is enough to allow two to take place for perhaps 30 min but once the As_2O_3 is depleted further arsenic cannot be precipitated, because Eq. (1) is inhibited in the dry nitrogen ambient and hence the Ga_2O_3 ceases to form.

Table 1
Number density of gallium droplets for various storage times/temperatures

Sample	Temperature of storage (°C)	Time of storage	Number of Ga droplets ($\times 10^8$ cm^{-2})	S.D. ($\times 10^8$ cm^{-2})
Stored	20	24 months	1.8	0.1
Aged	100	3 weeks	0.6	0.1
Aged	200	20 h	1.6	0.1
Aged	200	12 h	0.5	0.05
Stored	−20	24 months	0.0	

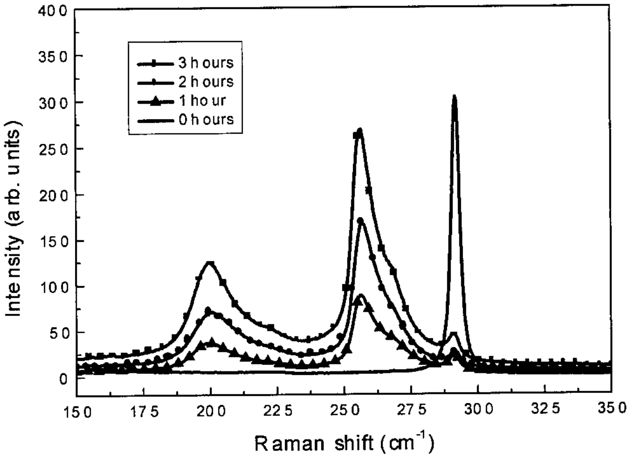

Fig. 10. Raman spectra of GaAs, fresh and after several hours at 600 °C in oxygen ambient.

We also examined this elemental arsenic peak in a sample held at various temperatures between 300 and 750 °C for 1 h. The amount of elemental arsenic present increased with temperature. Fig. 11 shows an Arrhenius plot of the integrated arsenic Raman peak intensity as a function of temperature. Calculations from curve fitting constants provide an activation energy, for the formation of elemental arsenic of 0.46 eV. It should be stressed

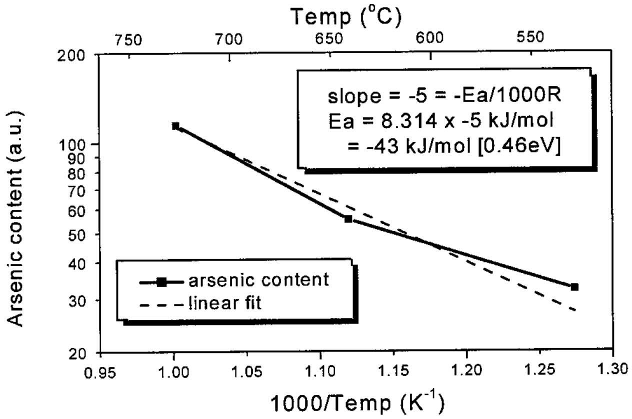

Fig. 11. Logarithmic plot of arsenic content vs. reciprocal absolute temperature. The grey line is a linear fit to the data.

Table 2
Estimated relative ageing rate of GaAs surface oxides for different storage temperatures using data from Fig. 11

Storage temperature (°C)	Relative rate of ageing	Age at loss of epireadiness (months)
20	1.00	3
0	0.26	12
−10	0.13	24
−20	0.06	48

that this is an approximate value since there are only three data points present and the values of each of these are subject to considerable uncertainty. However, it is in good agreement with values in the literature [21].

These two results from the Raman measurements have two important implications for the storage of GaAs wafers. Firstly, the activation energy suggests that storage at reduced temperatures might lead to the slowing of the reaction in Eq. (2) and thus a slowing in the degradation of the GaAs wafer. Secondly, storage in an inert gas filled bag will not, of its self stop Eq. (2) taking place and the wafer will degrade until all the As_2O_3 has been consumed, it will then stop. Table 2 shows approximate values for the decrease in rate of ageing by storage at various temperatures. These data suggested to us that storage in a domestic freezer was worth investigating as a means of enhancing the life expectancy of an epiready wafer. We stored two wafers under ambient conditions, two at 0 °C in a domestic fridge and two at −20 °C in a domestic freezer. Two years later, the wafers were removed from the freezer and assessed by annealing as above. No evidence of gallium droplets was observed for those wafers stored at −20 °C suggesting that the above hypothesis was sound. These wafers are being assessed by other techniques such as growth and the results, which look very encouraging, will be reported with the final results of the ageing trial.

4. Discussion

One of the difficulties in assessing the literature on investigations into the thickness and nature of the oxides found on GaAs is that often there is no information as to the conditions under which the wafers have been stored or prepared. Discrepancies between various authors concerning both the thickness and the type of oxide present could be accounted for by the age of the sample or by the way it was prepared. An oxidative etch such as sulfuric acid/hydrogen peroxide [22] leaves the surface with Ga_2O_3 present and will affect any surface studies compared to an epiready surface [22] which will initially have little Ga_2O_3 if prepared under an alkali environment [7,18].

Substrates that have been stored for longer than 3 months can be re-generated by dipping in HCl/water but this is nearly as time consuming as etching in sulfuric acid/hydrogen peroxide and so cannot be recommended as a way of avoiding the problems of a unepiready wafer. Instead, storage in a domestic freezer has been found to be highly successful in preventing the degradation associated with Eq. (2). This is of particular use where substrates have to be bought in large quantities to save money but then would otherwise languish on a shelf for several months and deteriorate and prove a false economy. Provided the wafer is removed from the freezer 1 h before it is needed, to allow the temperature inside the polyethylene packaging to equilibrate with the ambient (thus preventing any condensation) we have seen no deleterious effects by storage under these conditions.

We have not seen any difference between doped and undoped GaAs in the measurements made here, despite the fact that subtle differences have been reported [23]. We have found some differences when looking at vicinal substrates (specifically 2° off towards [111]A) compared to the on-axis substrates studied here but these will form part of our next report on the full ageing trial.

5. Conclusions

Epiready GaAs wafers have been stored under a variety of conditions with temperatures between 200 and −20 °C and assessed by measuring the surface in an AFM after various tests including annealing in molecular hydrogen using a MOVPE reactor.

The primary source of ageing on an epiready GaAs wafer has been found to be the transfer oxidation from the native As_2O_3 (present at time=0) to Ga_2O_3. The kinetics of this equation has allowed us both to enhance it as a means of accelerated ageing, and attenuate it as a means of storage over a period of 2 years (at −20 °C) that allows the wafer to be used as if it were freshly polished.

References

[1] R. Fornari, Mater. Sci. Eng. 9 (1991) 9.
[2] J. Schwar, Mater. Sci. Eng. 9 (1991) 23.
[3] D.A. Allwood, I.R. Grant, N.J. Mason, R.A. Palmer, P.J. Walker, J. Cryst. Growth 221 (2000) 160.
[4] D.A. Allwood, N.J. Mason, in: Dr. L. Vescan (Ed.), Handbook of Thin Film Process Technology, Part G—Substrate Preparation for Thin Film Deposition, Institute of Physics, Bristol, England, 2000.
[5] A. Knauer, E. Richter, M. Weyers, J. Cryst. Growth 146 (1995) 549.
[6] D.A. Allwood, N.J. Mason, P.J. Walker, J. Cryst. Growth 195 (1998) 163.
[7] D.A. Allwood, N.J. Mason, P.J. Walker, Mater. Sci. Eng. B—Solid State Mater. Adv. Technol. 66 (1999) 83.
[8] S. Osakabe, S. Adachi, Jpn. J. Appl. Phys. Part 1—Regular Pap. Short Notes Rev. Pap. 36 (1997) 7119.

[9] Z.S. Song, S. Kawasaki, M. Suemune, I., J. Vacuum Sci. Technol. B 13 (1995) 77.
[10] O.E. Tereshchenko, S.I. Chikichev, A.S. Terekhov, J. Vacuum Sci. Technol. a—Vacuum Surf. Films 17 (1999) 2655.
[11] H. Yang, V.P. Labella, D.W. Bullock, P.M. Thibado, J. Vac. Sci. Technol. B 17 (1999) 1778.
[12] H. Yang, V.P. LaBella, D.W. Bullock, Z. Ding, J.B. Smathers, P.M. Thibado, J. Cryst. Growth 202 (1999) 88.
[13] K. Iizuka, Y. Sakamaki, T. Suzuki, H. Okamoto, J. Cryst. Growth 227 (2001) 41.
[14] C.T. Foxon, J.A. Harvey, B.A. Joyce, J. Phys. Chem. Solids 34 (1973) 1693.
[15] D.W. Weyburne, B.S. Ahern, J. Cryst. Growth 170 (1997) 77.
[16] C.D.S. Thurmond, G.P. Kammlott, G.W. Schwartz, B., J. Electrochem. Soc.: Solid-State Sci. Technol. 127 (1980) 1366.
[17] B.K. Tanner, D.A. Allwood, N.J. Mason, Mater. Sci. Eng. B—Solid State Mater. Adv. Technol. 80 (2001) 99.
[18] D.A. Allwood, R.T. Carline, N.J. Mason, C. Pickering, B.K. Tanner, P.J. Walker, Thin Solid Films 364 (2000) 33.
[19] S.P. DenBaars, B.Y. Maa, P.D. Dapkus, A.D. Danner, H.C. Lee, J. Cryst. Growth 77 (1986) 188.
[20] A. Evans, University of Wales, Aberystwyth, Private Communication (2001).
[21] A.B. Rim, R., J. Appl. Phys. 74 (1993) 897.
[22] J.C. Massies, J.P., J. Appl. Phys. 58 (1985) 806.
[23] A. Rim, R. Beserman, J. Appl. Phys. 74 (1993) 897.

ELSEVIER

Thin Solid Films 412 (2002) 84–88

thin solid films

www.elsevier.com/locate/tsf

Post-growth thermal treatment of self-assembled InAs/GaAs quantum dots

Adam Babinski[a,]*, J. Jasinski[b]

[a]Grenoble High Magnetic Field Laboratory, MPI/FKF-CNRS, BP 166X, F-38042 Grenoble Cedex 9, France
[b]Materials Science Division, Lawrence Berkeley National Laboratory, 1 Cyclotron Rd, Berkeley, CA 94720, USA

Abstract

Results of a post-growth rapid thermal annealing (RTA) on GaAs proximity-capped structures with high density ($\sim 10^{11}$ cm^{-2}) of self-assembled InAs/GaAs quantum dots (QDs) are presented. Features due to the QDs, bi-dimensional platelets (2DP) and InAs wetting layer (WL) were identified in photoluminescence (PL) spectrum of the as-grown sample. It is shown, using transmission electron microscopy, that RTA at temperature up to 700 °C (for 30 s) results in an increase of QDs lateral sizes. After RTA at 800 °C or higher temperatures, no QDs can be distinguished and substantial thickening of the WL can be seen. The main PL peak blueshifts as a result of RTA in all investigated temperature ranges, which is accompanied by a quenching of the 2DP and WL PL. It is proposed that the main PL peak, which is due to the QDs in the as-grown sample, results from optical recombination in the modified WL in the samples, after RTA at 800 °C and higher temperatures. Laterally-enhanced Ga/In interdiffusion induced by strain is proposed to explain a relatively fast dissolution of QDs. © 2002 Elsevier Science B.V. All rights reserved.

Keywords: Self-assembled quantum dots; Thermal treatment; Intermixing

1. Introduction

One of the ways of tuning the properties of semiconductor quantum dots (QDs) [1,2] is their postgrowth thermal treatment [3–15]. The postgrowth annealing is usually performed in a growth chamber [4,8,15] or in a rapid thermal annealing (RTA) system with SiO_2 capping [5,9,12–14] or proximity capping, (which means an annealing with a piece of GaAs substrate in close proximity to the sample surface) [3,6,7]. It is also known that RTA of samples without any capping leads to surface degradation, due to As outdiffusion [5]. Thermally-induced intermixing of the QDs leads to a blueshift, a narrowing of optical emission from QDs as well as to a reduction in the QDs interlevel spacing. It is well established that the sample capping during the thermal cycling of strained InGaAs/GaAs multi quantum wells can critically influence the results of the annealing procedure [16], however, comparative studies of the effect on thermal annealing of QDs have been published just recently [12,13]. In this paper, the results of the effect of RTA on InAs/GaAs QDs with GaAs proximity capping are presented and discussed [17].

2. Experimental procedure

The structure investigated was grown by metaloorganic vapor phase epitaxy in the Institute of Experimental Physics, Warsaw University. The GaAs buffer layer was grown at 650 °C on a nominaly (100) oriented GaAs substrate. Self-assembled InAs QDs were formed in Stranski-Krastanow mode by growing nominally 2ML of InAs at temperature 470 °C. Then, the temperature was raised to 500 °C, while growing 100 nm of the GaAs capping layer. Samples cut from the wafer were proximity capped and RTA treated in nitrogen ambient for 30 s at 600, 700, 800, 850, 900 and 950 °C. A reference sample with wetting layer (WL) and no QDs was also grown, and RTA treated under proximity cap for 30 s at 700, 750, 800, 850 and 900 °C. The surfaces of investigated samples were not affected during the RTA procedure. The microstructures of as-grown and all annealed samples with QDs were studied using transmission electron microscopy (TEM). Cross-section-

---

*Corresponding author. Tel.: +33-476-88-74 44; fax: +33-476-85-56-10.

E-mail address: babinski@polycnrs-gre.fr (A. Babinski).

0040-6090/02/$ - see front matter
PII: S0040-6090(02)00317-6

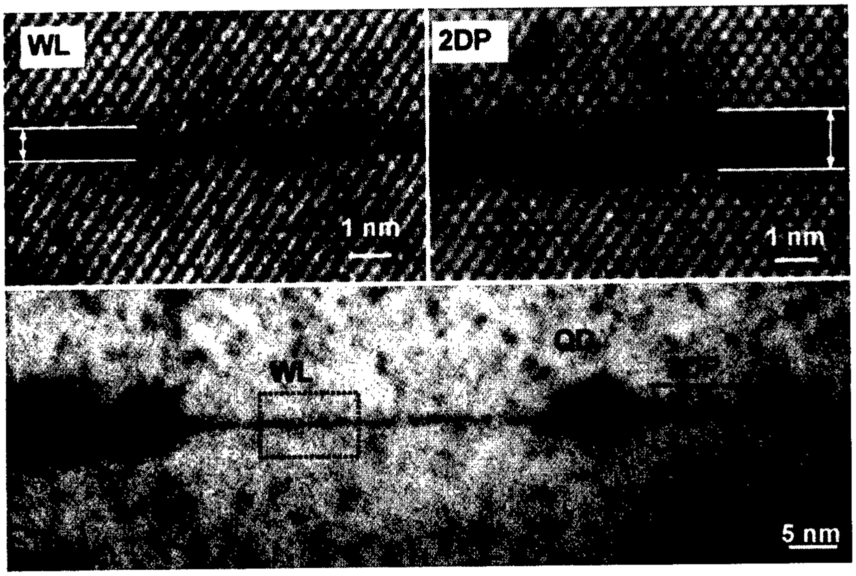

Fig. 1. High resolution cross-sectional electron microscopy images of the as-grown sample: InAs quantum dots (QDs), InAs wetting layer (WL) and InAs bi-dimensional platelets (2DP) are identified.

al TEM specimens were prepared from the samples by a standard method of mechanical thinning, followed by ion milling. In addition, plan-view specimens were prepared from the as-grown sample. Photoluminescence (PL) measurements of both the as-grown and all annealed samples were performed at liquid-helium temperature, with laser excitation ($\lambda = 780$ nm). The signal was dispersed by a monochromator and collected onto a liquid-nitrogen-cooled germanium detector. Standard lock-in technique was applied.

3. Results

The presence of high-density self-assembled QDs in the as-grown sample was confirmed by plan-view TEM. The average size of QDs was approximately 10 nm. Their density, as estimated from the plan-view observation, was of the order of 10^{11} cm^{-2}. There was no indication of any strain relaxation in the form of large, dislocated islands or dislocations threading through the capping layer.

The QDs can be seen in the cross-sectional TEM image of the as-grown sample (Fig. 1). A 1-ml-thick InAs wetting layer (WL) can also be seen in Fig. 1. Moreover, a presence of bi-dimensional platelets (2DP) can be detected in Fig. 1. The 2DP are 2-ML-thick and they form during the growth of QDs, just before the 2D–3D transition. It has been proposed that transport and accumulation of atoms from a few 2DP leads to formation of one QD [18]. Similar coexistence of planar and three-dimensional QDs has also been reported in CdSe/ZnSe QDs system [19]. The morphology of the as-grown sample was confirmed by PL measurements. The PL spectrum (Fig. 2) of the as-grown sample is dominated by two peaks, which are due to optical recombination within the InAs QDs ($E = 1.155$ eV) and within the InAs WL ($E = 1.42$ eV) [20]. A PL feature at $E = 1.34$ eV can also be seen in Fig. 2. Its attribution to optical recombination within the 2DP is confirmed by a band-filling effect observed in Fig. 2. No band-filling of the QDs was observed, which was probably due to their high surface density.

The RTA results in substantial changes of the sample microstructure (Fig. 3). Well-defined QDs can still be seen in samples annealed at 600 and 700 °C. The lateral sizes of the QDs increase with increasing temperature

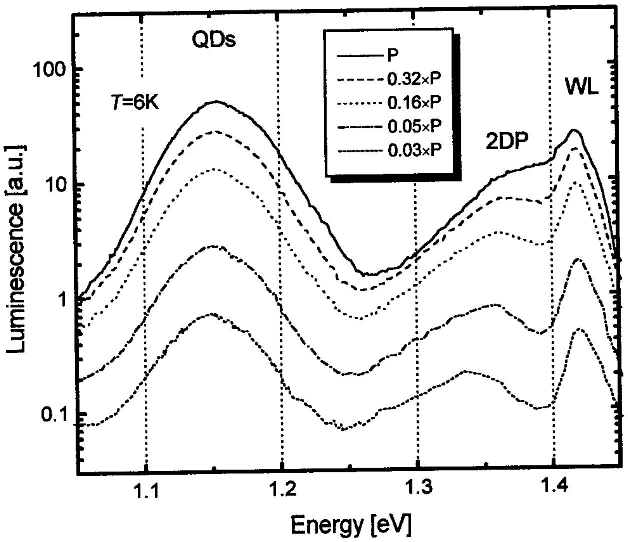

Fig. 2. Power dependence of the photoluminescence ($T = 4.2$ K) from the as-grown InAs/GaAs QDs. Note the band-filling effect on the 2DP-related PL feature [20].

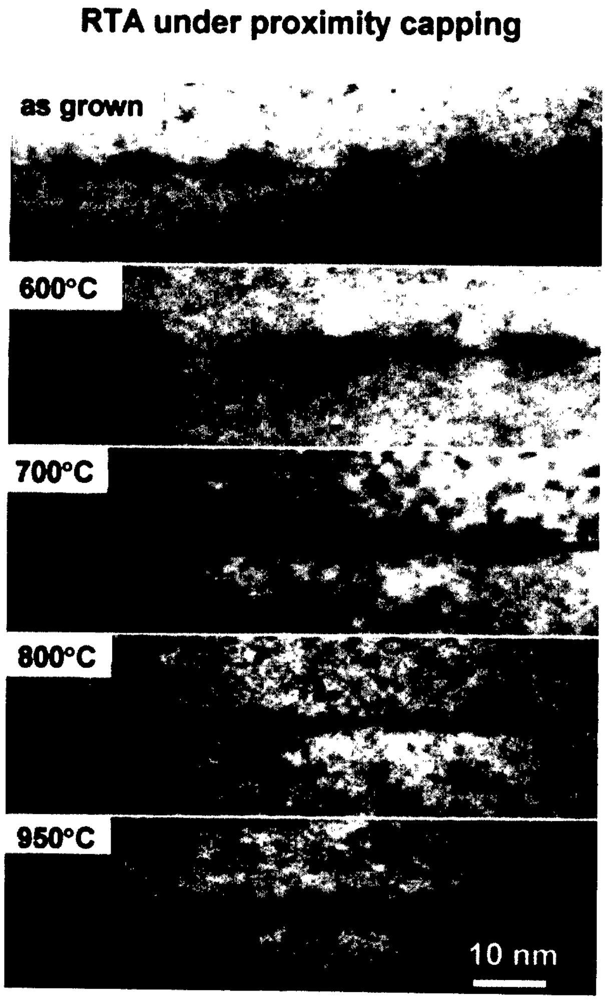

Fig. 3. High resolution cross-sectional TEM images of the as-grown sample and samples annealed for 30 s at 600, 700, 800 and 950 °C.

in those samples. In samples annealed at 800 °C or higher temperatures, no QDs were observed. A broadening of the modified WL was observed instead. The layer thickness increases to approximately 3 nm after annealing at 800 °C and to approximately 8 nm after annealing at 950 °C.

RTA-induced changes in the microstructure can be compared with the results of the PL measurements (Fig. 4). Annealing at 600 °C (for 30 s) results in no significant change to the QDs PL peak position (with a slight decrease of its intensity) and in a substantial decrease of the WL and 2DP PL intensity. Further changes to the PL spectrum can be observed after thermal treatment at 700 °C or higher temperatures. The RTA treatment of the samples results in a quenching of the 2DP and WL PL. Spectral position of a weak feature due to optical recombination in the WL seen after RTA at 700 °C confirms an existence of the WL of the same thickness and composition as in the as-grown sample. One peak dominates the PL spectra for samples annealed at $T \geq 700$ °C, with the peak energy shifting from 1.33 eV (700 °C) to 1.427 eV (950 °C). In addition, a significant narrowing and intensity increase of this PL peak takes place with the increase of the annealing temperature.

A weak shift in the optical emission energy as a result of the RTA was observed in the PL spectrum of the WL sample (Fig. 5). This was accompanied by a decrease in the WL PL intensity after the RTA at highest temperatures.

4. Discussion

As it can be seen from the TEM pictures, the RTA at lowest temperatures (600 and 700 °C) results in the intermixing of the QDs. Mainly, the lateral sizes of the QDs increase as a result of that process. This must be accompanied by a change in the QDs composition, which results in a shallower potential and the PL blueshift. Simultaneously, an existence of a thin WL PL is confirmed by both TEM and PL results. After RTA at 800 °C, the QDs cannot be distinguished in the TEM images and both 2DP and WL PL peaks quench. This suggests that the QDs dissolve into the surrounding WL. The main PL peak seen from that sample must be due to the modified WL. This layer, enriched with indium from the QDs, broadens with increasing RTA temperature. Diffusion coefficients for the intermixed WLs,

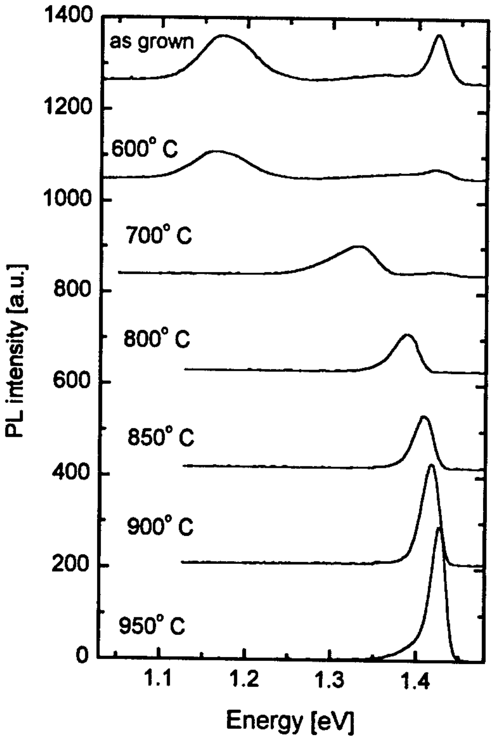

Fig. 4. Photoluminescence ($T = 4.2$ K) from the as-grown and annealed samples with InAs/GaAs QDs.

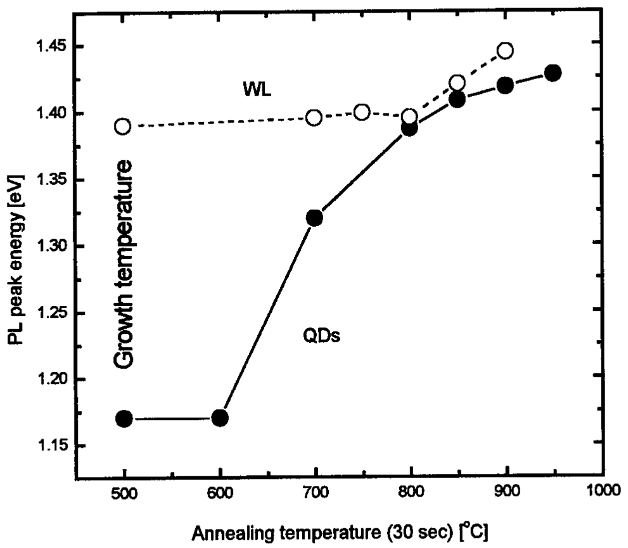

Fig. 5. Photoluminescence peak energy position as a function of annealing temperature in the samples with the InAs/GaAs QDs and the InAs WL.

estimated from their thickness measured by TEM (2.3×10^{-16} cm^2/s, at 800 °C to 4.1×10^{-16} cm^2/s at 900 °C and 1.7×10^{-15} cm^2/s at 950 °C) were similar to those reported for GaAs proximity-capped intermixed $In_{0.35}Ga_{0.65}As/GaAs$ multi-quantum wells [16].

A dissolution of QDs after the RTA at high temperature (850 °C for 50 s [9] or 950 °C for 30 s [5]) has previously been observed in SiO_2-capped samples with InAs/GaAs QDs. That was, however, accompanied by a substantial degradation in material quality, which has not been observed in our samples. On the other hand, it has been shown that the three-dimensional character of the QDs confinement potential could be retained even after RTA at a relatively high temperature (30 s at 900 °C [5] or at 950 °C [14] and 60 s [13] at 900 °C). In our opinion, two factors are responsible for the relatively fast dissolution of the QDs in the investigated samples. These are: the GaAs proximity capping during the RTA procedure and high density of QDs.

It is well known that the interdiffusion process strongly depends on the density of such defects as vacancies, interstitials and dislocations. A number of Ga vacancies available for In/Ga interdiffusion in proximity-capped samples are limited to those existing in the sample. This can explain a weaker blue-shift of the QDs PL as a result of (nominally) defect-free interdiffusion in SrF_2-capped samples, as compared to that in SiO_2 defect-induced interdiffusion reported in [13]. Relatively low number of Ga vacancies in the proximity-capped structures results in a weak In/Ga interdiffusion [16] across the dot/cap interface, which is known to be a main mechanism of the RTA-induced PL blueshift in SiO_2-capped structures with QDs. Another process can be of importance during RTA treatment of proximity-capped structures with QDs. This is the non-Fickian strain-enhanced interdiffusion [21], which has already been suggested as an explanation of some results of RTA treatment of InGaAs/GaAs QDs [3,7]. There is a large strain in and around QDs [22]. Moreover, it has recently been shown that strain fields due to lattice mismatch extend from the QDs into surrounding GaAs matrix over ≥ 10 nm [23]. Such a strain field increases vacancy concentration [23] and is likely to enhance the lateral In/Ga interdiffusion. In such a process, In atoms would replace Ga atoms in highly strained region around the QDs base. Such a behavior has already been reported in the uncapped InP/GaAs system [24]. Laterally enhanced interdiffusion could cause relatively fast dissolution of the QDs. After RTA at 600 and 700 °C, an increase in QDs lateral sizes and changes in their composition, result in a blueshift of the main PL peak. Simultaneously, sample areas covered with 1-ML-thick WL decrease, which might explain the quenching of the WL emission. Further increase in QDs lateral sizes, which occurs after RTA at higher temperatures, cancels the lateral confinement of carriers. A blueshift of the PL peak, observed after RTA in this temperature region, is due to an intermixing of the modified WL, which is enriched by indium from dissolved QDs. This blueshift is similar to that of the PL peak in the RTA samples with WL only (see Fig. 5). This must result from low Ga/In interdiffusion coefficients, characteristic for proximity-capped samples.

On the contrary, in the SiO_2-capped samples, a large number of Ga vacancies form at the SiO_2/GaAs interface during RTA. This is due to a fast Ga outdiffusion into the SiO_2 layer during thermal annealing [25]. Those Ga vacancies diffuse into the QDs region during RTA, enhancing the In/Ga interdiffusion through a dot/cap interface [12,13]. That process mainly affects the QDs height, which results in a blue-shift and narrowing of an optical emission, with no destruction of the three-dimensional carrier confinement in the QDs. It is very likely that the density of Ga vacancies introduced during RTA with SiO_2 capping is much larger than the concentration of strain-induced vacancies around the QDs (especially in the case of low-density QDs). This would explain presumably weaker lateral intermixing and preserve the three-dimensional confinement in SiO_2-capped RTA QDs reported in the literature. It has to be noted that some previous reports confirm the three-dimensional confinement in InGaAs/GaAs QDs after RTA under proximity capping [6]. In our opinion, this points out the role of stress in the intermixing process. InGaAs/GaAs QDs investigated in the cited work were larger (30 nm) and their surface density was lower (4×10^{8} cm^{-2}) than in the case of InAs QDs investigated in our report. Both factors are likely to decrease a strain in the structures, which might explain the difference in the annealing results.

5. Conclusions

In conclusion, we studied the effect of thermal treatment on the proximity-capped structures of self-assembled InAs/GaAs QDs and InAs WL. TEM shows a complete dissolution of QDs into surrounding WL after RTA at $T=800$ °C for 30 s. Substantial thickening of the modified WL is observed after RTA at higher temperatures. It has been shown that the blueshift of the PL peak accompanies those morphology changes. It is proposed that the strain-enhanced lateral In/Ga interdiffusion is responsible for the fast disappearance of QDs in the investigated samples. This process may be of importance in proximity-capped annealing, when no group III vacancy formation takes place at the sample/capping interface.

Acknowledgments

A. Babinski kindly acknowledges support from EC program ICAI-CT-2000-70018 (Center of Excellence CELDIS). Authors are grateful to R. Bozek from the Institute of Experimental Physics, Warsaw University, Warsaw, Poland for growing the investigated structures and to Dr E. Kaminska and Z. Szopniewski from Institute of Electron Technology, Warsaw, Poland for the RTA processing of the investigated samples. PL measurements were performed in part by A. Szepielow. This work was supported in part by Polish Committee for Scientific Research Grant No. 7 T08 A 040 17 and by the US Department of Energy, under Contract No. DE-AC03-76SF00098. The use of the facilities at the National Center for Electron Microscopy at Lawrence Berkeley National Laboratory is greatly appreciated. Authors are on leave from the Institute of Experimental Physics.

References

[1] B. Book, in: D. Bimberg, M. Grundmann, N.N. Ledentsov (Eds.), Quantum Dot Heterostructures, Wiley, Chichester, 1998, For review.

[2] L. Jacak, P. Hawrylak, A. Wojs, Quantum Dots, Springer, Berlin, 1998, For review.

[3] R. Leon, Y. Kim, C. Jagadish, M. Gal, J. Zou, D.J. Cockayne, Appl. Phys. Lett. 69 (1888) 1996.

[4] A.O. Kosogov, P. Werner, U. Goesele, N.N. Ledentsov, D. Bimberg, V.M. Ustinov, A.Y. Egorov, A.E. Zhukov, P.S. Kopev, N.A. Berst, Z.I. Alferov, Appl. Phys. Lett. 69 (1996) 3072.

[5] S. Malik, C. Roberts, R. Murray, M. Pate, Appl. Phys. Lett. 71 (1987) 1997.

[6] R. Leon, S. Fafard, P.G. Piva, S. Ruvimov, Z. Liliental-Weber, Phys. Rev. B 58 (1998) R4262.

[7] C. Lobo, R. Leon, S. Fafard, P.G. Piva, Appl. Phys. Lett. 72 (1998) 2850.

[8] F. Heinrichsdorff, M. Grundmann, O. Stier, A. Krost, D. Bimberg, J. Cryst. Growth 195 (1998) 540.

[9] S.J. Xu, X.C. Wang, S.J. Chua, C.H. Wang, W.J. Fan, J. Jiang, X.G. Xie, Appl. Phys. Lett. 72 (1998) 3335.

[10] S. Fafard, C.N. Allen, Appl. Phys. Lett. 75 (1999) 2374.

[11] S. Fafard, Z.R. Wasilewski, C.N. Allen, D. Picard, M. Spanner, J.P. McCaffrey, P.G. Piva, Phys. Rev. B 59 (1999) 15368.

[12] A. Bhattacharyya, A. Saher Helmy, A.C. Bryce, E.A. Avrutin, J.H. Marsh, J. Appl. Phys. 88 (2000) 4619.

[13] N. Perret, D. Morris, L. Franchomme-Fosse, R. Cote, S. Fafard, V. Aimez, J. Beauvais, Phys. Rev. B 62 (2000) 5092.

[14] T.M. Hsu, Y.S. Lan, N.T. Yeh, J.-I Chyi, Appl. Phys. Lett. 76 (2000) 691.

[15] R. Hao Lee, T.J. Lowe-Webb, W.Yang Johnson, P.C. Sercel, Appl. Phys. Lett. 73 (1998) 3556.

[16] S. Burkner, M. Baeumler, J. Wagner, E.C. Larkins, W. Rothermund, J.D. Ralston, J. Appl. Phys. Lett. 79 (1996) 6818.

[17] A. Babinski, J. Jasinski, R. Bozek, A. Szepielow, J.M. Baranowski, Appl. Phys. Lett. 79 (2001) 2576.

[18] M. Berti, A.V. Drigo, G. Rossetto, G. Torzo, J. Vac. Sci. Technol. B 15 (1997) 1794.

[19] M. Strassburg, T. Deniozou, A. Hoffmann, R. Heitz, U.W. Pohl, D. Bimberg, D. Litvinov, A. Rosenauer, D. Gerthsen, S. Schwedhelm, K. Lischka, D. Schikora, Appl. Phys. Lett. 76 (2000) 685.

[20] A. Szepielow, MSc Thesis, Warsaw University, 2001.

[21] S.W. Ryu, I. Kim, B.D. Choe, W.G. Jeong, Appl. Phys. Lett. 67 (1995) 1417.

[22] M. Grundman, O. Stier, D. Bimberg, Phys. Rev. B1 52 (1995) 11969.

[23] L.J.M. Selen, L.J.van Ijzendoorn, M.J.A. de Voigt, P.M. Koenraad, Phys. Rev. B 61 (2000) 8270.

[24] J. Johansson, W. Seifert, V. Zwiller, T. Junno, L. Samuelson, Appl. Surf. Sci. 134 (1998) 47.

[25] A.H. Van Ommen, Appl. Surf. Sci. 30 (1987) 244.

ELSEVIER

Thin Solid Films 412 (2002) 89–95

thin solid films

www.elsevier.com/locate/tsf

CdSe quantum islands in ZnSe: a new approach

E. Kurtz[a,1,*], B. Dal Don[a], M. Schmidt[a], H. Kalt[a], C. Klingshirn[a], D. Litvinov[b], A. Rosenauer[b], D. Gerthsen[b]

[a]*Institut für Angewandte Physik, Universität Karlsruhe, D-76128 Karlsruhe, Germany*
[b]*Labor für Elektronenmikroskopie, Universität Karlsruhe, D-76128 Karlsruhe, Germany*

Abstract

While providing a general overview over the current status of self-organization of quantum islands in the II–VI semiconductor system, with the main focus on CdSe embedded in ZnSe, this paper shall give an introduction to the possibilities opened by a modification of the standard growth technique. In molecular beam epitaxy, we have substituted the generally used Cd-elemental source with a CdS-compound source. The sulfur is usually not included in the growing layer. However, its presence can be surfactant-like while the elevated Cd-temperature of the dissociated CdS leads to changed thermodynamic conditions on the growth front. Using migration enhanced epitaxy, nearly perfect quantum wells with respect to lateral homogeneity can be obtained by suppressing the inherent Cd segregation and clustering. These processes are generally responsible for the formation of small islands (SI) (lateral diameter 3–5 nm) even when not attempting to grow island like structures. The suppression of these SI was a first step to gain control over the island formation. Larger islands with central Cd concentrations above 40% are more of interest for device applications, since a population at room temperature is necessary. In particular, high-density systems are required. Using the modified growth mode, well correlated, stacked island systems were obtained. Their outstanding structural and optical properties will be discussed in detail. The absence of a closed wetting layer in the CdSe/ZnSe system and the appearance of island like structures, even at submonolayer nominal deposition, further corroborate the assumption that island formation does not readily occur in a standard Stranski–Krastanow growth mode, which is assumed for InAs/GaAs.

PACS: 68.65.Hb; 78.67.Hc; 78.55.Et; 78.20.Dx; 78.66.Hf; 81.05.Dz

Keywords: MBE growth; Self-organized structures; CdSe/ZnSe; Quantum islands

1. Introduction

The large variety of new possible applications exploiting the quasi zero-dimensional nature of quantum dots (QD) has drawn attention to self-organizing semiconductor systems, such as the well investigated InAs/GaAs [1] and II–VIs like CdSe/ZnSe [2–4] and CdTe/ZnTe [5,6]. The latter system would be suitable for optoelectronic devices in the green visible spectral range. InAs QDs form on GaAs in the Stranski–Krastanow (SK) mode [7]. Elaborated techniques like indium flush [8] allow for very controlled embedding and coherent stacking of the QDs. With this method, the first outstanding near infra-red emitting laser devices have been demonstrated by various groups [9]. For CdSe-based islands, the formation mechanisms are not completely understood, and recent results indicate that the formation does not occur in an SK mode, but rather is driven by a strong tendency of segregated Cd to form clusters. The strong differences in growth kinetics and island formation mechanisms are responsible for the very different behavior of CdSe based islands, as compared to the classical InAs/GaAs-system. In particular, to obtain a controlled island formation with predictable island sizes and ordering appears to be difficult as the competition between island formation and misfit dislocation formation as strain relaxing mechanisms plays an important role. Furthermore, a surface activated interduffusion occurs between Cd and Zn which leads to washed out and broadened Cd concentration profiles

---

*Corresponding author. Tel.: +49-931-354400; fax: +49-931-3544010.

E-mail address: elisabeth.kurtz@physik.uni-karlsruhe.de (E. Kurtz).

[1] KurtzDesign@t-online.de.

0040-6090/02/$ - see front matter © 2002 Elsevier Science B.V. All rights reserved.
PII: S0040-6090(02)00318-8

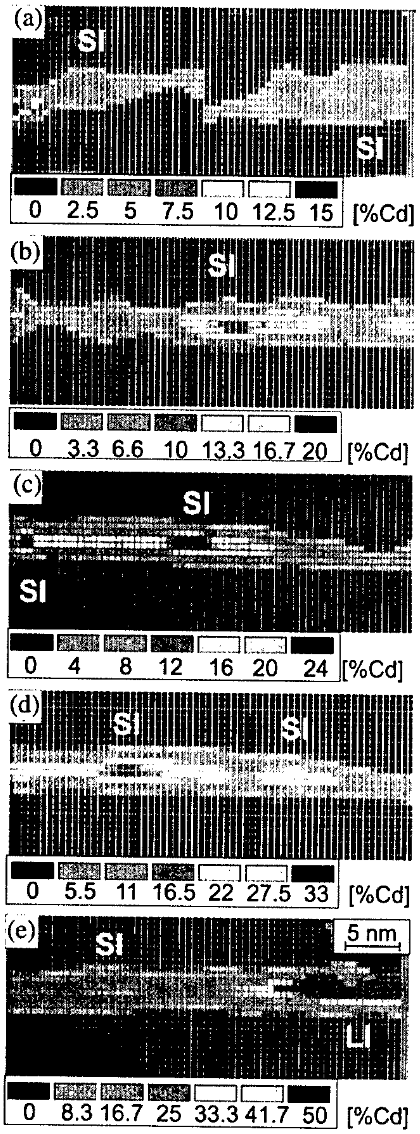

Fig. 1. Color coded Cd concentrations obtained by CELFA for a series of CdSe/ZnSe layers with varying nominal CdSe deposition: (a) 0.5 ML; (b) 1 ML; (c) 1.5 ML; (d) 2.5 ML; and (e) 3.5 ML. Cd concentrations are given in [%] according to the color code. Cd accumulations corresponding to SIs are observed even for 0.5 ML; one LI was captured for 3.5 ML.

[10,11]. In the following, we will discuss the implications and demonstrate ways to partially overcome some of these problems.

2. Classical growth methods

Using molecular beam epitaxy (MBE) under standard growth conditions (employing elemental Cd and Se at growth temperatures in the range of 270–320 °C), island formation has been demonstrated by various groups [2,12,13]. First indications that quasi-zero-dimensional states might play a role in the strong lateral localization observed in CdSe/ZnSe submonolayer structures date back to 1993 [14]. Nowadays, it is common knowledge [15–18] that a type of smaller island is generally formed when embedding CdSe in ZnSe, which we will refer to in the following as 'small islands' (SI) for simplicity. Fig. 1 demonstrates this unintentional type of islands which manifests in Cd accumulations of typically 3–5 nm lateral diameter in a series of quantum wells (QW). Composition evaluation by lattice fringe analysis (CELFA) [19] allows a direct access of the Cd concentration in ternary (Cd, Zn)Se alloys with respect to pure ZnSe. The color code is directly related to the Cd concentration as given in the individual figures. The thickness of the QWs was varied from 0.5 to 3.5 ML deposited by controlled atomic layer epitaxy (ALE) where one shutter cycle corresponds to approximately 0.5 ML [20]. Surface activated interdiffusion leads to the generally broad Cd distribution in growth direction. A strong indication for this mechanism is the fact that all distributions, shown in Fig. 2, have basically the same width (≈11 ML), while the central Cd concentration increases with increasing nominal deposition and is independent of the total cap layer thickness. The appearance of islands even for a sub-monolayer deposition and the absence of a closed wetting layer corroborate the assumption that SIs do not form in an SK mode.

The SIs are of general interest for investigating fundamental physical properties of quasi-zero-dimensional systems [5,21–24], in particular, lateral interactions, which can be observed by time and temperature resolved optical measurements. The SI, however, are not suitable for room temperature device applications since they are unoccupied due to thermal activation at temperatures above 150 K [25,26]. The time-evolution of the photoluminescence (PL) for the 2.5 and 3.5 ML QWs containing SIs from Fig. 1 is shown in Fig. 3. A strong lateral interaction is indicated by a pronounced

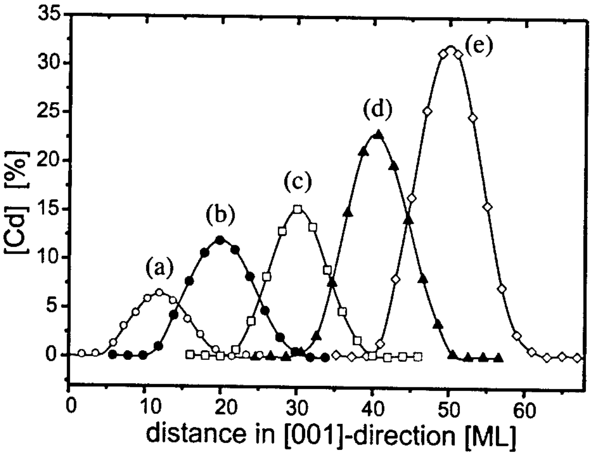

Fig. 2. Cd concentration profiles extracted from Fig. 1 with a typical, approximately Gaussian distribution. The labels correspond to (a–e) of Fig. 1; the curves are shifted horizontally for clarity.

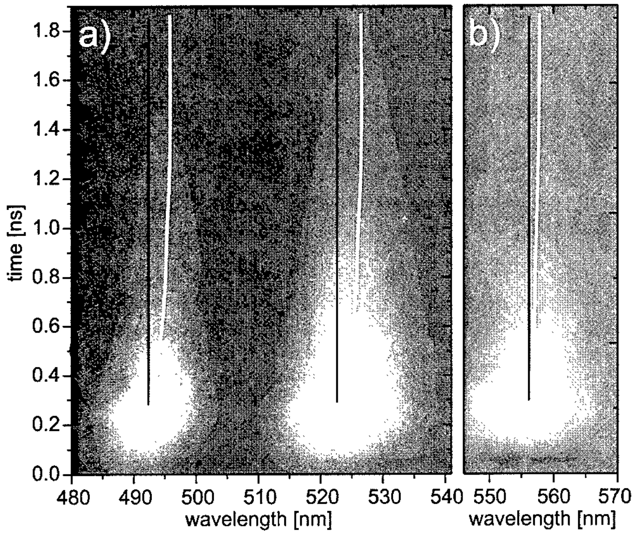

Fig. 3. Time resolved PL maps for: (a) the two thicker QWs of Fig. 1 consisting of laterally strongly interacting SIs. (b) A sample containing LIs with weak lateral interaction, mirroring in a reduced red shift with time. The evolution of the respective PL maxima has been indicated by a white line.

red shift of the luminescence emission peak, which is explained by the lateral transfer of excitons into deeper neighboring islands with time. This is only possible because the typical SI densities are of the order of 5×10^{11}–10^{12} cm^{-2}. The appearance of phonon replica with a distinct temporal evolution fingerprint points to a recombination of the transfer exciton in a different island and gives a hint of how this transfer is achieved: by phonon assisted hopping [27].

Large islands (LI) with a higher central Cd concentration of more than 40% and diameters of the order of 10 nm are desired for potentials deep enough to allow a room temperature population [18]. Such islands are formed if the nominal CdSe coverage exceeds ≈1.8 ML [28]. Density and sizes can roughly be controlled by intentional Ostwald ripening, i.e. introducing short growth interrupts of the order of few seconds. LI densities are typically of the order of 1–5×10^{10} cm^{-2} and are possibly more comparable to the SK islands observed in the III–V system InAs/GaAs. The lateral interaction between these islands is weaker due to the larger average distance, and the pronounced red shift observed in Fig. 3b is reduced in comparison with the SI, since excitons recombine in the LI in which they were captured initially; see also [13,29].

It has to be noted that the formation mechanism of the LIs is not yet understood. These islands are subject to a strong Ostwald ripening when left uncapped if the nominal CdSe deposition exceeds 2.5 ML [28] and can be associated with a stacking fault when exceeding a maximum size [30–32].

In order to control the formation of LIs, techniques such as low temperature ALE have been introduced [3,13,33,34]. However, it would be desirable to avoid the extensive temperature ramps when growing multilayer stacks. Introducing sulfur in the growth process by using CdS as a Cd supply seems to allow a rather reproducible formation of CdSe-based LIs. The islands are directly formed at the standard growth temperature of the ZnSe buffer layer at 280 °C.

3. Introducing sulfur by using a CdS compound instead of elemental Cd in MBE

In order to gain control over the island formation, we first tried to suppress island formation all together. The technique that proved to be most suitable was to substitute the commonly used Cd-elemental source with a CdS-compound source and use a migration enhanced growth mode with long waiting times after the Cd deposition to allow excess Cd to chemically bind onto the surface [11]. While the interface driven interdiffusion remains a problem (as seen in Fig. 4), the Cd segregation and clustering could be almost completely suppressed, as demonstrated by the rather sharp interfaces and the plateau-like Cd distribution observed for these QWs. Few Cd accumulations are observed which may be associated with stacking faults propagating and penetrating the layer from the GaAs/ZnSe interface. The strain field leads to an attraction of Cd or even an enhanced interdiffusion Cd/Zn, which is consistent with the findings Shubina et al. [35] and Lüerßen et al. [36]. The photoluminescence (PL) emission spectral halfwidth (shown in [11]) is, at 12 and 16 meV, respectively, close to the theoretical limit for ternary QWs, where a random distribution of the Cd leads to an inhomogeneous broadening [37,38]. Calculations according to the model of Mathieu et al. [39] lead to the suggestion that in the calculations used, the valence band offset between CdSe/ZnSe of 16% [40] needs to be corrected to higher values when considering the absence of SIs, since this type of laterally varying potential was neglected in the early measurements of (Cd,Zn)Se-based quantum structures [11].

Using a CdS compound source has several advantages. The oven temperature is, at 650 °C, much higher than for elemental Cd (220 °C) allowing the incoming atoms/molecules to transfer a higher thermal energy to the surface, which possibly leads to a higher surface temperature and a higher mobility or diffusion length of adatoms. As has been shown by Goldfinger et al. [41], CdS decomposes into atomic Cd and sulfur dimers when desorbed. The low sticking coefficient of sulfur with respect to Se, therefore, leads to only a minor sulfur contamination $\leq2\%$ [42]. Schikora et al. [43] have recently shown by the observation of the recovery of a streaky 2D-RHEED (reflection high energy electron

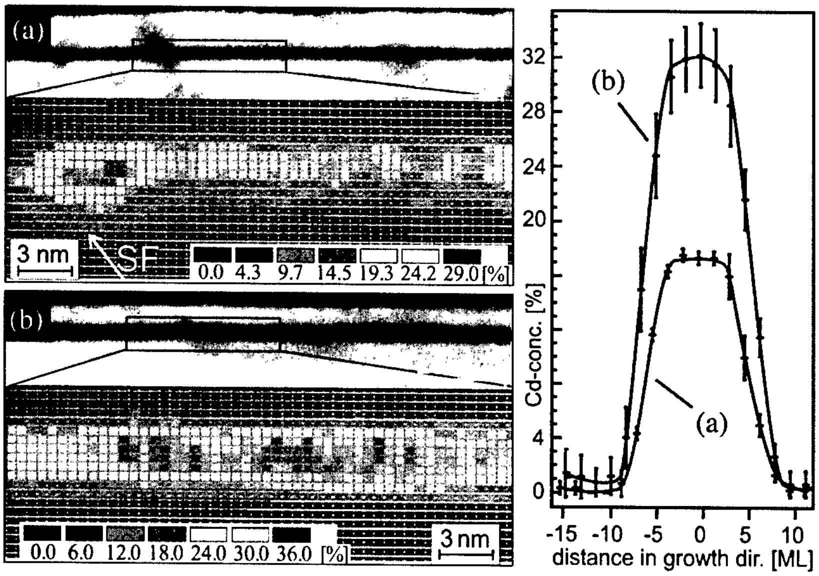

Fig. 4. CELFA of two quantum wells grown by CdS+Se MEE. Nominal CdSe deposition: (a) 1.6 ML; (b) 3.2 ML. Panel (c) shows the Cd concentration profiles extracted from (a) and (b). The steepness of the flanks is mainly resolution limited.

diffraction) pattern, typical for flat surfaces, that the presence of a massive sulfur flux may cause a resolution of previously formed CdSe islands. In our case, only a small amount of sulfur is present at the surface, which may act as a surfactant improving the CdSe nucleation. In case of the QWs, the long waiting times lead to a complete desorption of the sulfur, while in the case of continuous growth the presence of the sulfur seems to enhance the nucleation of islands. In that matter, a more controlled island formation was achieved, which enabled us to coherently stack CdSe LIs.

4. Stacked CdSe islands

To truly exploit the strong enhancement of the oscillator strength in a narrow spectral range expected for a quasi-zero-dimensional QI system, it is necessary to guarantee a narrow ensemble size distribution and to enhance the island density. This is best achieved by subsequently stacking multiple QI layers with a suitable spacer thickness. In the III–V case, elaborate techniques allow for very good control of island stacks, which have been used in the first devices [44].

Very few reports exist for II–VI systems of correlations in stacked layers [6,31,32,45]. Early reports [45] cover the dependence of correlation and anti-correlation in short period submonolayer CdSe/ZnSe stacks on stacking conditions such as barrier thickness. Litvinov et al. [31,32] demonstrated coherently stacked islands obtained at elevated growth temperatures of 400 °C in triple stacks if the barrier thickness corresponded to 12–20 monolayers (ML), while for a smaller thickness, a complete intermixing due to interdiffusion occurred. To study stacked LIs, we have chosen a spacer layer thickness of 4 nm, i.e. 14 ML. Even though the formation of LIs may not occur in the SK mode, the strain induced by an underlying layer of islands leads to a favorable accumulation of Cd on top of these islands. Stacks with very similar appearance, as in comparable InAs/GaAs structures, are formed, which can be seen in Fig. 5. In this example, an unusually high central Cd concentration above 80% has been observed; for further details, see Kurtz et al. [16]. The resulting contrast inversion allows the island stacks to be easily distinguished from the surrounding regions, which consist of laterally strongly interacting SIs [25,27]. This region will be referred to as uncorrelated region (UR) in the following, since no direct positional correlation could be observed for SIs in subsequent layers in CELFA. In PL, two transitions can be distinguished, which are assigned to the emission from the correlated LIs and the UR, as shown in Figs. 6 and 7. While similar spectra are observed from InAs/GaAs single layers showing wetting layer and island emission, in the case of CdSe/ZnSe based single layer structures, only one emission band is observed in general. This emission band corresponds to the LI band if a sufficient number of radiating LIs are present or to the SI band if the LI density is too low. The stacking appears to improve the ordered LI formation. The high quality and homogeneity of the stacks is demonstrated by the rather narrow PL linewidth of typically 30–40 meV. It has to be noted, however, that initially formed islands are partially dissolved in the cap layer [42], which changes the appearance of the islands to a pancake or lens shape. The emission energy is more two-dimensional like, and seems to be determined by the island height rather than the lateral size, which generally exceeds the exciton

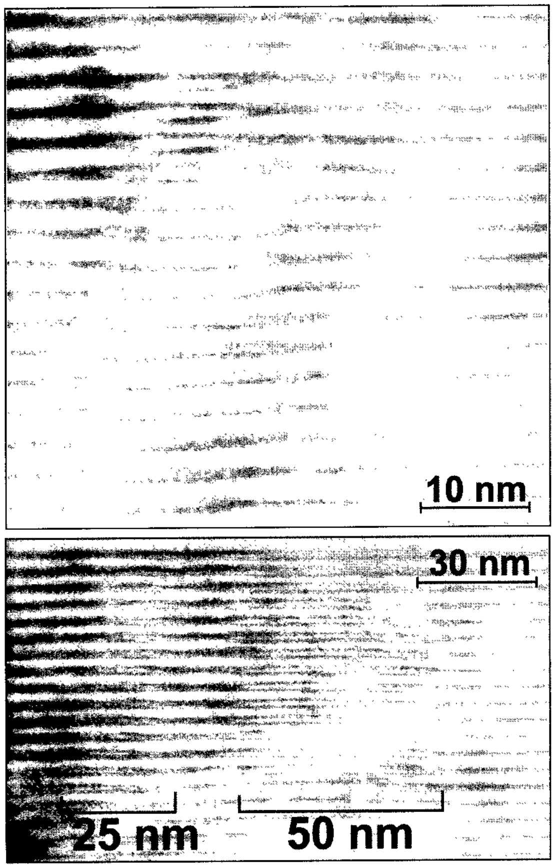

Fig. 5. Cross-sectional (002) dark field TEM images of a sample with 50 stacked layers with 4 nm ZnSe spacers. The island stacks are clearly observable by the contrast inversion owing to a rather high central Cd concentration of more than 80% [16].

Bohr radius and can vary between 20 and 50 nm within one sample. Nevertheless, the lateral size remains roughly constant within a single stack, as seen in Fig. 5.

With an increasing number of stacked layers (2, 4 and 8) the UR-PL band is enhanced as shown in Fig. 6. Two reasons could be responsible. The higher probability of finding deeper localization sites within the SI contained in the UR by vertical interaction can reduce the transfer of excitons from the UR to the LI stack. Even more reasonable appears to be the saturation of the LI emission due to the strong vertical interaction of the stacked islands. A vertical localization is expected within one stack due to variations in the island sizes. Thus, the stack states can be filled and the number of deepest LI states does not increase with increasing the number of stacked layers, while the weaker vertical interaction of the SIs leads to an increasing number of SI states proportional to the number of stacks, which can be seen in an approximate doubling of the integrated intensity of the UR peak for twice the number of layers; see Fig. 6. Furthermore, only a minor red shift occurs for the UR region when increasing the number of layers,

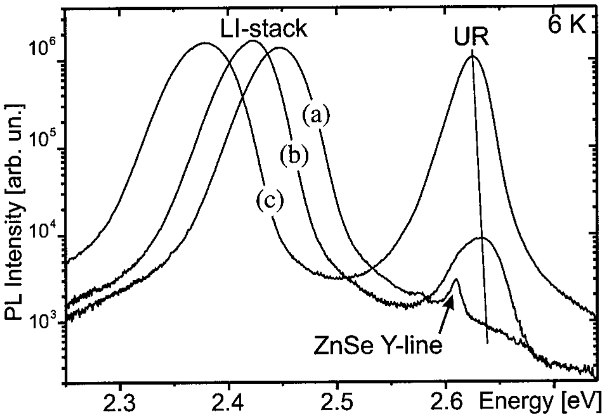

Fig. 6. Photoluminescence spectra for a series of stacked CdSe layers with constant nominal CdSe deposition (≈2 ML) and varying number of layers: (a) two; (b) four; and (c) eight layers, respectively. The barrier width was set to 4 nm.

showing that these layers are mainly independent while the strong red shift of the LI stack corroborates the assumption of a strong interaction within a single stack.

As shown in Fig. 7, an increasing total CdSe deposition at a fixed number of stacked layers of 12 leads to an enhanced splitting of the LI and UR emission, which is an indication of the increasing height of the LI islands with respect to the SI, while both types gain in the central Cd concentration.

Looking at the temperature dependent PL intensity of the intermediate sample (b) of Fig. 7, plotted in Fig. 8, a strong transfer of excitons into the LI stack is observed by the enhancement of the LI emission at temperatures above 50 K. Excitons are easily thermally activated

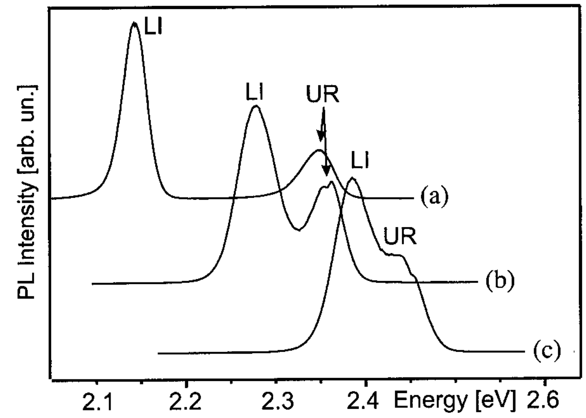

Fig. 7. Photoluminescence spectra for a series of stacked CdSe layers with constant number of layers (12) and varying nominal CdSe deposition: (a) 3–4 ML; (b) ≈2.5 ML; and (c) ≈2 ML. The CdSe growth rate was approximately twice as fast than for the previous series leading to a smaller LI–UR separation, as smaller islands are formed. Sample (a) contains stacking faults bounded by 60°-dislocations starting in the first CdSe layer. The islands are aligned along these similar to [35].

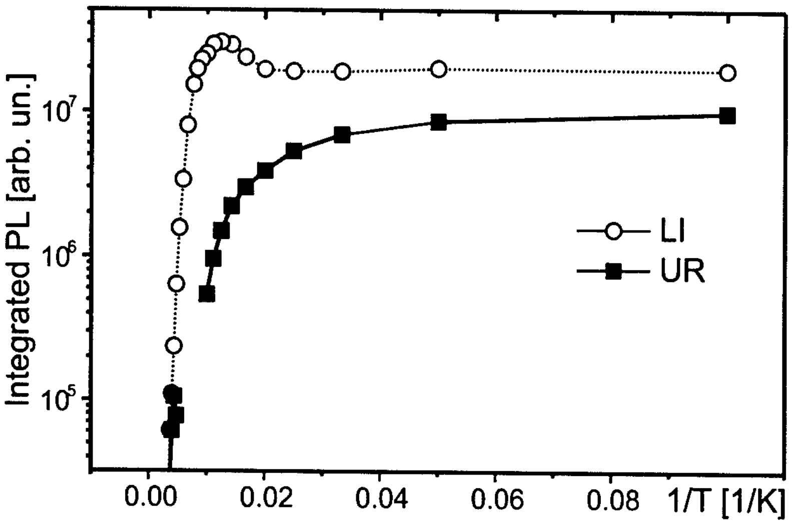

Fig. 8. Arrhenius plot of the PL intensity vs. the inverse of temperature demonstrating the thermal activation of excitons from the UR (full squares) which are then captured by the LI (open circles), indicated by a strong increase of the LI intensity at temperatures above 50 K.

from their localization in the SIs into the continuum of the UR as mentioned in Section 2. These excitons can then be recaptured by the LI stack, thus feeding the LI emission with an activation energy of ≈8–9 meV corresponding to 90–100 K. The activation energy for a depopulation of the LI, at ≈70 meV, corresponds reasonably well to the energy separation of 82 meV between LI and UR emission peaks observed at low temperatures.

5. Conclusions

Using a modified growth technique we have demonstrated that the suppression of Cd/Zn segregation can lead to QWs with very weak lateral confinement. In contrast, a better control over the island formation is achieved and it was possible to obtain well-correlated CdSe-based quantum island stacks. The optical properties gave a first insight into interactions between the various types of islands and will allow a very detailed study by time- and spatially resolved PL in the future to gain a better insight into the fundamental physical transfer mechanisms and types of interactions.

Acknowledgments

The authors would like to thank the Deutsche Forschungsgemeinschaft (DFG) for support.

References

[1] D. Bimberg, M. Grundmann, N.N. Ledentsov, Quantum Dot Heterostructures, John Wiley and Sons, Chichester, 1999.
[2] S.H. Xin, P.D. Wang, A. Yin, C. Kim, M. Dobrowolska, J.L. Merz, J.K. Furdyna, Appl. Phys. Lett. 69 (1996) 3884.
[3] M. Rabe, M. Lowisch, F. Henneberger, J. Cryst. Growth 184/185 (1998) 248.
[4] E. Kurtz, J.X. Shen, M. Schmidt, M. Grün, S.K. Hong, D. Litvinov, D. Gerthsen, T. Oka, T. Yao, C. Klingshirn, Thin Solid Films 367 (2000) 68.
[5] L. Besombes, K. Kheng, L. Marsal, H. Mariette, Phys. Rev. B 63 (2001) 155307.
[6] S. Mackowski, 4th Int. Workshop MBE and VPE Growth Phys. Technol. Warsaw, Poland (2001), to appear in Thin Solid Films (2002), this volume, and references therein.
[7] W. Seifert, N. Carlsson, M. Miller, M.E. Pistol, L. Samuelson, R. Wallenberg, J. Prog. Crystal Growth Charact. Meter. 33 (1997) 423.
[8] Z.R. Wasiliewski; 4th Int. Workshop MBE and VPE Growth Phys. Technol. (01-MBE&VPE-GPT) Warsaw, Poland (2001), to appear in Thin Solid Films (2002), this volume.
[9] e.g. chapter *Quantum dot lasers* in: Proc. Int. Conf. on Semicond. Quantum Dots (QD2000), Munich, Germany 2000; Phys. Stat. Sol. 224 (2001) 787
[10] N. Peranio, A. Rosenauer, D. Gerthsen, S.V. Sorokin, I.V. Sedova, S.V. Ivanov, Phys. Rev. B 61 (2000) 16015.
[11] E. Kurtz, M. Schmidt, M. Baldauf, S. Wachter, M. Grün, H. Kalt, C. Klingshirn, D. Litvinov, A. Rosenauer, D. Gerthsen, Appl. Phys. Lett. 79 (2001) 1118.
[12] F. Flack, N. Samarth, V. Nikitin, P.A. Crowell, J. Shi, J. Levy, D.D. Awshalom, Phys. Rev. B 54 (1996) R17312.
[13] E. Kurtz, J. Shen, M. Schmidt, M. Grün, S.K. Hong, D. Litvinov, D. Gerthsen, Y. Oka, T. Yao, C. Klingshirn, Thin Solid Films 367 (2000) 68.
[14] Z. Zhu, H. Yoshihara, K. Takebayashi, T. Yao, Appl. Phys. Lett. 63 (1993) 1678.
[15] D. Litvinov, A. Rosenauer, D. Gerthsen, N.N. Ledentsov, Phys. Rev. B 61 (2000) 16819.
[16] E. Kurtz, M. Schmidt, D. Litvinov, B. Dal Don, R. Dianoux, Hui Zhao, H. Kalt, A. Rosenauer, D. Gerthsen, C. Klingshirn, 10th Int. Conf. on II-VI Compounds, Bremen, Germany (2001); to appear in Phys. Stat. Sol. (2002).
[17] D. Schikora, S. Schwedhelm, D.J. As, K. Lischka, D. Litvinov, A. Rosenauer, D. Gerthsen, M. Strassburg, A. Hoffmann, D. Bimberg, Appl. Phys. Lett. 76 (2000) 418.
[18] M. Strassburg, Th. Denizou, A. Hoffmann, R. Heitz, U.W. Pohl, D. Bimberg, D. Livtinov, A. Rosenauer, D. Gerthsen, S. Schwedhelm, K. Lischka, D. Schikora, Appl. Phys. Lett. 76 (2000) 685.

[19] A. Rosenauer, D. Gerthsen, Adv. Imaging Electron Phys. 107 (1999) 121–230.

[20] J.M. Hartmann, G. Feuillet, M. Charleux, H. Mariette, J. Appl. Phys. 79 (1996) 3035.

[21] G. Bacher, R. Weigand, J. Seufert, V.D. Kulakovskii, N.A. Gippius, A. Forchel, K. Leonardi, D. Hommel, Phys. Rev. Lett. 83 (1999) 4417.

[22] F. Gindele, K. Hild, W. Langbein, U. Woggon, K. Leonardi, D. Hommel, T. Kummell, G. Bacher, A. Forchel, J. Lumin. 83-84 (1999) 305.

[23] T. Flissikowski, A. Hundt, M. Lowisch, M. Rabe, F. Henneberger, Phys. Rev. Lett. 86 (2001) 3172.

[24] G. Von Freymann, E. Kurtz, C. Klingshirn, M. Wegener, Appl. Phys. Lett. 77 (2000) 394.

[25] S. Wachter, B. Dal Don, M. Schmidt, M. Baldauf, A. Dinger, E. Kurtz, C. Klingshirn, H. Kalt, Phys. Stat. Sol. (b) 224 (2001) 437.

[26] S. Wachter, B. Dal Don, M. Baldauf, M. Schmidt, E. Kurtz, C. Klingshirn, H. Kalt, D. Litvinov, D. Gerthsen, in: K. Cho, A. Matsui (Eds.), Proc. Exc. Proc. Cond. Matter (EXCON 2000), Osaka, Japan, World Scientific, Singapore, 2001, p. 17.

[27] B. Dal Don, R. Dianoux, S. Wachter, M. Schmidt, E. Kurtz, G. von Freymann, C. Klingshirn, M. Wegener, H. Kalt, 10th Int. Conf. on II–VI Compounds, Bremen, Germany (2001); to appear in Phys. Stat. Sol. (2002).

[28] H. Preis, K. Fuchs, W. Gebhardt, Phys. Stat. Sol. (b) 224 (2001) 527.

[29] E. Kurtz, T. Sekiguchi, Z. Zhu, T. Yao, J.X. Shen, Y. Oka, M.Y. Shen, T. Goto, Superlattices Microstruct. 25 (1999) 119.

[30] D. Litvinov et al., 10th Int. Conf. on II–VI Compounds, Bremen, Germany (2001); to appear in Phys. Stat. Sol. (2002)

[31] D. Litvinov, A. Rosenauer, D. Gerthsen, H. Preis, E. Kurtz, C. Klingshirn, Phys. Stat. Sol. 224 (2001) 147.

[32] D. Litvinov, A. Rosenauer, D. Gerthsen, H. Preiss, E. Kurtz, J. Appl. Phys. 89 (2001) 3695.

[33] M. Rabe, M. Lowisch, F. Henneberger, J. Cryst. Growth 184/185 (1998) 248.

[34] P.R. Kratzert, M. Rabe, F. Henneberger, Phys. Stat. Sol. (b) 224 (2001) 179.

[35] T.V. Shubina, A.A. Sitnikova, V.A. Solov'ev, A.A. Toropov, I.V. Sedova, S.V. Ivanov, M. Keim, A. Waag, G. Landwehr, J. Cryst. Growth 214/215 (2000) 727.

[36] D. Lüerßen, R. Bleher, H. Kalt, H. Richter, T. Schimmel, A. Rosenauer, D. Litvinov, A. Kamilli, D. Gerthsen, B. Jobst, K. Ohkawa, D. Hommel, J. Cryst. Growth 214/215 (2000) 634.

[37] A. Klochikhin, A. Reznitskii, L. Tenishev, S. Permogorov, S. Ivanov, S. Sorokin, Kh. Mumanis, R. Seisyan, C. Klingshirn, JETP Lett. 71 (2000) 242.

[38] A. Klochikhin, A. Reznitsky, S. Permogorov, M. Grün, M. Hetterich, C. Klingshirn, V. Lyssenko, W. Langbein, J.M. Hvam, Phys. Rev. B 59 (1999) 12947.

[39] H. Mathieu, P. Lefebvre, P. Christol, Phys. Rev. B 46 (1992) 4092.

[40] S. Lankes, T. Reisinger, B. Hahn, C. Meier, M. Meier, W. Gebhardt, J. Cryst. Growth 159 (1995) 480.

[41] P. Goldfinger, M. Jeunehomme, Trans. Faraday Soc. 59 (1963) 2851.

[42] E. Kurtz, M. Schmidt, M. Baldauf, S. Wachter, M. Grün, D. Litvinov, S.K. Hong, J.X. Shen, T. Yao, D. Gerthsen, H. Kalt, C. Klingshirn, J. Cryst. Growth 214/215 (2000) 712.

[43] D. Schikora et al., 10th Int. Conf. on II–VI Compounds, Bremen, Germany (2001); to appear in Phys. Stat. Sol. (2002).

[44] K. Hinzer, M. Bayer, J.P. McCaffrey, P. Hawrylak, M. Korkusinski, O. Stern, Z.R. Wasiliewski, S. Fafard, A. Forchel, Phys. Stat. Sol. (b) 224 (2001) 385.

[45] I.L. Krestnikov, M. Strassburg, M. Caesar, A. Hoffmann, U.W. Pohl, D. Bimberg, N.N. Ledentsov, P.S. Kopev, Zh.I. Alferov, D. Litvinov, A. Rosenauer, D. Gerthsen, Phys. Rev. B 60 (1999) 8695.

ELSEVIER

Thin Solid Films 412 (2002) 96–106

thin solid films

www.elsevier.com/locate/tsf

CdTe/ZnTe quantum dots—growth and optical properties

Sebastian Mackowski*

Institute of Physics Polish Academy of Sciences, Al. Lotników 32/46, Warsaw, Poland

---

Abstract

This paper gives an overview of molecular beam epitaxy growth aspects and of optical properties of CdTe quantum dots grown on ZnTe by self-assembly. It is shown that quantum dots in this material system can be obtained either by depositing CdTe at a high substrate temperature or by subjecting CdTe layer to a healing process, up to 70 s long before its capping or, eventually, by applying these two methods simultaneously. Moreover it is found, that one can also use the atomic layer epitaxy method to achieve the formation. From optical measurements performed on large quantum dot ensembles it is found out that the quantum dot emission is much broader than that from quantum wells, and that it is observable up to much higher temperatures, which indicates strong exciton localization. The latter is also evidenced by an insensitivity of the decay time of the exciton recombination (~300 ps) to the temperature. From the presence of a second, very long decay time (~5 ns) and from disappearance of the sharp lines related to recombination in single dots, the acoustic phonon scattering of excitons is found to play an important role in these quantum dot structures. From a magnetic field dependence of the single dot emission energy, the exciton effective g-factor and spatial extension of the exciton wave function are deduced to be equal to -3 and 3 nm, respectively. Both the g-factor and the value of the diamagnetic shift are found to be independent of the energy of the quantum dot emission at $B=0$ T and of the in-plane symmetry of its potential. © 2002 Elsevier Science B.V. All rights reserved.

Keywords: Cadmium telluride; Molecular beam epitaxy; Nanostructures; Optical spectroscopy

---

1. Introduction

In this paper several aspects of growth and optical properties of self-assembled CdTe quantum dots (QDs) in ZnTe matrix are reviewed. This particular material system is interesting from the point of fabrication of QDs [1–3] since the lattice mismatch between these two constituents is similar to that of InAs/GaAs [4], which is the most widely studied system in the context of QDs. However, as one can expect, different chemical properties of II–VI compounds such as diffusion coefficients could influence the formation process of this type of nanostructure [5].

We indicate that both healing of CdTe layer after its deposition on ZnTe as well as growth of CdTe at the substrate temperature higher than that used typically for obtaining high quality quantum wells (QWs) [6] result in the formation of three-dimensional structures with nanometric scale on a two-dimensional layer. Moreover, the formation of QDs is also observed when a CdTe layer is grown by atomic layer epitaxy, as reported by another group [3].

The formation of the QDs is evidenced by optical spectroscopy measurements. The low temperature luminescence (PL) emission is characterized by a broad band [5] which exhibits roughly temperature independent decay time [7–9] equal to 300 ps, as long as the effects of carrier redistribution between the dots do not play an important role [8,10]. When decreasing the size of the excitation laser spot this inhomogeneously broadened emission splits into a series of sharp lines with the linewidth of approximately 100 μeV [11–13]. However, with an increase of the temperature the sharp line pattern disappears, as does the intensity of the emission, which is characterized by a very long decay time of the order of several nanoseconds [14–17]. These effects are ascribed to a broadening of the single dot PL line caused by acoustic phonon scattering of excitons [14,17].

The results of PL experiments performed with ultrahigh spatial and spectral resolution on CdTe QDs show that the optical properties of an exciton localized by a single QD potential strongly depend on the in-plane symmetry of the particular QD. Namely, for elongated QD the exciton line splits into linearly polarized doublet [9,13,18]. Furthermore, it is found that the reduction of the dimensionality results in an enhancement of the

---

*Tel.: +48-22-843-1331; fax: +48-22-843-0926.
E-mail address: macko@ifpan.edu.pl (S. Mackowski).

PII: S0040-6090(02)00319-X

effective excitonic g-factor. Surprisingly, the value of g-factor is found to be independent either of the QD confinement energy as well as of the particular in-plane symmetry of the dot. From the magnetic field dependence of the emission energy the value of exciton diamagnetic shift is obtained [11] from which, in turn, the extension of excitonic wavefunction is evaluated to be equal to 3 nm. This value agrees reasonably with the average size of the QDs estimated from transmission electron microscopy data [1].

The present paper is organized as follows. After a detailed description of the samples which includes not only the growth conditions but also the procedure of obtaining small apertures in a metal mask (making experiments with single QDs possible), the experimental set-ups which were used for investigating the optical properties of QDs are briefly presented. In the next part the results of optical experiments are discussed starting from PL characterization of the samples. Then the temperature and the time dependencies of the PL emission are described. The experimental part is completed by a description of microluminescence spectroscopy as a function of the temperature and the magnetic field.

2. Samples and experimental details

The investigated structures were grown by molecular beam epitaxy on (100)-oriented GaAs substrates. In order to avoid dislocations formed due to lattice mismatch between GaAs and CdTe, first buffer layers of CdTe and ZnTe with the thickness ranging between 4 and 5 μm were grown. Since one of the purposes of viewed studies was to describe the influence of the growth conditions on formation of the quantum dots, several procedures of CdTe deposition were employed. Usually, the growth of high quality CdTe quantum wells (QWs) was carried out at a relatively low substrate temperature, namely at approximately $T=300$ °C [6]. At such temperatures the surface diffusion is quite low which results in sharp interfaces between barriers and the well layers. From that point of view an increase of the substrate temperature enhances the mobility of atoms on the surface which could lead to the formation of structures which can localize excitons stronger than in QWs. Another parameter that can help in a process of a QD formation could be the time between stopping the growth of the CdTe layer and capping it next with a ZnTe barrier. If that time is long enough one can expect that the atoms can migrate more easily on the surface. Thus, the effect of such a growth interruption is qualitatively similar to an increase of the substrate temperature. However, in the latter approach some amount of the deposited material could be desorbed from the surface.

The results presented in this paper were basically obtained for four groups of structures. All samples are listed in Table 1 together with the substrate temperature during the growth, time of growth interruption (healing), number of CdTe layers as well as the nominal thickness of the CdTe layer. The last two samples containing just a single CdTe layer were grown by the atomic layer epitaxy method. In all these samples the ZnTe capping barrier layers were thick enough to prevent any interaction between neighboring layers of quantum dots [2]. The reason for growing 10 layers of CdTe QDs was to enhance the optical response from each sample. On the other hand, the samples that contain only one layer of CdTe QDs were explored by means of single dot spectroscopy methods.

Table 1
Parameters of the samples studied in this paper: substrate temperature, time of healing, nominal CdTe thickness and the number of CdTe layers

Sample number	Substrate temperature (°C)	Healing time (s)	Nominal CdTe thickness (ML)	Number of CdTe layers
1	480	0	5	10
2	300	0	5	10
3	300	70	4	10
4	300	0	4	10
5	420	10	1.5	10
6	420	10	2	10
7	420	10	2.5	10
8	320	0	2	1 (ALE)
9	320	0	4	1 (ALE)

Various experimental methods were employed to investigate the optical properties of these structures. The continuous wave PL was excited non-resonantly above the ZnTe barrier gap energy ($\lambda=457$ nm line of an argon laser). The emission was analyzed by a Jobin-Yvon spectrograph equipped with a LN_2-cooled charge-coupled-device (CCD) detector. The temperature of the sample was changed from 4.2 to 200 K. The exciton dynamics was studied by time-resolved PL utilizing the time-correlated single photon counting technique. In this case the signal, after being dispersed by a monochromator, was detected by a fast microchannel plate. As an excitation source for time-resolved PL experiments the frequency-doubled (370 nm) Ti:sapphire laser giving 6 ps long pulses with 80 MHz repetition was used. The temporal resolution of the set-up was equal to 40 ps.

Apart from these methods, which probe the whole QD ensemble, the techniques that allow studying single quantum dots were also used. It becomes possible basically either by focusing the laser spot on the sample surface or by patterning the sample in order to allow optical probing of a very limited number of dots. Part of the microluminescence measurements was performed in a set-up, which allowed to reduce the spot of the laser down to the 2 μm in a diameter by the microscope objective. The sample was mounted in the continuous-flow helium cryostat and the temperature was changed from 6 to 100 K. As the excitation the 514 nm line of an argon later was used, while the PL emission was detected by a CCD camera after being dispersed by a double 1 m monochromator. The spectral resolution of the set-up was equal to 20 μeV. However, due to the large surface density of the dots in the studied structures, by the use of the above-described set-up it was not possible to isolate single emission lines even if a sample contained only one layer of the dots. Thus, in order to suppress further the influence of an inhomogeneous broadening of the QD-related PL emission band (arising from the size, chemical composition or strain fluctuations), the opaque metal (Au/Pd) masks with small apertures were fabricated on the sample surface by electron beam lithography and standard lift-off technique. The size of the apertures estimated by atomic force microscopy was found to be as small as 150 nm.

High-resolution PL measurements were carried out at $T = 4.2$ K at magnetic fields up to 12 T applied parallel to the growth direction. As the excitation source the 514 nm line of an argon laser was used. The laser beam was focused on the sample surface by using a microscope objective down to a spot with the diameter of approximately 0.7 μm. In order to resolve the polarization of the light, the emission was analyzed either by a linear polarizer or by a quarter wave plate combined with a linear polarizer. For spectral detection the signal was dispersed by 0.64 m Jobin-Yvon monochromator and detected by a LN_2-cooled CCD detector. The spectral resolution of the set-up was approximately 100 μeV.

In the following part the experimental results obtained for the CdTe/ZnTe quantum structures will be described in detail together with the analysis of the data. We will start with the PL characterization of the structures and after that the results of the temperature dependent PL and time-resolved PL experiments will be discussed followed by microluminescence spectroscopy both as a function of temperature and magnetic field.

3. Experimental results and discussion

3.1. Photoluminescence characterization of the structures

Low temperature ($T = 4.2$ K) luminescence spectra for all samples listed in Table 1 are presented in Fig. 1. In the case of the sample grown at the high substrate temperature of 480 °C (Fig. 1a) as well as the one subjected to 70 s healing after CdTe deposition (Fig. 1b) substantial differences are visible when comparing the spectra with those obtained for QWs. Namely, in both cases the PL line is broadened and the PL emission shifts towards higher energies.

The most probable explanation of this behavior could be an effective narrowing of the deposited CdTe layer during the growth at such conditions. Namely, at higher growth temperatures the desorbtion from the surface becomes very important. This results with the narrowing of the well width. Because the PL emission energy increases with the decrease of the well width one can see by comparing the data displayed in Fig. 1a,b that the narrowing of the well width is much stronger in the case of sample 1. The blue-shift is almost twice as large as in the case of sample subject to the healing. The difference is intuitively understood since at such a high growth temperature the desorbtion processes are expected to be very effective.

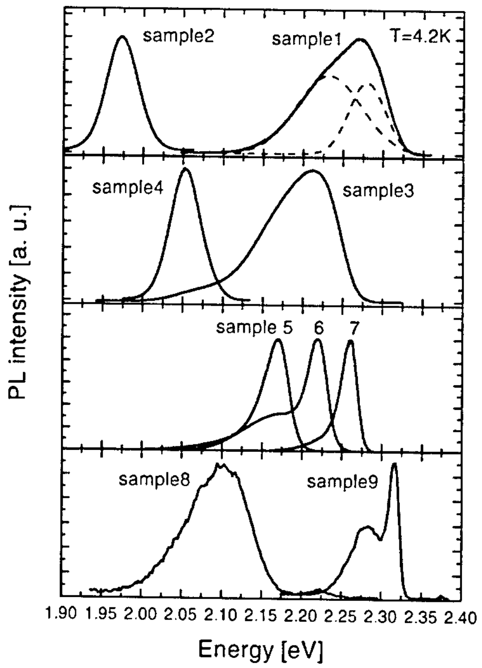

Fig. 1. Low temperature ($T = 4.2$ K) PL spectra for all studied structures: (a) growth at high substrate temperature ($T = 480$ °C); (b) growth with applying long time healing after CdTe deposition; (c) growth at $T = 420$ °C combined with several seconds long healing in Cd atmosphere; (d) growth at 320 °C by atomic layer epitaxy. In two first cases also the spectra of the reference samples are shown.

Together with the blue-shift and the broadening of the PL lines in these two structures the lineshape of the PL emission becomes more complicated and, in particular, it is no longer possible to approximate it by a single Gaussian. In Fig. 1a the dashed lines show the result of a fitting of two Gaussians to the PL spectra. Both effects, the broadening of the PL linewidth and its complicated shape can not be fully attributed to the evaporation of CdTe during the epitaxy. The broadening is most probably caused by two mechanisms. On the one hand, due to the large lattice-mismatch between CdTe and ZnTe, the CdTe/ZnTe interface is no more ideally flat. Consequently, the well width fluctuations are likely to occur. Then, if the exciton recombination originates from such an ensemble of quantum wells with different thickness, the observed emission should be obviously much broader than in the case of a quantum well with flat interfaces. On the other hand, apart from QW thickness fluctuations, the interdiffusion of Cd and Zn across the interface seems to be also the process of importance, apparently in the case of sample 1 shown in Fig. 1a.

Both these effects are most probably responsible for the observed broadening of the PL line in the investigated structures. As will be shown in the following, applying either a long healing time or growing the structure at a high temperature lead to a strong excitonic localization. The properties of excitons confined in these two structures are very similar to that observed for self-assembled quantum dots.

In Fig. 1c the PL spectra obtained for the structures where both several seconds long healing (up to 10 s) as well as medium-high substrate temperature ($T=420$ °C) conditions were applied during the growth. In this case for all three structures with a different nominal thickness of CdTe (samples 5, 6 and 7), two emission bands are present in the spectra. On the basis of the results of optical measurements the high-energy emission is assigned to the recombination of excitons in a two-dimensional quantum well, while the low energy line represents the recombination in CdTe quantum dots. Thus, at this stage we may assume that at these growth conditions the self-assembly process takes place, which leads to the formation of quantum dots. From the transmission electron microscopy data reported elsewhere, the average diameter and surface density of QDs in these structures were estimated to be 4 nm and 10^{11}–10^{12} cm^{-1}, respectively [1].

However, as compared with the results reported for InAs QDs in GaAs matrix, the CdTe/ZnTe structures exhibit a substantial different behavior, which indicates that the formation of QDs in the latter system is more complicated than that observed for III-V compounds. Namely, in the III–V systems, when the transformation of the growth mode occurs and the QDs are spontaneously formed on the thin QW called a wetting layer (WL), the thickness of the WL remains unchanged even if the material the dots are formed of is still deposited on the surface [19–21]. In other words, after the transformation all the material is accumulated within the dots: their density as well as their size increases with the increase of the nominal thickness of the QD layer.

Contrary to that, as evidenced in Fig. 1c, with the increase of the nominal thickness of CdTe both the QW and the QD-related emission lines shift towards lower energies. Moreover, together with this shift the ratio between QW and QD recombination intensity is getting smaller. This result indicates that when putting more and more material (i.e. CdTe) on the surface both the two-dimensional QW is getting thicker and the dots are developing in sizes and density, as well.

Such a behavior is even more visible in Fig. 1d, where the PL spectra for the structures grown by atomic layer epitaxy are presented (sample 8 and sample 9). Namely, in the case of the sample with the nominal CdTe thickness of 2 ML one can easily distinguish both QW- and QD-related emissions, while for the sample with the nominal CdTe thickness of 4 ML the QW emission is no longer present. The only visible line is related to excitonic recombination in CdTe quantum dots.

The absence of abrupt growth mode change, from a two-dimensional to three-dimensional one, as observed in CdTe/ZnTe material system, results in a gradual change of reflection high-energy electron diffraction (RHEED) pattern. Contrary to the case of II–VI semiconductor QDs [5], for InAs/GaAs materials sharp transformation of the RHEED pattern, i.e.: from a streaky (characteristic for two-dimensional growth) to spotty (characteristic for three-dimensional growth) was observed [4]. In particular, such a change in RHEED pattern is usually recognized as a signature of QD formation during the growth. On the basis of scanning transmission electron microscopy results obtained for CdSe QDs in ZnSe matrix the following scenario for QD formation was proposed [5]. At the early stage of growth two-dimensional platelets are formed which may be considered as precursors for coherent QDs formation. Eventually, these two-dimensional platelets could form a uniform QW. During this process coherent dots are developed when more and more material the dots are formed of is deposited. The optical spectra shown in Fig. 1 reveal indeed the presence of such two types of structures. This indicates that the QD formation in CdTe/ZnTe system is very similar to that observed in another II–VI material pair, namely CdSe/ZnSe one.

We would like to point out here, that although in order to obtain self-assembled QDs we applied either molecular beam epitaxy (samples shown in Fig. 1c) or atomic layer epitaxy (samples shown in Fig. 1d), the spectral features observed for these two types of structures are qualitatively very similar to each other. One could then conclude that the principle of the dot formation in this system is independent of the growth method applied, although the parameters of obtained QDs such as shape, size or chemical composition can depend on the particular growth procedure.

3.2. Temperature dependence of the photoluminescence

In the following part the influence of the temperature on the PL emission is discussed. From the results of these measurements we can assign the high-energy emission present in the majority of spectra shown in Fig. 1 to a quasi two-dimensional excitonic recombination while the low-energy emission seems to be related to excitons confined in quantum dots. Since, in general,

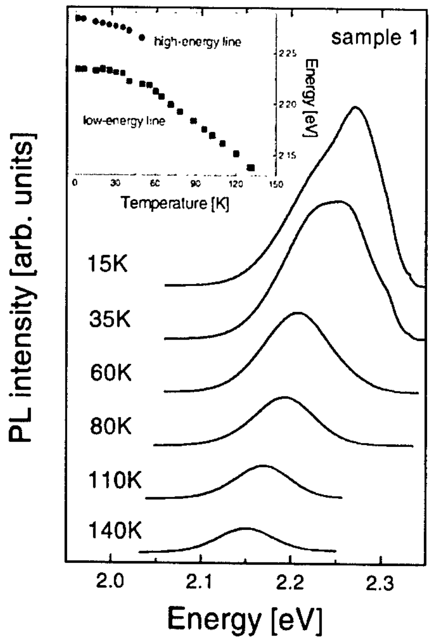

Fig. 2. Temperature evolution of PL emission obtained for sample 1. In the inset the dependence of the emission energy extracted from the spectra is also given.

the observed behavior in the case of all structures was quite similar, we shall consider only the case of the sample 1 (i.e. the one shown in Fig. 1a), which was grown at the substrate temperature equal to 480 °C.

The PL spectra measured for this particular sample at different temperatures are presented in Fig. 2. With an increasing temperature the spectra change substantially. Namely, apart from shifting towards lower energies and decreasing the total intensity of the emission, the shape of the PL line also changes. While the emission observed at $T=4.2$ K shows a rather complicated shape, which requires at least two Gaussians to be used to model the line (Fig. 1a), at sufficiently high temperatures (which is above 100 K) the emission line could be nicely fitted only by a single Gaussian shape. This allows, in turn, to follow the temperature dependence of the energies corresponding to the maximum emission of both bands obtained from the fitting. The result is presented in the inset in Fig. 2. The striking feature is that the observed red-shift of the low energy peak with increasing temperature is much larger than one would expect from the temperature induced shrinking of the CdTe bandgap. Qualitatively identical effects observed for other self-assembled quantum dots were associated with the thermally induced redistribution of carriers within the dot ensemble [8,10,22]. Thus, one may preliminarily conclude that, due to a strong interdiffusion activated by a high temperature of the growth, the fluctuations of e.g. chemical composition present in the structure are able to confine excitons. Then, the transfer of carriers between those fluctuations with a different depth of the corresponding potential causes the observed red-shift of the PL energy.

In order to analyze the temperature dependence of the PL intensity, which would provide the information about the non-radiative recombination in the structure, it is necessary to get rid of the influence of the carrier redistribution effects evidenced by the large red-shift of the energy. In other words, it is improper to trace the intensity change with the temperature just by following the shift of the respective energy peak of the PL emission obtained by fitting. Since, as it is going to be shown later, the energy shift with the temperature for excitons localized in a single QD is described by the temperature variation of CdTe bandgap energy, it is reasonable to apply the following procedure to determine the temperature dependence of the PL intensity. Namely, for the certain energy position in the spectrum measured at $T=4.2$ K the emission intensity as a function of the temperature was determined at the photon energy that follows the shift of the energy gap of CdTe. The energy gap dependence of CdTe on the temperature was assumed to be the same as reported previously for CdTe/ZnTe QWs [6] with the temperature coefficient equal to -0.34 meV/K. Such a procedure was carried out for several values of initial PL energy at $T=4.2$ K. The result of this analysis is presented in Fig. 3. The solid points are the intensities of the PL line measured for different energies marked by arrows in the inset of the figure. The line represents the PL intensity dependence on the temperature obtained for CdTe/ZnTe QWs [6]. For an easier comparison, each curve in Fig. 3 was normalized to its value at $T=4.2$ K. The obtained result

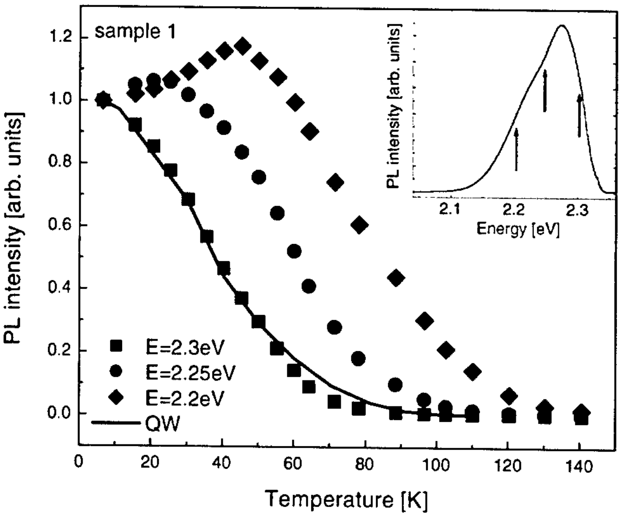

Fig. 3. The analysis of PL intensity dependence on the temperature performed for sample 1. The solid points are the intensities of the PL line measured for different energies marked by arrows in the inset of the figure. The line represents the PL intensity dependence on the temperature obtained for CdTe/ZnTe QWs [6]. For easier comparison, all data are normalized to the intensity at $T=4.2$ K.

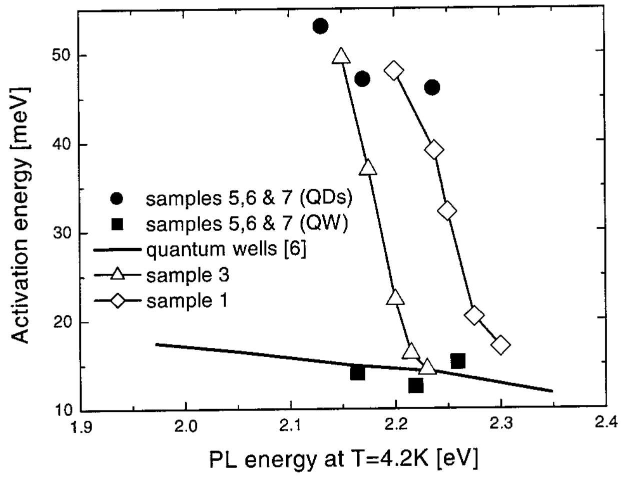

Fig. 4. The values of activation energies of the PL quenching as a function of the emission energy at $T=4.2$ K for different structures. The open points are the values obtained for samples number 1 (diamonds) and 3 (triangles). The squares and the circles represent the activation energies obtained for quantum well emission and QD PL measured for samples 5, 6 and 7. The solid line gives the values reported previously for CdTe QWs.

reveals a strong dependence of the PL intensity temperature behavior on the energy. For the highest energy, namely 2.3 eV (squares in Fig. 3), the intensity dependence is identical as the one obtained for a pseudomorphic QW (solid line). This indicates that the recombination at this energy is predominantly related to excitons localized in a QW-like potential. Recombination of these excitons quenches rapidly with increasing temperature due to their dissociation. This may explain fast disappearance of the high-energy peak, as depicted in Fig. 2. In contrast, the low-energy band is observed at much higher temperatures. This is clearly evidenced in Fig. 3, where the diamonds represent the temperature behavior of the intensity of this band. Up to 50–70 K the emission remains constant or its intensity even slightly increases. Such an effect is commonly recognized as a characteristic QD behavior [8,9,23].

Some more quantitative information about the excitonic localization in the quantum structures can be obtained by estimating the activation energies of the PL thermal quenching. To fit the data the following formula was used:

$$I=I_0/[1+C\exp(-E_A/kT)]$$

where E_A is the thermal activation energy of the excitonic emission, C is the ratio of non-radiative to radiative transition probabilities and I_0 is the proportionality constant. The results are presented in Fig. 4, where the activation energy of the PL quenching as a function of the emission energy at $T=4.2$ K is plotted.

The open points represent activation energy obtained for different emission energies for samples 1 (diamonds) and 3 (triangles). Additionally, the results obtained for samples 5, 6 and 7 are shown: the squares and the circles represent the activation energy evaluated, respectively, for the two-dimensional QW emission and for QD-related luminescence. The solid line gives the values reported previously for pseudomorphic CdTe/ZnTe QWs [6].

The comparison between the activation energy obtained for samples grown at different conditions indicates that in the case of structures grown either at $T=480$ °C or with a long healing after CdTe deposition a gradual evolution in the exciton confinement takes place. Namely, starting from two-dimensional QW-like localization, with a decrease of the emission energy, the excitons become further localized in all three directions, resembling that in QD. Thus, we conclude that the enhancement of the atom mobility during the growth leads to the formation of quantum dot-like objects. This conclusion is additionally corroborated by the presence of clearly separated emission bands related to QW and QD emissions in structures where both methods were employed during the growth: the high substrate temperature and the healing after QD layer deposition.

The results of PL temperature dependence which allowed us to distinguish between QW-like and QD-like exciton localization let us also concentrate in the following only on one type of the exciton confinement, namely that of QD zero-dimensional excitons.

3.3. *Time-resolved photoluminescence*

The degree of the excitonic localization influences not only the steady state optical properties but has also its strong impact on the dynamics of excitons in quantum structures. As an example of the typical behavior, the transients collected at $T=1.8$ K for several detection energies for sample 1 are presented in Fig. 5. In the inset, the extracted values of the decay time are also shown together with the PL spectrum. A gradual increase of the decay time value from 140 to 400 ps with a decrease of the detection energy was found, similarly to other systems with a large scale of potential fluctuations [24,25]. This increase, however, is not purely related to a possible dependence of the decay time on the size of the quantum dot but rather is an evidence of some exciton scattering mechanism present in a QD ensemble. One probable explanation of the observed behavior would be the phonon-assisted tunneling between different quantum dots. Since the results of Fig. 5 were obtained at low temperature one can exclude the optical phonon contribution in this kind of process. Thus, just low energy acoustic phonons could take part in such a mechanism. In particular, the exciton–acoustic phonon scattering processes were found to be responsible for the similar effects in thin CdTe/ZnTe QWs [26].

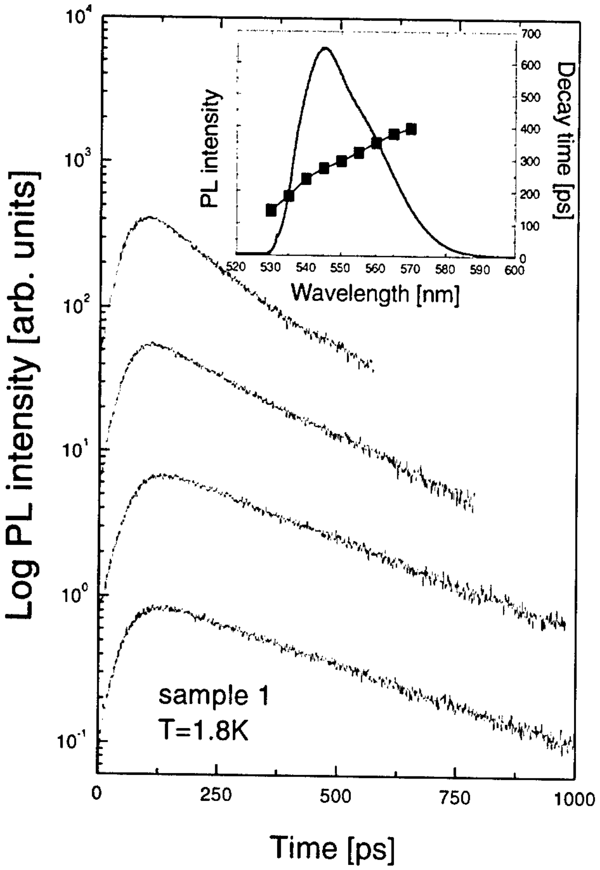

Fig. 5. The transients collected at $T=1.8$ K for several detection energies for sample 1. In the inset, the extracted values of the decay time are shown together with the PL spectrum.

Closer inspection of the time-resolved spectra reveals, apart from the main decay discussed above, also a second component, which is of approximately two orders of magnitude lower in its intensity. Moreover, it is substantially longer decaying, reaching up to 9 ns. When studying the temperature behavior of the time-resolved PL for all structures collected in Table 1 it is found out that, as shown in Fig. 6, the intensity of the long time component decreases quite fast with increasing temperature. In contrast, the intensity connected to the faster decay stays unchanged up to even $T=100$ K. Furthermore, the value of the shorter decay constant is independent of the temperature until the redistribution of carriers between the quantum dots with different localization potentials starts to influence the optical properties. Namely, for temperatures higher than 30 K, the decay time starts to depend on the excitation power. These effects are going to be discussed elsewhere [27].

The presence of two decay times was very recently reported for QDs in other material systems, in particular for CdSe QDs in ZnSe matrix [15]. The origin of this decay is still under debate, the possible explanations will be considered in the next part of this paper devoted to the temperature dependence of the microluminescence of QDs.

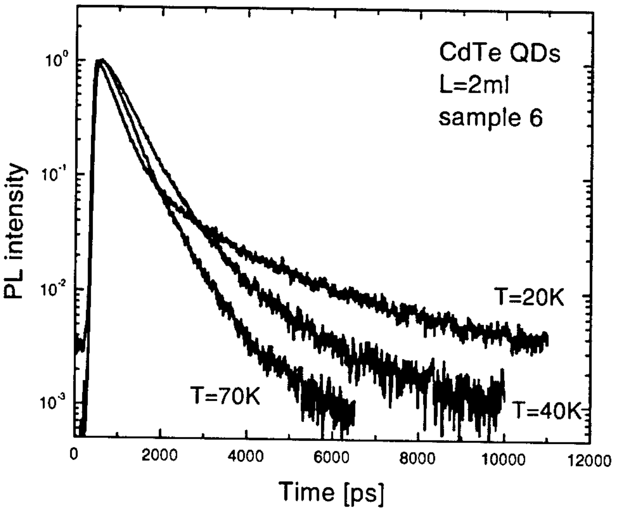

Fig. 6. Temperature behavior of the time-resolved PL obtained for sample 6. The transients are normalized to the maximum intensity.

3.4. Microluminescence as a function of the temperature

When decreasing the number of the quantum dots accessed in optical experiment, for example by reducing the size of the laser spot, the broadened spectrum splits into the sharp spikes related to recombination in single dots. This is in contrast to the case of QW, where for free excitons the PL emission does not depend on the size of the probed area of the structure. In Fig. 7 the results of a microluminescence at $T=6$ K obtained for the sample with 10 layers of CdTe QDs with a nominal thickness equal to 2 ML are presented. According to the expectations, the spectrum measured with a micrometer size laser spot consists of a series of narrow emission lines superimposed on a broad PL band. The line pattern

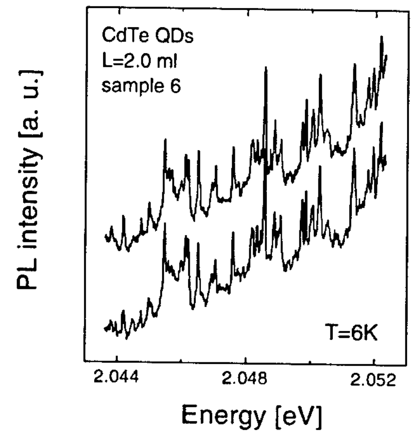

Fig. 7. Microluminescence results obtained at $T=6$ K for sample 8. The two spectra were subsequently one after another.

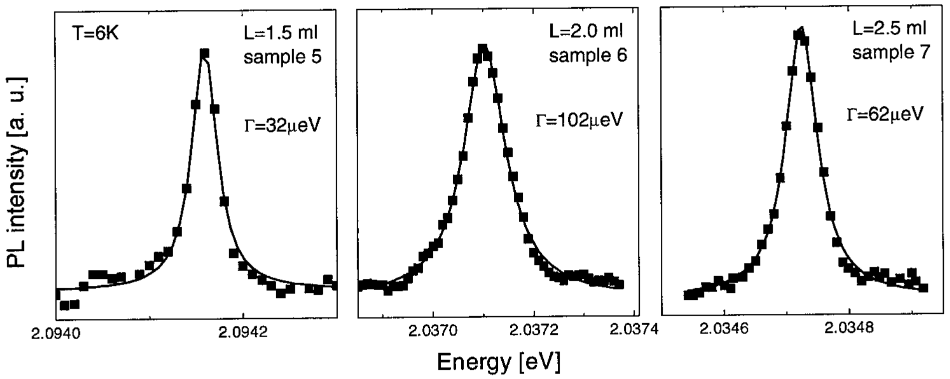

Fig. 8. The comparison between individual QD emission lines measured experimentally and fitted by the Lorentzian shape. The spectra were obtained for samples 5, 6 and 7.

is reproducible, as evidenced in Fig. 7, where two spectra taken subsequently one after another are shown. It is clear that the observed line sequence changes when the laser spot moves from one place on the sample to another. This fact demonstrates, indeed, that the quantum dots with different parameters such as size and/or chemical composition are participating in the total ensemble broad emission shown in Fig. 1c.

The linewidth of the individual lines was estimated by fitting a Lorentzian shape to a spectrum of the single dot and it was found to be in the order of 100 μeV. In Fig. 8 the comparison between experimentally obtained lines ($T=6$ K) and those fitted is given for three samples with different nominal thickness of CdTe layer. The Lorentzian shape of the line is due to the fact that an ideal quantum dot one should consider, in principle at least, as a homogenous system (no inhomogeneous broadening). There were, however, recent reports showing that due to the interaction between a QD and its neighborhood, the PL emission associated with that particular dot could exhibit fluctuations of both its energy and its intensity [28,29]. Also internal degrees of freedom such as spin in magnetic QDs can contribute to modification of the linewidth of the PL emission [30]. The effect reported in [28,29] was, however, ascribed to the changing of the charge configuration in a QD surrounding induced for example by structural defects. If such an effect is present then, obviously, the measured linewidth strongly depends on the relation between the duration time of the spectra acquisition and the characteristic time of charge configuration changes in QD surroundings. If the latter is much shorter, then the measured linewidth will considerably increase with the acquisition time. In an opposite case, the linewidth measured for a single dot should not depend on the time of collection of the spectra. In the case of CdTe QDs studied in this paper the width of the lines related to a single QD emission remained unchanged within the timescale of hundreds of second. Additionally, we did not observe any influence of either excitation power or acquisition time on the single dot PL energy and on the emission line width. The absence of such effects indicate that our structures are either free from defects (which was further confirmed by transmission electron microscopy measurements, where no signature of dislocations or other structural imperfections were observed) or that the charges on those defects that exist are frozen within the timescale of collecting the spectra (typically approx. 1 min).

The temperature evolutions of the microluminescence spectra obtained for the samples number 5 and 6 are presented in Fig. 9. The spectra in Fig. 9a are normalized in order to allow an easy comparison. The main result of these experiments is that a sharp structure composed of the lines related to single QD emissions quenches with an increase in temperature, while the broad background survives up to much higher temperatures, similarly to the case of CdSe QDs, as recently observed [15,16]. Smearing out of the sharp lines correlates with a decrease of the PL intensity related to the long-decay component in the time-resolved spectra, as described earlier (Fig. 6). This correlation allows, then, to assume that both behaviors are caused by the same effect. Such an assumption is supported by recent experiments performed on a single dot, which reveals the presence of two decay times in the time-resolved PL spectra [15], with exactly the same values as those obtained by means of macro-PL measurements. On the basis of these results we can ascribe the spread of the microluminescence spectrum shown in Fig. 9a to an exciton–acoustic phonon scattering in QDs. This scattering process was found to be significantly enhanced in QDs as compared with excitons confined in systems of higher dimensionality. Therefore, it can give rise to the broadening of the line with temperature [17].

By following the single QD-related emission line it is possible to extract the temperature dependence of its energy shift and its linewidth, as presented in Fig. 9b. The energy of a single emission line was found to follow the shrinkage of the bandgap of CdTe (solid line

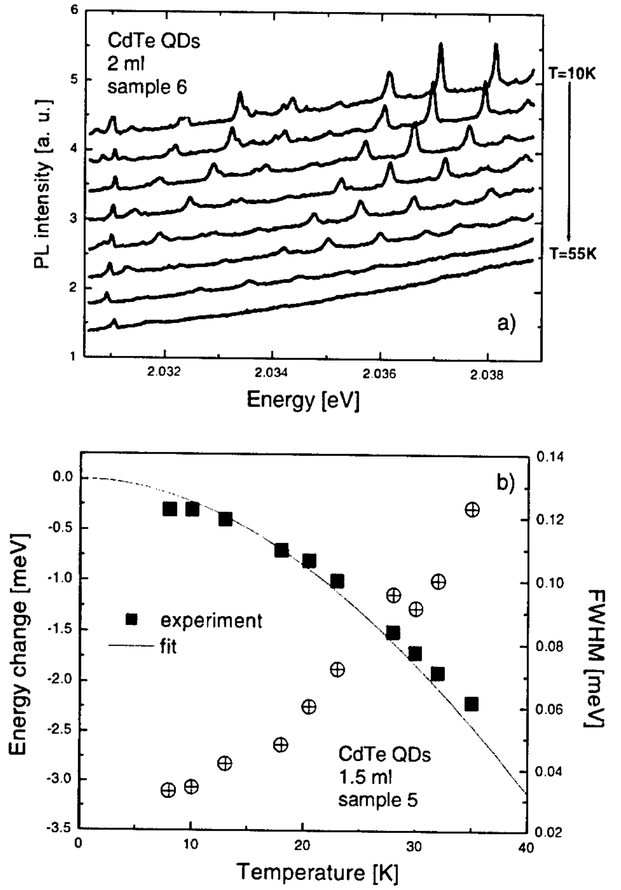

Fig. 9. (a) The temperature evolution of the PL spectra obtained for sample 6. The spectra are normalized for an easier comparison. (b) typical energy and linewidth dependence of the single exciton line obtained for sample 5. The solid line represents the CdTe bandgap temperature shrinkage, while points are experimental data.

in Fig. 9b) for most of the dots investigated. However, the linewidth increases superlinearly with the temperature as reported for GaAs QDs [13]. Contrary to this behavior, in both bulk semiconductor material and in QWs, the homogenous linewidth of the excitons increases linearly [13]. As discussed in [13] this is a direct result of the δ-like density of states in QDs.

The single QD spectroscopy provides also the insight into a particular in-plane symmetry of the dot. From theoretical considerations [31,32] it is known how the exchange electron-hole interaction and the symmetry act on the internal exciton level structure. In particular, for the in-plane symmetric QD (with a circular in-plane potential) the bright exciton level ($m = \pm 1$, m representing the effective spin of exciton) is two-fold degenerate and it is split from the dark exciton states ($m = 2$ and $m = -2$) by the exchange interaction. However, if the dot is elongated (asymmetric) which means that the symmetry is lowered, the bright level degeneracy if lifted.

In Fig. 10 the spectra measured for three different quantum dots are shown in two linear polarizations, along (110) and (1 − 10) crystallographic directions. It is evidenced that both the sign as well as the magnitude of the splitting vary from one dot to another. Moreover, when analyzing the splitting for larger number of dots it was found that these two parameters were distributed randomly within the ensemble, with no systematic trends. Since the splitting between the two linearly polarized components is caused by the in-plane anisotropy of the dot potential [9,13,16,18], then from the obtained results we may conclude that there is no preferential orientation of the elongation of the QDs in our structures. The results of the PL measurements performed on the entire QD ensemble, where no sign of the anisotropy of linear polarization was found, support additionally this conclusion.

3.5. Microluminescence as a function of magnetic field

Single QD spectroscopy performed as a function of magnetic field offers a possibility to study the influence of the confinement and the symmetry on the diamagnetic shift and on the Zeeman splitting of excitons [3,11,18]. In Fig. 11 the PL spectra for two dots with different in-plane symmetry are presented as functions of the magnetic field. The data were obtained for sample 9 through apertures in a sputtered metal mask. In both cases with an increase of the magnetic field the splitting between the lines observed in different circular polarizations

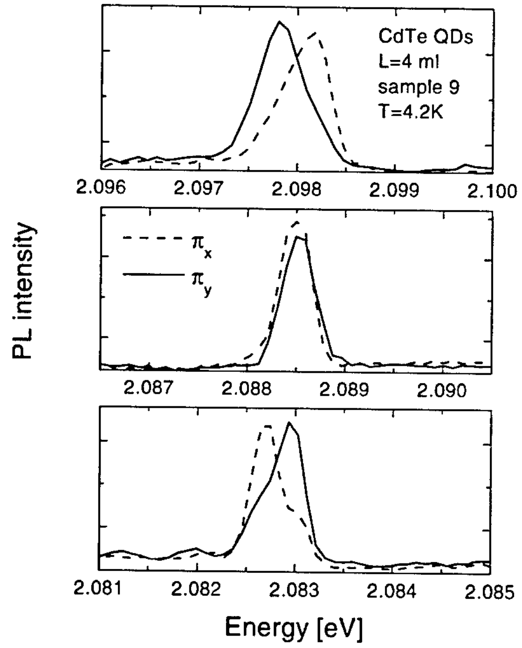

Fig. 10. Zero-field PL spectra measured for three different quantum dots in two linear polarizations. The results were obtained for sample 9.

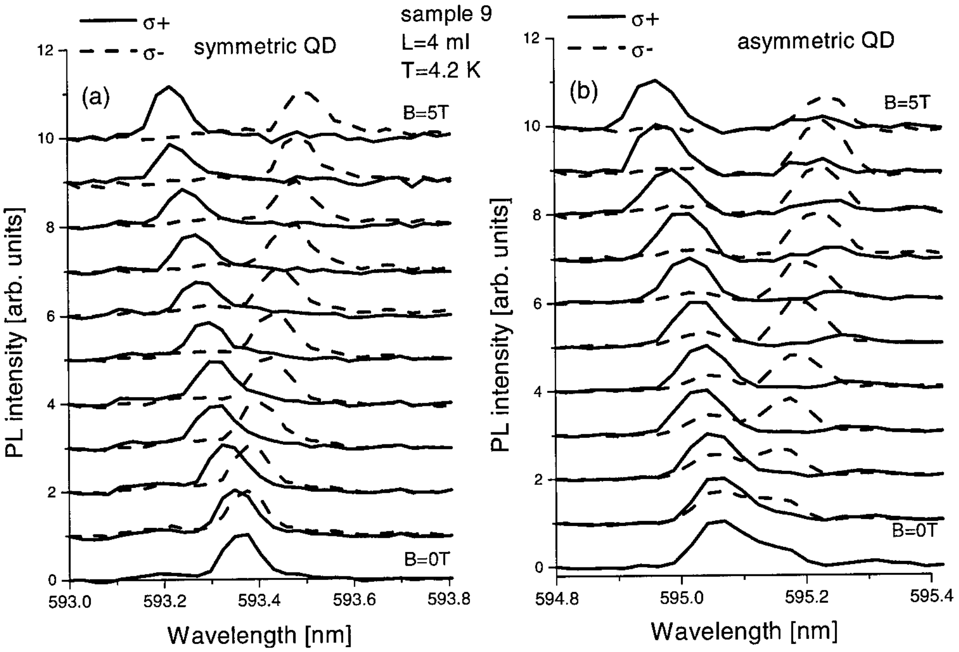

Fig. 11. PL spectra obtained for the sample 9 at $T=4.2$ K showing the magnetic field behavior of two QDs with different in-plane symmetry.

increases. Moreover, both spin-up and spin-down emission lines are slightly shifted to high energy due to the diamagnetic shift of the exciton line. The fact that the two emission lines are observed for every single dot indicates that the spin relaxation time of excitons in our CdTe QD is much longer that the time of the radiative recombination. Indeed, as shown in [33], the linear polarization of the QD ensemble emission does not change at the time scale of several tens of nanoseconds, although the decay time of excitonic recombination is equal to 700 ps.

The influence of the in-plane symmetry on the optical properties is observed in the polarization behavior of the emission. Namely, in the case of the symmetric dot (left panel) the emission is almost completely circularly polarized already at $B=0.5$ T. Contrary to that, the asymmetric QD emission is not completely polarized, and even at the highest magnetic field used ($B=5$ T) the degree of the circular polarization does not reach 100%. This is a consequence of the initial linear polarization of the PL doublet related to in-plane asymmetry of the zero-dimensional potential.

Concerning the exchange energy in CdTe QDs studied in this work the only solid information, which appears from the experimental results, is that the value of the splitting between the bright and the dark excitonic levels is larger than the Zeeman splitting caused by the magnetic field. If it were the opposite case, then it would be possible to observe the dark levels due to the mixing with the bright states, as reported for larger quantum dots [3]. Since, obviously, the magnitude of the exchange interaction increases with a decreasing size of the dot [34], then the absence of the levels characterized by $m=\pm 2$ is not surprising for such small quantum dots as studied in present paper.

The model presented in Kuther et al. [11] and Kulakovskii et al. [18] enables to evaluate the extension of the exciton wavefunction in a QD taking into account the diamagnetic shift of the exciton. The value estimated for our structures is equal to 3 nm, which agrees reasonably with the size of the dots obtained from transmission electron microscopy investigations [1]. Furthermore, by fitting the magnetic field dependence of the energy, the value of effective exciton g-factor was obtained to be equal to -3. The value is almost twice that obtained in bulk CdTe indicating that the g-factor increases with a degree of quantum confinement. By analyzing the diamagnetic shift and the value of the exciton g-factor for several tens of QDs it was found that both these parameters exhibit no systematic dependence on the zero-field PL energy. This insensitivity to the ground state QD energy may suggest that the confinement of excitons is quite homogeneous within the QD ensemble. The assumption is justified to some extent by the result of theoretical modeling of CdTe QDs [35] showing that in order to reproduce the PL emission shown in Fig. 1d the size should vary from 2.6 to 3.4 nm. Thus, with respect to the CdTe exciton Bohr radius (10 nm in bulk) this change is negligible.

4. Conclusions

The optical properties of CdTe/ZnTe quantum structures in dependence of their growth conditions were discussed. It was shown that growth either at a high temperature of 480 °C or subjecting the CdTe layer to a healing after its deposition lead to formation of quantum dots. The self-assembly of quantum dots is also achievable when a combination of these two techniques as well as applying atomic layer epitaxy when growing CdTe at 320 °C are used. Optical spectroscopy allows unambiguous distinguishing of the type of the excitonic confinement present in a particular structure. The QD emission is observable up to temperatures of approximately 200 K, considerably higher than in the case of CdTe/ZnTe QW structures. Moreover, the QD PL is characterized by two decay times at low temperature: one at approximately 300 ps and the other one, which is more than the order of magnitude longer. When decreasing the laser spot size, the QD spectrum splits into a series of sharp lines related to exciton recombination in single dots. The temperature dependence of the long decay time as well as the disappearance of the sharp lines with increasing temperature is related to exciton–acoustic phonon scattering in single dots. The single dot spectroscopy reveals that some of the dots have an oblong in-plane shape, however, no preferential direction of this elongation is found. From the magnetic field dependence of the single dot PL the values of diamagnetic shift and effective exciton *g*-factor are estimated. Both these quantities show are independent on the ground state emission energy of the dot as well as of its particular in-plane symmetry.

Acknowledgments

The author would like to gratefully acknowledge the assistance of and fruitful collaboration with all who were involved in this project, in particular J. Wróbel, K. Fronc, A. Wawro, F. Kyrychenko, J. Kossut, G. Karczewski, G. Prechtl, W. Heiss, F. Pullizi, P.C.M. Christianen, J.C. Maan. The work was supported by Committee for Scientific Research in Poland (grant 5P03B02120), FOM (The Netherlands), FWF (Austria), The Foundation for Polish Science and the Center of Excellence Celdis IAC1-CT-2000-70018.

References

[1] G. Karczewski, S. Mackowski, M. Kutrowski, T. Wojtowicz, J. Kossut, Appl. Phys. Lett. 74 (1999) 3011.
[2] S. Mackowski, G. Karczewski, T. Wojtowicz, J. Kossut, A. Heiss, Appl. Phys. Lett. 78 (2001) 3884.
[3] L. Besombes, L. Marsal, K. Kheng, T. Charvolin, L.S. Dang, A. Wasiela, H. Mariette, J. Cryst. Growth 214/215 (2000) 742.
[4] D. Bimberg, M. Grundmann, N.N. Ledentsov, Quantum Dot Heterostructures, Wiley, New York, 1999.
[5] C.S. Kim, M. Kim, S. Lee, J.K. Furdyna, M. Dobrowolska, H. Rho, L.M. Smith, H.E. Jackson, E.M. James, Y. Xin, N.D. Browning, Phys. Rev. Lett. 85 (2000) 1124.
[6] S. Mackowski, G. Karczewski, F. Kyrychenko, T. Wojtowicz, J. Kossut, Thin Solid Films 367 (2000) 210.
[7] G. Wang, S. Fafard, D. Leonard, J.E. Bowers, J.L. Merz, P.M. Petroff, Appl. Phys. Lett. 64 (1994) 2815.
[8] S. Mackowski, F. Kyrychenko, G. Karczewski, J. Kossut, W. Heiss, G. Prechtl, Phys. Status Sol. (b) 224 (2001) 465.
[9] T. Kummell, R. Weigand, G. Bacher, A. Forchel, K. Leonardi, D. Hommel, H. Selke, Appl. Phys. Lett. 73 (1998) 3105.
[10] D.I. Lubyshev, P.P. Gonzalez-Borrero, E. Marega, E. Petitprez, N. La Scala, P. Basmaji, Appl. Phys. Lett. 68 (1996) 205.
[11] A Kuther, M. Bayer, A. Forchel, A. Gorbunov, V.B. Timofeev, F. Schafer, J.P. Reithmaier, Phys. Rev. B 58 (1998) 7508.
[12] F. Flack, N. Samarth, V. Nikitin, P.A. Crowell, J. Shi, J. Levy, D.D. Awschalom, Phys. Rev. B 54 (1996) 17312.
[13] D. Gammon, E.S. Shaw, B.V. Shanabrook, D.S. Katzer, D. Park, Science 273 (1996) 87.
[14] T. Flissikowski, A. Hundt, M. Lowisch, M. Rabe, F. Henneberger, Phys. Rev. Lett. 86 (2001) 3172.
[15] L.M. Robinson, H. Rho, J.C. Kim, H.E. Jackson, L.M. Smith, S. Lee, M. Dobrowolska, J.K. Furdyna, Phys. Rev. Lett. 83 (1999) 2797.
[16] V. Nikitin, P.A. Crowell, J.A. Gupta, D.D. Awschalom, F. Flack, N. Samarth, Appl. Phys. Lett. 71 (1997) 1213.
[17] L. Besombes, K. Kheng, L. Marsal, H. Mariette, Phys. Rev. B 63 (2001) 155307.
[18] V.D. Kulakovskii, G. Bacher, R. Weigand, T. Kummel, A. Forchel, E. Borovitskaya, K. Leonardi, D. Hommel, Phys. Rev. Lett. 82 (1999) 1780.
[19] R. Leon, S. Fafard, Phys. Rev. B 58 (1998) 1726.
[20] R. Heitz, T.R. Ramachandran, A. Kalburge, Q. Xie, I. Mukhametzhanov, P. Chen, A. Madhukar, Phys. Rev. Lett. 78 (1997) 4071.
[21] W. Seifert, N. Carlsson, M. Miller, M.E. Pistol, L. Samuelson, L.R. Wallenberg, Prog. Cryst. Growth Charact. 33 (1996) 423.
[22] S. Sanguinetti, M. Henini, M.G. Alessi, M. Capizzi, P. Frigeri, S. Franchi, Phys. Rev. B 60 (1999) 8276.
[23] S.H. Xin, P.D. Wang, A. Yin, C. Kim, M. Dobrowolska, J.L. Merz, J.K. Furdyna, Appl. Phys. Lett. 69 (1996) 3884.
[24] M. Lowisch, M. Rabe, B. Stegemann, F. Henneberger, M. Grundmann, V. Turck, D. Bimberg, Phys. Rev. B 54 (1996) 11074.
[25] J.H. Collet, H. Kalt, L.S. Dang, J. Cibert, K. Samindayar, S. Tatarenko, Phys. Rev. B 43 (1991) 6843.
[26] H. Kalt, J. Collet, S.D. Baranovskii, R. Saleh, P. Thomas, L.S. Dang, J. Cibert, Phys. Rev. B 45 (1992) 4253.
[27] S. Mackowski, et al., unpublished.
[28] J. Seufert, R. Weigand, G. Bacher, T. Kummel, A. Forchel, K. Leonardi, D. Hommel, Appl. Phys. Lett. 76 (2000) 1872.
[29] V. Turck, S. Rodt, O. Stier, R. Heitz, R. Engelhardt, U.W. Pohl, D. Bimberg, R. Steingruber, Phys. Rev. B 61 (2000) 9944.
[30] S. Mackowski, S. Lee, J.K. Furdyna, M. Dobrowolska, G. Prechtl, W. Heiss, J. Kossut, G. Karczewski, Phys. Stat. Sol. b 229 (2002) 469.
[31] H.W. van Kesteren, E.C. Cosman, W.A.J.A. van der Poel, C.T. Foxon, Phys. Rev. B 41 (1990) 5283.
[32] E. Blackwood, M.J. Snelling, R.T. Harley, S.R. Andrews, C.T.B. Foxon, Phys. Rev. B 50 (1994) 14246.
[33] M. Paillard, X. Marie, P. Renucci, T. Amand, A. Jbeli, J.M. Gerard, Phys. Rev. Lett. 86 (2001) 1634.
[34] U. Woggon, F. Gindele, W. Langbein, M. Hetterich, Phys. Stat. Sol. (a) 164 (1997) 505.
[35] S. Mackowski, F. Kyrychenko, J. Wróbel, K. Fronc, A. Wawro, J. Kossut, F. Pulizzi, P.C.M. Christianen, J.C. Maan, G. Karczewski, in press.

ELSEVIER

Thin Solid Films 412 (2002) 107–113

thin solid films

www.elsevier.com/locate/tsf

Investigations of optical properties of active regions in vertical cavity surface emitting lasers grown by MBE

K. Regiński[a,*], T. Ochalski[a], J. Muszalski[a], M. Bugajski[a], J.P. Bergman[b], P.O. Holtz[b], B. Monemar[b]

[a]*Department of Physics and Technology of Low Dimensional Structures, Institute of Electron Technology, 02-668 Warsaw, Poland*
[b]*Department of Physics and Measurement Technology, Linköping University, S-581 83 Linköping, Sweden*

Abstract

The design of the vertical cavity surface emitting lasers (VCSELs) needs proper tuning of many different optical parameters of those structures. So, the optimisation of the VCSELs requires deep understanding of optical processes occurring in the active regions of such lasers. In a series of MBE processes, active regions of VCSELs as well as the whole VCSELs were grown. The active regions of the VCSEL structures were designed for $\lambda = 1000$ nm and 980 nm emission. They consisted of a pair of distributed Bragg reflectors (DBRs) composed of AlAs and GaAs quarter wavelength layers and a cavity made of GaAs. The cavities contained one or several quantum wells (QWs) made of $In_{0.2}Ga_{0.8}As$. To optimise the optical characteristics of the active regions, several experimental methods have been applied. The Bragg reflectors and the whole microcavities were investigated by optical reflectivity. For selective excitation of a QW in a cavity active layer, a Ti–sapphire tuneable laser has been used. The fine tuning between the QW emission and the cavity Fabry–Pérot resonance has been investigated by photoluminescence at varying temperatures of the sample. For monitoring the temporal evolution of the luminescence from the active region of the laser, time-resolved spectroscopy has been employed. The combination of many methods of optical investigations enabled a comprehensive characterisation and as a result an optimisation of the whole laser structure.

Keywords: Molecular beam epitaxy; Planar microcavities; Vertical cavity surface emitting lasers

---

1. Introduction

Vertical cavity surface emitting lasers (VCSELs) have attracted much attention in recent years because of their potential for practical applications. VCSELs are also fascinating objects of fundamental studies as they have many dramatically different features in contrast with conventional semiconductor lasers. A variety of different devices have been demonstrated so far by using various growth techniques [1–3]. One of the frequently used methods of growing VCSELs is by molecular beam epitaxy (MBE).

The laser cavity of a VCSEL is usually constructed normal to the substrate plane by stacking multilayer films including an active region and two dielectric mirrors. Such a structure forms a Fabry–Pérot cavity resonator. A dielectric mirror can be formed with a periodic stack of quarter wavelength thick layers of alternating high and low refractive index material. Such a mirror is referred to as a distributed Bragg reflector (DBR). The dielectric layers can be semiconductor layers deposited via MBE growth. The active region consists usually of a layer of GaAs of the thickness of one wavelength or two wavelengths and of one or several quantum wells (QWs) of InGaAs. (In our case $In_{0.20}Ga_{0.80}As$ has been applied.) The QWs are typically situated in the antinodes of a standing electromagnetic wave [4]. An example of such a structure is presented in Fig. 1, which shows the whole VCSEL structure designed for $\lambda = 1000$ nm emission. A 2λ-cavity is made of GaAs and contains 3×3 QWs made of $In_{0.20}Ga_{0.80}As$.

The procedure of designing the MBE process for growing the VCSEL structure comprises two classes of problems. The first one is connected with growing the materials of high quality for all parts of the structure. This optimisation concerns GaAs, Al(Ga)As, and InGaAs compounds. The problem is typical for MBE technology and can be solved by standard methods (see Regiński et al. [5]). The second group of problems is characteristic of the VCSEL structure. Optimisation of such a structure requires a precise tuning of its main

---

*Corresponding author. Institute of Electron Technology, 32/46 Al. Lotników, PL-02-668 Warsaw, Poland. Tel.: +48-22-5487-920; fax: +48-22-8470-631.

E-mail address: reginski@ite.waw.pl (K. Regiński).

0040-6090/02/$ - see front matter © 2002 Elsevier Science B.V. All rights reserved.
PII: S0040-6090(02)00320-6

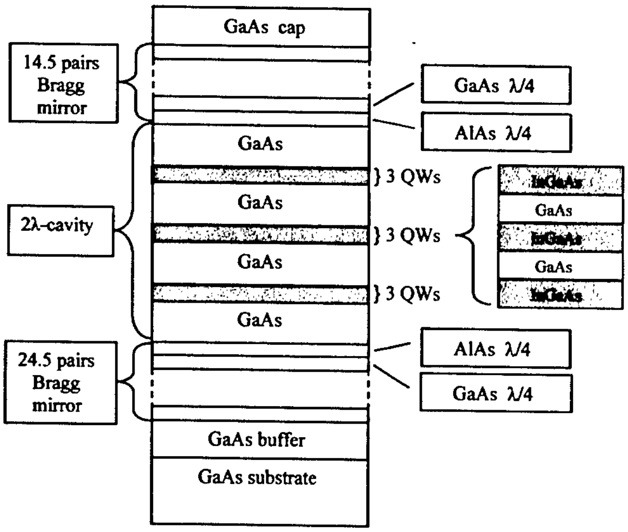

Fig. 1. Schematic VCSEL structure with 3×3 InGaAs QWs active region designed for $\lambda = 1000$ nm emission.

parts—DBRs, GaAs cavity, and QWs. This is the reason why the structure performance is very sensitive to variations in thickness of layers and their compositions. The wavelength of radiation from the QW depends on both the composition and thickness. The reflectivity of DBRs in the case of GaAs/AlAs reflectors depends on the layer thickness in the mirrors. Similarly, the position of the cavity resonance depends on the thickness of the spacer layers between the mirrors and the QWs region together with the phase of the reflection from the mirrors. Thus, the optimal growth of the structure requires simultaneous alignment of all three features. However, some variation of those parameters can be tolerated depending on how much variation in the threshold and efficiency is acceptable from device to device.

From the theoretical modelling as well as from the test processes it follows that the structure perfection is very sensitive to variation in thickness of the separate layers and their composition [4]. So the required accuracy can hardly be achieved without additional non-standard internal control in the MBE system. Thus, besides the careful calibration of the growth rate and composition, some non-standard methods of internal control should be applied. Moreover, to test the grown structures, we should combine several methods of post-growth characterisation. The most important one is the investigation of the optical properties of active regions. It comprises post-growth characterisation of separate DBRs, microcavities, and complete VCSEL structures. Naturally, the experimental work should be combined with theoretical calculations of the optical properties of the structures.

The goal of this paper is a demonstration how to combine different optical methods of post-growth characterisation in order to optimise the VCSEL structures and to achieve precise control of MBE processes. We concentrate rather upon the methodology of measurements than on the detailed experimental results. Special emphasis is put on a time-resolved spectroscopy which is a non-standard technique rarely used for such applications (see Shah [8] and the literature therein). It allows us to study certain features of laser dynamics before producing the complete VCSEL structure, which is an element of novelty.

2. Design and growth of the structures

The structures investigated in this study were typical active regions of VCSELs. They consisted of cavity resonators with one or more quantum wells (QWs) situated in the antinodes of a standing electromagnetic wave. The thickness of the GaAs layer was typically one wavelength (λ-cavity) or two wavelengths (2λ-cavity). The DBRs were composed of semiconductor layers (AlAs and GaAs) and the QWs are of $In_{0.20}Ga_{0.80}As$. An example of such a structure containing 3×3 QWs is presented in Fig. 1. To the structure, for completeness, a cap layer is added, so in effect this is the whole VCSEL structure designed for $\lambda = 1000$ nm emission.

The growth processes reported in this study have been performed by the Elemental Source MBE technique on a RIBER 32P machine equipped with ABN 135L evaporation cells. The molecular fluxes were measured by a Bayard–Alpert gauge mounted on the sample manipulator. The manipulator could be rotated so as to place the Bayard–Alpert gauge at the standard position of the substrate. Thus the gauge could measure the beam equivalent pressure (BEP) of the As_4, Ga, Al and In beams.

For monitoring the state of the crystal surface during the growth, a reflection high-energy electron diffraction (RHEED) system with a 10-keV electron gun was used. The RHEED patterns were registered by a CCD camera and then processed in real time and recorded by a computer acquisition system. This system consists of a personal computer equipped with a frame grabber, two monitors, and a high-resolution laser printer. The RHEED pictures could be processed by a specially written computer program and stored on a hard disc. The system also enables us to register the RHEED intensity oscillations and, as a result, to determine the growth rate of a layer.

The substrate temperature was measured with a thermocouple and simultaneously with an IRCON Modline Plus pyrometer. This particular model of pyrometer is specially designed to measure the GaAs surface temperature by monitoring the radiation emitted in a narrow range of wavelengths (0.940 ± 0.03 μm) which is shorter than the band edge of GaAs (but longer than $Al_xGa_{1-x}As$, $x > 0.25$) at the temperatures which are of

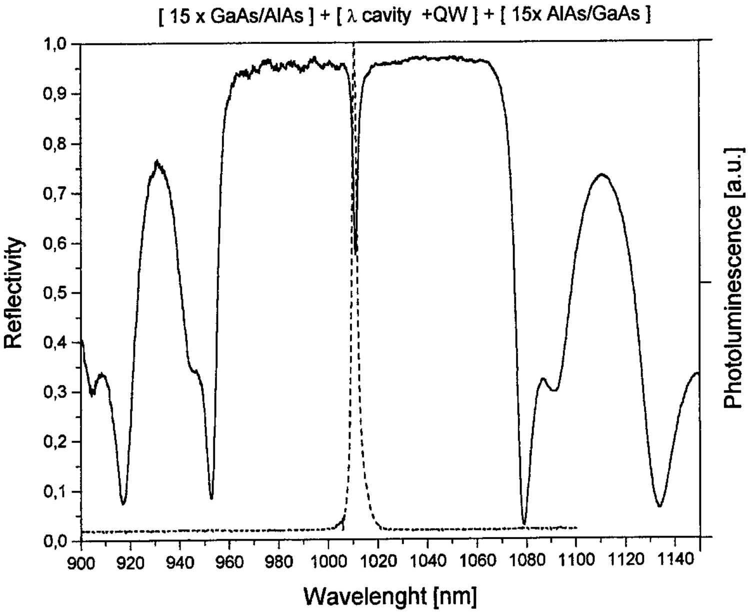

Fig. 2. Reflectance and photoluminescence spectra from the structure consisting of Bragg reflectors, λ-cavity, and $In_{0.2}Ga_{0.8}As$ QW.

interest for MBE (400–750 °C). The pyrometer is connected to a computer system enabling registration of the pyrometric temperature as a function of time. During the growth of the structure, even if the temperature registered by a thermocouple is constant, the pyrometric temperature oscillates in time. The source of those apparent temperature oscillations is the interference of the radiation emitted from the substrate and the radiation reflected at the underlying layer/grown layer and grown layer/vacuum interfaces. The phase information and the period of oscillations provide information on the actual growth rate, whereas the mean value of the pyrometer readout correlates with the true substrate temperature. Analysis of the oscillation curve after the growth gives a direct information about the thickness of all the layers in the grown structure. Thus, the interference pyrometry offers a convenient alternative to a standard laser reflectometry when it is necessary to control growth rate of layers with high precision.

The presented system enabled to control the growth rate of the individual layers with an accuracy of approximately 1%. More details about this control system can be found in [6]. The procedure of calibration of the growth process has been presented elsewhere [5].

The growth processes have been performed on heavily doped (p- or n-type) GaAs substrates of (001) orientation. Sometimes, for optical pumping experiments, the structures were undoped. The optimised growth temperatures were as follows: the GaAs:Be buffer layer was grown at 590 °C; the AlAs/GaAs Bragg reflectors, the GaAs cavities and the $In_{0.2}Ga_{0.8}As$ QWs were grown at a constant temperature 520 °C. The growth rate for GaAs and AlAs was 1 μm/h. The background pressure during the growth was 5×10^{-8} torr. The whole process was performed without interuption. During the growth of the main structure, the substrate temperature shown by a thermocouple was kept constant. The pyrometer readouts demonstrated that this method of regulation leads to a really good thermal stabilisation of the substrate.

The grown structures were initially characterised by transmission electron microscopy (XTEM). It demonstrated that the interfaces between separate layers are sharp and the periodicity of the AllAs/GaAs layers is in a good accordance with the project. The interfaces between the QWs and the cavity as well as those between the cavity and the Bragg reflectors are strait and sharp. No defects of the structure are visible. This is a proof that the InGaAs layers are stressed and no misfit dislocations are generated. The detailed procedure of XTEM characterisation has been presented elsewhere [5].

3. Reflection and photoluminescence measurements

The process of optimising the technology comprised post-growth characterisation of the separate Bragg reflectors, the microcavities, and the complete VCSEL structures. Optical properties of the grown structures were investigated by optical reflectivity, photoluminescence, and time-resolved spectroscopy. The reflectivity spectra were measured in an experimental arrangement by using a halogen lamp as a source of incident white light. After reflection the relevant wavelength was selected by a monochromator and registered by a Ge detector. Fig. 2 shows a typical reflectance spectrum

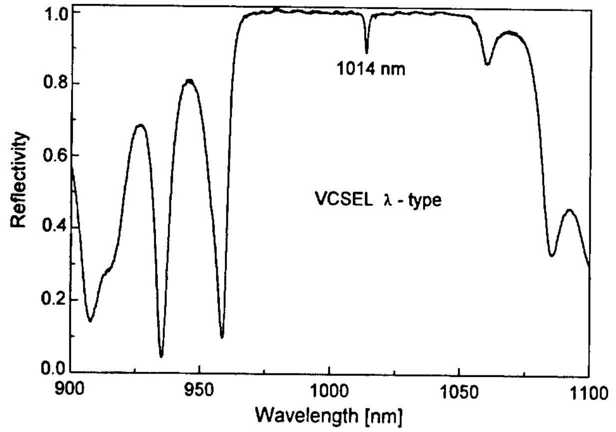

Fig. 3. Reflectance spectrum from a VCSEL of λ-type with an $In_{0.2}Ga_{0.8}As$ QW.

measured from the structure consisting of Bragg reflectors, λ-cavity and $In_{0.2}Ga_{0.8}As$ QW. A reflectance spectrum for the whole VCSEL structure is presented in Fig. 3. The measured spectra are similar to those calculated for ideal structures and exhibit the cavity resonance centred in the high reflectivity band of the Bragg reflectors. All the spectra exhibit broad stop bands, where the plot is almost flat. The reflectivity within those frequency intervals attains nearly 100%. The stop bands are bounded by deep minima which also testifies the good quality of the DBRs.

Photoluminescence (PL) measurements give us important information about the InGaAs quantum wells. To excite the quantum well, a Ti–sapphire tuneable laser has been used. Depending on the size of the cavity we observed either an enhancement or suppression of the coupling of 1e–1hh electronic dipole transitions into the resonant Fabry–Pérot mode of the planar microcavity structure.

The structures were excited with a laser beam perpendicular to their surface. The emission was recorded either from the edge of the structure (in plane photoluminescence) or in the direction perpendicular to its surface. The emission from the edge does not show any modifications (comparing with a separate QW) and can be treated as a reference. The emission from the surface shows the resonance with a Fabry–Pérot resonator. The large amplitude of this signal can be regarded as proof of good tuning between the wavelength emitted from the quantum well and the cavity resonance. An example of PL measurements is shown in Fig. 2. This figure shows a typical PL spectrum measured from the structure consisting of Bragg reflectors, λ-cavity and $In_{0.2}Ga_{0.8}As$ QW. The narrow PL peak corresponds to the case of good tuning.

The fine tuning between the QW emission and the cavity Fabry–Pérot resonance has also been investigated by PL for varying temperature of the sample. Even when the whole system is not well tuned, we can test the structure by monitoring the luminescence as a function of temperature. By changing the temperature we can shift the frequency of the wave emitted from the QW and achieve the resonance for a certain temperature.

The perfection of the cavity is characterised by the quality factor Q (see Sale [4] for definition). In low-Q cavities the spontaneous emission from QWs can be described by the Fermi's golden rule and the system is classified to be in a weak coupling regime. In contrast, in high-Q semiconductor microcavities the exciton and photon interact coherently with each other forming a new eigenstate of the system called a cavity–polariton. The cavity–polariton can be considered as a two-dimensional version of exciton–polariton in bulk semiconductors [7]. In such a case the system is classified to be in a strong coupling regime. The energy difference between these two polariton modes at the exciton–cavity resonance is called the Rabi splitting. This splitting can be observed in reflection, transmission, absorption, or photoluminescence spectra. In the case of photoluminescence, under excitation above the exciton gap, the energy separation between the two peaks as well as their intensities depend on the detuning between the exciton and the cavity. This detuning can be regulated by changing the temperature of the sample. Such a type of photoluminescence measurements is presented in Fig. 4. The figure shows the luminescence spectra of the sample containing a 2λ-cavity made of GaAs with 3×3 QWs made of $In_{0.20}Ga_{0.80}As$. The wavelength used for excitation was 800 nm, i.e. the excitation was above the band-gap in GaAs. The measurements were carried out at variable sample temperature. At the temperatures of 90 K and 100 K, we can observe the Rabi splitting of the luminescence peak.

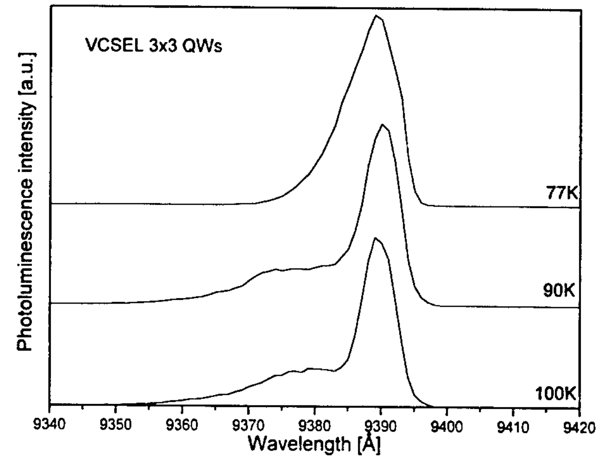

Fig. 4. Photoluminesence spectra of a VCSEL structure with 3×3 InGaAs QWs active region for variable temperature of the sample.

The precision requirements concerning the MBE processes are presented elsewhere [5]. The results presented above demonstrate good quality of grown structures, comparable with the results obtained by other authors (see Coldren et al. [3] and the literature therein). So, we can conclude that applying the presented methodology we can fulfil the assumed technological requirements.

The dynamical behaviour of the emission from cavity–polaritons depends on the way of excitation, i.e. the centre frequency and the bandwidth of the excitation light pulse. At resonant excitation, the type of response depends on whether only one or both of the two polariton modes are excited. When only one of the polariton modes is excited, the emission intensity from the microcavity decreases monotonously with time, since each polariton mode is an eigenstate of the system. When two modes are excited simultaneously, one can observe the mode oscillation, providing that the resolving power of the experimental set-up is sufficiently high.

In the case of non-resonant excitation, the excitons are created at an energy above the exciton gap. In this case, during the relaxation process, the phase coherence of the excitons is lost. Moreover, the excitons are distributed over a range of in-plane wavevector $\mathbf{k}_{\|}$, where they couple to the 'open window modes'. The intensity of such modes is almost unchanged in comparison with those in free space. Therefore, under non-resonant excitation, the spontaneous emission characteristics in the strong coupling regime is not much different from that in the weak coupling regime. However, we can still observe the mode splitting.

The photoluminescence measurements presented above are also connected with time-resolved spectroscopy, which is the subject of Section 4.

4. Time-resolved spectroscopy

The time-resolved spectroscopy enables us to study many important features of the active region of the laser, such as the time of increasing of the spontaneous emission after the excitation, the decay time of the exciton population, the threshold of lasing action, etc. [8]. These features are connected directly with the perfection of the microcavity (characterised by the quality factor Q) and its tuning to the oscillators (QWs).

The dynamics of the luminescence after excitation is mainly determined by relaxation processes in the exciton population. Thus, the time-resolved spectroscopy enables us to investigate the relaxation processes of the excitons. The thermalisation and relaxation time of the excitons is determined primarily by exciton–acoustic phonon and the exciton–exciton interactions. The second mechanism depends strongly on the density of excitons and dominates for high densities.

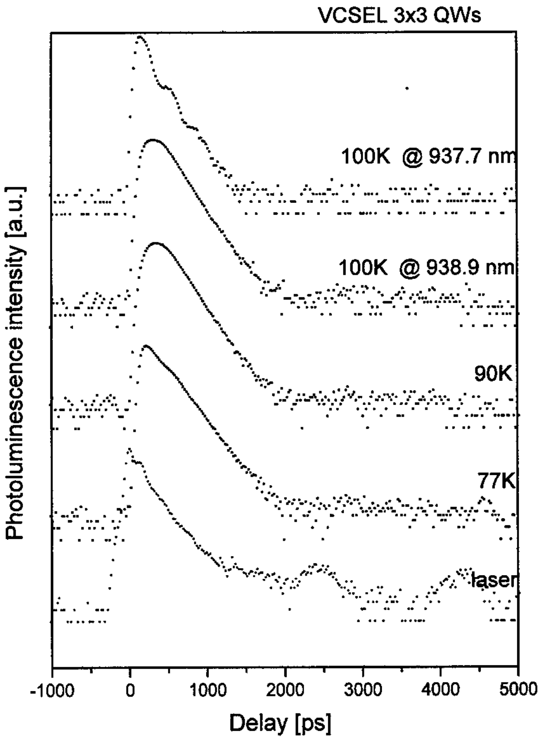

Fig. 5. Emission decay for an optically pumped VCSEL structure with 3×3 InGaAs QWs active region for variable temperature of the sample. Experimental points are presented on a semi-logarithmic scale and displaced vertically for clarity.

To measure time-resolved luminescence spectra, a standard experimental set-up has been employed. It consisted of a pulsed laser generating the exciting pulses, a photomultiplier as a detector and time-to-amplitude conversion electronics. The laser pulse width was 100 fs and the temporal resolution of the whole experimental arrangement was approximately 50 ps. The wavelength used for excitation was 800 nm, i.e. the excitation was above the band-gap of GaAs. The set-up enabled us to carry out the measurements at variable sample temperature starting from 77 K until ambient temperature and for different pulse energy.

All the time-resolved measurements presented below were carried out on the sample containing a 2λ-cavity made of GaAs with 3×3 QWs made of $In_{0.20}Ga_{0.80}As$.

As it was mentioned in the previous section, in the case of non-resonant excitation in the strong coupling regime we observe the characteristic Rabi splitting in the luminescence spectra. In such a case, we can monitor time-resolved luminescence spectra corresponding to either peak. An example of such measurements is presented in Fig. 5. The main luminescence peak is attributed to the wavelength of 938.9 nm and the secondary one to 937.7 nm. The measurements have been performed for variable temperature of the sample and at very low pulse energy of the excitation. This

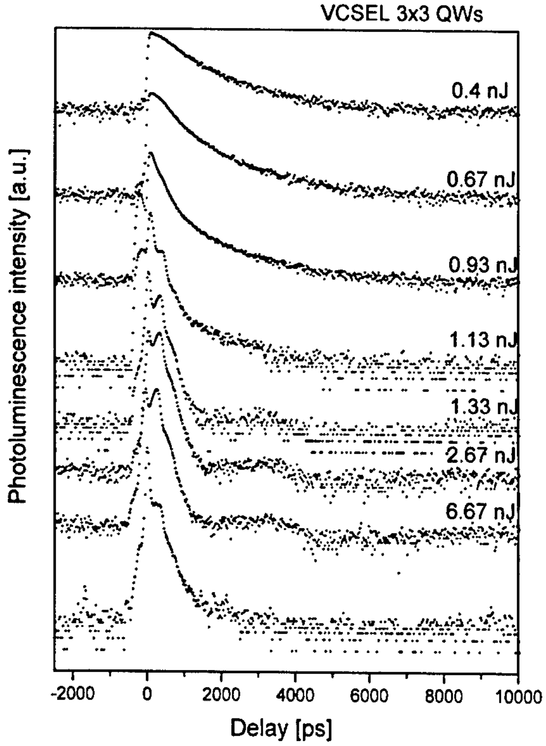

Fig. 6. Emission decay for an optically pumped VCSEL structure with 3×3 InGaAs QWs active region at 77 K for variable pumping pulse energy. Experimental points are presented on a semi-logarithmic scale and displaced vertically for clarity.

type of measurement confirms the nature of both the luminescence peaks.

In what follows in this section, we will restrict ourselves to the temperature of 77 K and the investigation of the dynamics of the main peak.

Shown in Fig. 6 are the examples of temporal behaviour of the emission intensity from the active region of VCSEL for different excitation densities. It is well visible that the luminescence intensity increases faster at higher excitation densities. As it was expected, higher density of excitons increases exciton–exciton interaction and hence the rate of thermalisation of excitons. The decrease of intensity at each decay curve shows a simple exponential form. Such a behaviour is qualitatively similar to the case of bare QW excitons in the strong coupling regime. This part of the curve is dominated by the population dynamics of the incoherent excitons distributed over a wide range of $\mathbf{k}_{\parallel}$ and in the different spin states. Therefore, the excitons can couple to the 'open window modes' and radiate photons similarly to the case of bare QWs. The 'splitting' of the uppermost part of the decay curves is caused by a complicated shape of the exciting pulse, which is composed of a main pulse followed by a secondary pulse.

Another important feature shown in Fig. 6 is connected with a threshold of lasing action. When the pulse energy is greater than 1.13 nJ, the form of the decay curves changes rapidly. First, the decay time is much shorter than that for weaker excitations. Next, the height of the two split peaks is almost equal, which shows saturation of the luminescence. These results correlate well with those presented in Fig. 7 where the luminescence from the active region is presented as a function of pulse energy of the exciting laser. It is evident that above 1.13 nJ, both the amplitude and the shape of the luminescence spectra change rapidly. The shape of the

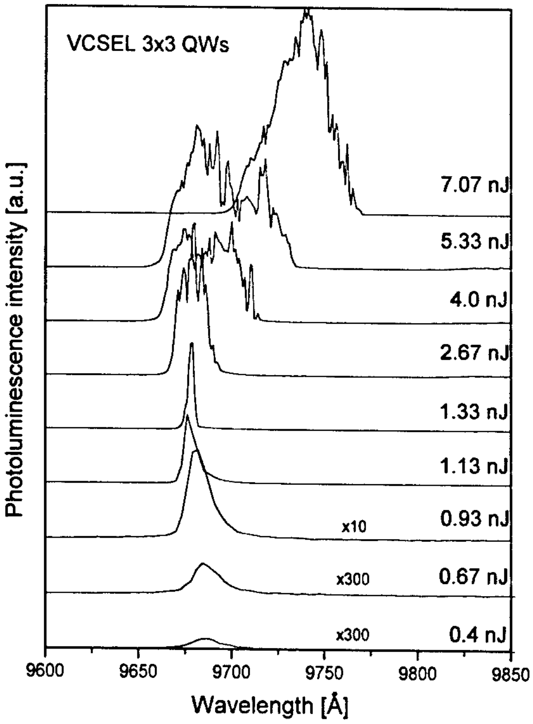

Fig. 7. Photoluminescence spectra of a VCSEL structure with 3×3 InGaAs QWs active region for variable pumping pulse energy.

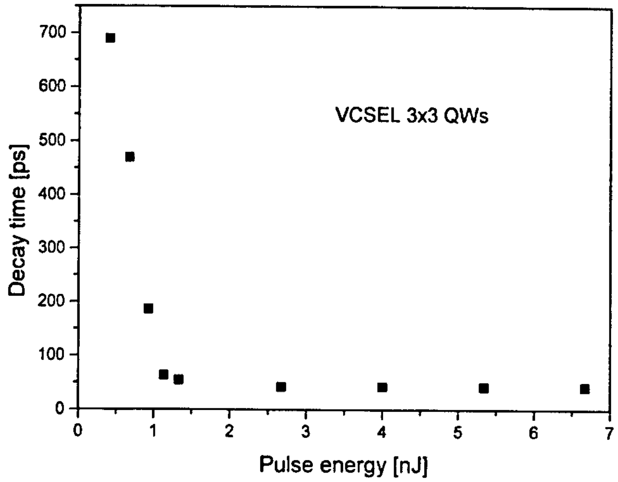

Fig. 8. Carrier lifetime vs. pumping pulse energy for a VCSEL structure with 3×3 InGaAs QWs active region.

spectra does not represent properly the lasing modes of the laser because of instability of the investigated system. Nevertheless, certain characteristic features of the mode structure are well visible. Moreover, the peak amplitude for excitations above 1.13 nJ is two orders of magnitude higher than that for the lower excitations.

The dependence of the decay time on the pulse energy of the excitation is shown in Fig. 8. It is well demonstrated that above 1.13 nJ, this time does not decrease with increasing energy. It confirms our claim that this energy corresponds to the threshold of lasing action. Additionally, this plot enables us to estimate the temporal resolution of the experimental set-up to approximately 50 ps.

5. Conclusions

We have presented several optical methods of post-growth characterisation of the active regions of VCSELs grown by MBE. The optical properties of grown structures were investigated by optical reflectivity, photoluminescence, and time-resolved spectroscopy. The investigations comprised optical characterisation of the separate Bragg reflectors, the microcavities, and the complete VCSEL structures. Combining the selected methods we were able to estimate in detail the quality of the DBRs and the microcavities as well as the tuning of the quantum wells to the microcavities. Optical methods also enabled us to estimate whether the system works in a strong coupling regime. Finally, we could investigate in detail the threshold of the lasing action. Thus, by using the above-described methods, we could optimise the construction of the VCSEL structures. Moreover, we have achieved a very precise ex situ control of the MBE processes.

References

[1] T. Baba, T. Hamano, F. Koyama, K. Iga, Spontaneous emission factor of a microcavity DBR surface emitting laser, IEEE J. Quantum Electron. 27 (1991) 1347.

[2] C.J. Chang-Hasnain, Vertical-cavity surface-emitting lasers, in: G.P. Agrawal (Ed.), Semiconductor Lasers; Past, Present, and Future, AIP Press, Woodbury, 1995, pp. 145–180.

[3] L.A. Coldren, E.R. Hegblom, Y.A. Akulova, J. Ko, E.M. Strzelecka, S.Y. Hu, VCSELs in 98: What we have and what we can expect, in: K.D. Choquette, R.A. Morgan (Eds.), Vertical-Cavity Surface-Emitting Lasers II, Proceedings of SPIE, vol. 3286, pp. 2–16.

[4] T.E. Sale, Vertical Cavity Surface Emitting Lasers, Research Studies Press, Taunton, 1995, p. 55.

[5] K. Regiński, J. Muszalski, M. Bugajski, T. Ochalski, J.M. Kubica, M. Zbroszczyk, J. Kątcki, J. Ratajczak, MBE growth of planar microcavities with distributed Bragg reflectors, Thin Solid Films 367 (2000) 290–294.

[6] J. Muszalski, Pyrometric interferometry during MBE growth of laser heterostructures, Thin Solid Films 367 (2000) 299–301.

[7] Y. Kadoya, Microcavity effects in semiconductor quantum wells, in: T. Ogawa, Y. Kanemitsu (Eds.), Optical Properties of Low-Dimensional Materials, World Scientific, Singapore, 1998.

[8] J. Shah, Ultrafast Spectroscopy of Semiconductors and Semiconductor Nanostructures, Springer, Berlin, Heidelberg, New York, 1999.

ELSEVIER

Thin Solid Films 412 (2002) 114–121

thin solid films

www.elsevier.com/locate/tsf

Photoluminescence mapping and angle-resolved photoluminescence of MBE-grown InGaAs/GaAs RC LED and VCSEL structures

A. Wójcik, T.J. Ochalski, J. Muszalski*, E. Kowalczyk, K. Goszczyński, M. Bugajski

Institute of Electron Technology, Al. Lotników 32/46, 02-668 Warsaw, Poland

Abstract

In this paper we report a systematic investigation of emission properties of microcavity devices [resonant-cavity light-emitting diodes (RC LEDs) and vertical-cavity surface-emitting lasers (VCSELs)] fabricated from molecular beam epitaxy (MBE)-grown heterostructures. The optimization of such structures requires proper tuning of the wavelength of radiation emitted from the quantum-well active region, the peak reflectivity of Drs and the cavity resonance. We demonstrate results of two techniques used to study InGaAs/GaAs RC LED and VCSEL structures. The first method is spatially resolved photoluminescence, i.e. mapping of the spontaneous emission and the cavity resonance wavelength over the whole epitaxial structure, which allows for precise determination of wavelength tuning of the structure with resonant cavity. On the other hand, it should be borne in mind that the frequency of the cavity resonance depends on the angle of observation. To study this effect we performed angle-resolved emission measurements, which yield information about the directionality of RC LED emission. The results of the study provide a better understanding of the physical processes underlying light generation in microcavity devices. The information provided by both methods is crucial for designing optimum MBE growth processes and for selecting the areas of the wafer from which useful devices can be fabricated. Since the measurements were made at room temperature they are directly applicable to devices.

Keywords: Photoluminescence; Photoluminescence mapping; Angle-resolved photoluminescence; Microcavity; Resonant cavity light emitting diode (RC LED); Vertical cavity surface emitting laser (VCSEL)

1. Introduction

Vertical-cavity surface-emitting laser (VCSEL) and resonant-cavity light-emitting diodes (RC LED) belong to the new generation of semiconductor optoelectronic devices. Such devices benefit from the utilization of specific effects resulting from placing the active structure inside a Fabry–Perot-type microcavity. The main advantage of resonant-cavity LEDs is higher emission intensity, higher spectral purity and more directional emission patterns. In addition, such devices are small in size, which enables single-mode operation with large-modulation bandwidth. Therefore, despite the complicated growth technique, microcavity devices have attracted much attention in recent years [1].

Epitaxial growth of VCSELs and RC LEDs represents possibly the greatest challenge among optical devices. The high degree of complexity of the epitaxial structure (often with more than 100 discrete epitaxial layers, including complex composition and doping schemes), along with the precision and uniformity required, has posed strong limitations on the process and necessitated a massive efforts at characterization to evaluate the structures grown. One of the basic conditions to obtain high quantum efficiency for surface emitter structures is proper tuning of the wavelength of radiation emitted from the active region (quantum well), the peak reflectivity of DBRs and the resonance of the GaAs microcavity (see Fig. 1). The optimum performance of the structure requires simultaneous alignment of all three features. This is the reason why the performance of surface emitters is very sensitive to variations in thickness of the individual layers and their composition.

In this study we mainly concentrated on the emission properties of InGaAs/GaAs RC LEDs, although the methods used are equally applicable to more complicated VCSEL structures. The device structures were grown by molecular beam epitaxy (MBE) using a Riber 32P reactor. Details of the growth can be found in our earlier

---

*Corresponding author. Tel.: +48-22-5487-920; fax: +48-22-8470-631.

E-mail address: muszal@ite.waw.pl (J. Muszalski).

0040-6090/02/$ - see front matter © 2002 Elsevier Science B.V. All rights reserved.
PII: S0040-6090(02)00322-X

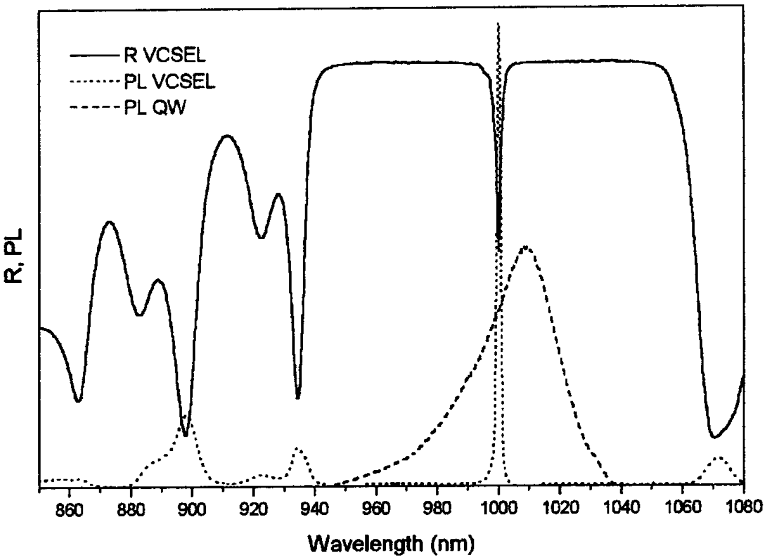

Fig. 1. Reflectance and photoluminescence spectra of surface emitter structure.

paper [2]. This technology allows control of the growth rate of particular layers and their composition with high accuracy (in our case better than 2%). In an MBE reactor, molecular beams hit the center of a rotating sample. However, due to the transversal distribution of the molecular beam intensity, the growth rate is radially non-uniform. This in turn produces a similar inhomogeneity in the layer thickness. This is an inherent property of MBE technology, which cannot be completely eliminated. For typical 2-inch-diameter substrates, the maximal difference in layer thickness over the sample may reach a few percent. Such inhomogeneity of the sample parameters means that proper tuning between the quantum well (QW) emission and the cavity resonance can be achieved only on limited area of the sample (see Fig. 2). In general, the surface emitter structures are very dependent on the capability and limitations of the epitaxial process. Thus, the critical issue is to non-destructively evaluate the wafers grown with respect to the degree of tuning, and select material for further processing. For that purpose we propose fully automated, spatially resolved photoluminescence (PL) mapping and angle-resolved local PL measurements. This high-resolution technique consists of intensity and peak-wavelength mapping over the whole epitaxial wafer and is an extension of previously proposed intensity mapping [3]. The information provided by the spatially resolved PL maps are very useful for determining areas where the cavity resonance and QW emission are aligned to each other. In addition, it should be borne in mind that the frequency of the cavity resonance depends on the angle of observation. This means that emission from surface emitter structures shifts to shorter wavelengths with increasing angle between the direction of observation and the normal to the surface. Therefore, the angle-resolved emission studies, as well as the spatial PL mapping, are important for understanding the emission features of RC LED and VCSEL structures, as well as the RC LED device itself, for which they help in selecting a proper cavity design for high brightness and maximum extraction efficiency of the diodes.

2. Experimental

In this paper we report a systematic investigation of InGaAs/GaAs RC LED structures optimized for emission at 1000 nm. The design, fabrication and basic characteristics of these devices have been previously

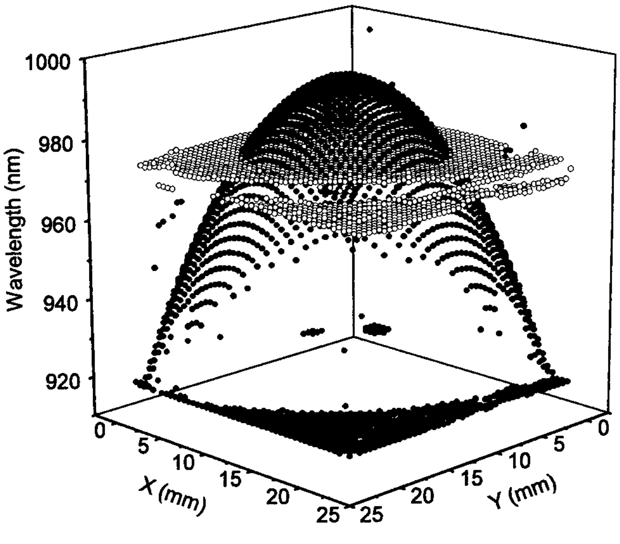

Fig. 2. Typical set of data representing wavelength distribution of PL maximum from QW (*white circles*) and Fabry–Perot microcavity resonance (*black circles*).

described [4]. The RC LEDs utilize the λ-type resonance cavity, constructed normal to the substrate plane by stacking multilayer films, including an active region (consisting of three 80-Å $In_{0.2}Ga_{0.8}As$ quantum wells), a spacer and two dielectric mirrors. Such a structure forms a one-dimensional Fabry–Perot cavity resonator and, due to photon confinement, enhances and concentrates QW emission into a narrow (~1.5 nm half-width), intense line [5].

For the PL measurements we used a tunable titanium–sapphire laser pumped by an ion argon laser. The exciting beam is focused on the sample by special imaging optics, providing a spot diameter of the order of 3 μm. The excitation wavelength of 700 nm at 300 mW of power allows penetration of the multilayer structure deep enough to excite the optically active region, but does not cause heating effects. The scanning module used in spatial PL mapping is based on an *X–Y* piezo-stage combined with mechanical encoders for approximate positioning. The measurement points are nodes of square mesh of constant step, which cover the surface of the sample. A CCD camera records the whole emission spectrum for the structure being investigated for each measurement point at once. The same procedure is then repeated for the next measurement point. However, saving and processing such a huge amount of data is difficult, so each spectrum is numerically processed and only the main signatures of the spectra, such as the wavelength of PL maximum, the half-width and the integrated intensity, are saved on disk. In this way we obtain a set of three characteristic maps from each measurement cycle. The spectral signatures are calculated in real time. The full measurement cycle takes on average from 10 min to few hours, depending on the wafer size, the resolution and the intensity of the signal. The set-up used for angle-resolved photoluminescence studies was analogous to the spatial mapping system. The only difference is in the way the signal is detected, i.e. a fiber-optic cable placed on rotary arm collects the PL signal from a small solid angle for a particular angle of observation, instead of collecting the signal from a large solid angle, as is the case for the CCD camera. The angle-resolved photoluminescence is locally investigated, but due to the fact that the sample is mounted on an *X–Y* stage, the points at which measurements are taken can be precisely identified, and thus the results can be correlated with spatially resolved PL maps.

3. Results and discussion

3.1. Spatially resolved PL mapping

Before the final device structures were grown and investigated, photoluminescence measurements were made on substrate wafers and structures containing device-active regions (3×QW) but no DBRs. In both cases the complete set of maps representing characteristic features of the wafers being investigated was recorded. These maps served as a reference when the final RC LED structures were assessed and allowed us to identify the areas of the wafers suitable for making devices. All measurements were made on one-quarter 2-inch wafers. Fig. 3 shows PL maps of the GaAs substrate (i.e. PL peak wavelength, half-width and intensity). The

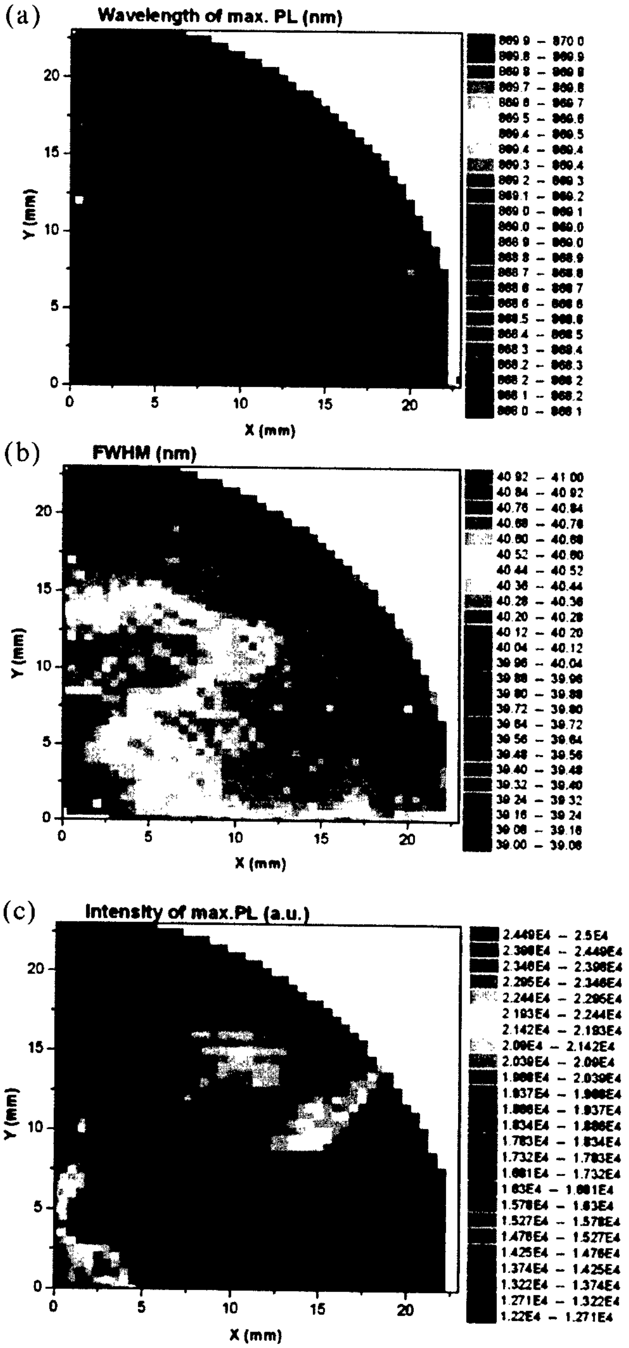

Fig. 3. PL maps of n^+-type GaAs substrates: the distribution of PL maximum wavelength from (a) QW, (b) FWHM and (c) the intensity of the PL signal.

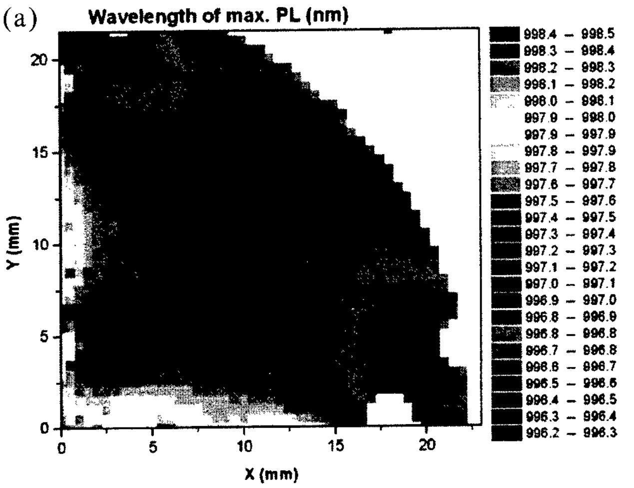

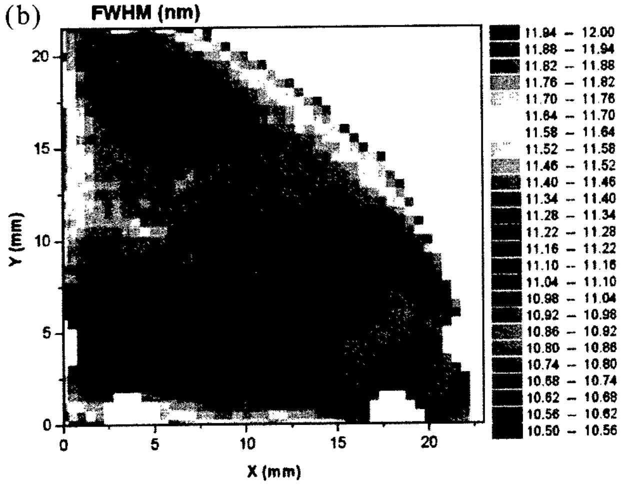

Fig. 4. Set of device active region maps (3×QW InGaAs/GaAs): the distribution of the wavelength of PL emission from (a) QW and (b) FWHM.

peak wavelength variations (see Fig. 3a) over the whole wafer are within 0.5 nm (868.0–8685 nm) with no specific pattern visible, except that the longer peak wavelengths are observed at the outer edges of the wafer. The full width at half-maximum (FWHM) value is also very uniform and equal to approximately 40 nm (Fig. 3b). Slightly higher values of the half-width (up to 41 nm) are observed at the center of the wafer. Finally, the PL intensity distribution is shown in Fig. 3c. It can be correlated with a typical liquid-encapsulated Czochralski (LEC) crystal dislocation distribution. The macroscopic distribution of dislocations over such wafers demonstrates quadruple symmetry predicted theoretically [6,7] and observed experimentally [8]. The variations of the FWHM can be interpreted as resulting from the dislocation-induced strain in the substrate. Nevertheless, all non-uniformities of the PL features observed are small and within acceptable limits for standard GaAs substrates.

The subsequent set of PL maps, shown in Fig. 4, refers to a diode structure without DBRs. The map of maximum PL wavelength (Fig. 4a) and map of FWHM (Fig. 4b) provide information about uniformity of PL features of active region, which consist of three InGaAs quantum wells embedded in GaAs. The emission wavelength distribution is practically constant, because the several-percent change in QW thickness does not have a significant influence on the ground-state exciton energy. The small differences observed in PL wavelength and half-width can be explained as resulting from inhomogeneity of the indium distribution (affecting the QW composition) over the sample. The lower left corner of the wafer emits the longest wavelengths. It corresponds to the highest indium concentration in the quantum wells, i.e. the lowest substrate temperature during growth of the InGaAs layers. The lower right and top left areas emit shorter wavelengths. The center of the sample is characterized by high uniformity of the PL wavelength: the differences observed do not exceed 2 nm. The source of the wavelength variation is the non-uniform temperature distribution over the substrate caused by preferential heat extraction by the substrate holders (note the darker regions at the corners of the wafer). In addition, the map of FWHM confirms the uniformity of emission over the whole wafer (relative changes of FWHM value are lower than 5%).

Fig. 5 shows mapping results for the final device structure. The characteristic circular symmetry of the PL wavelength distribution from the 3×QW active region embedded in the GaAs cavity enclosed by DBRs is evident (see Fig. 5a). The longest PL wavelength ($\sim$1000 nm) is observed at the center of the sample, where the thickness of the layers is the highest and the PL wavelength decreases (down to 930 nm) moving towards the edges of the sample. In the case of a λ-type cavity, the peak wavelength of the photoluminescence emerging outside the microcavity is directly related to its thickness. For the range of changes in the emission wavelength observed, the optical thickness of the GaAs microcavity ($n=3.5$) varies from 286 nm at the center to 266 nm at the wafer edges. Although QWs emit at practically a constant wavelength (approx. 997 nm) the emission extracted from the structure is filtered by the Fabry–Perot (F-P) resonance, which is strongly dependent on the optical thickness of the cavity. The PL intensity map is shown in Fig. 5c. The signal is largest in areas where the peak of QW emission matches the resonant cavity wavelength. The best coupling occurs at 975 nm, and the area of the sample for which this condition is nearly satisfied takes the shape of a ring. We can observe that the value of PL intensity is five-fold higher in the 'tuned area' compared to that observed at the center of the sample. The origin of the high-intensity ring can be understood looking at Fig. 2, which shows the wavelength distribution for QW emission and

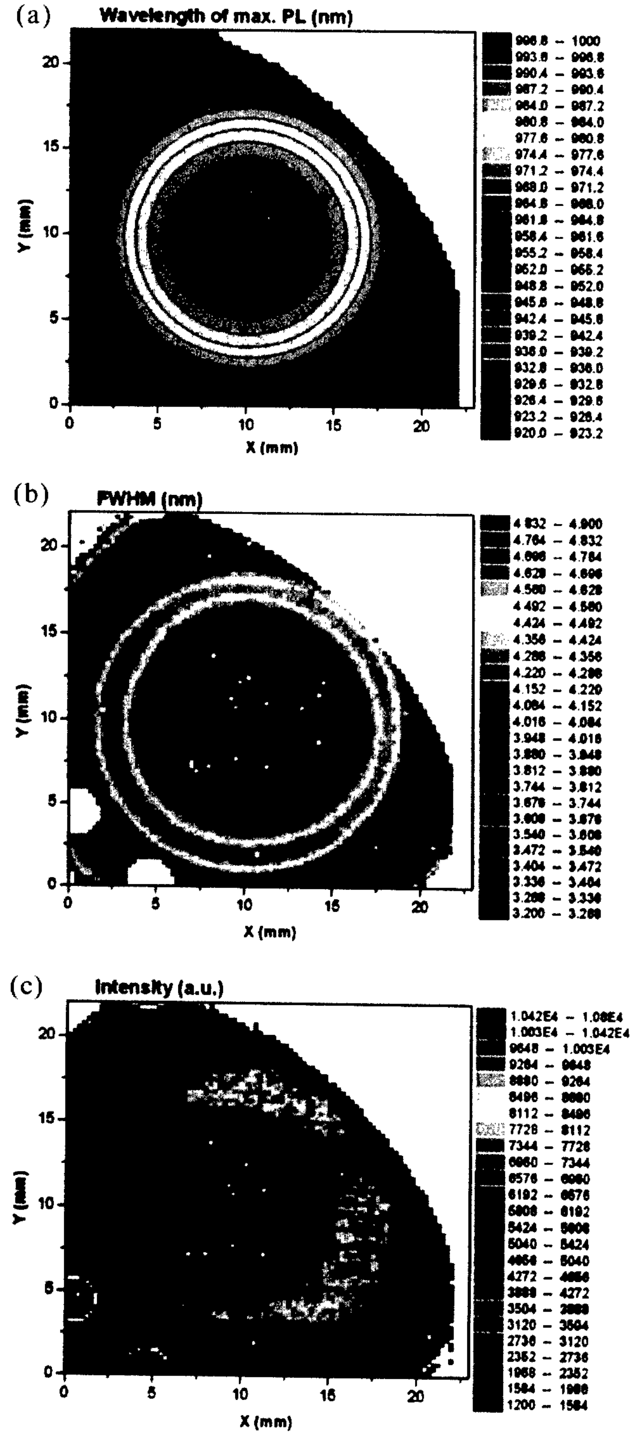

Fig. 5. Maps of characteristic features of RC LED structure: the distribution of PL maximum wavelength from (a) QW, (b) FWHM and (c) the intensity of the PL signal.

that of cavity resonance. In addition, it can be noted that the areas of greatest emission intensity in the final structure overlap with the highest-intensity areas of the substrate; however, emission tuning is still the main factor determining the PL intensity. Finally, Fig. 5b shows a map of FWHM of the structure emission. The values of FWHM are largest in the areas where the QW emission overlaps with the resonant cavity wavelength (4.9 nm), and smallest in the center of the sample (3.2 nm). The distribution of FWHM values also takes a regular ring shape.

In summary, the basic condition to obtain high quantum efficiency for surface emitter structures is proper tuning of the wavelength of radiation emitted from the active region (quantum well) and of the resonance of the GaAs microcavity. The performance of surface emitters is very sensitive to variations in thickness of the individual layers and their composition. PL mapping can be used as the main method to assess the technology and select material meeting the device requirements.

3.2. Angle-resolved photoluminescence

For the purpose of coupling light from an RC LED into a multimode optical fiber, we are only interested in the main emission lobe of the microcavity. Therefore, it is important to obtain high light intensity along the normal direction, where it best couples to the fiber. As has been demonstrated in the previous section, in order to obtain high quantum efficiency of surface emitter structures, the wavelength of radiation emitted from the quantum well must be tuned to the cavity resonance.

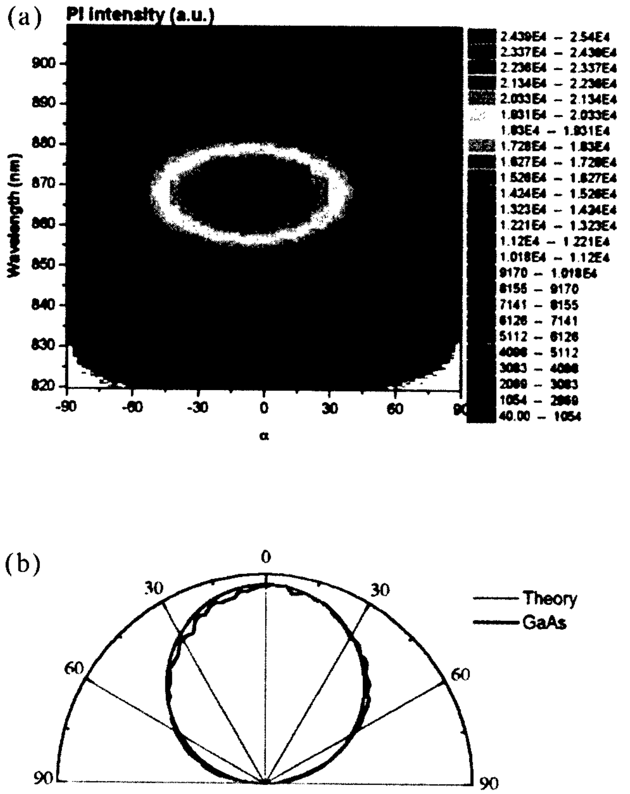

Fig. 6. (a) Angle-resolved map of PL intensity for GaAs substrate and (b) directional characteristics of emission presented in polar coordinates.

On the other hand, it should be borne in mind that the frequency of the cavity resonance depends on the angle of observation. This means that for the cavity, which is positively detuned, i.e. for which cavity resonance occurs at longer wavelength than QW emission, it is possible to enhance the emission by extracting light at a non-zero angle with respect to the normal direction. This occurs, however, at the cost of the directional emission characteristic, which becomes multi-lobed. We now address these issues in some detail. To study the above-mentioned effects, we performed angle-resolved emission measurements, which yield information about the directionality of RC LED emission. As a reference we investigated the angular emission properties of the substrate and the QW active region. Fig. 6a shows an angle-resolved map of the photoluminescence of the GaAs substrate. The horizontal axis represents the angle at which emission is observed (0 refers to normal direction) and the vertical axis represents the wavelength; the tones denote PL intensity. The whole map is characteristic for a particular point on the sample. For bulk material the character of the map does not depend on the position on the sample. In accordance with expectations, the highest intensity of emission occurs at the direction normal to the surface and then decreases with angle. Over the whole range of angles, the wavelength of PL maximum equals 870 nm and corresponds to the bandgap energy of GaAs at room temperature. The FWHM of the PL signal is also constant and equal to 40 nm. The integrated PL intensity vs. angle of observation is shown in Fig. 6b. It agrees very well with the theoretical dependence: $I = I_0 \cos(\alpha)$.

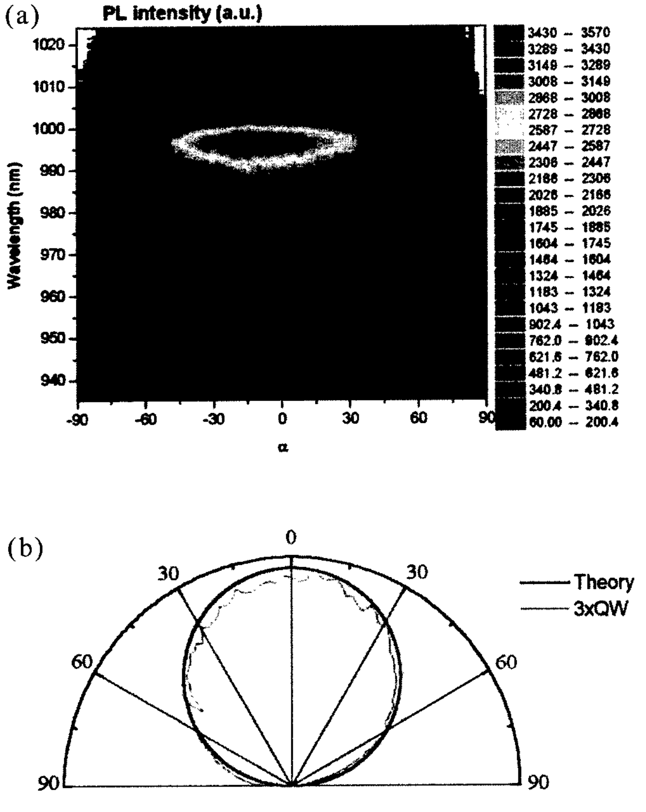

Fig. 7. (a) Angle-resolved map of PL intensity of active region ($3\times$QW) and (b) directional characteristics of emission presented in polar coordinates.

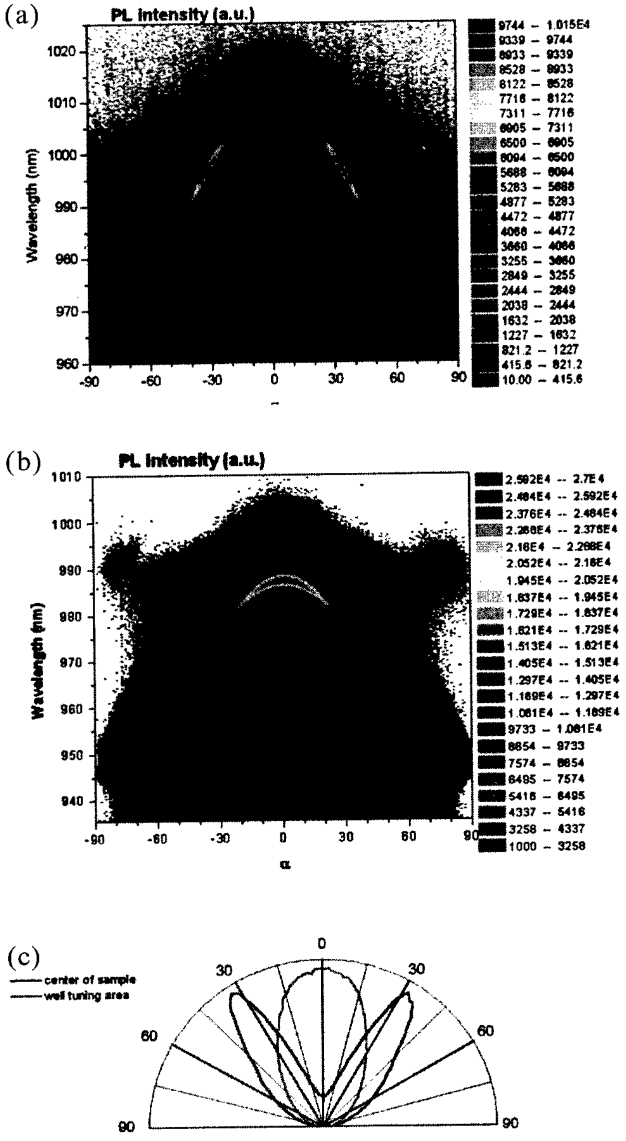

Fig. 8. Angle-resolved spectra of photoluminescence intensity of final RC LED structure: (a) positively detuned and (b) tuned; and (c) directional characteristics of emission presented in polar coordinates.

The angle-resolved PL measurements of the QW active region demonstrated similar behavior, i.e. there was no difference in the spectra observed at various angles. The map of angle-resolved PL of the QW active region is shown in Fig. 7a. The PL maximum is observed at 998 nm and the FWHM value is equal to 15 nm. The integrated PL intensity vs. angle of observation shown in Fig. 7b obeys the cosine law.

When the QW active region is embedded in the planar microcavity with DBRs, we deal with completely different behavior. In that case not only are the spectral characteristics of emission modified, but we observe also very complex directional features in the spectra. The angular PL maps, shown in Fig. 8, exhibit different features at different positions on the wafer. Their character depends on the tuning between QW emission and the cavity resonance at a given point on the sample. The general feature of angle-resolved PL is its shift to shorter wavelengths with increasing observation angle with respect to the normal direction. The first set of results, shown in Fig. 8a, is characteristic for a positively detuned area located at the center of the wafer (within the high PL intensity ring, cf. Fig. 5c). The second set shows features typical for tuned areas, i.e. from the high PL intensity ring (see Fig. 8b). At the geometrical center of the sample the cavity is the thickest, and the resonance occurs at longer wavelength than QW emission, i.e. at 1010 compared to 995 nm. Consequently, the PL intensity in the direction perpendicular to the surface is rather low. With increasing angle of observation the cavity resonance moves towards shorter wavelengths and PL intensity grows, reaching a maximum at 34°, after which it decreases again. This behavior is shown in Fig. 8a. The corresponding angular distribution of emission intensity is shown in Fig. 8c. A full spatial distribution of emitted radiation can be obtained by rotating the characteristics around the normal to the surface. If we observe the area of the sample which is tuned (see Fig. 8b), the angular characteristics show the same behavior in terms of wavelength shift. However, in this case the maximum PL intensity is observed in the direction perpendicular to the sample and the integrated intensity characteristic is single-lobed (Fig. 8c). In addition, the angular characteristics of the integrated intensity are more directional (much narrower) than in the case of emission from planar sources without a microcavity. This is an important feature and a clear advantage when coupling into the fiber is considered. Thus, for tuned microresonators we obtain spectrally concentrated, narrow emission with the majority of photons emitted in the direction perpendicular to the surface of the resonator, which may also be wavelength-shifted by changing the angle of observation. Such light sources can find interesting applications in molecular spectroscopy, gas analysis and detection systems.

4. Conclusions

We report results of spatially resolved PL mapping and angle-resolved PL measurements of surface emitter structures (RC LEDs and VCSELs). We have found that a small non-uniformity in the radial thickness of the layers, inherent in MBE technology, does not practically influence the spectral position of PL emission from QWs; on the other hand, it is high enough to substantially influence the cavity resonance wavelength. This makes it difficult to grow surface emitter structures that are perfectly tuned over large areas. Results of PL investigations confirm that the emission intensity from RC LED structures is highest in areas of sample where the optical thickness of the microcavity is equal to the wavelength of emission from the QW. The high-resolution mapping method developed allows for identification of areas of the wafer that meet design criteria and can be used for device fabrication. The technique of global spatially resolved PL mapping has been found very useful in technological practice; however, the local measurement technique—angle-resolved PL—is indispensable for correct description of the emission characteristics of microcavity devices. The optical studies reported in this paper have strict connection with MBE technology and should be useful for designing an optimum growth process, and since the measurements were made at room temperature they are directly applicable to the devices. The results of the paper also contribute to better understanding of light emission from optical microresonators, where spatial dimensions are of the order of the wavelength of light. Spontaneous emission, which has long been believed to be uncontrollable, is strongly modified. The changes include not only the emission rate, but also the spectral purity and emission pattern. The last two parameters were studied in considerable detail in the present paper. These changes can be employed to make more efficient and brighter optoelectronic semiconductor devices.

Acknowledgments

This work has been partly supported by the State Committee for Scientific Research (Poland), under Contract No 8T11B 020 18

References

[1] C. Wilmsen, H. Temkin, L.A. Coldren (Eds.), Vertical-Cavity Surface-Emitting Lasers: Design, Fabrication, Characterization and Applications, Cambridge University Press, 1999.

[2] K. Reginski, J. Muszalski, M. Bugajski, T. Ochalski, J.M. Kubica, M. Zbroszczyk, J. Katcki, J. Ratajczak, Thin Solid Films 367 (2000) 290.

[3] M. Bugajski, P. Edelman, M. Wesolowski, J. Ornoch, W. Lewandowski, K. Kucharski, Mater. Sci. Eng. B 20 (1993) 186.

[4] J. Muszalski, T. Ochalski, E. Kowalczyk, A. Wójcik, H. Wrzesinska, B. Mroziewicz, M. Bugajski, 9th International

Symposium on Nanostructures: Physics and Technology, St. Petersburg, Russia, 18–22 June, 2001, p. 171.

[5] T. Ochalski, J. Muszalski, M. Zbroszczyk, J. Kubica, K. Reginski, J. Katcki, M. Bugajski, in: M.L. Sadowski, et al. (Eds.), Optical Properties of Semiconductor Nanostructures, NATO Science Series 3, High Technology, vol. 81, Kluwer Academic Publishing, 2000, p. 201.

[6] A.S. Jordan, R. Caruso, A.R. von Neida, J.W. Nielsen, J. Appl. Phys. 52 (1981) 3331.

[7] A.S. Jordan, A.R. von Neida, R. Caruso, J. Cryst. Growth 70 (1988) 555.

[8] M. Bugajski, P. Edelman, J. Ornoch, Acta Phys. Pol. A 77 (1989) 145.

ELSEVIER

Thin Solid Films 412 (2002) 122–128

thin solid films

www.elsevier.com/locate/tsf

Ferromagnetic GaMnAs/GaAs superlattices—MBE growth and magnetic properties

J. Sadowski[a,b,c,*], R. Mathieu[d], P. Svedlindh[d], M. Karlsteen[a], J. Kanski[a], Y. Fu[a], J.T. Domagala[b], W. Szuszkiewicz[b], B. Hennion[e], D.K. Maude[f], R. Airey[g], G. Hill[g]

[a]*Department of Experimental Physics, Chalmers University of Technology and Göteborg University, SE-412 96 Göteborg, Sweden*
[b]*Institute of Physics Polish Academy of Sciences, al. Lotników 32/46, PL-02-668 Warszawa, Poland*
[c]*Oersted Laboratory, Copenhagen University, Copenhagen, Denmark*
[d]*Uppsala University, Department of Materials Science, SE-751 21 Uppsala, Sweden*
[e]*Laboratoire Leon Brillouin, CE Saclay, 91191 Gif-sur-Yvette, France*
[f]*Grenoble High Magnetic Field Laboratory, 38042 Grenoble, France*
[g]*Department of Electronic and Electrical Engineering, University of Sheffield, Sheffield, UK*

Abstract

We have studied the magnetic properties of $(GaMnAs)_m(GaAs)_n$ superlattices with magnetic GaMnAs layers of thickness between eight and 16 molecular layers (ML) (23–45 Å), and with non-magnetic GaAs spacers from 4 to 10 ML (11–28 Å). While previous reports state that GaMnAs layers thinner than 50 Å are paramagnetic in the whole Mn composition range achievable using MBE growth (up to 8% Mn), we have found that short period superlattices exhibit a paramagnetic-to-ferromagnetic phase transition with a transition temperature which depends on both the thickness of the magnetic GaMnAs layer and the non-magnetic GaAs spacer. The neutron scattering experiments have shown that the magnetic layers in superlattices are ferromagnetically coupled for both thin (below 50 Å) and thick (above 50 Å) GaMnAs layers. © 2002 Elsevier Science B.V. All rights reserved.

Keywords: Ferromagnetic semiconductors; Molecular beam epitaxy; Semiconductor superlattices

1. Introduction

III–V Ferromagnetic semiconductors such as InMnAs [1–5] and GaMnAs [6–11] have been gaining an increasing interest in recent years due to the expanding research activity in the field of spintronics [12], where the possibility of integrating spin-dependent effects into the electronic devices seems to be very attractive. In this context, low dimensional structures like superlattices, quantum wires and dots incorporating ferromagnetic semiconductor materials are particularly interesting. So far, mainly two-dimensional structures based on III–V ferromagnetic semiconductors have been investigated in detail, however, the understanding of their properties is far from being complete. In previous studies of superlattices (SL) with magnetic GaMnAs layers and non-magnetic AlGaAs and InGaAs spacers the ferromagnetic properties were reported to disappear when the thickness of the individual magnetic layers decreased below 50 Å [13–18]. On the one hand, recent theoretical modelling of magnetism in GaMnAs quantum well structures [19], based on Monte Carlo simulations on a confinement-adapted RKKY exchange interaction model, predicts a lower limit for the GaMnAs thickness of 9 ML (25 Å) for the ferromagnetic phase to occur. However, theoretical modelling of magnetism in GaMnAs/GaAs SL structures found no evidence of a corresponding GaMnAs thickness limit [20]. Moreover, Jungwirth et al. [20] predict an oscillating character of the magnetic coupling between 7-ML thick GaMnAs layers in GaMnAs/GaAs SL structures—antiferromagnetic or ferromagnetic depending on the GaAs spacer layer thickness.

Our results show that GaMnAs/GaAs superlattices have a paramagnetic-to-ferromagnetic phase transition for a magnetic layer thickness of eight molecular layers, i.e. 22.8 Å, which is much below the 50 Å thickness limit previously reported [13–18]. We have also con-

---

*Corresponding author. Tel.: +46-46-222-43-31; fax: +46-46-222-47-10.
E-mail address: sadow@maxlab.lu.se (J. Sadowski).

0040-6090/02/$ - see front matter © 2002 Elsevier Science B.V. All rights reserved.
PII: S0040-6090(02)00323-1

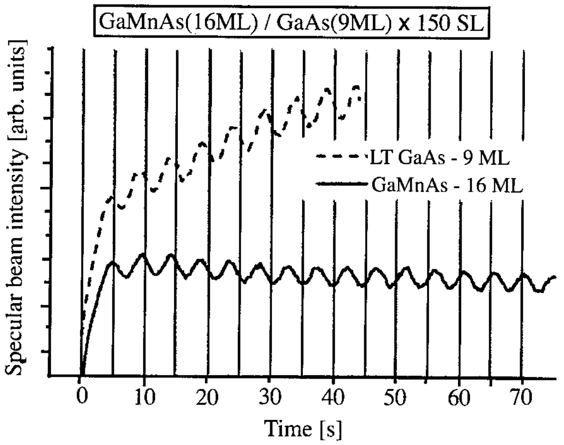

Fig. 1. Reflection high energy electron diffraction (RHEED) intensity oscillations recorded for the specular RHEED beam during the MBE growth of a $Ga_{0.93}Mn_{0.07}As$ (16 ML)/GaAs (9 ML) superlattice structure.

firmed using neutron scattering experiments, that for a GaAs spacer thickness of 4 to 6 ML there is a ferromagnetic coupling between GaMnAs layers [21].

2. MBE growth and properties of single GaMnAs layers

GaMnAs samples were grown in a MBE system (KRYOVAK) equipped with an As_2 valve cracker source. As substrates we used semi-insulating, epi-ready GaAs (100) wafers. The MBE growth of superlattice structures was preceded by a standard high-temperature (HT) growth of a 5000-Å thick GaAs buffer. Subsequently, the substrate temperature was decreased to 200 °C and stabilized for 1 h. Afterwards, SL structures were grown with 30-s growth interruptions at each interface. The number of repetitions of the GaMnAs/GaAs sequence was between 100 and 250 depending on the type of structure.

The substrate temperature during MBE growth was close to 200 °C, and the As_2 vs. Ga flux ratio was chosen to be approximately 2. Before the MBE growth of each GaMnAs/GaAs SL, the growth rates of GaAs and GaMnAs were carefully calibrated using reflection high energy electron diffraction (RHEED) intensity oscillations. Analyzing RHEED oscillations recorded during growth of different SL layers we have also calibrated in situ the Mn composition in GaMnAs. Because the sticking coefficients of Ga and Mn atoms are equal to 1 at low growth temperature, the Mn content in GaMnAs layers is proportional to the growth rate increase of GaMnAs with respect to GaAs. Fig. 1 shows RHEED oscillations recorded during growth of an SL structure having 16 monolayers (ML) of $Ga_{0.93}Mn_{0.07}As$ and 9 ML of GaAs.

As reported by several groups [22–24], the properties of GaMnAs depend strongly on the LT MBE growth conditions, such as substrate temperature (T_s) and As/Ga flux ratio. The differences in T_s as well as in As/Ga give different values of the lattice parameter of GaMnAs [24,25]. In our case: $T_s = 200$ °C and As_2/Ga = 2, and the relaxed (unstrained) lattice constant of GaMnAs increases with the Mn content according to the formula [26]:

$$a(Ga_{1-x}Mn_xAs) = 5.65469 * (1-x) + 5.9013 * x \qquad (1)$$

This gives the lattice constant of LT GaAs as $a_{LTGaAs} = 5.65469$ Å, and that of a hypothetical zinc-blende MnAs as $a_{MnAs} = 5.9013$ Å. The first value, a_{LTGaAs}, is slightly higher than the lattice parameter of bulk GaAs, as well as GaAs epilayers grown at standard, high substrate temperatures (500–600 °C), which is equal to 5.65333 Å. The lattice parameter expansion of LT GaAs is due to the presence of As antisites [27–29], which are incorporated at the concentrations up to 0.5% [29] under LT MBE growth conditions. As it has been previously found [28,30,31], the lattice expansion depends linearly on the concentration of As antisites, implying that the lattice parameter of LT GaAs deduced from Eq. (1), as well as verified by X-ray diffraction (XRD) measurements of LT GaAs layers grown under the same conditions as GaMnAs, gives the concentration of As antisites (As[Ga]) in LT GaAs. The lattice constant a_{LTGaAs} taken from Eq. (1) corresponds to a concentration of As antisites equal to 3×10^{19} cm^{-3}.

The a_{MnAs} (zinc-blende) = 5.903 Å lattice parameter is lower than the value of 5.98 Å most frequently cited by other authors [6,8,9]. It was confirmed recently by Schott et al. [24] that a_{MnAs} (zinc-blende) extrapolated from the $a_{Ga(1-x)Mn(x)As}$ vs. x relation depends on the MBE growth temperature (T_s), giving 5.90 Å for $T_s =$ 220 °C and 5.98 Å in the case of $T_s = 270$ °C. All GaMnAs samples studied in this work were grown at low substrate temperature ($T_s = 200$ °C) and the results of Schott et al. are thus in accordance with our findings.

Theoretical work has shown that As antisites play an important role in GaMnAs [32,33], strongly influencing the magnetic properties of this material. Sanvito et al. [32] found that not only the total concentration of antisites, but also their position with respect to the Mn ions are relevant for the magnetic properties of GaMnAs.

For the electronic structure of GaMnAs, the donor-like character of As[Ga] is essential. As is well known [6–9], Mn is an acceptor in GaMnAs. However, the hole densities in GaMnAs, measured directly [34] or calculated within the mean-field model using experimental values of the ferromagnetic phase transition temperatures [35], are only a small fraction (from 10 to 30%) of the concentration of Mn ions. The missing holes can be associated with charge carrier compensation by As antisites, which form deep donor states. However, since the antisite density in our GaMnAs films is

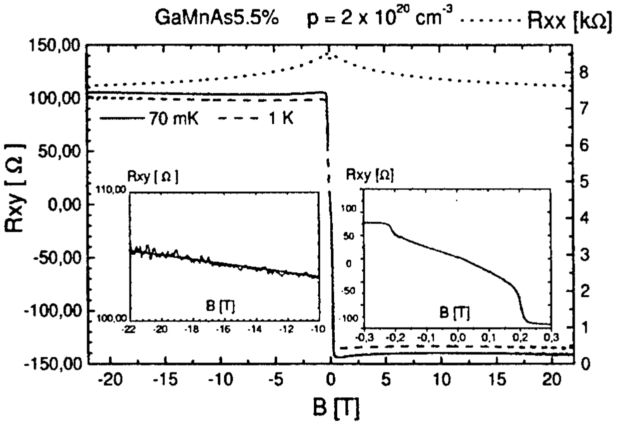

Fig. 2. Hall effect results for a 500-Å thick $Ga_{0.945}Mn_{0.55}As$ layer capped with 100 Å LT GaAs. The right side inset shows the low field region dominated by the anomalous Hall effect. The left side inset shows the high field region, at which the hole density has been determined from the $R(xy)$ vs. B slope.

estimated to be 4×10^{19} cm^{-3} or smaller, it means that not more than $\sim10^{20}$ cm^{-3} holes can be compensated by these defects, whereas an order of magnitude higher compensation would be necessary to explain the much lower than expected hole concentration. Other mechanisms based on hole localization [35,36] have been proposed to explain the low value for the hole concentration, but no definite explanation has been accepted so far.

3. Hole density distribution

A high density of holes is a crucial factor for the ferromagnetic phase to occur in GaMnAs as well as in other ferromagnetic semiconductors [10,36–39], as is described theoretically by several models [10,37,40,41], and being well established experimentally [22,23,42]. We have measured the density of holes in 500-Å thick $Ga_{0.945}Mn_{0.055}As$ reference layers grown at the same conditions (As_2/Ga flux and substrate temperature) as the GaMnAs/GaAs SL structures. Fig. 2 shows the Hall voltage vs. magnetic field, measured at 70 mK and for magnetic field intensities up to 22 T. In the low field region, shown in detail in the right inset, the Hall voltage traces the sample magnetization (anomalous Hall effect), rising steeply for fields between 0 and 0.2 T and then saturating. In the high field region, shown in detail in the left inset, the magnetization is saturated and the ordinary Hall coefficient prevails. The Rxy vs. B slope gives the concentration of holes as 2×10^{20} cm^{-3}, which is slightly lower than the value of 3.5×10^{20} reported by Ohno et al. [34] for GaMnAs containing 5.3% Mn. This may be connected with the lower growth temperature (200 °C) used by us. The dependence of the GaMnAs lattice constant on Mn concentration in our case [see Eq. (1)] compared to that established by Ohno et al. [6,9] [giving a_{MnAs} (zinc-blende) = 5.98 Å] suggests, in connection to the observation of Schott et al. [24], that the GaMnAs samples studied by Ohno et al. were grown at a higher temperature than our samples.

Having established the concentration of holes in single GaMnAs layers and knowing the concentration of As antisites in the GaAs spacer layers it is possible to calculate the hole concentration profiles in the GaMnAs/GaAs SL structures by solving the one-dimensional Schrödinger equation self-consistently with the Poisson equation [43]. The results of such calculations for SL structures with 8 ML GaMnAs and two different GaAs spacer thickness: 4 and 10 ML, are shown in Fig. 3. A 50% difference in the maximum concentration of holes in these two structures can be seen. The average hole concentration integrated over the 8-ML thick GaMnAs layer in the structure with 10-ML thick GaAs spacers decreases significantly in comparison to the situation in the SL structure with 4-ML thick spacers. It should be noted, however, that our calculations are valid only above T_c (i.e. in the paramagnetic state). Below T_c,

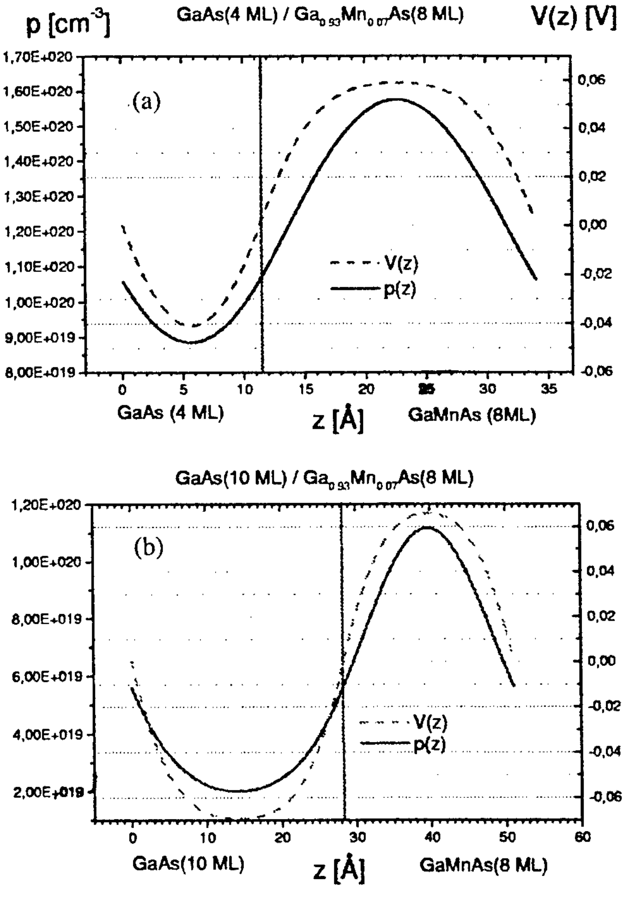

Fig. 3. Calculated hole densities—$p(z)$ and electrostatical potentials $V(z)$ in $Ga_{0.93}Mn_{0.07}As$ (m ML)/GaAs (n ML) superlattice structures for thickness of GaMnAs (m) and GaAs (n) being equal to: (a) $m=8$, $n=4$; (b) $m=8$, $n=10$.

when the Mn ions are ferromagnetically coupled, a strongly asymmetric distribution of spin-up and spin-down holes are predicted [44]. This asymmetry should lead to an enhanced T_c since the spin-down holes mediating the ferromagnetic interactions between Mn ions are confined in the GaMnAs layers. The simple model calculations used here are thus not expected to give quantitative information on the hole concentration, but are used to give the qualitative behavior of the charge carrier concentration profiles in GaMnAs/GaAs SLs and how it develops as, for instance, the spacer layer thickness is varied.

For the set of samples with 8, 12 and 16-ML thick GaMnAs, we observe that the ferromagnetic phase transition disappears for structures with GaAs spacers thicker than 10 ML. One possible reason for this may be the above-mentioned decrease of hole concentration in GaMnAs with increasing GaAs spacer thickness. However, as can be seen in Fig. 3, the average hole density in the GaMnAs layers in the SL with 10-ML thick GaAs spacers is $\sim 7\times10^{19}$ cm^{-3}, which according to the mean field model of Dietl et al. [36] should yield a paramagnetic-to-ferromagnetic transition at ~10 K in GaMnAs with 7% of Mn. The disappearance of the ferromagnetic phase in structures with GaAs spacers thicker than 10 ML, should thus be caused by some other effect than the low value of the hole density in GaMnAs. One possible origin may be interface imperfections. The interface roughness of approximately two monolayers, may give an effective thickness of the magnetic GaMnAs layers smaller than eight monolayers. This together with the low concentration of holes may explain the disappearance of the paramagnetic-to-ferromagnetic transition in SLs having a spacer layer thickness being larger than 10 ML.

4. Structural and magnetic properties of GaMnAs/GaAs superlattices

Before the MBE growth of each GaMnAs/GaAs SL, the growth rates of constituent SL layers were carefully calibrated on a test sample via RHEED intensity oscillations. The MBE growth of the SLs was controlled by RHEED oscillations too. The sequence of shutter opening times was chosen in such a way, that the growth of each layer was terminated at the maximum intensity of the specular RHEED beam, as can be seen in Fig. 1. The thickness of the GaMnAs and GaAs layers was thus controlled with a submonolayer accuracy. This is in our opinion a key factor to obtain short period GaMnAs/GaAs SLs structures with ferromagnetic properties. At each interface the growth was stopped for 30 s in order to enhance the surface smoothness. Using this growth procedure it was usually possible to record RHEED intensity oscillations for up to 50 superlattice periods.

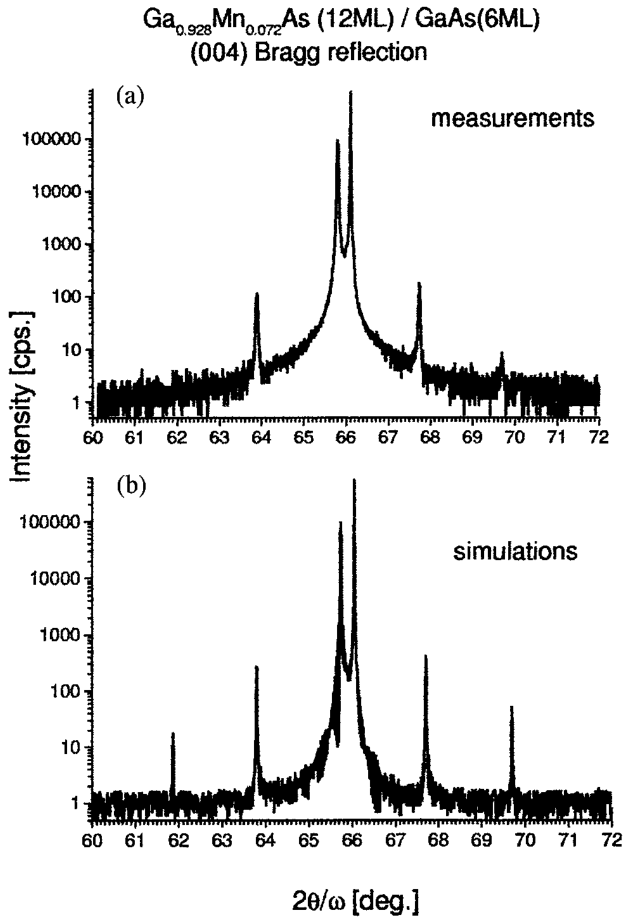

Fig. 4. (004) X-Ray Bragg reflection for a $Ga_{0.928}Mn_{0.072}As$(12 ML)/GaAs(6 ML)×100 superlattice: (a) measured spectrum; (b) calculated spectrum.

The structural quality of the SLs was estimated by X-ray diffraction (XRD) measurements. Fig. 4 shows an example of XRD results for the SL structure with 12-ML thick GaMnAs layers and 6-ML thick GaAs spacers. The position of the zero-order SL (004) Bragg peak as well as the positions of the satellites of order +1 and −1 are well reproduced by XRD simulations. The parameters extracted for each SL structure, that is the thickness and the composition of each layer in a SL, are in good accordance with parameters measured by RHEED oscillations during the MBE growth. Fig. 5 shows the measured XRD spectra for three GaMnAs/GaAs SL structures with 8-ML thick $Ga_{0.96}Mn_{0.04}As$ and GaAs spacers having a thickness ranging from 5 to 9 ML in 2 ML steps. It can be clearly seen that the angular spacing of the first-order satellites decreases with increasing spacer thickness, which is in agreement with the expected behavior for the XRD spectrum in a system with increasing period. It should be noted that the fact that only first order (and in some cases second order) satellites can be seen in XRD spectra is due to both low chemical contrast between GaAs and GaMnAs

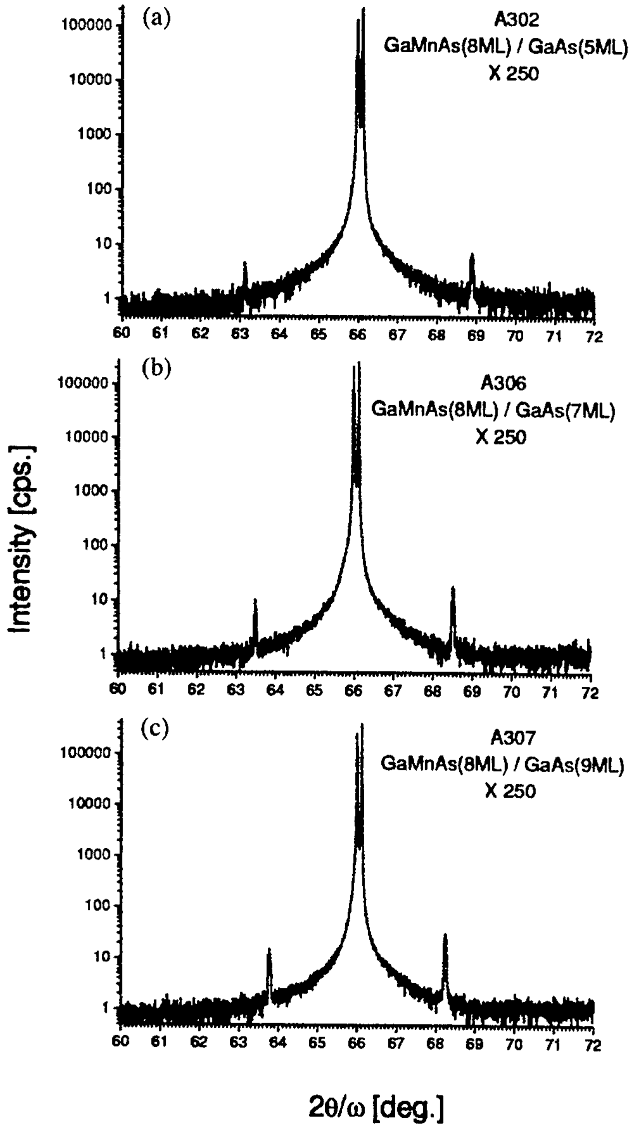

Fig. 5. (004) X-Ray Bragg reflections for $Ga_{0.96}Mn_{0.04}As$ (8 ML)/GaAs (n ML): (a) $n=5$; (b) $n=7$; (c) $n=9$.

with only up to 7% of Mn, and low lattice parameter contrast (only 0.3% lattice mismatch between $Ga_{0.93}Mn_{0.07}As$ and LT GaAs).

The reciprocal space maps measured by us for some SL structures demonstrate in all cases that the SL structures are totally strained to the GaAs(100) substrate. In relation to this, the GaMnAs/GaAs SL structures are in a compressive strain state, which induces in-plane magnetic anisotropy in this system [9].

Magnetic properties of GaMnAs/GaAs SLs were investigated by means of magnetization measurements using a superconducting quantum interference device (SQUID). Fig. 6 shows SQUID results for a $Ga_{0.93}Mn_{0.07}As$/GaAs SL structure with a magnetic layer thickness of 8 and 4-ML thick GaAs spacer layers. The number of repetitions of the GaMnAs/GaAs sequence was in this case equal to 100. The inset shows magnetization vs. temperature curves for 0.8-μm thick reference GaMnAs films with 5.5 and 7% of Mn. The T_c value close to 60 K for the GaMnAs/GaAs SL is close to the value obtained for the single GaMnAs sample containing 5.5% of Mn. Also, the saturation magnetization measured at 4 K is the same for both samples ($\sim 2\ \mu_B$/Mn atom). It is interesting to find that T_c for the SL structure with $Ga_{0.93}Mn_{0.07}As$ layers is higher than the transition temperature obtained for the 0.8-m thick reference $Ga_{0.93}Mn_{0.07}As$ sample. The average Mn concentration in the SL structure, calculated as for a digital alloy, equals 4.67%. A single thick layer of GaMnAs containing 4.67% of Mn has a T_c value slightly lower than that of GaMnAs with 5.5% of Mn (known to exhibit the maximum value of T_c [9]). We have verified by XRD measurements that this superlattice is well defined (i.e. that there is a negligible interdiffusion at the interfaces). It thus appears that the paramagnetic-to-ferromagnetic transition temperature can be enhanced when magnetic GaMnAs layers are separated by non-magnetic GaAs spacers in a superlattice structure. Similar type of behavior has been observed in digital GaAs/MnAs structures [45], where fractional MnAs monolayers (with 50% GaAs surface coverage) are separated by GaAs spacers having a thickness of the same order magnitude as the GaAs spacers in GaMnAs/GaAs SL structures investigated in this work.

Recent theoretical work [44,46] interpret a T_c enhancement in SLs structures containing GaMnAs as a result of confinement of spin-down holes in the magnetic layers and predict in some specific cases T_c values in SLs to be higher than in single GaMnAs layers [46].

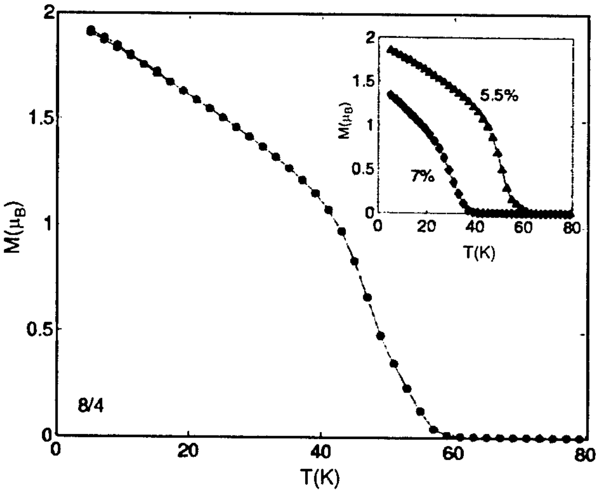

Fig. 6. Temperature dependence of the magnetization for a $Ga_{0.93}Mn_{0.07}As$ (8 ML)/GaAs (4 ML)×100 SL. The inset shows results for two 0.8-m thick reference GaMnAs samples, containing 5.5 and 7% of Mn, respectively.

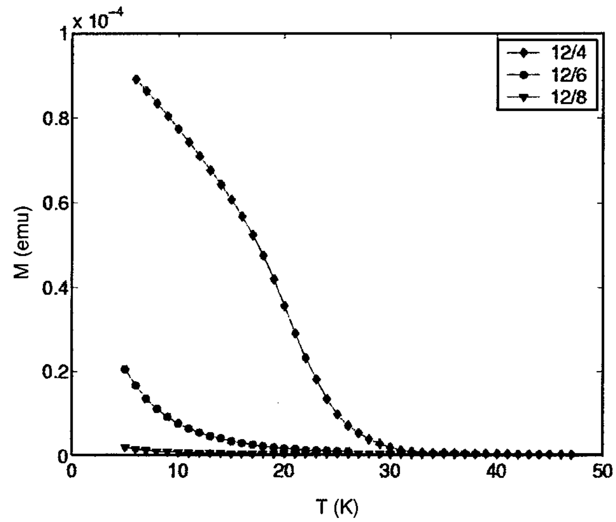

Fig. 7. Temperature dependence of the magnetization for $Ga_{0.96}Mn_{0.04}As$ (12 ML)/GaAs (*n* ML) superlattices. In superlattice structures with the thickness of GaAs being larger than 10 ML, no ferromagnetic phase transition was detected.

The dependence of the magnetic properties on thickness of the GaAs spacer can be seen in Fig. 7 for GaMnAs/GaAs SLs with 12-ML thick $Ga_{0.96}Mn_{0.04}As$ layers. The magnetic transition temperature decreases monotonously with increasing thickness of the GaAs spacer; for a spacer thickness of 10 ML or larger, it was not possible to detect a low temperature ferromagnetic phase. Similar results with a ~10 ML lower limit of the GaAs layer thickness have been obtained for GaMnAs/GaAs SL structures with 8 and 16-ML thick GaMnAs layers.

Structures with 8, 10, 12 and 16-ML thick GaMnAs layers, as well as structures having much thicker GaMnAs layers (25 and 50 ML) were investigated by polarized neutron reflectivity [47] and neutron diffraction [21]. In both cases, ferromagnetic coupling between magnetic GaMnAs layers was detected for spacer layer thickness of six to eight monolayers. Fig. 8 shows the temperature dependence of the intensity of the first-order neutron diffraction satellite for a GaMnAs (10 ML)/GaAs (6 ML) SL structure with 250 repetitions. An increase in intensity of this satellite diffraction peak below T_c (T_c was determined by SQUID measurements) proves that the adjacent GaMnAs layers are ferromagnetically coupled [21]. So far, we have not detected the theoretically predicted [20] antiferromagnetic interlayer coupling in this system.

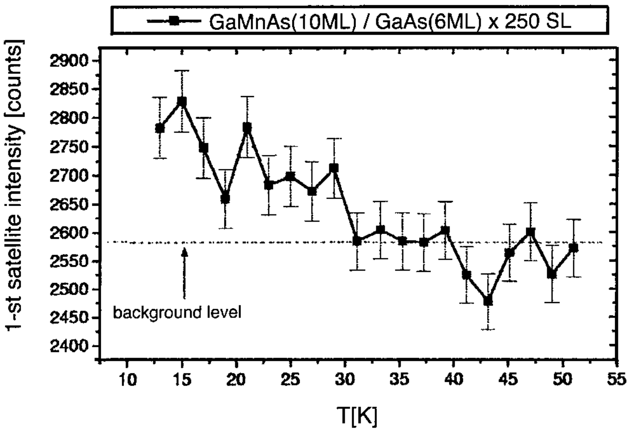

Fig. 8. Intensity of the first satellite peak in a $Ga_{0.93}Mn_{0.07}As$ (10 ML)/GaAs (6 ML). SL vs. temperature, detected in neutron diffraction experiments. An increase of the satellite intensity below T_c indicates that the adjacent GaMnAs superlattice layers are ferromagnetically coupled.

5. Conclusions

We have observed a ferromagnetic phase transition in GaMnAs/GaAs superlattices with ultrathin GaMnAs layers (from 8 to 16 ML). This is much below the so far established limit for the GaMnAs layer thickness (50 Å) at which GaMnAs/Ga(Al)As superlattices were reported to lose their ferromagnetic properties. We have verified that the paramagnetic-to-ferromagnetic phase transition occurs in short period GaMnAs/GaAs superlattices with 8, 12 and 16 ML GaMnAs layer thickness. In most cases, the ferromagnetic phase in these superlattices disappears when the thickness of the GaAs spacer layer is larger than 10 ML (28 Å). We interpret this 10 ML spacer thickness limit for the ferromagnetic phase in short period GaMnAs/GaAs superlattices as a result of the decrease of hole density in the magnetic layers due to diffusion and partial recombination of holes in the GaAs spacer layers. At low spacer layer thickness (4 ML) the opposite effect occurs—the temperature of the paramagnetic-to-ferromagnetic phase transition in SL structures is higher than in a thick reference GaMnAs sample having the same Mn concentration. The enhancement of T_c in this case can be explained as an effect of confinement of spin-down holes in the GaMnAs layers. Neutron diffraction measurements on structures with 6 and 8-ML thick GaAs spacers demonstrate that adjacent GaMnAs layers in the SL structures are ferromagnetically coupled.

Acknowledgments

This work was supported by grants from the Swedish Natural Science Research Council (NFR), the Swedish Research Council for Engineering Sciences (TFR), and via cooperation with the Nanometer Structure Consortium in Lund, the Swedish Foundation for Strategic Research (SSF). Measurements at high magnetic fields have been supported by the European Community within the 'Access to Research Infrastructure action of the Improving Human Potential Programme'.

References

[1] H. Munekata, H. Ohno, S. von Molnár, A. Segmüller, L.L. Chang, L. Esaki, Phys. Rev. Lett. 63 (1989) 1849.
[2] H. Ohno, H. Munekata, T. Penney, S. von Molnár, L.L. Chang, Phys. Rev. Lett. 68 (1992) 2664.
[3] H. Munekata, T. Abe, S. Koshihara, A. Oiwa, M. Hirasawa, S. Katsumoto, Y. Iye, C. Urano, H. Takagi, J. Appl. Phys. 81 (1997) 4862.
[4] H. Ohno, D. Chiba, F. Matsukura, T. Omiya, E. Abe, T. Dietl, Y. Ohno, K. Ohtani, Nature 408 (2000) 944.
[5] D.D. Awschalom, R.K. Kawakami, Nature 408 (2000) 923.
[6] H. Ohno, A. Shen, F. Matsukura, A. Oiwa, A. Endo, S. Katsumoto, Y. Iye, Appl. Phys. Lett. 69 (1996) 363.
[7] T. Hayashi, M. Tanaka, T. Nishinaga, H. Shimada, Y. Otuka, J. Cryst. Growth 175/176 (1997) 1063.
[8] A. Van Esch, L. Van Bockstal, J. De Boeck, G. Verbank, A.S. van Steenbergen, P.J. Wellman, B. Grietens, R. Bogaerts, F. Herlach, G. Borghs, Phys. Rev. B 56 (1997) 13103.
[9] H. Ohno, Science 281 (1998) 951.
[10] T. Dietl, H. Ohno, F. Matsukura, J. Cibert, D. Ferrand, Science 287 (2000) 1019.
[11] J. Sadowski, J.Z. Domagała, J. Bąk–Misiuk, S. Koleśnik, M. Sawicki, K. Świątek, J. Kanski, L. Ilver, V. Ström, J. Vac. Sci. Technol. B 18 (2000) 1697.
[12] S.A. Wolf, D.D. Awschalom, R.A. Buhrman, J.M. Daughton, S. von Molnár, M.L. Roukes, A.Y. Chtchelkanova, D.M. Treger, Science 294 (2001) 1488.
[13] T. Hayashi, M. Tanaka, K. Seto, T. Nishinaga, K. Ando, Appl. Phys. Lett. 71 (1997) 1825.
[14] T. Hayashi, M. Tanaka, K. Seto, T. Nishinaga, H. Shimada, K. Ando, J. Appl. Phys. 83 (1998) 6551.
[15] M. Tanaka, Physica E 2 (1998) 372.
[16] A. Shen, H. Ohno, F. Matsukura, H.C. Liu, N. Akiba, Y. Sugawara, T. Kuriowa, Y. Ohno, Physica B 249/25 (1998) 809.
[17] M. Tanaka, J. Vac. Sci. Technol. B 16 (1998) 2267.
[18] M. Tanaka, H. Shimizu, T. Hayashi, H. Shimada, K. Ando, J. Vac. Sci. Technol. A 18 (2000) 1247.
[19] M.A. Boselli, A. Ghazali, I.C. da Cunha Lima, Phys. Rev. B 62 (2000) 8895.
[20] T. Jungwirth, W.A. Atkinson, B.H. Lee, A.H. MacDonald, Phys. Rev B 59 (1999) 9818.
[21] W. Szuszkiewicz, E. Dynowska, B. Hennion, F. Ott, M. Jouanne, J.F. Morhange, M. Karlsteen, J. Sadowski, Acta Physica Polonica A 100 (2001) 335.
[22] H. Shimizu, T. Hayashi, T. Nishinaga, M. Tanaka, Appl. Phys. Lett. 74 (1999) 398.
[23] M. Tanaka, H. Shimizu, T. Hayashi, H. Shimada, K. Ando, J. Vac. Sci. Technol. A 18 (2000) 1247.
[24] G.M. Schott, W. Faschinger, L.W. Molenkamp, Appl. Phys. Lett. 79 (2001) 1807.
[25] J. Sadowski, E. Hankiewicz, J. Domagała, unpublished.
[26] J. Sadowski, R. Mathieu, P. Svedlindh, J.Z. Domagała, J. Bąk-Misiuk, K. Świątek, M. Karlsteen, J. Kanski, L. Ilver, H. Åsklund, U. Södervall, Appl. Phys. Lett. 78 (2001) 3271.
[27] J.I. Landman, C.G. Morgan, J.T. Schick, Phys. Rev. Lett. 74 (1995) 4007.
[28] X. Liu, A. Prasad, J. Nishio, E.R. Weber, Z. Liliental-Weber, W. Walukiewicz, Appl. Phys. Lett. 67 (1995) 279.
[29] T.E.M. Staab, R.M. Nieminen, J. Gebauer, R. Krause-Rehberg, M. Luysberg, M. Haugk, Th. Frauenheim, Phys. Rev. Lett. 87 (2001) 045504.
[30] A. Suda, N. Otsuka, Surf. Sci. 458 (2000) 162.
[31] G. Apostolopoulos, J. Herfort, W. Ulrici, L. Däweritz, K.H. Ploog, Phys. Rev. B 60 (1999) R5145.
[32] S. Sanvito, N.A. Hill, Appl. Phys. Lett. 78 (2001) 3493.
[33] P.A. Khorzhavyi, I.A. Abrikosov, E.A. Smirnova, L. Berqvist, P. Mohn, R. Mathieu, P. Svedlindh, J. Sadowski, E.I. Isaev, Yu. Kh. Vekilov, O. Eriksson, submitted to Phys. Rev. Lett. (2001).
[34] T. Omiya, F. Matsukura, T. Dietl, Y. Ohno, T. Sakon, M. Motokawa, H. Ohno, Physica E 7 (2000) 976.
[35] R.R. dos Santos, L.E. Oliveira, and J. d'Albuquerque e Castro, arXiv: cond-mat/0108245 (2001).
[36] T. Dietl, H. Ohno, F. Matsukura, Phys. Rev. B 63 (2001) 195205.
[37] J. König, J. Schlieman, T. Jungwirth, A.H. MacDonald, arXiv: cond-mat/0111314 (2001).
[38] T. Story, R.R. Gałązka, R.B. Frankel, P.A. Wolf, Phys. Rev. Lett. 56 (1986) 777.
[39] D. Ferrand, J. Cibert, A. Wasiela, C. Bourgognon, S. Tatarenko, G. Fishman, T. Andrearczyk, J. Jaroszyński, S. Koleśnik, T. Dietl, B. Barbara, D. Dufeu, Phys. Rev. B 63 (2001) 085201.
[40] A. Chattopadhyay, S. Das Sarma, A.J. Millis, Phys. Rev. Lett. 87 (2001) 227202.
[41] S. Sanvito, P. Ordejon, N.A. Hill, Phys. Rev. B 63 (2001) 165206.
[42] T. Hayashi, Y. Hashimoto, S. Katsumoto, Y. Iye, Appl. Phys. Lett. 78 (2001) 1691.
[43] Y. Fu, T.H. Wang, M. Wilander, J. Appl. Phys. 89 (2001) 1759.
[44] L. Louriero da Silva, M.A. Boselli, I.C. da Cunha Lima, X.F. Wang, A. Ghazali, Appl. Phys. Lett. 79 (2001) 3305.
[45] R.K. Kawakami, E. Johnston-Halperin, L.F. Chen, M. Hanson, N. Guebels, J.S. Speck, A.C. Gossard, A.A. Awschalom, Appl. Phys. Lett. 77 (2000) 2379.
[46] I. Vurgaftman, J.R. Meyer, Phys. Rev. B 64 (2001) 245207.
[47] H. Kępa, J. Kutner-Pielaszek, A. Twardowski, C.F. Majkrzak, J. Sadowski, T. Story, T.M. Giebultowicz, Phys. Rev. B 64 (2001) 121302R.

ELSEVIER

Thin Solid Films 412 (2002) 129–138

thin solid films

www.elsevier.com/locate/tsf

MBE growth and characterization of Hg based compounds and heterostructures

C.R. Becker*, X.C. Zhang, K. Ortner, J. Schmidt, A. Pfeuffer-Jeschke, V. Latussek, Y.S. Gui, V. Daumer, J. Liu, H. Buhmann, G. Landwehr, L.W. Molenkamp

Physikalisches Institut der Universität Würzburg, Am Hubland, 97074 Wurzburg, Germany

Abstract

The MBE growth of Hg$_{1-x}$Cd$_x$Te alloys and type III HgTe/Hg$_{1-x}$Cd$_x$Te heterostructures has been discussed, including similarities and differences between the (0 0 1) and (1 1 2)B orientations. Furthermore the MBE growth of HgTe based quantum wells (QWs) with the incorporation of Mn are additional topics. An investigation of the optical properties of type III superlattices with a normal band structure has lead to information about band structure of these heterostructures as well as information about the interface and the semimetallic QW. For example, by means of the full 8×8 Kane Hamiltonian in the envelope function approximation, it has been demonstrated that the energy separation between the H1–E1 and L1–E1 intersubband transition energies is primarily determined by the valence band offset, Λ, between HgTe and CdTe. This has led to unambiguous values for the offset and its temperature dependence, i.e. $\Lambda(T)=570\pm60$ meV and $d\Lambda/dT=-0.40\pm0.04T$ meV/K. Furthermore the energy gap of HgTe at room temperature has also been determined. Magneto-transport measurements of n-type QWs show very pronounced Shubnikov-de Haas (SdH) oscillations and well developed quantum Hall plateaus for temperatures up to approximately 60 K. A large Rashba spin–orbit splitting of the first conduction subband, H1, has been observed in HgTe/Hg$_{1-x}$Cd$_x$Te QWs with an inverted band structure. Self-consistent Hartree calculations of the band structure based on the above model allows us to quantitatively describe the experimental results and demonstrates that the heavy hole nature of the H1 subband greatly influences the spatial distribution of electrons in the QW and thus enhances the Rashba spin splitting, i.e. $\Delta E_{H1}=\beta k_{\parallel}^{3}$. Furthermore, the presence of two periodic SdH oscillations in p-type QWs with an inverted band structure has been observed and is the first direct evidence that these heterostructures are indirect semiconductors. The influence of Mn in the upper barrier on the 2D electrons in the well has been investigated as a function of their separation. With spacer thicknesses of 10 and 15 nm, no appreciable change is observed, however, a reduction of the spacer thickness to 5 nm results in an increase in the maximum population difference between the two Rashba spin split H1 subbands by a factor of approximately two.

Keywords: Molecular beam epitaxy growth; HgTe; Hg$_{1-x}$Cd$_x$Te; Superlattices; Quantum wells; Valence band offset; Band structure; Rashba spin splitting; Indirect band gap

1. Introduction

The Hg$_{1-x}$Cd$_x$Te alloy has been one of the most commercially exploited alloys in recent decades. Both bulk samples and epitaxial layers over the entire composition range can be produced. Due to applications requiring increasingly complex heterostructures [1], molecular beam epitaxy (MBE) is now one of the more important growth techniques. The MBE growth and the dependence of the composition and surface structure on crystal orientation will be discussed. The topics include surface structure, incorporation of Hg and Cd, n and p type doping, modulation doping of both n and p type quantum wells (QWs), etc.

The band structure and hence the optical and electrical properties of type III heterostructures are largely determined by that of the QW. For example the band gap of HgTe and its temperature dependence directly influences the temperature dependence of the superlattice (SL) subbands and thus the temperature dependence of the intersubband transition energies [2]. The magnitude of the negative band gap of HgTe at room temperature is subject to large experimental uncertainties due to difficulties in the conventional magneto-optical method at temperatures above 100 K [3]. Another such property is the deformation potential of HgTe relative to that of CdTe which has only recently been experimentally

---

*Corresponding author.

E-mail address: becker@physik.uni-wuerzburg.de (C.R. Becker).

0040-6090/02/$ - see front matter

PII: S0040-6090(02)00324-3

determined by means of an optical absorption investigation of HgTe/$Hg_{0.32}Cd_{0.68}Te$ SLs under hydrostatic pressure [4]. Furthermore, it has been shown that the valence band offset is to a good approximation primarily responsible for the energy difference between the first heavy hole, H1, and the first light hole, L1, subband of a HgTe/$Hg_{1-x}Cd_xTe$ SL with normal band structure [2]. This energy difference is nearly independent of other SL parameters, and consequently leads to a precise determination of the valence band offset, Λ, between HgTe and CdTe.

The band structure and consequently the optical properties depend on the band structure of the QWs and barriers, i.e. HgTe and $Hg_{1-x}Cd_xTe$, their widths, and the potential energy differences between these two components. The latter depends in turn on their composition, the valence band offset as well as the shape and width of the Cd concentration profile across the interfaces. A profile described by an error function similar to an experimental profile according to Kim et al. [5] is assumed and leads to a consistent description of the experimental results. Finally, the width of this interface, d_t, has been shown to be a convenient variable for the study of interdiffusion in these SLs [6].

If the HgTe layer is less than 6 nm thick then the heterostructure is a normal semiconductor, however, if the thickness is greater than 6 nm then the band structure is inverted, i.e. the Γ_6 and Γ_8 bands exchange places and the energy gap is negative. Magneto-transport experiments have been conducted on both n and p type modulation doped HgTe/$Hg_{1-x}Cd_xTe$ QWs with an inverted band structure. An analysis of Shubnikov-de Haas (SdH) oscillations in gate controlled n type QWs reveals a large Rashba spin–orbit splitting [7,8]. This is due to the heavy hole character of the first conduction subband. In a p-type QW two periodic SdH oscillations are observed which are caused by the indirect band structure [9].

2. Experimental details

The epitaxial alloys and heterostructures were grown in a Riber 2300 MBE system as has been described elsewhere [2,10]. After the growth of a thin CdTe buffer layer, the alloys and heterostructures were grown on (0 0 1) and (1 1 2)B oriented $Cd_{0.96}Zn_{0.04}Te$ substrates at 180 °C. The (0 0 1) QWs were modulation doped symmetrically, on both sides of the QW, and asymmetrically, on one side only, with either iodine or arsenic for n and p type structures, respectively. The $Hg_{0.3}Cd_{0.7}Te$ barriers are comprised of a 50 Å thick spacer and a 90 Å thick doped layer.

Asymmetric HgTe/$Hg_{0.3}Cd_{0.7}Te$(0 0 1) modulation doped n type QWs, were grown with Mn in the upper barrier. Mn is separated from the HgTe layer by means of a $Hg_{0.3}Cd_{0.7}Te$ spacer, which was varied between 5 and 15 nm. Then a $Hg_{0.3}Cd_{0.7}Te$ cap was grown, thereby maintaining the same total thickness of all layers above the HgTe layer, i.e. 34 nm.

The composition of the barrier material [11] has been determined by means of transmission measurements on thick test layers of $Hg_{1-x}Cd_xTe$ grown under identical conditions. SL periods and HgTe(0 0 1) layer widths have been determined via a dynamic simulation of the (0 0 2) and (0 0 4) Bragg reflections measured in a six crystal X-ray diffractometer [2]. A simulation of (1 1 2)B oriented heterostructures is more complicated and the results less accurate [12,13].

After growth of the QWs, standard Hall bars were fabricated by means of a wet chemical etch, then a 200 nm thick Al_2O_3 film, which serves as an insulating layer, was deposited by electron beam evaporation. Finally Al was evaporated to form a gate electrode.

Optical transmission measurements were carried out in the middle and near infrared with a Fourier transform spectrometer, Bruker IFS88. A $LiTaO_3$ detector was usually employed rather than a liquid nitrogen cooled detector e.g. $Hg_{1-x}Cd_xTe$, because of its better linearity. The aperture was kept as small as possible for the same reason, i.e. a diameter of 2–3 mm. The absorption coefficient, α, was determined by fitting the experimental transmission spectra to a theoretical description of the multi-layer system using standard matrix procedures [14].

3. Theoretical details

A large number of **k·p** band structure calculations using the envelope function approximation for the HgTe/$Hg_{1-x}Cd_xTe$ SL have been published during the last decade [15–18]. A brief review of these and other investigations pertinent to the results presented here can be found in Ref. [2].

The bands of both bulk HgTe and CdTe are described by Kane's four-band model (8×8 **k·p**) including second-order remote band contributions. The envelope function method has been used to calculate the band structure of the HgTe/CdTe SL. The results of the axial approximation are not exact, however, they give a good approximation, within 1 or 2 meV, for the subband energies at $k_{\parallel}=0$ as well as for an average of the subband dispersion over all $k_{\parallel}$ directions. Consequently all absorption coefficient calculations and most intersubband transition energy calculations were carried out using an adapted Hamiltonian in the axial approximation, in order to reduce the calculation time.

The effects of strain due to lattice mismatch were also taken into consideration. The lattice mismatch between HgTe and its environment is less than 0.1% which results in a shift in intersubband transition energies of less than 3 meV and can therefore be neglected. In contrast to the [0 0 1] direction [17], the strain tensor for the [1 1 2] direction has a shear strain component. This results in a piezoelectric field in the growth direction [19]. We have calculated the strain for a free standing, strained (1 1 2)B SL and a fully strained (1 1 2)B SL on a $Cd_{0.96}Zn_{0.04}Te$ substrate. From these results the piezoelectric field has been calculated to be less than 5 mV/100 Å whose influence on intersubband transition energies is less than 1 meV and can therefore be neglected in the calculations.

A revised set of values for the band parameters ($\Delta = 1.0$ eV, $\gamma_1 = 4.1$, $\gamma_2 = 0.5$, $\gamma_3 = 1.3$, $F = 0$ and $E_p = 18.8$ eV) deduced from measurements on bulk HgTe and $Hg_{1-x}Cd_xTe$ by Weiler [20] were employed which nevertheless reproduce the same bulk band structure:

$$m^*_{\mathrm{hh}}(1\,1\,2) = \left(\gamma_1 - 2\gamma_2 - \frac{3}{2}(\gamma_3 - \gamma_2)\right)^{-1} m_0 = 0.53 m_0 \qquad (1)$$

and

$$m^*_{\mathrm{hh}}(0\,0\,1) = (\gamma_1 - 2\gamma_2)^{-1} m_0 = 0.32 \quad \text{at 5 K.} \qquad (2)$$

The energy gaps of HgTe and $Hg_{1-x}Cd_xTe$ were taken from the empirical $E_g(x, T)$ relationship according to Laurenti et al. [11] with the exception of HgTe at temperatures greater than 5 K as discussed below. The valence band offset between HgTe and $Hg_{1-x}Cd_xTe$ is employed as an adjustable variable and is assumed to vary linearly with x for $Hg_{1-x}Cd_xTe$, i.e. $x\Lambda$ [21]. An interface width, d_t, which results during growth or from interdiffusion of the two types of layers was integrated into the theory. The concentration profile across the interface is described by an error function similar to an experimental profile according to Kim et al. [5].

Self-consistent Hartree calculations of modulation doped $HgTe/Hg_{1-x}Cd_xTe$ QWs have been carried out using Kane's four-band model (8×8 **k·p**) described above in order to quantitatively describe the observed Rashba spin–orbit splitting, see Ref. [8] for details.

4. Results and discussion

4.1. Growth and characterization of $Hg_{1-x}Cd_xTe$

The growth of undoped $Hg_{0.80}Cd_{0.20}Te(1\,1\,2)B$ has been investigated with regard to the mobility μ and the surface structure [22]. The mobility has a maximum value of approximately 3×10^5 $cm^2\,V^{-1}\,s^{-1}$ for a Hg/Te flux ratio of between 150 and 180. In contrast the void density has a maximum value of 6×10^5 cm^{-2} at low ratios and falls rapidly to a nearly constant value of 2×10^3 cm^{-2} for ratios $\geqslant 200$. At a ratio of 180 the void density is approximately 4×10^3 cm^{-2}. In order to obtain maximum mobilities, a Hg/Te flux ratio of 180 was employed for the n-type layers in this investigation. Hence these samples have slightly higher void densities than the minimum values.

The optimum Hg/Te flux ratio for the (1 1 2)B orientation is about half of the optimum value for $Hg_{0.80}Cd_{0.20}Te(0\,0\,1)$ according to He et al. [23]. The latter value was chosen with regard to mobility and density of hillocks. Obviously the incorporation of Hg is more efficient in the (1 1 2)B alloys. This is also the case for Cd; the Cd/Te flux ratio necessary to grow an (1 1 2)B alloy with $x = 0.20 \pm 0.01$ at 180 °C is approximately 20–30% smaller than the ratio needed for the same composition in the (0 0 1) orientation [10]; and a (1 1 2)B alloy grown with only the CdTe and Hg sources results in $x = 0.95 \pm 0.02$, but a (0 0 1) alloy grown under the same conditions has a composition given by $x = 0.68 \pm 0.02$ [2].

The n and p type doping of $Hg_{1-x}Cd_xTe$ has been investigated using iodine in the form of CdI_2, and either arsenic as Cd_3As_2 or plasma activated nitrogen, respectively. n Type doping has been successful for the (0 0 1) and (1 1 2)B orientations [10,22] over the entire composition range with the exception of large Cd concentrations in the (1 1 2)B orientation. Producing p type alloys is more difficult and to our knowledge in situ doping has never been consistently successful. There is one exception; CdTe can be p type doped with plasma activated nitrogen up to concentrations of approximately 10^{18} cm^{-3}, however, at high charge carrier concentrations the crystalline quality is adversely effected. Normally p type doping of the alloy with As requires an ex situ anneal in Hg vapor at high temperatures. Nevertheless p type conductivity has been achieved in HgTe QWs by means of in situ doping and activation of Cd_3As_2 in a CdTe layer [24].

A low resolution atomic force microscope (AFM) image of an $Hg_{0.80}Cd_{0.20}Te(1\,1\,2)B$ epitaxial layer is shown in Fig. 1. Long parallel ridges and trenches are observed whose height difference is approximately 30 Å. These ridges and trenches are parallel to the edges of the sample, i.e. the {1 1 0} surface. The (1 1 2)B surface can be thought of as an (1 1 1)B surface with a high ledge density [25]. If the height of the individual steps is the distance between nearest neighbors, i.e. between cation and anion, then the distance between steps is 11.2 Å. Experimentally, a pattern in the reflection of high energy electron diffraction is observed whose period in real space is 11.1 ± 0.3 Å, which is in very good agreement with the above step width. These microscopic edges are parallel to the [1 1 0] direction and consequently parallel to the ridges and trenches shown in Fig. 1. Apparently preferential growth along these ledges result in these trenches and ridges.

The $Hg_{0.80}Cd_{0.20}Te(0\,0\,1)$ surface [22], is radically different. Nearly elliptically shaped mounds with a height of approximately 300 Å are observed which are similar to the mounds observed on the HgTe(0 0 1)

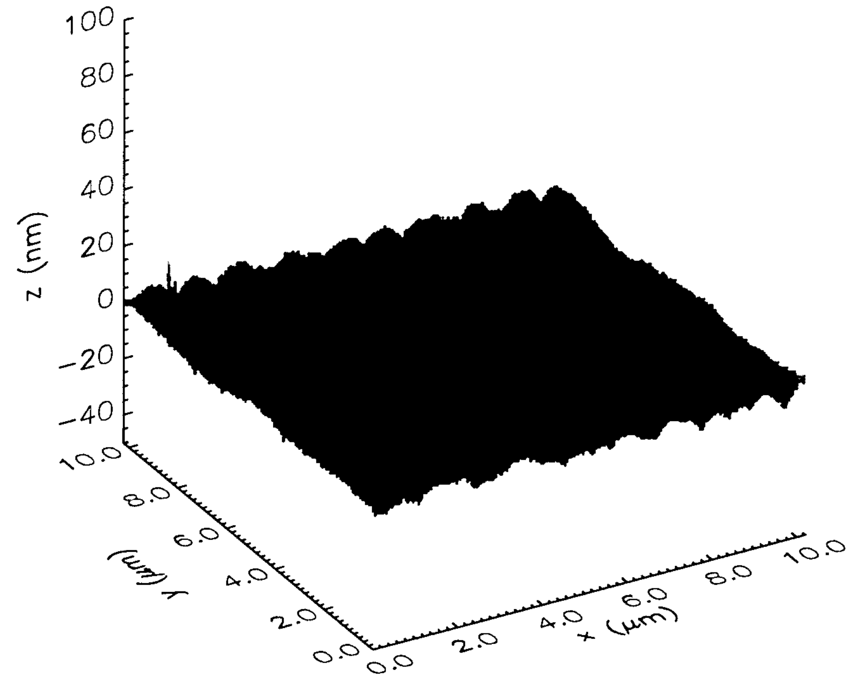

Fig. 1. A low resolution AFM image of a $Hg_{0.80}Cd_{0.20}Te$(1 1 2)B epitaxial layer.

surface by Oehling et al. [26] with a scanning tunnel microscope. The latter mounds consist of a series of terraces whose height is that of one monolayer, i.e. 3.2±0.3 Å, and width is approximately 500 Å. A high resolution AFM image of an $Hg_{0.80}Cd_{0.20}Te$(1 1 2)B surface demonstrates that these long ridges also consist of terraces whose height difference is one monolayer and average width is approximately 180 Å [22].

4.2. Optical absorption; intersubband transitions in SLs

The experimental and theoretical absorption spectra for a (1 1 2)B $HgTe/Hg_{0.05}Cd_{0.95}Te$ SL at 5 K are shown in Fig. 2. Three distinctive steps are observed which we have assigned to the H1–E1, L1–E1 and H2–E2 intersubband transitions. H, L and E are the heavy hole, light hole and electron subbands, respectively. In contrast, Yang et al. [27] attributed the first two steps at lower energies in a similar SL to the H1–E1 and H2–E2 transitions, and the weak shoulder near 240 meV to L1–E1. A correct assignment requires agreement between the calculated transition probabilities and the observed absorption coefficient spectrum as well as between the calculated and experimental frequencies. That this is the case here, is demonstrated in Fig. 2. The relative heights of the three steps are in good agreement with experiment, even though their absolute magnitudes are underestimated due to the neglect of Coulomb interaction between electron and hole [28]. The energies of the H1–E1 and L1–E1 transitions are in good agreement whereas agreement is only fair at higher energies, e.g. for H2–E2, as expected for a perturbation theory. The weak shoulder near 240 meV is due to the H2–E1 transition which is allowed only for **k**>0. For these reasons and others which will become apparent below, we shall concentrate on the H1–E1 and L1–E1 transitions.

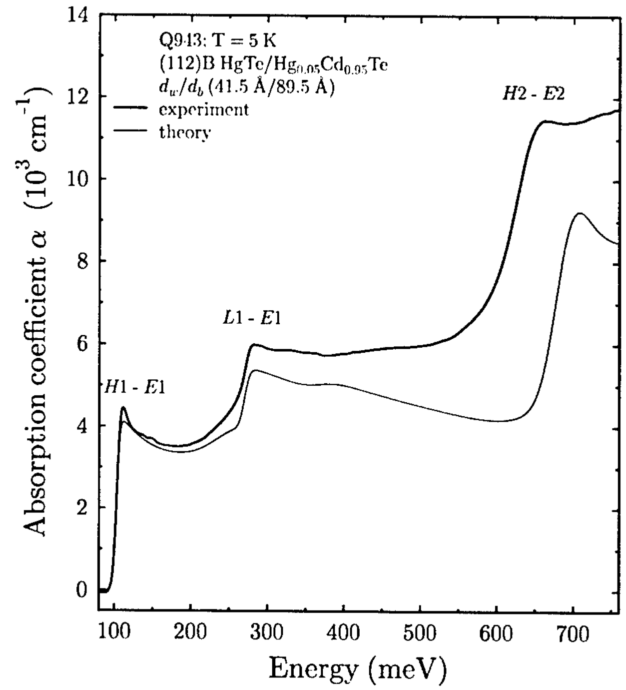

Fig. 2. The experimental and theoretical absorption coefficients of the (1 1 2)B $HgTe/Hg_{0.05}Cd_{0.95}Te$ SL Q943 at 5 K.

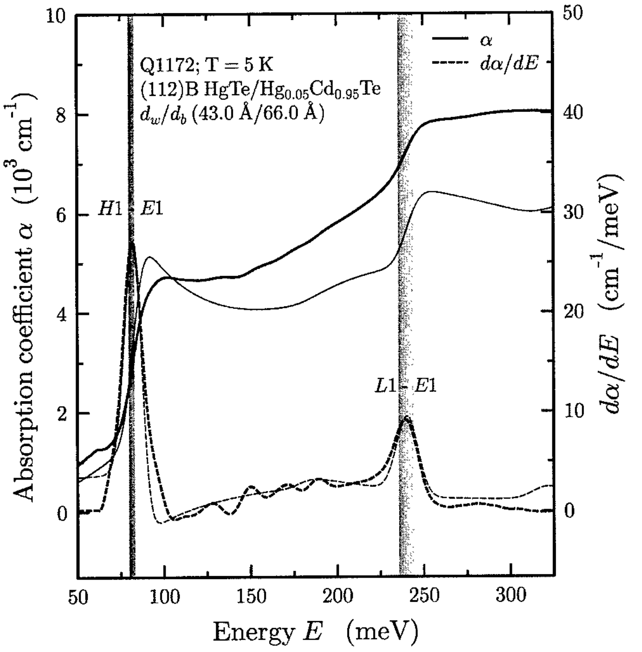

Fig. 3. The experimental (thick line) and theoretical (thin line) absorption coefficients, their first derivatives (thick and thin dashed lines, respectively) for the (1 1 2)B HgTe/Hg$_{0.05}$Cd$_{0.95}$Te SL Q1172 at 5 K. The intersubband transition energies are indicated by vertical lines and their dispersion for **q**||**z**, the miniband width, by the width of these vertical lines

A determination of the experimental intersubband transition energies is not trivial, due largely to a lack of knowledge about the position of a particular band gap relative to the frequency of photoluminescence peaks [27,29,30], or that of the absorption edges [31]. The method employed by Becker et al. [2] is to determine the position of the absorption edge and then its position relative to the intersubband transition energy itself. This can be accomplished by calculating the transition energies as well as the corresponding absorption coefficient. Finally, by fitting the theoretical and experimental absorption coefficients, one can determine the experimental intersubband transition energies relative to their absorption edges.

The absorption edges have been determined by two different methods. In the first method, the absorption edge is defined as the energy at the maximum value of the first derivative of the absorption coefficient. In the second method the absorption edge is determined from the temperature dependence of the transmission according to

$$\frac{\Delta T}{T}=\frac{T_2}{T_1}-1\approx d\Delta\alpha \tag{3}$$

where T and d are the transmission and sample thickness, respectively. Hence a good approximation of $\Delta\alpha$ can be obtained merely from a ratio of transmission spectra at slightly different temperatures [2] without the complications and uncertainties in calculating the absorption spectrum of the SL in a multi-layer structure [14]. The absorption edges according to both of these methods coincide with the H1–E1 and L1–E1 intersubband transition energies to within ±2 meV for all investigated SLs with one exception in which a systematic discrepency of 4 meV for L1–E1 is observed [2].

Good agreement between experimental and theoretical values of the absorption edges, i.e. $d\alpha/dE$, is demonstrated for a (1 1 2)B orientated SL in Fig. 3. The full width at half maximum, FWHM, of $d\alpha/dE$ for the H1–E1 and L1–E1 intersubband transitions is approximately 13 and 16 meV, respectively, and thus sufficiently narrow to allow a determination of these energies with a precision of ±2 meV or better. The absorption edges for Q943 shown in Fig. 2 are even sharper with corresponding FWHMs of 8.5 and 12 meV.

The H1–E1 and L1–E1 intersubband transition energies at 5 K for all of the investigated (1 1 2)B SLs are plotted vs. QW width, d_w, in Fig. 4. Also shown is the energy difference between these two intersubband transitions, i.e. $E_{H1}-E_{L1}=E_{L1-E1}-E_{H1-E1}$. The strong inverse dependence of both transitions on d_w is obvious, whereas $E_{H1}-E_{L1}$ is nearly independent of d_w. The latter energy difference depends nearly linearly on the valence band offset, Λ. Hence a determination of Λ is possible which is not influenced by uncertainties in d_w. The three sets of lines in Fig. 4 are theoretical results for a series

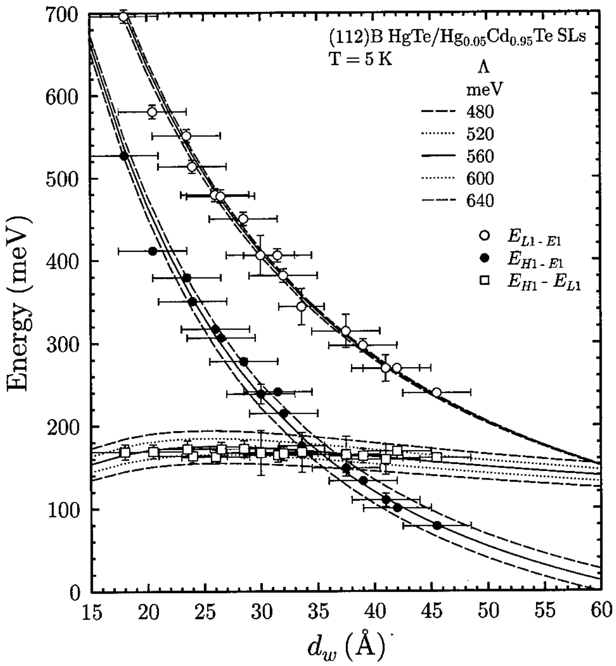

Fig. 4. The experimental values for E_{H1-E1} (filled circles), E_{L1-E1} (empty circles) and the energy difference, $E_{H1}-E_{L1}$ (empty squares), for all (1 1 2)B SLs together with theoretical results at 5 K (lines) are plotted vs. d_w. Calculated results using $d_t=24$ Å for possible values of Λ are shown. d_t is the interface width.

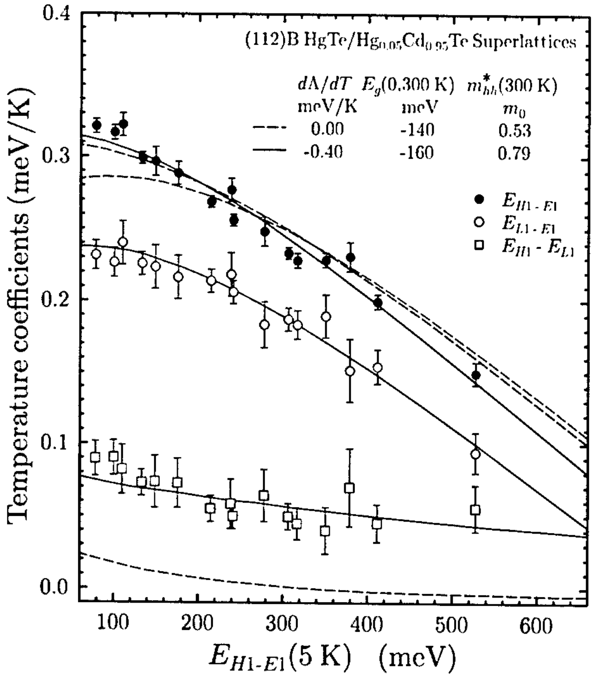

Fig. 5. Linear temperature coefficients for $E_{\mathrm{H1-E1}}$ (filled circles), $E_{\mathrm{L1-E1}}$ (empty circles) as well as $E_{\mathrm{H1}}-E_{\mathrm{L1}}$ (empty squares) are plotted vs. $E_{\mathrm{H1-E1}}$ at 5 K for all (1 1 2)B SLs. Calculated results for $\mathrm{d}\Lambda/\mathrm{d}T=$ 0.00 meV/K and E_g(HgTe, 300 K) $= -140$ meV are reproduced as dashed lines, and the results when $\mathrm{d}\Lambda/\mathrm{d}T = -0.40$ meV/K, E_g(HgTe, 300 K) $= -160$ meV and in addition m^*_{hh} is temperature dependent, i.e. $m^*_{\mathrm{hh}} = 0.79 m_0$ at 300 K, as solid lines.

of Λ values. By means of an error analysis involving all relevant bulk and SL parameters together with their uncertainties, the valence band offset between HgTe and CdTe has been determined to be $\Lambda = 570 \pm 60$ meV for both the (0 0 1) and (1 1 2)B orientations [2]. A detailed comparison of this value and literature values can be found in Ref. [2].

Experimental values of $E_{\mathrm{H1}}-E_{\mathrm{L1}}$ display a significant temperature dependence [2]. Therefore according to the conclusions presented above, Λ is also temperature dependent. Linear temperature coefficients have been calculated for the three pertinent energies using the SL parameters determined below. The calculated results are obviously in excellent agreement with the experimental values according to Ref. [2]. Because the temperature dependence of $E_{\mathrm{H1}}-E_{\mathrm{L1}}$ is linear within experimental uncertainties, the authors concluded that this is also the case for Λ.

The temperature dependence has been determined using a procedure which relies only on experimentally determined energies and not on d_{w} or other SL parameters. This is illustrated in Fig. 5 where the temperature coefficients for $E_{\mathrm{H1-E1}}$, $E_{\mathrm{L1-E1}}$ and $E_{\mathrm{H1}}-E_{\mathrm{L1}}$ are plotted vs. $E_{\mathrm{H1-E1}}$ (5 K) for the (1 1 2)B SLs. The dashed lines are results of the theory when Λ is assumed to be temperature independent and the energy gap of HgTe at room temperature, E_g(0, 300 K), is taken to be -140 meV [32]. Even though the temperature dependence of the H1–E1 transition can be reproduced, this is clearly not the case for either L1–E1 or the energy separation between these two transitions, $E_{\mathrm{H1}}-E_{\mathrm{L1}}$. Consequently the results of previous investigations, which are based merely on the H1–E1 transition can be misleading. For example the conclusion of von Truchsess et al. [33] that Λ is temperature independent, is obviously incorrect.

It has been demonstrated that the temperature dependence of the L1–E1 intersubband transition is determined by the temperature dependence of both the HgTe band gap and Λ. A least square fit to the experimental values of L1–E1, shown as a solid line in Fig. 5, results in $E_g(0,\ 300\ \mathrm{K}) = -160 \pm 2$ meV and $\mathrm{d}\Lambda/\mathrm{d}T = -0.40 \pm 0.04$ meV/K [2], which are listed in Table 1. This value for E_g(0, 300 K) differs appreciably from literature values of -140 and -120 meV [11,32], which clearly lie outside of the experimental uncertainties in this investigation. However, these two values are not experimental values: they have been determined by extrapolating experimental results for $T < 100$ K up to room temperature.

On the basis of X-ray photoemission spectroscopy, and ultra violet spectroscopy (UPS) Sporken et al. [34] concluded that the valence band offset between CdTe and HgTe was independent of temperature between 50 K and room temperature with an uncertainty of ±0.25 meV/K. However the valence band offset was not determined at $\mathbf{k} = 0$: their UPS samples were sputtered and they employed the He I and He II emission lines whose energies correspond to a position in the Brillouin zone far removed from $\mathbf{k} = 0$ [35].

The results for $E_{\mathrm{H1-E1}}$ and $E_{\mathrm{H1}}-E_{\mathrm{L1}}$ using $\mathrm{d}\Lambda/\mathrm{d}T = -0.40$ meV/K and $E_g(0,\ 300) = -160$ meV are in good

Table 1

Experimentally determined values together with their uncertainties for E_g(0, 300 K), Λ_0, Λ(300 K), $\mathrm{d}\Lambda/\mathrm{d}T$ and m^*_{hh}(300 K), for the (1 1 2)B and (0 0 1) orientations

	E_g(0, 300 K) meV	Λ_0 meV	Λ(300 K) meV	$\mathrm{d}\Lambda/\mathrm{d}T$ meV/K	m^*_{hh}(5 K)[a] m_0	m^*_{hh}(300 K) m_0
(1 1 2)B	−160±2	572±60	452±60	−0.40±0.04	0.53	0.79±0.04
(0 0 1)	−157±4	566±60	458±60	−0.41±0.10	0.32	0.40±0.11

The valence band offset is given by $\Lambda(T) = \Lambda_0 + (\mathrm{d}\Lambda/\mathrm{d}T)T$.

[a] After Ref. [20].

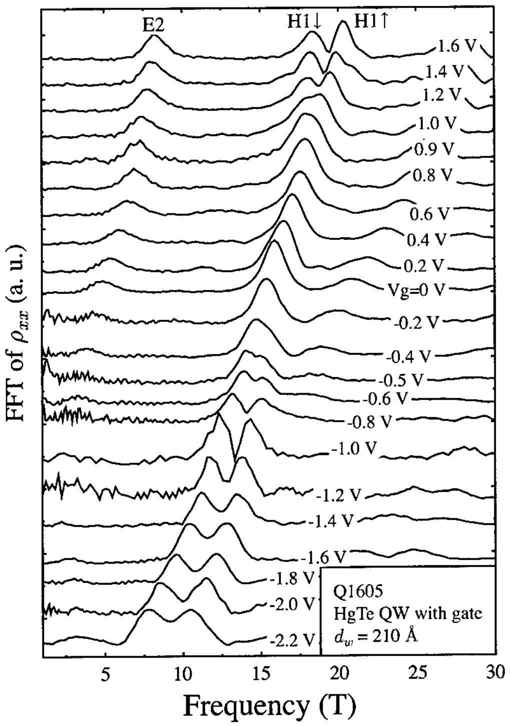

Fig. 6. FFT of SdH oscillations in $\rho_{xx}(B)$ for a n type symmetrically modulation doped HgTe QW (Q1605) measured at 1.6 K and various gate voltages. The up and down arrows represent the two spin states of the H1 subband.

agreement with experiment at lower values of $E_{\mathrm{H1-E1}}$ (5 K) as previously reported [36], however, at higher energies this is not the case [2]. Better agreement with experiment over the entire energy range can only be achieved by assuming that the heavy hole effective mass is also temperature dependent. A least square fit to the experimental values of $E_{\mathrm{H1-E1}}$, which is shown as a solid line in Fig. 5 results in $m^*_{\mathrm{hh}}(1\ 1\ 2)=0.79\pm0.04m_0$ at 300 K [2], see Table 1.

The experimental temperature dependence of $E_{\mathrm{L1-E1}}$ and $E_{\mathrm{H1-E1}}$, as well as that of $E_{\mathrm{H1}}-E_{\mathrm{L1}}$ cannot be explained unless Λ and m^*_{hh} are temperature dependent. Within experimental error the results for the (0 0 1) and the (1 1 2)B orientations are equivalent [2] as can be seen in Table 1, with the exception of the heavy hole effective mass as expected according to Eq. (1) and Eq. (2).

4.3. Magneto-transport; n type modulation doped QWs

As expected from their high electron mobility, all n type, modulation doped QWs show very pronounced SdH oscillations and well developed quantum Hall plateaus [8]. The results of a Fourier transformation of the complex SdH oscillations for the symmetrically modulation doped sample Q1605 with a well width of 21 nm are shown in Fig. 6. At a gate voltage, V_g, of 0.2 V, when the QW potential is nearly symmetric only two frequencies, which correspond to the H1 and E2 subbands, are resolved and no splitting of the H1 subband can be observed. For either more positive or more negative gate voltages, a large splitting of the H1 subband is apparent. Besides the main peaks labelled by E2, H1+ and H1−, peaks due to the sums of the E2 and H1 peaks can be observed. The largest Hall mobility was 6×10^5 cm^2 V^{-1} s^{-1} at a gate voltage of 2.0 V; to our knowledge this is the highest value that has been observed for HgTe QWs.

According to self-consistent band structure calculations the first two conduction subbands are H1 and E2, and the valence band is the H2 subband. This is a consequence of the inverted band structure of QWs with a large well width. No splitting of the H1 and E2 subbands for the symmetric case was predicted and none was observed [8]. However, in the asymmetric case, a small spin splitting of the E2 subband at finite $k_\|$ is predicted as well as a substantially larger splitting of the H1 subband. It should be mentioned here that the two spin split branches of the H1 subband cannot be designated as spin-up and spin-down because their eigenstates are not linearly polarized and do not carry a net magnetic moment [37]. The H1 and E2 subbands which are a mixture of states with different symmetries contain an equal contribution of up and down spinor components at finite $k_\|$. The degeneracy of the H2 valence subband is also removed and one spin component has a larger maximum at finite $k_\|$, i.e. here we are dealing with an indirect semiconductor.

The experimental values and the theoretical calculations of the difference in population, Δn_{H1}, between the two spin states of the H1 subband have been compared. The total carrier density, n_{SdH}, has been employed in the calculations rather than the carrier density in only the H1 subband, n_{H1}, because the electric field $\langle E\rangle$ is, to a good approximation, proportional to n_{SdH}.

The calculated carrier densities in both the H1 and E2 subbands at various gate voltages agree with the experimental values for a well width, d_w, of 21±2 nm. A simulation of the X-ray diffraction results in 22±2 nm, in agreement with the above value. It should be emphasized that the occupation of the E2 subband depends mainly on the well width and not on the details of the self-consistently calculated Hartree potential. Furthermore the well width and hence the calculated carrier densities for two additional QWs, an asymmetric and a symmetric QW, have been corroborated by simulations of the corresponding X-ray diffraction results.

Finally Rashba spin–orbit splitting has also been observed and described quantitatively for a number of QWs in which only one conduction subband is occupied. No abnormal temperature and B dependence has been observed [38], ruling out magneto-intersubband scattering [39].

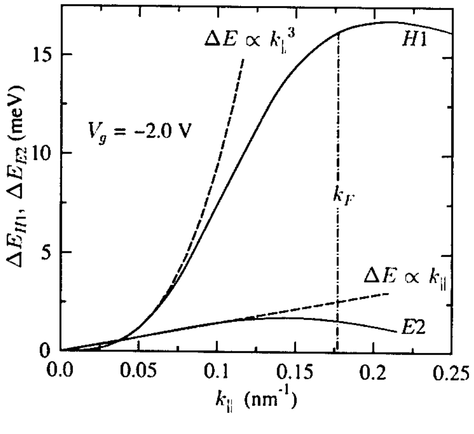

Fig. 7. The calculated spin splitting energy of the H1 and E2 subbands (solid curves), ΔE_{H1} and ΔE_{E2}, versus in-plane wave vector $k_\parallel$ for sample Q1605. The position of the Fermi wave vector k_F is denoted by the dotted-dashed line. The two dashed lines demonstrate the proportionality to $k_\parallel^3$ and $k_\parallel$, respectively, at small $k_\parallel$ values.

Winkler [37] has demonstrated that spin splitting for the heavy hole like state $|\Gamma_8, \pm 3/2\rangle$ should be proportional to $k_\parallel^3$ for small $k_\parallel$ values. The spin split heavy hole subband dispersion can be expressed as

$$E_\pm(k_\parallel) = \frac{\hbar^2 k_\parallel^2}{2m^*} \pm \beta k_\parallel^3 \tag{4}$$

where β is the spin–orbit coupling constant between the Γ_8 and Γ_6 bands. In contrast, spin splitting for the electron like state $|\Gamma_6, \pm 1/2\rangle$ and the light hole like state $|\Gamma_8, \pm 1/2\rangle$, should be a linear function of $k_\parallel$. This is in good agreement with the self-consistently calculated ΔE_{H1} and ΔE_{E2} vs. $k_\parallel$ behavior shown in Fig. 7; the H1 conduction subband in a type III HgTe QW with an inverted band structure is principally a heavy hole state, and the E2 subband is an admixture of the light hole and electron state.

4.4. Magneto-transport; p type modulation doped QWs

Experimental results shown in Fig. 8 for a p type asymmetrically modulation doped QW, Q1441, with an inverted band structures display pronounced and complex SdH oscillations, which begin below 0.3*T*, and well developed quantum Hall plateaus. This QW also has a large mobility, i.e. $\mu = 1.0 \times 10^5$ cm^2 V^{-1} s^{-1}. If dρ_{xx}/dB is plotted vs. $1/B$, two periods can easily be distinguished, which are due to the indirect band gap. A Fast Fourier transformation (FFT) of the SdH oscillations for various hole concentrations in this gated p type QW results in two frequencies corresponding to the concentrations p_1 and p_2. The total hole concentration, p_2, is in good agreement with the Hall concentration at low magnetic fields. $p_2/p_1 = 4$, within experimental uncertainties, for $p_2 < 5 \times 10^{11}$ cm^{-2} [9]. p_2 can be increased up to 1.1×10^{12} cm^{-2}, however, above 5×10^{11} cm^{-2} the peak corresponding to p_1 disappears, in good agreement with theoretical calculations discussed below.

At hole concentrations of less than approximately 5×10^{11} cm^{-2} a contour plot of the intersection of the Fermi energy with that of the first valence subband, H2, results in four equivalent unconnected areas. For $p_2 > 5 \times 10^{11}$ cm^{-2} the Fermi contour resembles a single distorted ring [40]. The experimental results are in good agreement with the theoretical prediction of four equivalent valleys.

4.5. Magneto-transport; n type modulation doped QWs with Mn

QWs with Mn in the upper barrier with different spacer thickness between the HgTe and Hg$_{0.3}$Cd$_{0.68}$Mn$_{0.02}$Te layers have different transport properties; when the spacer is reduced from 15 to 10 nm both the carrier concentration and mobility remain the same within experimental uncertainties or decrease slightly, however, a further reduction to 5 nm causes a significant reduction in these values.

As expected from their high mobilities, well developed SdH oscillations have been observed. Fourier analysis of these spectra reveal two spin split components of the H1 subband as well as the sum frequencies. The population difference between the two spin split components decreases with more positive gate voltages. This is caused by a reduction in the structure inversion asymmetry due to a larger electron concentration and hence a higher Fermi energy. The relative population difference $\Delta n_{H1}/n_{sym}$, where $n_{sym} = n_{H1}$ when $\Delta n_{H1} = 0$, is plotted in Fig. 9 vs. the normalized charge carrier concentration, $(n_{sym} - n_{H1}/n_{sym})$, in order to facilitate a suitable comparison of the QWs with spacer thicknesses of 5, 10 and 15 nm.

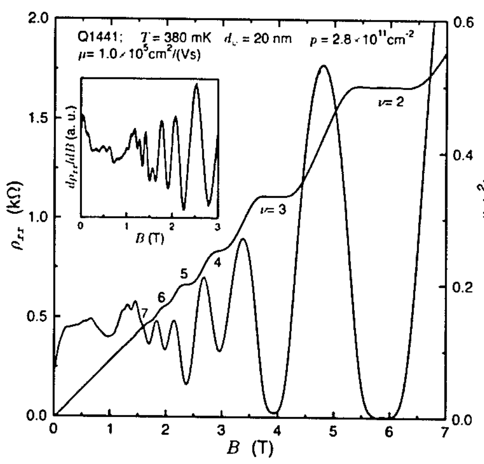

Fig. 8. ρ_{xx} and ρ_{xy} vs. B for a p type asymmetrically modulation doped QW with an inverted band structure at 380 mK. dρ_{xx}/dB is plotted vs. B in the inset.

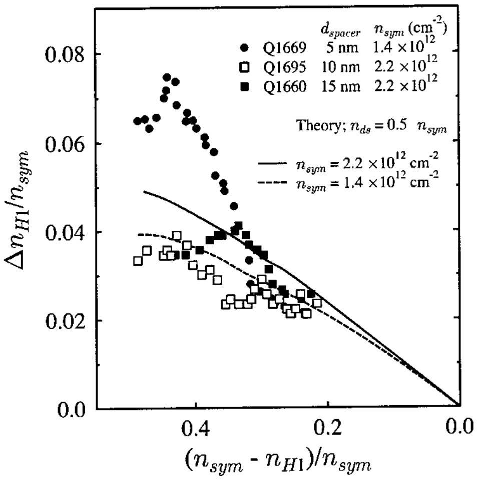

Fig. 9. The relative difference in population of the H1− and H1+ subbands as a function of normalized charge carrier concentration for QWs with spacer thicknesses of 5, 10 and 15 nm.

As can be seen in Fig. 9, theoretical calculations are in good agreement with experiment for the two QWs with thicker spacers. In contrast self-consistent Hartree calculations for the case of a 5 nm spacer, which do not take Mn into account, under estimate the experimental population difference by a factor of approximately 2.

If this enhanced population difference were due to *giant* Zeeman splitting, then it should be strongly temperature dependent [41] contrary to experimental results which show no change between 380 mK and 4.2 K. Therefore we infer that Mn increases the asymmetry of the QW structure and thus enhances Rashba spin–orbit splitting.

In addition to this desired influence of Mn, decreasing the spacer thickness reduces both the 2D electron concentration and the electron mobility. Nevertheless, electron mobilities of 0.6, 0.8 and 1.1×10^5 cm^2 V^{-1} s^{-1} have been achieved when Mn is separated from the well by 5, 10 and 15 nm thick spacers, respectively.

5. Conclusions

Selected aspects of MBE growth of $Hg_{1-x}Cd_xTe$ and $HgTe/Hg_{1-x}Cd_xTe$ heterostructures have been discussed.

By means of an optical investigation of $HgTe/Hg_{1-x}Cd_xTe$ SLs with a normal band structure combined with calculations based on an (8×8 **k·p**) model, it has been demonstrated that the energy separation between the H1–E1 and L1–E1 intersubband transition energies is primarily determined by the valence band offset, Λ, between HgTe and CdTe. This has led to unambiguous values for the offset and its temperature dependence, i.e. $\Lambda(T)=570\pm60$ meV and $d\Lambda/dT=-0.40$ meV/K. Furthermore the energy gap of HgTe at room temperature has also been determined to be -160 meV.

Magneto-transport studies have been performed on both n and p type modulation doped HgTe single QWs with inverted band structure. Rashba spin splitting in n type QWs with an inverted band structure has been investigated at different electron concentrations via a gate voltage. A large Rashba spin splitting has been observed, which is due to the heavy hole nature of the first conduction subband, H1. SdH oscillations of p type QWs display two periods, which have been shown to be due to their indirect band gap and the resulting multiple valleys, and not due to Rashba spin–orbit splitting. Both n and p modulation doped HgTe QWs, have high mobilities of up to 6×10^5 and 1.0×10^5 cm^2 V^{-1} s^{-1}, respectively.

The results of magneto-transport experiments on HgTe QWs with Mn in the upper barrier are in good agreement with self-consistent Hartree calculations when the Mn is separated from the 2D electrons by spacers of 10 and 15 nm. However, the observed population difference of the two spin split states for a QW with a 5 nm spacer is larger than theoretical predictions by at least a factor of two. We conclude that Mn increases the asymmetry of the QW.

Acknowledgments

The support of the Deutsche Forschungsgemeinschaft via SFB 410, the Volkswagen Foundation (X.C. Zhang) and the Max Plank Gesellschaft (Y.S. Gui) is gratefully acknowledged.

References

[1] R.D. Rajaval, D.M. Jamba, J.E. Jensen, J.A. Wilson, J.L. Johnson, E.A. Patten, K. Kosai, P. Goetz, S.M. Johnson, J. Cryst. Growth 184/185 (1998) 1272.
[2] C.R. Becker, V. Latussek, A. Pfeuffer-Jeschke, G. Landwehr, L.W. Molenkamp, Phys. Rev. B 62 (2000) 10353.
[3] M. Dobrowolska, A. Mycielski, W. Dobrowolski, Solid State Commun. 27 (1978) 1233.
[4] V. Latussek, C.R. Becker, G. Landwehr, R. Bini, L. Ulivi, unpublished.
[5] Y. Kim, A. Ourmazd, M. Bode, R.D. Feldman, Phys. Rev. Lett. 63 (1989) 636.
[6] C.R. Becker, V. Latussek, W. Spahn, F. Goschenhofer, S. Oehling, G. Landwehr, in: R.E. Longshore, J.W. Baars (Eds.), Growth and Characterization of Materials for Infrared Detectors, SPIE Proc., vol. 2554, 1995, p. 6.
[7] Y.A. Bychkov, E.I. Rashba, J. Phys. C 17 (1984) 6039.
[8] X.C. Zhang, A. Pfeuffer-Jeschke, K. Ortner, V. Hock, H. Buhmann, C.R. Becker, G. Landwehr, Phys. Rev. B 63 (2001) 245305.
[9] K. Ortner, X.C. Zhang, A. Pfeuffer-Jeschke, C.R. Becker, G. Landwehr, L.W. Molenkamp, Phys. Rev. B, in press.
[10] F. Goschenhofer, J. Gerschütz, A. Pfeuffer-Jeschke, R. Hellmig, C.R. Becker, G. Landwehr, J. Electron. Mater. 27 (1998) 532.
[11] J.P. Laurenti, J. Camassel, A. Bouhemadou, B. Toulouse, R. Legros, A. Lusson, J. Appl. Phys. 67 (1990) 6454.
[12] M. Li, C.R. Becker, R. Gall, W. Faschinger, G. Landwehr, Appl. Phys. Lett. 71 (1997) 1822.

[13] M. Li, R. Gall, C.R. Becker, T. Gerhard, W. Faschinger, G. Landwehr, J. Appl. Phys. 82 (1997) 4860.
[14] D. Fasold, K. Heil, S. Jetschke, Phys. Stat. Sol. A 86 (1984) 125.
[15] L.R. Ram-Mohan, K.H. Yoo, R.L. Aggarwal, Phys. Rev. B 38 (1988) 6151.
[16] N.F. Johnson, H. Ehrenreich, P.M. Hui, P.M. Young, Phys. Rev. B 41 (1990) 3655.
[17] A. Simon, D. Bertho, D. Boiron, C. Jouanin, Phys. Rev. B 42 (1990) 5221.
[18] J.R. Meyer, C.A. Hoffman, F.J. Bartoli, Semicond. Sci. Technol. 5 (1990) S90.
[19] L. De Caro, L. Tapfer, Phys. Rev. B 51 (1995) 4374.
[20] M.H. Weiler, in: R. Willardson, A.C. Beer (Eds.), Semiconductors and Semimetals, 16, Academic Press, New York, 1981, p. 119.
[21] C.K. Shih, W.E. Spicer, Phys. Rev. Lett. 58 (1987) 2594.
[22] J. Schmidt, K. Ortner, J.E. Jensen, C.R. Becker, J. Appl. Phys. 91 (2002) 451.
[23] L. He, C.R. Becker, R.N. Bicknell-Tassius, S. Scholl, G. Landwehr, J. Appl. Phys. 73 (1993) 3305.
[24] K. Ortner, X.C. Zhang, S. Oehling, J. Gerschütz, A. Pfeuffer-Jeschke, V. Hock, C.R. Becker, G. Landwehr, L.W. Molenkamp, J. Appl. Phys. 79 (2001) 3980.
[25] M.A. Berding, A. Sher, J. Electron. Mater. 28 (1999) 799.
[26] S. Oehling, M. Ehinger, T. Gerhard, C.R. Becker, G. Landwehr, M. Schneider, D. Eich, H. Neureiter, R. Fink, M. Sokolowski, E. Umbach, Appl. Phys. Lett. 73 (1998) 3205.
[27] Z. Yang, Z. Yu, Y. Lansari, S. Hwang, J.W. Cook, J.F. Schetzina, Phys. Rev. B 49 (1994) 8096.
[28] C. Tanguy, Phys. Rev. Lett. 75 (1995) 4090, and references therein.
[29] K.A. Harris, R.W. Yanka, L.M. Mohnkern, A.R. Riesinger, T.H. Myers, Z. Yang, Z. Yu, S. Hwang, J.F. Schetzina, J. Vac. Sci. Technol. B 10 (1992) 1574.
[30] J.R. Meyer, A.R. Reisinger, K.A. Harris, R.W. Yanka, L.M. Mohnkern, L.R. Ram-Mohan, J. Cryst. Growth 138 (1994) 981.
[31] C.L. Cesar, M.N. Islam, R.D. Feldman, R.F. Austin, D.S. Chemla, L.C. West, A.E. DeGiovanni, Appl. Phys. Lett. 56 (1990) 283.
[32] G.L. Hansen, J.L. Schmit, T.N. Casselman, J. Appl. Phys. 53 (1982) 7099.
[33] M. von Truchsess, V. Latussek, C.R. Becker, E. Batke, J. Cryst. Growth 159 (1996) 1128.
[34] R. Sporken, S. Sivananthan, J.P. Faurie, D.H. Ehlers, J. Fraxedas, L. Ley, J.J. Pireaux, R. Caudano, J. Vac. Sci. Technol. A 7 (1989) 427.
[35] D. Eich, K. Ortner, U. Groh, Z.N. Chen, C.R. Becker, G. Landwehr, R. Fink, E. Umbach, Phys. Stat. Sol. A 173 (1999) 261.
[36] C.R. Becker, V. Latussek, M. Li, A. Pfeuffer-Jeschke, G. Landwehr, J. Electron. Mater. 28 (1999) 826.
[37] R. Winkler, Phys. Rev. B 62 (2000) 4245.
[38] X.C. Zhang, A. Pfeuffer-Jeschke, K. Ortner, C.R. Becker, G. Landwehr, Phys. Rev. B 65 (2002).
[39] T.H. Sander, S.N. Holmes, J.J. Harris, D.K. Maude, J.C. Portal, Phys. Rev. B 58 (1998) 13856.
[40] G. Landwehr, J. Gerschütz, S. Oehling, A. Pfeuffer-Jeschke, V. Latussek, C.R. Becker, Physica E 6 (2000) 713.
[41] D. Keller, D.R. Yakovlev, B. König, W. Ossau, Th. Gruber, A. Waag, L.W. Molenkamp, Phys. Rev. B 65 (2002).

ELSEVIER

Thin Solid Films 412 (2002) 139

www.elsevier.com/locate/tsf

Author Index of Volume 412

PII: S0040-6090(02)00463-7

ELSEVIER

Thin Solid Films 412 (2002) 140–141

www.elsevier.com/locate/tsf

Subject Index of Volume 412

PII: S0040-6090(01)00464-9

Guide for Authors

Manuscript Preparation

Three copies of the manuscript should be submitted, in doublespaced typing on pages of uniform size with a wide margin on the left. Some flexibility of presentation will be allowed but authors are urged to arrange the subject matter clearly under such headings as Introduction, Experimental details, Results, Discussion, etc. Each paper should have an abstract of 100–200 words.

References should be numbered consecutively (numerals in square brackets) throughout the text and collected together in a reference list at the end of the paper. Journal titles should be abbreviated according to the Chemical Abstracts Service Source Index, 1970 edition, and supplements. The abbreviated title should be followed by volume number, year (in parentheses) and page number.

Authors in Japan please note that information about how to have the English of your paper checked, corrected and improved (before submission) is available from: Elsevier Science Japan, Editorial Service, 1-9-15 Higashi Azabu, Minato-ku, Tokyo 106, Japan; Tel: +81 3 5561 5032; Fax: +81 3 5561 5045; E-mail: info@elsevier.com

Submission of Papers

Manuscripts (original, two clear copies and accompanying diskette (MS-DOS or MAC format)) should be sent to: EDITORIAL OFFICE of *THIN SOLID FILMS,* Département de génie physique, École Polytechnique de Montréal, C.P. 6079, Succursale Centre-ville, Montréal, QC, CANADA H3C 3A7 Tel: (+1) 514-340-3730; Fax: (+1) 514-340-3218; e-mail: tsf@polymtl.ca

All the authors of a paper should sign the covering letter. Contributions are accepted on the understanding that the authors have obtained the necessary authority for publication. Submission of a manuscript implies that it is not under consideration for publication elsewhere.

Submission of Electronic Text

The final text should be submitted on a 3.5 in or 5.25 in diskette (in addition to a hard copy with original figures). Double density (DD) or high density (HD) diskettes formatted for MS-DOS or Apple Macintosh compatibility are acceptable, but must be formatted to their capacity before the files are copied on to them. The files should be saved in the native format of the wordprocessing program used. Most popular wordprocessor file formats are acceptable. It is essential that the name and version of the wordprocessing program, type of computer on which the text was prepared, and format of the text files are clearly indicated.

Illustrations

Line drawings should be in a form suitable for reproduction, drawn in black ink on drawing paper (letter height, 3–5 mm). They should preferably all require the same degree of reduction, and should be submitted on paper of the same size as, or smaller than, the main text to prevent damage in transit. Photographs should be submitted as clear black-and-white prints on glossy paper. Each illustration must be clearly numbered.

Illustrations can be printed in colour when they are judged by the Editor to be essential to the presentation. The publisher and the author will each bear part of the extra costs involved. Further information concerning colour illustrations and the costs to the author can be obtained from the publisher.

Legends to the illustrations must be submitted in a separate list.

All tables and illustrations should be numbered consecutively and separately throughout the paper.

Language

Papers will be published in English only.

Proofs

Authors will receive proofs, which they are requested to correct and return as soon as possible. Authors should answer clearly any question in the proofs. No new material may be inserted in the text at the time of proofreading. Elsevier will do everything possible to get your article corrected and published as quickly and accurately as possible. Therefore, it is important to ensure that all of your corrections are sent back to us in one communication. Subsequent corrections will not be possible, so please ensure your first sending is complete.

Offprints

Twenty-five offprints will be supplied free of charge to the author(s). Additional offprints can be ordered at prices shown on the offprint order form which accompanies the proofs.

Further Information

For enquiries relating to the submission of articles (including electronic submission), author Frequently Asked Questions and any other enquiries relating to Elsevier Science, please consult http://www.elsevier.com/locate/authors/

For specific enquiries on the preparation of electronic artwork, consult http://www.elsevier.com/locate/authorartwork/

Contact details for questions arising after acceptance of an article, especially those relating to proofs, are provided when an article is accepted for publication.

The full and complete Instructions to Authors can be found on the World Wide Web: access under http://www.elsevier.com/locate/tsf

Abstracting – Indexing Services

This journal is cited by the following Abstracting and/or Indexing Services.

Metal Abstracts, Chemical Abstracts, INSPEC-Physics Abstracts, Current Contents — Physical and Chemical Sciences, Current Contents —Engineering, Technology and Applied Sciences, Engineering Index, Cambridge Scientific Abstracts, Physikalische Berichte, Science Citation Index, Research Alert™, PASCAL (Centre National de la Recherche Scientifique), Fiz Karlsruhe.

Pre-publication abstracts of articles in Thin Solid Films and other related journals are now available weekly in electronic form via CoDas, a new direct alerting service in condensed matter and materials science run jointly by Elsevier Science Publishers and